THE UNIVERSITY *of* EDINBURGH

(Sub)millimetre-Selected Galaxies and the Cosmic Star-Formation History

Maciej Koprowski

A thesis submitted in fulfilment of the requirements
for the degree of Doctor of Philosophy
to the
University of Edinburgh
March 2015

Abstract

Understanding the time evolution of the star formation in the Universe is one of the main aims of observational astronomy. Since a significant portion of the UV starlight is being absorbed by dust and re-emitted in the IR, we need to understand both of those regimes to properly describe the cosmic star formation history. In UV, the depth and the resolution of the data permits calculations of the star formation rate densities out to very high redshifts ($z \sim 8-9$). In IR however, the large beam sizes and the relatively shallow data limits these calculations to $z \sim 2$.

In this thesis, I explore the SMA and PdBI high-resolution follow-up of 30 bright sources originally selected by AzTEC and LABOCA instruments at 1.1 mm and 870 μm respectively in conjunction with the SCUBA-2 Cosmology Legacy Survey (S2CLS) deep COSMOS and wide UDS maps, where 106 and 283 sources were detected, with the signal-to-noise ratio of > 5 and > 3.5 at 850 μm respectively. I find that the (sub)mm-selected galaxies reside and the mean redshifts of $\bar{z} \simeq 2.5 \pm 0.05$ with the exception of the brightest sources which seem to lie at higher redshifts ($\bar{z} \simeq 3.5 \pm 0.2$), most likely due to the apparent correlation of the (sub)mm flux with redshift, where brighter sources tend to lie at higher redshifts. Stellar masses, $M_\star$, and star formation rates, SFRs, were found ($M_\star \gtrsim 10^{10}\,M_\odot$ and SFR $\gtrsim 100\,M_\odot\ yr^{-1}$) and used to calculate the specific SFRs. I determine that the (sub)mm-selected sources mostly lie on the high-mass end of the star formation 'main-sequence' which makes them a high-mass extension of normal star forming galaxies. I also find that the specific SFR slightly evolves at redshifts $2-4$, suggesting that the efficiency of the star formation seems to be increasing at these redshifts.

Using the S2CLS data, the bolometric IR luminosity functions (IR LFs) were found for a range of redshifts $z = 1.2-4.2$ and the contribution of the SMGs to

the total star formation rate density (SFRD) was calculated. The IR LFs were found to evolve out to redshift ~ 2.5. The star formation activity in the Universe was found to peak at $z \simeq 2$ followed by a slight decline. Assuming the IR to total SFRD correction found in the literature the SFRD found in this work closely follows the best-fitting function of Madau & Dickinson (2014).

Declaration

Except where otherwise stated, the research undertaken in this thesis was the unaided work of the author. Where the work was done in collaboration with others, a significant contribution was made by the author. Also, this work has not been submitted for any other degree or professional qualification except as specified.

M. Koprowski
30th March 2015

Acknowledgements

First of all, I would like to thank my supervisors, Jim Dunlop and Michał Michałowski both for the fantastic opportunity you have given me, and for your guidance and patience throughout this journey. You have shown me what it means to be a top-notch and yet a humble researcher, have given me the best example of academic excellence and professionalism, and I can not describe how much I have learned from you. A big thanks to Isaac Roseboom and Ross McLure for many helpful scientific talks and to Michele Cirasuolo for all his help in this research.

I am also grateful to the postdocs and fellow Ph.D. students with whom I had many interesting discussions. Thanks to Jos Sabater Montes, Sylvain de la Torre, Fernando Buitrago, Eric Tittly, Esther Marmol-Queralto, Victoria Bruce, Tom Target, Pratika Dayal, Joao Ferreira, Rebecca Bowler, Vinod Arumugam, Marika Asgari, Jack Mayo and all the rest of the team. Thanks to the IfA computing support staff lead by Horst Meyerdierks and John Barrow, as well as world best administrators Paula Wilkie, Nathalie Dupin and Jane Patterson. So many people have helped me stay focused and motivated during the last four years, for which I am humbled and very grateful. Special thanks to Agnieszka Jallow and Michał Kepa who helped me relax, forget my worries for a few hours and helped me recharge my batteries. Special thanks to my beloved friends back home: Adam i Lidia Janic, Michał Gac, Ania i Grzegorz Domaradzcy, Łukasz Tarnowski, Krzysztof Matuskiewicz, Bartek i Dana Jakubek and the whole Lump Ekipa. When we are all together, it is the best time anyone can ask for. Thank you for all the fun moments, every summer and winter that you have helped me unwind, for making me laugh breathlessly, for all the little things. I want to share this achievement with all of you.

A very special thanks to my parents Zofia and Zbigniew, my sister Dominika

and her husband Paweł and most importantly my dear wife Madzia and son Franio. It is you whom I should thank for having a chance of being in Scotland and pursuing my dream. Your lifelong dedication, commitment and support have allowed me to reach this stage and for this I am eternally grateful. I dedicate this work to you.

Above all however, I wholeheartedly thank God Almighty, Father of Jesus Christ for giving me the opportunity of studying His beautiful Universe and for all the grace He has shown me throughout the years. Nothing I have done would be possible without His help. It is His very love that is the biggest mystery of all.

Contents

List of Figures

List of Tables

Chapter 1

Introduction

1.1 Selection of Submillimetre Galaxies

1.1.1 What are Submillimetre Galaxies?

One of the key objectives of observational astronomy has been to understand the history of the star formation in the Universe. Young and massive stars emit their light in the ultraviolet (UV) band and while this band has been used as the most natural tracer of star formation it has become increasingly evident that a significant portion of the starlight is being emitted in the far-infrared (FIR) and submillimetre (submm) wavebands (Dole et al., 2006).

The Far-InfraRed Absolute Spectrophotometer (*FIRAS*) aboard the space-based Cosmic Background Explorer (*COBE*) as well as the *IRAS* observations in the early 90s and 80s showed that the Universe emits as much energy in the FIR/submm wavelengths as it does in the UV. This simply means that if we focus on the UV alone, we will miss roughly half of the star formation activity of the Universe. It has been realised that there must be either a population of the galaxies enshrouded in the dust or/and galaxies with dust-enshrouded regions in which the bulk of the galaxy star formation occurs. The UV light coming from these newly formed stars is being absorbed by the dust and then reemitted as heat in the FIR and submm.

Such a late discovery of the IR background by *COBE* was caused by two main observational limitations: the water vapour in the atmosphere allows the FIR/submm observations to be conducted only from high and dry places on Earth

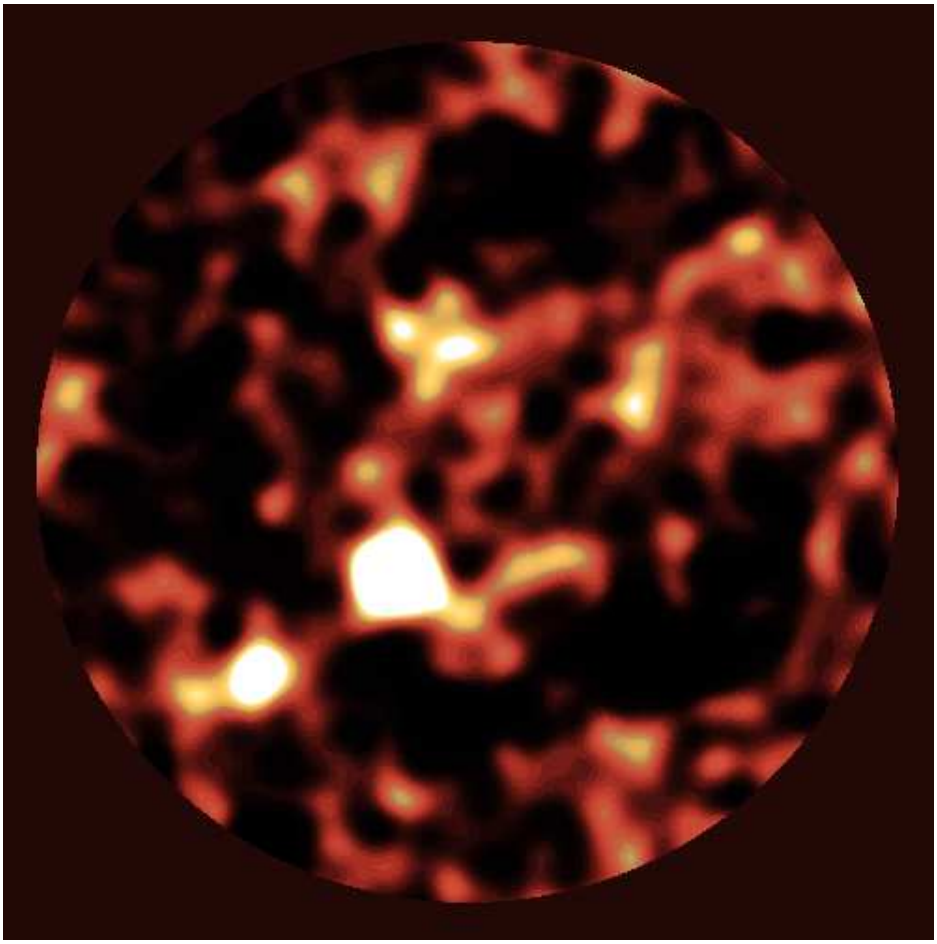

Figure 1.1: *The 850 μm SCUBA image of the Hubble Deep Field. The image shows a radius of 100 arcsec from the map centre and is orientated with North upwards and East to the right. It reveals that the cosmic infrared background consists of individual, primordial, dust-enshrouded galaxies - submillimetre galaxies (SMGs) from when the Universe was about one fifth of its current age. Figure adopted from Hughes et al. (1998).*

or from space and the poor resolution of the detectors at these wavelengths requires very large diameter telescopes to be used. Still, since the original *COBE* observations, submm astronomy has grown very rapidly. In the late 90s the Submillimetre Common-User Bolometer Array (SCUBA) on the James Clerk Maxwell Telescope (JCMT) discovered at 850 μm that the IR background consists of individual galaxies, called submillimetre galaxies (SMGs, Figure 1.1). Later work revealed that SMGs have huge far-infrared luminosities ($> 10^{11}$ $L_{\odot}$), tremendous star formation rates ($\sim 100-1000$ $M_{\odot}$ yr^{-1}) and lie at high redshifts with $\bar{z} \simeq 2$ (see Blain et al. 2002 and Casey, Narayanan, & Cooray 2014 for a review).

1.1.2 (Sub-)millimetre Facilities, Instruments and Most Important Surveys

Since the SCUBA discovery of the first SMGs we have witnessed a real explosion of submm astronomy. Table 1.1 lists the single-dish instruments used for SMGs discovery at wavelengths longward and including 250 μm. These include the MAx-planck Millimetre BOlometer (MAMBO) at the Institut de Radioastronomie Millimtrique (IRAM) 30 m Telescope at Pico Veleta in southern Spain, the BOLOmeter CAMera (Bolocam) at the Caltech Submillimetre Observatory (CSO), the Balloon-borne Large Aperture Submillimetre Telescope (BLAST), the Spectral and Photometric Imaging Receiver (Spire) aboard the *Herschel Space Observatory*, the Astronomical Thermal Emission Camera (AzTEC) operational in turn at the JCMT, the Atacama Submillimeter Telescope Experiment (ASTE) and the Large Millimetre Telescope (LMT), the Large Apex Bolometer Camera (LABOCA) at the Atacama Pathfinder EXperiment (APEX) telescope in Chile, the Atacama Cosmology Telescope (ATC) installed on Cerro Toco in Chile in 2007, the South Pole Telescope (SPT) located at the geographic south pole in Antarctica, the Submillimetre Apex BOlometer CAmera (SABOCA) operating at 350 μm at APEX on Cerro Chajnantor in Chile, the Goddard-Iram Superconducting 2-Millimetre Observer (GISMO) at IRAM 30m telescope in Spain and the Submillimetre Common User Bolometer Array-2 (SCUBA-2) at JCMT in Hawaii.

The most important submm surveys performed using the above-mentioned instruments are summarized in Table 1.2. They clearly differ in both survey area

Table 1.1: *Single-dish instruments used for SMG discovery. Table adopted from Casey et al. (2014).*

Instrument	Telescope	Years Active	Beam size /arcsec	Wavebands	1σ /mJy	Reference
SCUBA	JCMT	1997-2005	15	850 μm	1	Holland et al. (1999)
			7	450 μm	30	
SHARC	CSO	1997-2003	8	350 μm	...	Wang et al. (1996)
			10	450 μm	...	
SHARC-II	CSO	2003-	8	350 μm	...	Dowell et al. (2003)
			10	450 μm	...	
MAMBO-1	IRAM 30 m	1998-2002	11	1.2 mm	0.8	Kreysa et al. (1999)
MAMBO-2	IRAM 30 m	2002-2011	11	1.2 mm	0.8	
BOLOCAM	CSO	2002-2013	30	1.1 mm	1.9	Laurent et al. (2005)
BLAST	BLAST	2008	33	250 μm	18	Devlin et al. (2009)
			46	350 μm	13	
			66	500 μm	12	
SPIRE	*Herschel*	2009-2013	18	250 μm	5.8	Griffin et al. (2010)
			26	350 μm	6.3	
			36	500 μm	6.8	
AzTEC	JCMT	2005-2006	19	1.1 mm	1.5	Wilson et al. (2008)
	ASTE	2007-2008	29	1.1 mm	1.2	
	LMT 32 m	2011-2015	9	1.1 mm	...	
	LMT 50 m	2015-	6	1.1 mm	...	
LABOCA	APEX	2006-	19	870 μm	1.2	Siringo et al. (2009)
ACT	ACT	2007-	54	1.1 mm	6.0	Swetz et al. (2011)
			69	1.4 mm	3.7	
			98	2.0 mm	2.3	
SPT	SPT	2008-	69	2.0 mm	1.3	Mocanu et al. (2013)
			63	1.4 mm	3.4	Vieira et al. (2010)
SABOCA	APEX	2009-	8	350 μm	30	Siringo et al. (2010)
GISMO	IRAM 30 m	2011-	24	2.0 mm	0.1	Staguhn et al. (2012)
SCUBA-2	JCMT	2011-	15	850 μm	0.25	Holland et al. (2013)
			7	450 μm	1.5	

and depth. However, for most FIR/(sub)mm wavebands, the depth itself does not translate directly into the source detection rate. Galaxy's flux density at any given wavelength depends on its intrinsic luminosity as well as on the redshift and the dust temperature, i.e. the shape of the spectral energy distribution (SED). Moreover, the correct estimates of the physical properties of the galaxies discovered in a given survey will depend on the successful multi-wavelength identification. How will all these effects impact the results of a survey? What biases do we have to be aware of before reaching conclusions about a given galaxy population? The next two subsections address these issues in detail. The variations in SEDs will be explained in 1.1.3 and the multi-wavelength identification process in 1.1.4.

1.1.3 Variations in Spectral Energy Distributions

The observed flux density of a galaxy in a given waveband (with the exception of $\sim 850\mu$m) depends primarily on its distance. In addition however, the Universe itself expands which causes the redshifting of the incoming light. These effects are schematically shown in Figure 1.2. The SED of the local galaxy Arp220 is plotted for different redshifts. It can be seen that at millimetre wavelengths the effect of redshifting counters the decreasing flux and therefore galaxies can be probed up to very high redshifts. This is called the K-correction and needs to be taken into account when talking about the perceived completeness of a given survey. Surveys conducted at wavelengths of $\sim 250\,\mu\text{m} - 500\,\mu\text{m}$ are mostly sensitive to low redshift sources as oppose to the (sub)mm surveys conducted at longer wavelengths.

A similar effect is seen when considering the effective dust temperature of the galaxy. It has been found that SMGs' dust temperature varies between $10 - 60$ K (Michałowski et al., 2010a,b). Because the emission from the warmer dust is more luminous and peaks at shorter wavelengths, increasing the temperature of the dust has virtually the same effect on the dust emission curve as decreasing the redshift (dust temperature-redshift degeneracy). Galaxies with given luminosity and warmer dust (~ 50 K) will be less likely to be detected at 850 μm.

Table 1.2: *Single-dish submm surveys.*

Instrument	Wavebands	Fields	Area	Reference
SCUBA	450 μm 850 μm	A370 & CI 2244-02	~ 10 arcmin^2	Smail et al. (1997)
SCUBA	850 μm	Lockman Hole SSA13	~ 6 arcmin^2 ~ 6 arcmin^2	Barger et al. (1998)
SCUBA	850 μm	HDF	~ 9 arcmin^2	Hughes et al. (1998)
SCUBA	850 μm	7 cluster fields	45 arcmin^2	Smail et al. (1998)
SCUBA	850 μm	ELAIS N2 & Lockman Hole East	260 arcmin^2	Scott et al. (2002)
SCUBA	850 μm	HDF-N	165 arcmin^2	Borys et al. (2003)
SCUBA	850 μm	CUDSS	60 arcmin^2	Webb et al. (2003)
MAMBO	1.2 mm	Elais N2 & Lockman Hole	160 arcmin^2	Greve et al. (2004)
MAMBO	1.2 mm	COSMOS	400 arcmin^2	Bertoldi et al. (2007)
MAMBO	1.2 mm	GOODS-N	287 arcmin^2	Greve et al. (2008)
AzTEC	1.1 mm	COSMOS	0.15 deg^2	Scott et al. (2008)
LABOCA	870 μm	CDFS	0.25 deg^2	Weiß et al. (2009b)
BLAST	250 μm 350 μm 500 μm	ECDFS	10 deg^2	Devlin et al. (2009)
SPT	1.4 mm	...	87 deg^2	Vieira et al. (2010)
SCUBA	850 μm	Lockman Hole East SXDF	0.1 deg^2 0.1 deg^2	Coppin et al. (2006)
AzTEC	1.1 mm	Lockman Hole East SXDF	0.66 deg^2 0.81 deg^2	Austermann et al. (2010)
SPIRE	250 μm 350 μm 500 μm	H-ATLAS	~ 570 deg^2	Eales et al. (2010)
MAMBO	1.2 mm	Lockman Hole North	566 arcmin ^{2}	Lindner et al. (2011)
AzTEC	1.1 mm	COSMOS	0.72 deg^2	Aretxaga et al. (2011)
SPIRE	250 μm 350 μm 500 μm	HerMES	~ 380 deg^2	Oliver et al. (2012)
SCUBA-2	450 μm	UDS & COSMOS	210 arcmin^2	Roseboom et al. (2013) Geach et al. (2013)

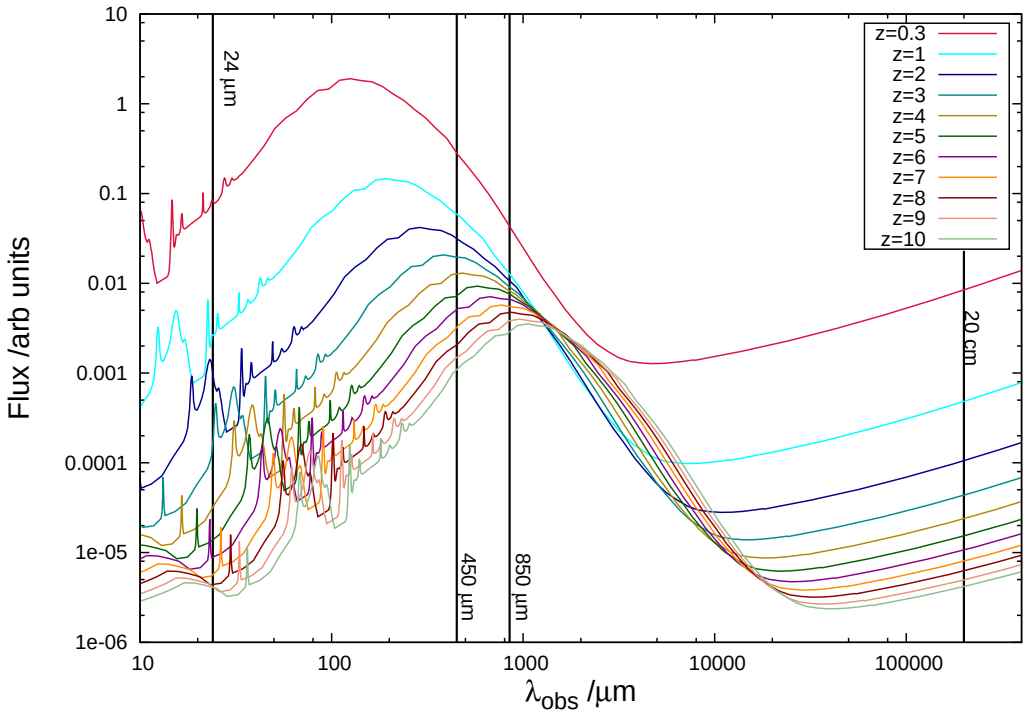

Figure 1.2: *The SEDs of the local galaxy Arp220 for a range of redshifts. The vertical lines depict the observed wavebands of 24 μm, 450 μm, 850 μm and 20 cm. It can be seen that as we go towards higher redshifts the galaxy becomes fainter. What is interesting is that at the observed wavelength of 850 μm the decreasing flux density is countered by the redshifting of the whole SED. This effect is called the negative K-correction.*

1.1.4 Multi-wavelength Identification & Multiplicity

The previous subsection described how the intrinsic variations in SEDs impact the redshift completeness of the survey conducted at the given wavelength. Another process that can affect the interpretation of a given population is the identification of the galaxy counterparts at other wavebands, which is crucial for the correct determination of its physical characteristics. The beam size for single-dish telescopes is so large that one cannot simply pick the closest optical counterpart; rather we must utilize statistical methods (Figure 1.3). For the reasons stated below, radio and 24 μm (with the occasional addition of the 8 μm) bands are most often used for finding the most probable counterparts. The beam sizes in these bands are much smaller than the submm beam which allows the direct comparison with the optical catalogues.

Radio counterparts: This was the most widely used band for identifying submm couterparts. The main reason is that the interferometric observations at this wavelength are much easier than in the submm due to the much better atmospheric transmission. Also, because the irregularities in the surface of the dish must not be larger than $\sim 1/10$ th of the wavelength at which we observe (which in radio translates to ~ 2 cm), building radio telescopes is much easier. For these reasons most of the fields observed at submm have already been surveyed by radio arrays at 1.4 GHz (20 cm) like the Very Large Array (called now the Jansky Very Large Array after being largely rebuilt and expanded).

Searching for the submm counterparts in the radio band is motivated by the correlation between the radio and submm emission, described first in Helou et al. (1985) and Condon (1992). As explained in subsection 1.1.1 the submm emission traces mainly the star formation (it can also indicate the AGN activity but mostly in the MIR regime) , where the UV light coming from newly formed stars gets absorbed by dust and reemitted as heat. The radio band is sensitive to the synchrotron emission coming from the relativistic electrons escaping supernovae and as such is also the tracer of the recent star formation. Even though the physics of this correlation is still debated, the effect is real and seems to be undergoing very little evolution up to high redshifts (Murphy, 2009).

The advantage of matching the submm source to a radio counterpart is that, with the current depth of radio data, the space density of radio sources is very

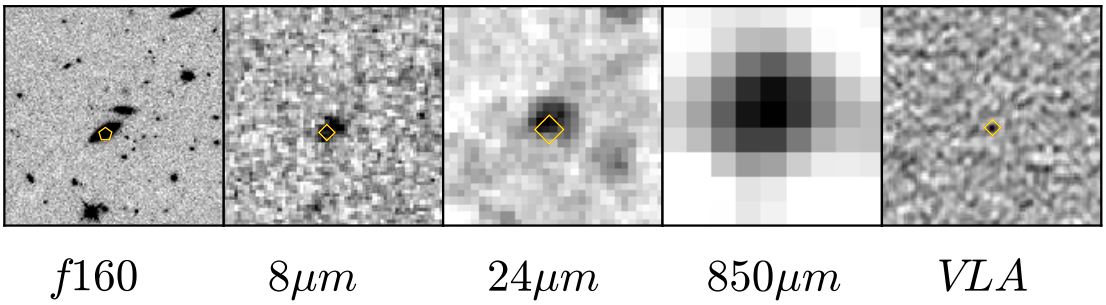

Figure 1.3: *Stamps of one of the the SMG observed in the COSMOS field with SCUBA-2 (Koprowski et al. 2014 in prep.). From left to right we have the HST* $f160$*, Spitzer IRAC 8* μm *and MIPS 24* μm*, JCMT SCUBA-2 850* μm *and VLA 1.4GHz. The large search radius (see Section 2.2) in 850* μm *makes it impossible to directly identify an optical counterpart and therefore other bands must be used. The yellow symbol depicts the most probable counterpart. Even though the 850* μm *and 24* μm *may indicate that the optical counterpart is the upper object in the* $f160$ *stamp, the radio ID is what gives the most probable counterpart with the most accurate coordinates and therefore drives the choice of the optical ID in this particular case.*

low ($\leq$ 1 source inside the search radius, see Section 2.2). This is in contrast with the optical band, where there is most often more than one source present. With the radio beam sizes of ~ 2 arcsec (as oppose to $\sim 15-20$ arcsec in single-dish submm imaging) identifying the optical counterpart is a much more precise process (see Figure 1.3).

The main disadvantage is that most of the faint submm sources do not have radio counterparts. As seen in Figure 1.2, in the radio we observe a very strong positive K-correction which means that it is very difficult to observe an SMG in the radio at high redshifts. This implies that the results of the submm surveys which rely on this correlation will be biased towards low redshift sources. Another possible reason may be that some of the SMGs are simply blends of a couple or few fainter sources (explained at the end of this subsection) which are then individually too faint to be seen in the higher resolution radio imaging.

24 μm counterparts: Another waveband used for the identification of the submm counterparts is the *Spitzer* MIPS 24 μm band. This band is sensitive to warm dust and since SMGs have been found to be massive, dusty galaxies, they are expected to be luminous in this band (Ivison et al., 2010). Despite the rough correlation between far-IR and mid-IR emission, there are couple of problems that need to be mentioned here. As seen in Figure 1.2, for sources at z $<$ 4 the warm dust continuum is being affected by the emission and absorption features from Polycyclic Aromatic Hydrocarbons (PAHs) and silicates which alter the detection

limits for a given redshift. Furthermore, the density of objects at 24 μm is much higher than in the radio, although still much lower than in the optical. Still, since there is so much more data available in 24 μm, it has been the most obvious second choice for submm counterpart matching.

8 μm counterparts: In order to maximise the ID success rate the IRAC 8.0 μm band is often explored. This band traces the rest-frame near-IR light coming from the old population of stars in SMGs. Since SMGs are massive and have been found to have a highly evolved stellar population, it is expected that they will be luminous in this waveband (Dye et al., 2008; Michałowski et al., 2010a; Biggs et al., 2011; Wardlow et al., 2011).

Counterparts matching: Because of the high density of sources (in both 24 and 8 μm bands), the closest counterpart matching is not sufficiently accurate. For these reasons techniques have been developed which can assess the statistical robustness of a given match.

The likelihood ratio (LR) attempts to quantify the probability that the potential counterpart to the submm peak is real, given its measured properties (e.g. radial offset, flux density, colour, etc.), versus the probability that it is a chance association (given the background source counts as a function of measured properties). This could be written as:

$$L = \frac{q(m,c)f(r)}{n(m,c)}, \tag{1.1}$$

where $q(m,c)$ is the probability distribution function of counterparts with mangitude m and 'type' c, where 'type' may be a discrete variable (star/galaxy), a continuous variable (colour) or may be redundant, $n(m,c)$ is the probability distribution of the 'background' sources with magnitude m and 'type' c and $f(r)$ is the probability distribution function of the positional errors of the submm sources. This method was developed by Sutherland & Saunders (1992) with additional improvements in Chapin et al. (2011) and Roseboom et al. (2013).

Similar to the LR method is the calculation of "*p-values*", or the corrected Poissonian probability, where within a given search radius one assesses the probability of a given population counterpart (e.g. 24 μm, 8 μm, radio) being there by chance. This technique was described in Downes et al. (1986) and is

described in detail in Section 2.2.

Multiplicity: The last main factor that can alter the results of a survey is the multiplicity of submm sources. This effect is most prominent in confusion-limited surveys (see subsection 1.2.1 for details), where the density of faint sources is so high that one expects to find more than one submm object within the area of the beam. This means that some of the brightest SMGs may in fact be multiples of a few fainter sources. Using the Submillimetre Array (SMA) interferometric observations Wang et al. (2011) found that a significant fraction of SMGs are in fact multiples. The most important work in this field was done in ALMA Cycle 0 where 122 870 μm sources were observed in the Extended Chandra Deep Field South (ECDFS) from the Laboca LESS survey (Weiß et al., 2009b). Hodge et al. (2013) and Karim et al. (2013) found that $30\% - 50\%$ of these SMGs break into multiple objects (Figure 1.4). Careful investigation of the ALMA data however, reveals that multiplicity is in fact not common and that only $\sim 10\%$ of brightest sources for which Hodge et al. (2013) report ALMA results, are showing a significant (e.g. $> 20\%$) flux contribution from a secondary component (Koprowski et al., 2014). Hezaveh et al. (2013) and Chen et al. (2013a) found in their work that only $\sim 10\%$ of > 10 mJy SMGs are in fact multiples. We are still to find out, with the arrival of much larger, statistically significant samples available with SCUBA-2 and ALMA, how exactly does the multiplicity affect the results of submm surveys.

1.2 Submillimetre Maps

1.2.1 Confusion Noise

In the previous section the submillimetre galaxies (SMGs) were introduced. The instruments and most prominent submm surveys were named and the most important biases, that have to be taken into account when interpreting the submm data, were explained. In this section I will describe the issues connected to working with submm maps.

One very important effect which ultimately limits the depth of any astronomical map is the confusion noise. It arises when the density of sources is so high that there are in fact many sources within the area of the beam masquerading

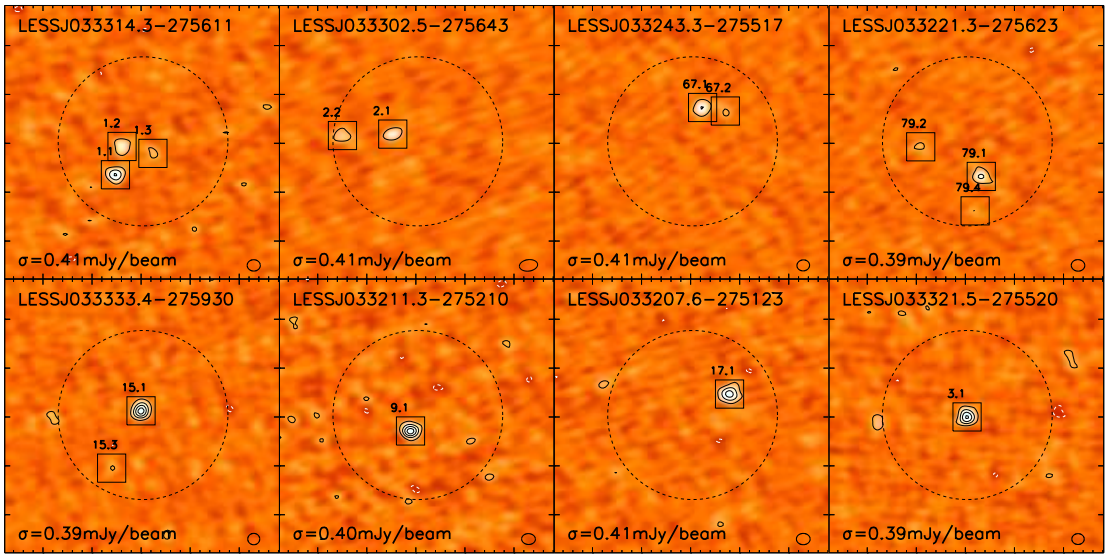

Figure 1.4: *Examples of the 870-m ALMA continuum maps towards eight of the submillimetre sources from the LESS survey from Karim et al. (2013). The two top-left corner sources are the two brightest LESS objects which proved to be multiples of three and two less luminous galaxies. As claimed by Karim et al. (2013) this work shows that multiplicity is very common. However, only* $\sim 10\%$ *of sources actually consist of more than one significantly bright object (contributing more than 20% of the original flux). Figure adopted from Karim et al. (2013).*

as one submm object. Since faint sources are much more numerous than the bright ones (see Figures 1.5 and 1.6), there will be a limit to the depth of the map, beyond which it will become confusion limited. This is currently not an issue in optical observations as the beam sizes are very small. In submm imaging however, it is an important effect and has to be taken into account. Even though the instrument might be able to integrate longer to decrease the instrumental noise, there will always be the ultimate threshold enforced by the confusion limit of the telescope.

1.2.2 Monte Carlo Simulations

Monte Carlo simulations are generaly used to characterize completeness, bias and false positive rates for the identification of the individual point sources in a submm map (Eales et al., 2000; Scott et al., 2002; Cowie et al., 2002). This technique has been used, amongst others, for the SCUBA HDF survey (Borys et al., 2003), the SCUBA SHADES survey (Coppin et al., 2006) and the *Herschel* HerMES survey (Smith et al., 2012). It is based on the injection of fake sources into the

noise-only maps. The distribution of the sources' spatial and flux densities is a free parameter, accuracy of which is determined by comparing the source-injected maps with the real one. The smaller the differences between the maps, the more correct the input parameters.

The noise-only maps are created by dividing a given submm data set into two halves and subtracting one from the other, with the noise scaled down accordingly (as such a subtraction represents an integration time of only $T/2$). The resulting map is called the 'jackknife' map and represents pure noise. Since the real sources are present in both halves of the data, they should no longer appear in the noise-only map.

The individual delta function sources are convolved with the appropriate beam and injected into the 'jackknife' map at random positions. For this purpose the functional form of the input population (sources per unit flux density per unit sky area, dN/dS) has to be assumed (see subsection 1.2.4). The map is then analysed for source detection (in a same manner as the real map). Whatever the functional form, the free parameters of dN/dS are being adjusted via the iterative Monte Carlo method until the differences between the simulated and real maps are minimised. In the same manner various other observational parameters may be found.

1.2.3 Estimation of Observational Parameters

Deboosted Flux Densities: There are two ways in which the flux of the source may be boosted. The first one is the statistical boosting, so called Eddington boosting (first described in Eddington 1913), which is caused by the statistical variations of the true values of galaxies' flux densities. This effect relies on the fact that there are many more low-flux sources than high-flux ones and therefore a galaxy of a given, observed flux density is much more likely an object with the observed brightness boosted up, rather than statistically lowered. The second way in which the real flux density of a source may be increased is confusion boosting. As explained in subsection 1.2.1, in a confusion limited map the surface density of faint sources is so high that it is very likely that at least one of those sources will fall into the area of the beam, increasing the galaxy's flux density.

Since both of these have the same effect, they are measured together as a function of the flux density (or signal-to-noise in the case where the noise in

the map is not uniform). In Monte Carlo simulations the boosting (or inversely deboosting) is measured as an average multiplicative factor between the input and measured output flux density of a source as a function of the signal-to-noise ratio.

One thing to add is that the high flux density (high signal-to-noise ratio) sources, like the gravitationally lensed galaxies, will have very little contribution from both Eddington and confusion boosting. Statistically there are very few sources with comparable flux densities, so Eddington boosting is not an issue. Also, the additional flux coming from the confusion boosting is in these cases negligible.

Positional Accuracy: As in the case of the flux densities, the positional accuracy suffers from similar limitations. Both the instrumental noise and confusion may distort the real position of a submm source. Again, the positional accuracy is estimated using a Monte Carlo method, where the input 'injected' sources maps are compared with the output one. It is measured as a function of the signal-to-noise ratio, since the positions of sources detected with higher significance will be less affected by the confusion. The results of the Monte Carlo simulations - average offsets between the input and output positions, are the rough indications of the positional accuracy of the submm sources and as such provide the initial search radius for matching multi-frequency counterparts.

However, as pointed by Hodge et al. (2013), the multiplicity may be an additional factor. The bright source (with high signal-to-noise ratio and therefore small search radius) which is composed of two or even three much fainter objects will potentially have counterparts sitting well outside its small search radius. Again, as explained in the last paragraph of subsection 1.1.4, the scale of this phenomenon is yet to be determined with bigger, more statistically significant submm samples.

Sample Contamination & Completeness: Other parameters that may be estimated using Monte Carlo simulations are the sample completeness and contamination, which can guide the choice of the signal-to-noise detection threshold of a given survey. If the detection threshold is high, the contamination of the sample will be low and the completeness high but the statistical significance will suffer. On the other hand, if the detection threshold is low the sample will

be incomplete and highly contaminated.

To estimate the completeness as a function of the flux density, S, one injects a number of sources with S into the noise-only maps and counts the number of recovered objects in the output maps. Since the noise in the submm maps is quite often not uniform, the completeness may also be estimated as a function of the signal-to-noise ratio. Knowing the fraction of the recovered sources, one can adjust the detection threshold to increase or decrease the completeness. In addition, it is important to be able to tell how many of the observed sources are in fact spurious. The contamination of the sample can arise from a few low flux density sources, all positioned within one beam area, masquerading as one bright object. Also, in some cases the faint source's flux density may be significantly boosted. Again, to test the contamination as a function of the signal-to-noise ratio, one compares the number of injected to recovered sources of a given flux S. The contamination rate of $\leq 5\%$ is considered satisfactory and results in the detection threshold between $3 < \sigma < 4$.

1.2.4 Number Counts

The number counts, dN/dS, is a very important function which ultimately describes the observational characteristics of a given population. It is crucial in determining the fraction of the cosmic infrared background (CIB) that can be resolved into individual galaxies at a given wavelength (described in subsection 1.2.5). It can be given in a raw units, determined directly from the maps, or corrected units (most often used in the literature), where sources' flux densities have been deboosted and the sample corrected for contamination and incompleteness. Most often the number counts are quoted as the number of galaxies per unit flux density per unit area (e.g. mJy^{-1} deg^{-2}). Occasionally however, depending on the scale of a given survey (deep and small or shallow and wide), the so-called Euclidean-normalised units are used, given as the number of galaxies times the flux density to the 1.5 power per unit sky area (e.g. $\mathrm{mJy}^{1.5}$ deg^{-2}). These alternate units are normal units multiplied by the flux density to the 2.5 power and are useful in converting the traditional number counts which can vary over several orders of magnitude, to something which is relatively flat and is much easier to perform the functional fits to.

Regardless of the type of units, functional forms of number counts of galaxies

are always of great interest, since they are very important for galaxy evolution models. Traditionally the parametrization is given as a Schechter function (first described in Schechter 1976):

$$\frac{dN}{dS} = \frac{N_0}{S_0}\left(\frac{S}{S_0}\right)^{-\alpha} e^{\left(-\frac{S}{S_0}\right)}, \tag{1.2}$$

where N_0/S_0 is the normalization constant that controls the vertical position of the fit and S_0 is the characteristic flux density. The Schechter function form is dominated by the power-law slope described by the index α at flux densities below S_0 (faint part of the number counts) and by the exponential form at $S > S_0$ (bright end of the number counts). A second popular functional form to describe the number counts is the double power law:

$$\frac{dN}{dS} = \begin{cases} \frac{N_0}{S_0}\left(\frac{S}{S_0}\right)^{-\alpha} & : S \leq S_0 \\ \frac{N_0}{S_0}\left(\frac{S}{S_0}\right)^{-\beta} & : S > S_0 \end{cases} \tag{1.3}$$

In reality however, the functional form of the number counts is much more complicated. The main reason for this is that the above fits are mostly applicable to functions which are more physically-motivated, like luminosity function (see Subsection 1.4.5). Converting from luminosity function to observationally-motivated number counts (which make use of the flux density) is not easy. If the luminosity function has a shape of a Schechter function (at a given redshift), then the corresponding shape of the number counts will not be Schechter. This is because the high flux density end of the number counts is dominated by the low redshift galaxies, as well as lensed sources, and the low flux density end is composed mostly of moderate to high redshift objects (except for the submm wavebands, where the bright end of the number counts is dominated by the high redshift galaxies due to the negative K-correction).

The best studied wavelength for number counts amongst the submm maps is the 850 μm band, where almost 20 literature sources are present spanning four orders of magnitude in flux density. Another band is the 450-500 μm band with the most recent additions from the *Herschel* and SCUBA-2 maps spanning over three orders of magnitude. Figure 1.5 shows the 850/870 μm number counts from SCUBA, SCUBA-2, LABOCA and ALMA observations (Blain et al., 1999; Scott et al., 2002; Chapman et al., 2002; Cowie et al., 2002; Borys et al., 2003; Webb

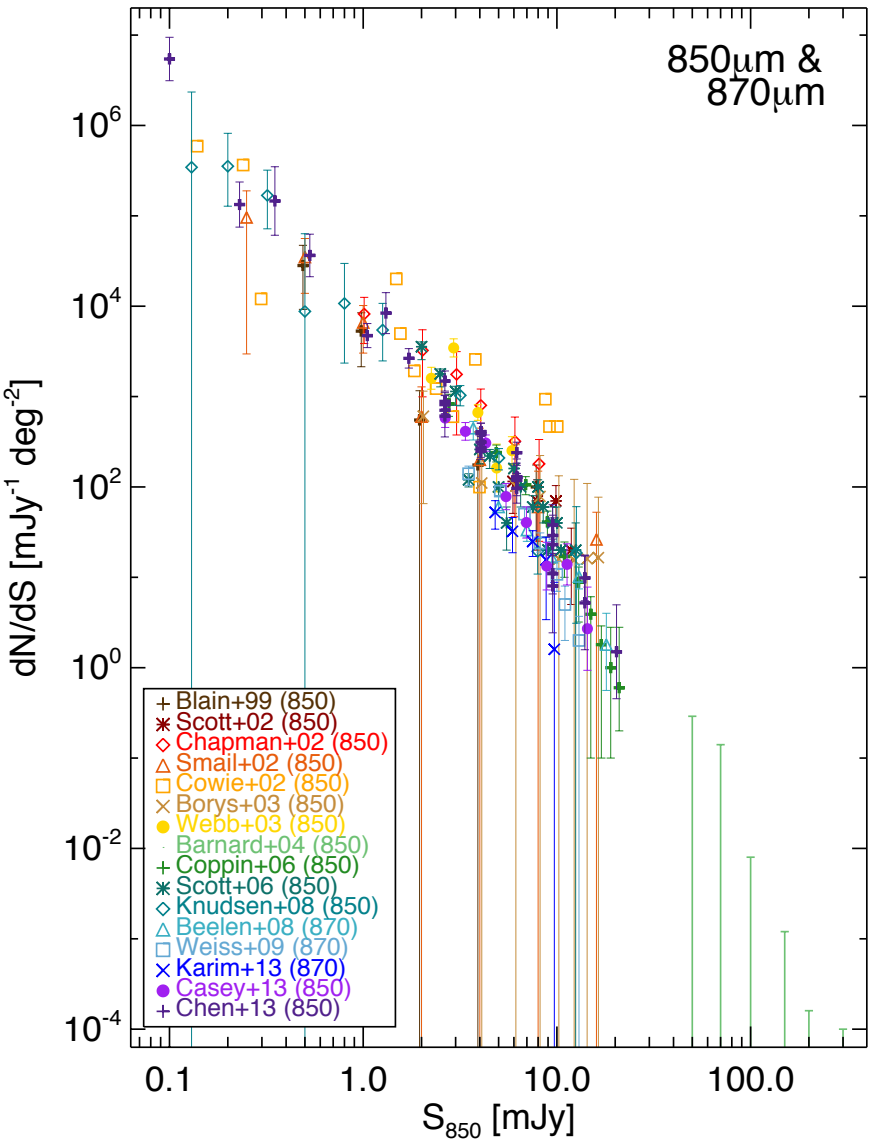

Figure 1.5: *Differential submm number counts at 850/870 μm. The 850 μm data comes from the SCUBA surveys (Blain et al. 1999; Scott et al. 2002; Chapman et al. 2002; Cowie et al. 2002; Borys et al. 2003; Webb et al. 2003; Barnard et al. 2004; Coppin et al. 2006; Scott et al. 2006; Knudsen et al. 2008, shown in brown, dark red, red, dark orange, orange, dark gold, yellow, light green, green, dark teal, and teal respectively) and SCUBA-2 surveys (Casey et al. 2013; Chen et al. 2013b in purple). The 870 μm data comes from LABOCA surveys (Beelen et al. 2008; Weiß et al. 2009a in blue) and the ALMA interferometric data (Karim et al. 2013 in dark blue). Figure adopted from Casey, Narayanan, & Cooray (2014).*

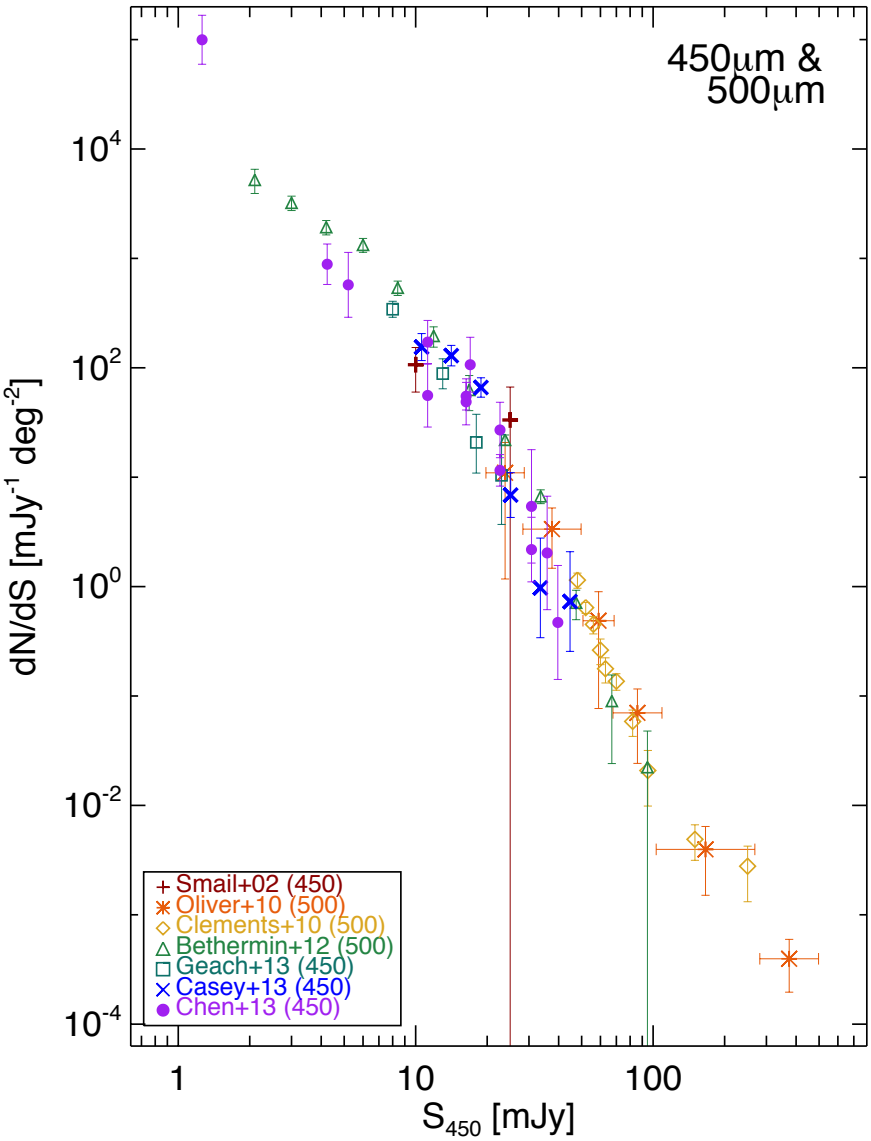

Figure 1.6: *Differential submm number counts at 450/500 μm. The 450 μm data comes from Smail et al. (2002); Geach et al. (2013); Casey et al. (2013) and Chen et al. (2013a) shown in brown, blue, dark blue and purple respectively. The 500 μm data comes from Oliver et al. (2010a); Clements et al. (2010) and Béthermin et al. (2012) in red, yellow and green respectively. Figure adopted from Casey, Narayanan, & Cooray (2014).*

et al., 2003; Barnard et al., 2004; Coppin et al., 2006; Scott et al., 2006; Knudsen et al., 2008; Casey et al., 2013; Chen et al., 2013b; Beelen et al., 2008; Weiß et al., 2009a; Karim et al., 2013) and Figure 1.6 shows the 450/500 μm number counts from the SCUBA, SCUBA-2 and *Herschel* observations (Smail et al., 2002; Geach et al., 2013; Casey et al., 2013; Chen et al., 2013a; Oliver et al., 2010a; Clements et al., 2010; Béthermin et al., 2012).

As seen in the above figures, the CIB at the given submm wavelength comprises of galaxies with various flux densities. There is roughly six orders of magnitude difference in the number of faint sources (with $S \sim 0.1\,\mathrm{mJy}$) and bright sources (with $S \sim 20\,\mathrm{mJy}$). The faint end of the number counts is constrained by the depth limitations of the submm surveys, with the confusion noise (subsection 1.2.1) being the major limiting factor. This will be improved with the arrival of deep interferometric ALMA maps. To better describe the bright end of the number counts we need wide and shallow surveys, since bright SMGs are very rare. In addition, a significant fraction of the bright end number counts is made up of the gravitationally lensed SMGs. One reason is that the gravitational lensing moves intrinsically faint sources into the bright end of the distribution. This causes the number counts to flatten out at the bright flux densities and was first described in Blain (1996). The second reason is that, due to the strong negative K-correction, submm wavelengths probe high redshifts where the probability of strong gravitational lensing increases dramatically (see Figure 6 in Weiß et al. 2013). At wavelengths shorter than 500 μm the gravitationally lensed SMGs are not so common and the main contribution to the bright end of the number counts comes from the low redshift star-forming galaxies (Wardlow et al., 2013).

The brightest SMGs can be roughly divided into few types: local star-forming galaxies, active galactic nuclei (AGNs) such as radio blazars, distant lensed SMGs and blends of few less luminous sources. Local galaxies can be identified with the help of wide shallow optical maps, where they appear as large, bright, close objects. The AGNs are relatively easy to find using the wide and shallow radio surveys, where essentially all radio sources are flat-spectrum blazars. The distant lensed SMGs can also be relatively easily identified when submm images are combined with the multi-wavelength data and blends are trivial to find with the high resolution interferometric data. Negrello et al. (2007) predicted that after taking into account all the local galaxies and radio blazars at 500 μm, lensed

SMGs make up all the remaining counts at $S_{500} > 80\,\mathrm{mJy}$ which means that SMGs with intrinsic 500 μm flux densities of $> 80\,\mathrm{mJy}$ simply do not exist. This is still to be observationally confirmed but there is some indication that even though some of the bright submm sources are in fact rare objects like the SMG-SMG mergers (Ivison et al., 2013) most of them ($> 90\%$), after excluding local galaxies and blazars, are indeed gravitationally lensed SMGs (Negrello et al., 2010; Wardlow et al., 2013) at 500 μm. At 870 μm Karim et al. (2013) followed-up LABOCA sources with ALMA and deducted that all the SMGs with $S_{870} > 9\,\mathrm{mJy}$ are in fact multiples of less luminous sources. This is at odds with the SMA follow-up of the AzTEC sources of Younger et al. (2007, 2009), where many sources with $S_{890} > 9\,\mathrm{mJy}$ were found to be compact objects. However, much larger areas of the sky must be surveyed interferometrically in order to determine the true contribution of the multiples to the bright end of the submm number counts.

1.2.5 Cosmic Infrared Background

As pointed out at the beginning of this thesis, it has been found by *COBE* that roughly half of the star formation activity is emitted in the far-IR and submm. Various surveys that have been performed, aim to resolve this cosmic infrared background (CIB) into individual dusty galaxies. However, the fraction of the sources that can be identified with such observations is fundamentally limited by the confusion noise (subsection 1.2.1). Due to this restriction, recent observations carried out by *Herschel* at 250, 350 and 500 μm resolved only 15%, 10% and 6% percent of the CIB respectively (Oliver et al., 2010b). At submm wavelengths surveys performed with SCUBA managed to resolve $\sim 20\% - 30\%$ percent of the CIB into distinct SMGs with $S_{850} > 2$ mJy (Barger et al., 1998; Hughes et al., 1998; Eales et al., 1999; Coppin et al., 2006) and similar fraction with LABOCA at 870 μm (Weiß et al., 2009b).

The simple consequence of the confusion limit is that a given survey cannot observe faint, most abundant sources ($S_{850} < 2$ mJy for SCUBA). One way to go below that limit is to make use of the gravitational lensing, where less luminuos objects are being magnified to observed flux densities above the confusion limit. This way more than 50% of the CIB have been resolved into individual galaxies (Smail et al., 1997, 2002; Cowie et al., 2002; Knudsen et al., 2008; Chen et al., 2013a). Devlin et al. (2009) stacked 24 μm sources against the BLAST maps

and resolved virtually the whole CIB. Another obvious way one could decrease the confusion noise is to use high resolution, interferometric data. Hatsukade et al. (2013) with their ALMA follow-up observations at 1.3 mm, assuming no correlation from clustering and lensing, resolved 80% of the CIB.

However, since large-area high-resolution surveys are very expensive observationally, one needs to have a way of disentangling the confusion noise and estimating the number counts below that limit. A method that attempts to take into account the confused fainter sources, in the case where the confusion noise dominates over the instrumental noise, is the probability of the deflection statistics, $P(D)$, the probability distribution function (pdf) for the observed flux in each sky area unit (usually a map pixel). It compares the pixel intensity histogram, after masking out the extended detected sources, with the similar histogram produced with Monte Carlo simulations. The simulated maps are populated with the sources below the confusion limit, where the slope and the normalization of the functional form of the number counts (see subsection 1.2.4) are free parameters. When the differences between the real and simulated histograms are minimised, the resulting functional form of the faint end of the number counts reveals the most probable contribution to the CIB from the sources below the confusion limit. Using this method Glenn et al. (2010) resolved $\sim 60\%$ and 45% of the CIB at *Herschel* bands of 250 and 450 μm respectively as oppose to 15% and 6% quoted above. The major caveat of the $P(D)$ analysis however, is its inability to account for the population clustering as well as the uncertainties resulting from the statistical nature of the method.

1.3 Spectral Energy Distribution Fitting & Redshifts

1.3.1 SED Fitting Techniques

Once the submm maps are properly processed, the multi-wavelength counterparts of SMGs identified and all the available photometry collected, one goes on to fit a spectral energy distribution (SED) to the data. SED fitting is necessary to extract basic physical properties like redshifts, infrared luminosity ($L_{\rm IR}$), thus obscured star formation rate (SFR) and AGN activity, dust temperature ($T_{\rm d}$), dust mass

($M_{\rm d}$), etc. Because of the different sources of emission responsible for the shape of the SED, it is usually divided into two regions: UV to near-IR (UV-NIR) and mid-IR to millimetre (MIR-mm). The former region is where the unprocessed emission from stars dominates. Depending on the dust content of the galaxy, a fraction of the starlight is being absorbed by the dust and re-emitted as heat in the MIR-mm region of the SED. Unlike data in the UV-NIR, where more than 30 bands are available, the MIR-mm suffers from the dearth of the photometric data, with ~ 10 bands available. SED fitting techniques could be divided into two main categories: direct comparison to models/templates using the χ^2 approach and the FIR fitting methods to the modified blackbody function.

Fitting to models: In the UV-MIR regime it is natural to use the stellar synthesis models, like that of Bruzual & Charlot (2003). Here an initial mass function is assumed (for instance the Chabrier 2003 IMF) with a given range of stellar masses, the star formation history (single burst, double burst or exponential), metallicity, dust reddening and HI absorption along the line of sight. Based on this model, a library of SED templates is created and compared with the available photometry using the χ^2 method. The main difference here is that the former one seeks the best parameter values and their uncertainties and the latter seeks the posteriori probability distribution for parameters.

To include the MIR-mm regime one needs to account for the dust. This is done with either radiative transfer models or energy balance techniques. The radiation transfer model deals with the propagation of the electromagnetic radiation from stars. Silva et al. (1998) developed the GRASIL code, where the dust absorption and emission is taken into account from the UV to FIR. The stellar population synthesis models are applied to generate spectra for stars of different ages and metallicities, a different dust geometry and dust grain size distributions (small versus PAHs). Chary & Elbaz (2001) use GRASIL to reproduce SEDs for four local galaxies (Arp 220, NGC 6090, M 82 and M 51) and then interpolated between the four SEDs to span intermediate luminosities. Dale et al. (2001) adopted a different approach where in the FIR portion of the SED is constructed of a various dust emission curves, with the assumption that dust masses (i.e. dust temperatures) undergo a power-law distribution (with small, large and PAH grains taken into account). Models are then constrained with the IRAS, ISOCAM and ISOPHOT data of 69 nearby galaxies.

Siebenmorgen & Krügel (2007) use the radiative transfer model which is spherically symmetric and they argue that this simplification, where the dust clumpiness is not taken into account, does not change the shapes of SEDs significantly. Their library consists of 7000 SEDs which can be used for local, as well as high-z galaxies.

One of the most widely used set of templates is that of Rieke et al. (2009). To construct the library of templates they use *Spitzer* observations of eleven local luminous infrared galaxies (LIRGs) in a wavelength range of $0.4\,\mu\mathrm{m} - 30\,\mathrm{cm}$ and with luminosities ranging from $5 \times 10^9 - 10^{11}\,L_\odot$. The spectral features at rest-frame wavelengths $< 35\,\mu$m are composed of IRS and ISO spectra and the FIR portion of the SED is a modified blackbody with $T_d = 38-64$ K and the emissivity index $\beta = 0.7 - 1$.

In addition da Cunha et al. (2008) describes the Multi-wavelength Analysis of Galaxy Physical Properties (MAGPHYS), the modeling package which empirically constrains the SED from UV to FIR using an energy balance argument. The stellar part of the SED is generated using the Bruzual & Charlot (2003) stellar population synthesis with the dust attenuation modelled by Charlot & Fall (2000) and re-radiated in the IR. The Code Investigating Galaxy Emission (CIGALE, Burgarella et al. 2005) is based on the spectra generated in the optical/IR by Maraston (2005) with the dust attenuation based on laws presented in Calzetti et al. (1994) and Calzetti (2001) and FIR SED templates from Dale & Helou (2002).

Fitting to modified blackbody functions: Before the launch of *Herschel* there was only one data point available in the submm imaging which was that corresponding to the detection band (850 μm). For this reason it was not possible to use complicated models, as they would simply be unconstrained. Instead, one had to use a simple, modified blackbody model of a fixed dust temperature, or an SED of a local ULIRG like Arp 220. The obvious disadvantage of this approach was that it does not account for the variations in the dust temperature.

However, as mentioned in subsection 1.1.4, FIR and radio emission correlates. This offers an additional radio data point which was used to estimate the IR luminosity and therefore the star formation rate, whereas the dust temperature was determined from the SED which best fitted these data points. This was the procedure adopted for 850 μm selected SMGs (Smail et al., 2002; Chapman et al.,

2004).

Armed with more photometric points, after the addition of the *Herschel* PACS and SPIRE bands, one could use a more sophisticated, direct SED fitting techniques. The simplest one is the blackbody fit but since the galaxies dust temperature as well as opacity varies significantly, the more complicated, modified blackbody fit is preferred:

$$S(\nu, T) \propto \frac{(1 - e^{-\tau(\nu)})\nu^3}{e^{h\nu/kT} - 1}, \tag{1.4}$$

where $S(\nu, T)$ is the flux density at ν for a given temperature T in units of $\mathrm{erg\,s^{-1}\,cm^{-2}\,Hz^{-1}}$ or Jy, $\tau(\nu)$ is the optical depth defined by $\tau(\nu) = \kappa_\nu \Sigma_{\mathrm{dust}}$ and is commonly represented as $\tau(\nu) = (\nu/\nu_0)^\beta$, where β is the spectral emissivity index and ν_0 is the frequency where optical depth equals unity.

While this fit does a good job in describing the galaxy's FIR emission, it fails in the MIR regime. It has been found that the dusty galaxies exhibit a noticeable excess of the MIR emission which is attributed to the more compact, hotter clumps of gas residing closer to the galaxy's nucleus. Several methods have been adopted to deal with this MIR excess accordingly. It has been proposed to use two modified blackbodies with two different temperatures. Colder for FIR portion of an SED and warmer for the MIR excess (Farrah et al., 2003; Galametz et al., 2012). However, this technique requires many more parameters to fit (two dust temperatures, two emissivities, etc.).

Another method uses a single temperature modified blackbody and at wavelengths lower than a given cut-off value, it replaces the blackbody with the power-law SED (Roseboom et al., 2013). While this method handles the MIR excess quite well, it requires first to fit the long-wavelength modified blackbody without the power-law. Alternatively, one assumes that the SED is in fact the composite of many different-temperature SEDs, where the temperatures follow a power-law:

$$S(\nu, T_c) = (\gamma - 1)T_c^{\gamma-1} \int_{T_c}^{\infty} (1 - e^{-\tau(\nu)})B_\nu(T)T^{-\gamma}dT \tag{1.5}$$

where the integrand is the Equation 1.4 multiplied by $T^{-\gamma}$ and T_c is the minimum temperature. These methods provide a more accurate fits to the SMG SED which better accounts for the MIR excess and produce very similar results

with indistinguishable luminosities and SED peak wavelengths. However, as pointed out in Kelly et al. (2012), the exact choice of the fitting method can impact the subtleties of these fits.

1.3.2 Acquiring Redshifts

Before any physical properties of a given galaxy can be extracted, its redshift must be found. This is however not a straightforward process, as dusty SMGs are very dim in the optical/UV (because of the dust) and the large beam sizes make the multi-wavelength identification process difficult (subsection 1.1.4).

In the case when no high-resolution counterparts are available, the only way to get a rough estimate of the redshift is to use the source's dust-continuum, FIR part of the SED. As explained in the previous subsection, one can fit an SED to the data points available in this regime to extract the 'millimetric redshift', based either on the shape of that fit or its colour. The shape of the FIR SED has to be roughly fixed for this purpose, as there are most often very few data points available. However, this method has a very low precision and depends strongly on the intrinsic variations of an SED (see subsection 1.1.3). The dust temperature of an SED can vary between $\sim 30 - 50$ K. If one assumes a 30 K SED and finds the 'millimetric redshift' of $z \simeq 2.5$, changing the temperature to 50 K will yield a redshift of $z \simeq 4.5$. For this reason it is only practical to use this method for extracting the statistical, aggregate properties of large populations (Greve et al., 2012).

If the optical counterpart to an SMG is identified, the determination of the optical photometric redshift is possible. This method relies on the availability of the ancillary data and because of the vast increase of the multi-wavelength coverage in the extragalactic fields, it became the most widely used technique for estimating SMGs' redshifts. As in the case of the millimetric redshift it requires the SED fitting. As explained in the previous subsection, to fit an optical part of an SED one uses a stellar synthesis models with various input parameters. The χ^2 test is then performed, where the best value of the redshift is determined by minimising the flux residuals between the observations and the template. However, large areas of the sky have not been surveyed in the optical yet at sufficient depth and so the determination of the optical photometric redshifts for the most rare and scattered submillimetre sources is not possible. In such

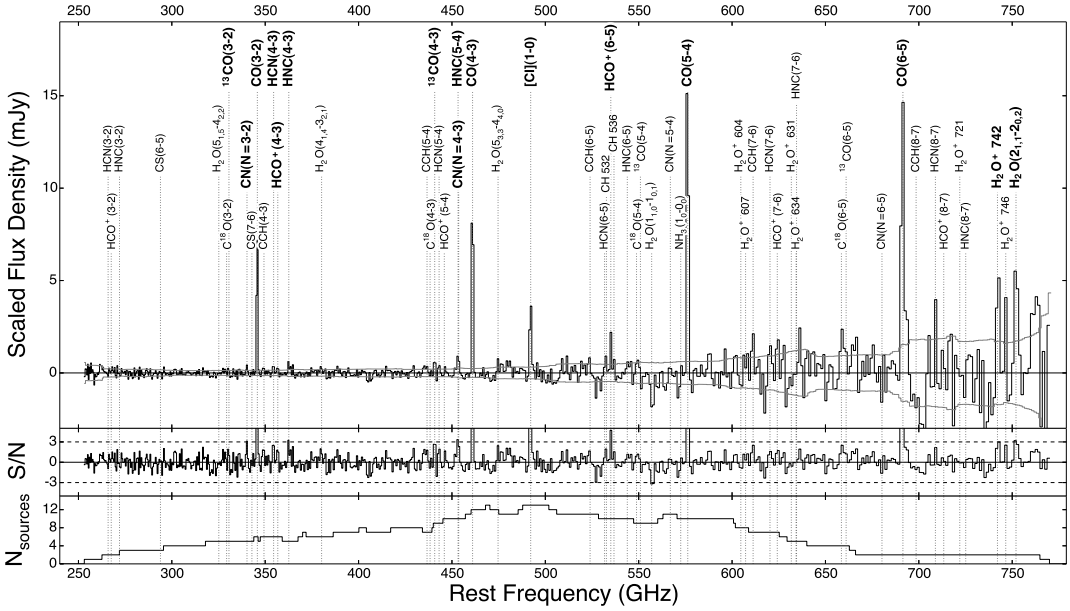
Scaled Flux Density (mJy)
S/N
N_sources
Rest Frequency (GHz)
250
300
350
400
450
500
550
600
650
700
750
HCN(3-2)
HNC(3-2)
HCO+ (3-2)
CS(6-5)
13CO(3-2)
CO(3-2)
HCN(4-3)
HNC(4-3)
CN(N = 3-2)
HCO+ (4-3)
13CO(4-3)
HNC(5-4)
CO(4-3)
CN(N = 4-3)
[CI](1-0)
HCO+ (6-5)
CO(5-4)
CO(6-5)
CO(7-6)
CO(8-7)
CO(9-8)
CO(10-9)
CO(11-10)
CO(12-11)
CO(13-12)
CO(14-13)
CO(15-14)
CO(16-15)
CO(17-16)
CO(18-17)
CO(19-18)
CO(20-19)
CO(21-20)
CO(22-21)
CO(23-22)
CO(24-23)
CO(25-24)
CO(26-25)
CO(27-26)
CO(28-27)
CO(29-28)
CO(30-29)
CO(31-30)
CO(32-31)
CO(33-32)
CO(34-33)
CO(35-34)
CO(36-35)
CO(37-36)
CO(38-37)
CO(39-38)
CO(40-39)
CO(41-40)
CO(42-41)
CO(43-42)
CO(44-43)

cases the only way to get a handle on the redshift may be to use the millimetric photometric redshift technique.

To get a precise determination of the redshift, the spectroscopic follow-up is necessary. As in the case of photometric redshifts, spectroscopy can be performed both in the optical and FIR. Again, without the unambiguously identified optical counterpart to an SMG one has to use the FIR/submm data. The submillimetre spectroscopy relies on the identification of various molecular gas emission lines and is a very precise method for determining redshifts. The main problem is that one needs to observe at least two emission lines to be able to identify them accurately. Because of the narrow correlators' bandwidths and a significant wavelength gaps between the most prominent emission lines (eg. CO and CI, Figure 1.7), this was always a very inefficient method for determining galaxies' redshifts. A major step forward was made with widening the millimetric receiver's bandwiths, as in the case of the WIDEX on the Plateau de Bure Interferometer (PdBI), with the 3.6 GHz wide band (four times better than its predecessors), EMIR receiver at the IRAM 30 m. This method has a number of advantages: it does not require an identification in the optical and since SMGs are detected in FIR/submm, they are expected to have prominent submillimetre emission lines. ALMA was designed optimally for the spectroscopic follow-up of the SMGs and was used for spectroscopic redshift determination of the lensed SMGs (Vieira et al., 2013). However, the millimetre spectroscopic redshift determination technique is not yet sufficiently efficient to use for large populations of unlensed sources and awaits ALMA to become fully operational.

The second regime for spectroscopic follow-ups is the optical (Figure 1.8). As in the case of the optical photometric redshifts, this method relies on the unambiguous identification of the optical counterpart to a submm source which is known to be often quite difficult. The requirement of having a radio, or 24 μm counterpart beforehand introduces various biases. Also, as in the case of the millimetric spectroscopy, one needs at least two lines to be able to determine redshift with 100% certainty. Despite these drawbacks this is a widely used technique (Swinbank et al., 2004; Chapman et al., 2005) whenever possible simply because of its superior accuracy in determining precise redshifts for SMGs.

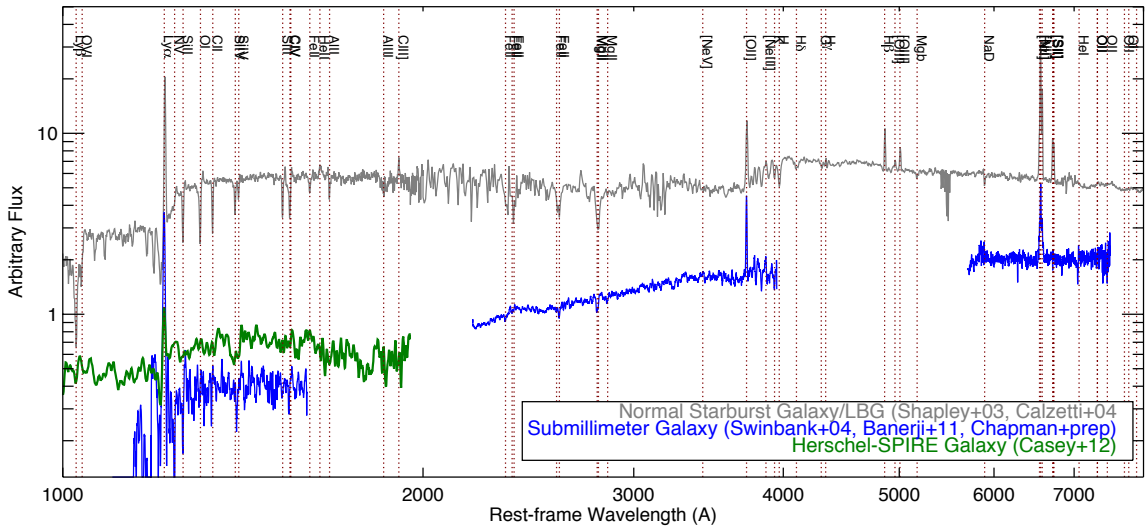

Figure 1.8: *The rest-frame ultraviolet and optical composite spectrum of a SMG (blue) comprising of the Swinbank et al. (2004) spectrum centred on the H emission line, the Banerji et al. (2011) spectrum centred on the OII line and the median stack of the star-formation dominated SMGs from Chapman et al. (2005) spectrum centred on the Lyα line. In grey is the composite spectrum for a normal, star forming Lyman Break Galaxy at $z \sim 2$ (Shapley et al., 2003; Calzetti, 2001) and in green is the rest-frame ultraviolet spectral stack of the Casey et al. (2012b) $z > 2$ subset of the Herschel-SPIRE selected galaxies (offset from the SMG for clarity). The most prominent emission and absorption lines are labeled. Figure adopted from Casey, Narayanan, & Cooray 2014.*

1.3.3 Redshift Distributions

450 μm selected samples: The left panel of Figure 1.9 shows the redshift distributions for samples surveyed in 450 μm using SCUBA-2 instrument. The big advantage of using this band is that it offers an angular resolution of only 7 arcsec (as oppose to 15 arcsec for 850 μm SCUBA-2 band or $\sim$ 36 arcsec for the *Herschel* 500 μm band). Plotted are redshift distributions from Casey et al. (2013), Roseboom et al. (2013) and Chen et al. (2013a). The 17 galaxies from Chen et al. (2013a) have redshifts derived from the SCUBA-2 850/450 colours and 850/radio ratios, with spectroscopic values wherever possible and have a mean value of $\bar{z} = 2.38 \pm 0.33$. Roseboom et al. (2013) and Casey et al. (2013) samples come from overlapping regions of the COSMOS field, with Roseboom et al. (2013) sample being four times smaller in area but four times deeper, with an RMS of 1.2 mJy (as oppose to 4.1 mJy in Casey et al. 2013). The mean redshifts found are $\bar{z} = 1.46 \pm 0.10$ and $\bar{z} = 1.85 \pm 0.15$ respectively. The difference is most probably caused by the fact that the sample of Casey et al. (2013) extends over larger area and probes more luminous, higher-z sources, whereas the sample of Roseboom et al. (2013) includes more faint, $z \sim 1 - 2$ galaxies.

850 μm/870 μm selected samples: This is the best studied wavelength in the submm region. The right panel of Figure 1.9 shows some of the redshift distributions from the literature. Probably the most important one is that of Chapman et al. (2005). They describe the 850 μm selected sample which have radio counterparts. These counterparts have an angular resolution of ~ 1 arcsec and are therefore ideal for the spectroscopic follow-up. 73 sources were spectroscopically confirmed using the LRIS instrument (Oke et al., 1995) at Keck Observatory and were found to have a mean redshift of $\bar{z} = 2.00 \pm 0.10$. However, the main problem with this sample is that it relies on the radio counterpart identification and therefore is biased against high-z galaxies (since radio band suffers from strong, positive K-correction, as seen in Figure 1.2). This is why there is no high-z tail in the Chapman et al. (2005) redshift distribution from the right panel of Figure 1.9.

Wardlow et al. (2011) present a sample of 126 SMGs selected in 870 μm using the LABOCA camera. This sample lacks the bias present in the Chapman et al. (2005) sample, since the author goes to great efforts to account for the

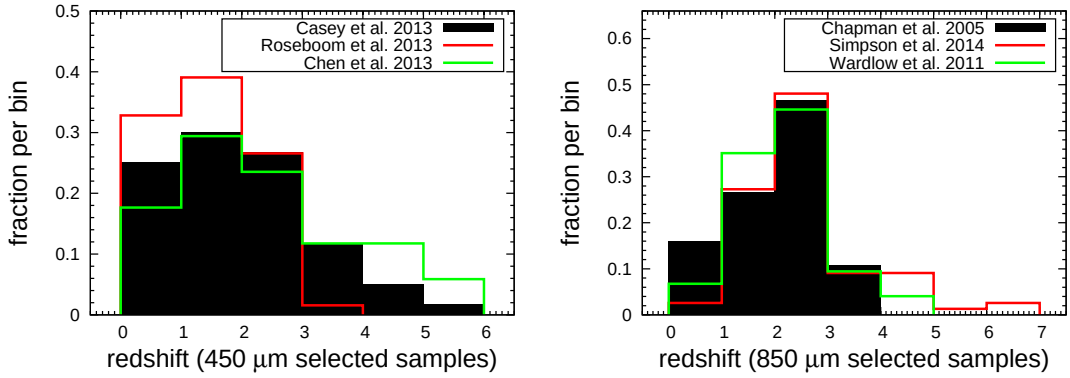

Figure 1.9: ***Left:*** *Redshift distribution of the 450* μm *selected samples. The results from Casey et al. (2013) with* $\bar{z} = 1.85 \pm 0.15$*, Roseboom et al. (2013) with* $\bar{z} = 1.46 \pm 0.10$ *and Chen et al. (2013a) with* $\bar{z} = 2.38 \pm 0.33$ *are depicted in black, red and green respectively.* ***Right:*** *Redshift distribution of the 850* μm*/870* μm *selected samples. The results from Chapman et al. (2005) with* $\bar{z} = 2.00 \pm 0.10$*, Simpson et al. (2014) with* $\bar{z} = 2.60 \pm 0.13$ *and Wardlow et al. (2011) with* $\bar{z} = 2.24 \pm 0.10$ *are depicted in black red and green respectively.*

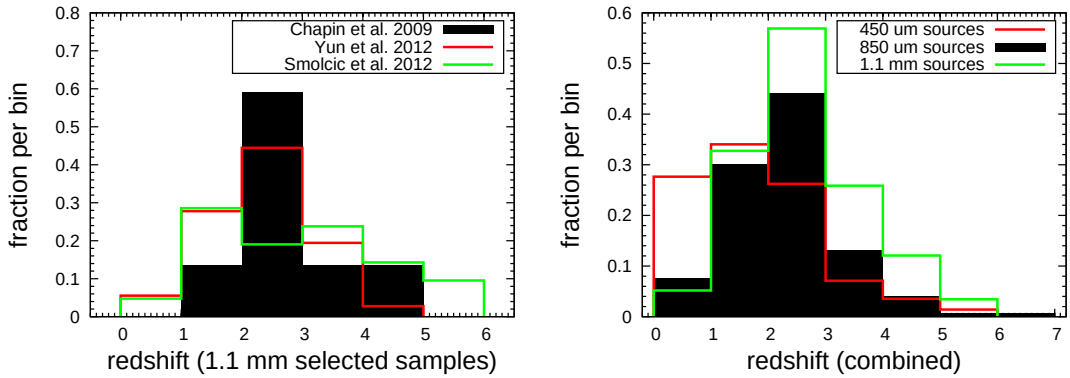

Figure 1.10: ***Left:*** *Redshift distribution of the 1.1 mm selected samples, all detected using AzTEC instrument. The results from Chapin et al. (2009) with* $\bar{z} = 2.64 \pm 0.15$*, Yun et al. (2012) with* $\bar{z} = 2.36 \pm 0.15$ *and Smolčić et al. (2012) with* $\bar{z} = 2.91 \pm 0.31$ *are shown in black, red and green respectively.* ***Right:*** *Redshift distribution of the 450* μm*, 850* μm *and 1.1 mm selected samples from Figures 1.9 and 1.10 combined. The 450* μm *selected samples have a mean redshift of* $\bar{z} = 1.73 \pm 0.09$*, the 850* μm *has* $\bar{z} = 2.32 \pm 0.05$ *and 1.1 mm selected samples have* $\bar{z} = 2.58 \pm 0.12$*. The differences in the mean redshifts are most probably attributed to the effect of the K-correction (see Figure 1.2).*

'missing' sources by statistical groupings of the NIR samples and indeed finds the mean redshift for his sample to be $\bar{z} = 2.24 \pm 0.10$, slightly higher than that of Chapman et al. (2005). This is the only 850/870 μm sample which was followed-up interferometrically (using ALMA). It was found that some of the brightest sources in the sample were split into few less luminous objects (Karim et al., 2013; Hodge et al., 2013) but as presented in Simpson et al. (2014) this does not impact the redshift distribution significantly ($\bar{z} = 2.60 \pm 0.10$ for the ALMA followed-up sample).

1.1 mm selected samples: At longer wavelengths the AzTEC 1.1 mm selected SMGs have been studied in a little less detail than the 850 μm selected samples. In the left panel of Figure 1.10 the most important AzTEC redshift distributions are shown. Chapin et al. (2009) found redshifts for 22 SMGs from the GOODS-N field with the mean value of $\bar{z} = 2.64 \pm 0.15$. Yun et al. (2012) studied a sample of 48 sources in the GOODS-S field. They used both the UV/optical and FIR/submm regions on an SED to deduce redshifts and in both cases found very similar values of $\bar{z} = 2.36 \pm 0.15$. One of the most important analysis in the 1.1 mm regime is that of Smolčić et al. (2012), who followed-up their SMGs from COSMOS field using a PdBI interferometer and found the mean redshift for their 1.1 mm selected sample of $\bar{z} = 2.91 \pm 0.31$.

Comparison of different redshift distributions: In the right panel of Figure 1.10 three redshift distributions for the 450 μm, 850 μm and 1.1 mm selected samples are shown. For a given selection band all the redshifts from a corresponding panel in Figures 1.9 and 1.10 have been combined and plotted. The mean redshifts are $\bar{z} = 1.73 \pm 0.09$ for the 450 μm selected samples, $\bar{z} = 2.32 \pm 0.05$ for the 850 μm selected samples and $\bar{z} = 2.58 \pm 0.12$ for the 1.1 mm selected samples. The differences in the mean redshifts are most likely caused by the effect of the K-correction (Figure 1.2). The 450 μm band is most sensitive to the lower-z galaxies, since it suffers from the positive K-correction, as opposed to the 850 μm and 1.1 mm bands, both of which are more likely to select higher-z sources (see Zavala et al. 2014).

1.4 Physical Properties

1.4.1 Stellar Masses

Once redshifts are known it is possible to attempt the determination of the physical properties of SMGs. One of the most basic properties of any galaxy is its stellar mass, $M_\star$. However, it has been shown that the values of the inferred stellar masses can significantly vary (Hainline et al., 2011; Michałowski et al., 2012a). To find stellar masses one uses a stellar population synthesis model (SPS) to fit an SED to a collected UV-NIR photometry. The main uncertainties in the stellar masses are attributed to the input parameters of a given model: the star formation history (SFH) and the initial mass function (IMF) as well as the model itself.

Star Formation History: The first component in determining the stellar masses of SMGs is the assumed star formation history (SFH). The choices involve a single, instantaneous burst of star formation, a continuous SFH, an exponentially declining SFH ('tau model') and a double (or multiple) burst of star formation. As noted by Dunlop (2011), the use of a multiple SFH generally leads to higher values of stellar masses than the use of a single SFH. This is caused by the fact that in a single burst scenario, the entire stellar population must be young in order to reproduce the UV emission. This way the less massive but much more abundant old stars are not properly accounted for which leads to an underestimation of stellar masses. Michałowski et al. (2014) used various SFHs and IMFs and found that the single-burst SFHs lead to an underestimation of the stellar masses by ~ 0.2 dex and the 'tau model', while finds values which are consistent with the true numbers, also underestimates the stellar masses. The SFHs which gives to the most accurate results, as found by Michałowski et al. (2014), are the double-burst SFHs, properly accounting for the old population of stars formed through the quiescent star formation which dominates the stellar mass in merging galaxies and a younger population formed in a recent starburst.

Initial Mass Function: The second key assumption in finding the SMGs' stellar masses is the choice of the IMF. Different choices can affect the inferred values of the stellar masses significantly. The adoption of the Salpeter (1955)

IMF gives stellar masses a factor 1.8 higher than when using the Chabrier (2003) IMF. On one hand the current models of galaxy evolution require the usage of the top-heavy IMF (more massive stars and less low-mass stars) in order to reproduce the submillimetre number counts (Baugh et al., 2005). On the other however, the work of van Dokkum & Conroy (2010) which investigates the present day elliptical galaxies (a likely descendants of SMGs), suggests that the IMF is in fact bottom-heavy.

Stellar Population Synthesis Models: The third key issue in determining the stellar masses is the choice of the SPS. Assuming an IMF (the number of stars of a given mass) and a SFH, all the stars are being advanced along the appropriate isochrones in the Hertzsprung-Russell (HR) diagram. At the time of observation the shape of an SED is determined by the collective emission from these stars (taking into account all the dust absorption effects). The main issue here is whether one adopts models with a significant contribution from the thermally pulsating asymptotic giant branch (TP-AGB, as in models of Maraston 2005), or models where the TP-AGB's contribution is negligible (as in the case of Bruzual & Charlot 2003).

In the light of the current research it is therefore natural to expect an inherent factor $\sim 2-3$ uncertainty in the determination of the SMGs stellar masses. Hainline et al. (2011) examined ~ 70 SMGs and found that the stellar masses have a median value of $\langle M_\star \rangle \simeq 7 \times 10^{10}\, M_\odot$. Working on the same sample, Michałowski et al. (2010a) found the median value of $\langle M_\star \rangle \simeq 3.5 \times 10^{11}\, M_\odot$. The reason for this discrepancy, as shown by Michałowski et al. (2012a), is caused by the different choices of stellar IMFs, star formation histories and stellar population synthesis models.

1.4.2 Star Formation Rates

Star formation rate (SFR) is, together with the stellar mass, the most important parameter that defines the galaxy. The determination of the rate at which galaxies form stars can be performed across the full electromagnetic spectrum, from the X-ray, through ultraviolet (UV), optical and infrared (IR), all the way to radio, and using both the continuum and line emission (for a review see Kennicutt & Evans 2012). Techniques for measuring the SFR vary but the aim is to identify the

emission that traces newly or recently ($10 - 100$ Myr) formed stars, while at the same time avoiding the more evolved stellar population. Therefore, to estimate the SFR one measures the luminosity of a given source, either monochromatic or integrated over some wavelength range. The conversion from the luminosity of massive, short-lived stars to the SFR relies then on a number of assumptions:

1. The star formation has been roughly constant over that timescale probed by the emission being used
2. The stellar IMF is known so that one can extrapolate from the massive end to the low mass end to account for all stars
3. The AGN contribution to a given emission has been recognised and removed if present

Three main ways of estimating the SFR are the continuum, unobscured stellar light as traced by the rest-frame UV light, the dust-reprocessed light as traced by the IR emission and the ionised gas emission as traced by various emission lines. Below I discuss very briefly all of them remembering, that since most of the star formation at $z \sim 1 - 3$ was enshrouded by dust (Reddy et al., 2012a), the most important and widely used method for determining the SFR in high-z dusty galaxies is the one based on the continuum IR emission.

SFR from direct stellar light. The emission from youngest stars peaks at the rest-frame UV ($< 0.3\,\mu$m), so if a negligible amount of dust is present, this is the best regime for investigating the star formation (timescales of $100 - 300$ Myr). The lifetime of an O6 star is ~ 6 Myr, while that of B8 is ~ 350 Myr. However, an O6 star is ~ 90 times more luminous than a B8 star at $0.16\,\mu$m, so assuming a Kroupa (2001) IMF the UV emission from all the O6 stars will be comparable to that from B8 stars, at zero age.

Assuming the Kroupa IMF and a constant star formation over 100 Myr, the UV stellar continuum ($0.0912\,\mu\text{m} < \lambda < 0.3\,\mu$m) can be translated to a SFR using the following expression:

$$\text{SFR(UV)} = 3.0 \times 10^{-47}\,\lambda L(\lambda), \tag{1.6}$$

where the SFR is in units of $M_\odot\,yr^{-1}$, λ is in Å and $L(\lambda)$ is in erg/s (Calzetti, 2013). For timescales longer than 100 Myr, the calibration constant only slightly decreases. For timescales of 10 and 2 Myr, the constant is a factor of 1.42 and 3.45 higher than that in Equation 1.6. This shows that for sources where the star formation was active for much less than 100 Myr, the careful calibration of the above scaling has to be performed.

SFR from the dust-reprocessed stellar light. Here we are focused on the IR luminosity which will depend on both, the dust content and the heating rate provided by stars, where the young, UV-bright stars heat the dust to higher mean temperatures than the old stellar populations (Helou, 1986). Because of the properties of the Planck function, the hotter dust in thermal equilibrium will be more luminous than the cold dust. Also, the dust grains 'favour' the UV light (the cross-section of the dust grains is higher for the UV stellar light than for the optical). Therefore, the emission from the dust heated by the young stars will be more luminous and will peak at shorter wavelengths ($\simeq 60\,\mu$m) than that from the dust heated by the old, low-mass stars ($\simeq 100 - 150\,\mu$m). This is the main reason why the bolometric IR emission ($\sim 8 - 1000\,\mu$m) is often used as a SFR estimator. Assuming the Kroupa IMF for continuous bursts the FIR continuum can be translated to the SFR via the following relation (Calzetti, 2013):

$$\mathrm{SFR(FIR)} = 2.8 \times 10^{-44}\, L_{FIR}, \tag{1.7}$$

where the SFR is again in units of $M_\odot\,yr^{-1}$ and L_{FIR} is in erg/s. For timescales much less than $\tau = 100$ Myr, the scaling in the above equation changes very similar to the one in equation 1.6. For the $\tau > 100$ Myr however, as opposed to the UV-based SFR calibration, the constant will keep changing. This is due to the build-up of the old stellar population which will contribute to the IR emission but not to the UV emission.

SFR from the ionised gas emission lines. The emission lines are produced by the surrounding gas being ionised by the energetic photons from the young, massive stars. The excited electrons are absorbed by the ionised gas and therefore emit a number of different nebular lines, the most important of which are Hα ($0.6563\,\mu$m) and Hβ ($0.4861\,\mu$m), but other recombination lines, Pα, Pβ, Brα,

and Brγ, can be used as well. The strength of the emission lines longward of the Lyman limit will depend directly on the integrated stellar luminosity and as such is a natural probe of the star formation.

Only the most massive and short-lived stars ($> 10\,M_\odot$ & < 20 Myr) contribute significantly to the ionising flux, so this method traces a nearly instantaneous SFR. The conversion factors are most often computed using the evolutionary synthesis models. For the Kroupa (2001) IMF the relation between the ionising photons and the SFR is (Calzetti, 2013):

$$\mathrm{SFR}(Q(\mathrm{H}^o)) = 7.4 \times 10^{-54}\, Q(\mathrm{H}^o), \tag{1.8}$$

where $\mathrm{SFR}(Q(\mathrm{H}^o))$ is in $M_\odot$ yr^{-1} and $Q(\mathrm{H}^o)$ is the ionising photon rate in s^{-1}. The relation between $Q(\mathrm{H}^o)$ and the luminosity of the Hα was given by Osterbrock & Ferland (2006):

$$L(\mathrm{H}\alpha) = 1.37 \times 10^{-12}\, Q(\mathrm{H}^o), \tag{1.9}$$

where the constant is for the electrons at the temperature of $T_e = 10000$ K and the density $n_e = 100$ cm^{-3}. Combining 1.8 and 1.9 we get:

$$\mathrm{SFR}(\mathrm{H}\alpha) = 5.5 \times 10^{-42}\, L(\mathrm{H}\alpha). \tag{1.10}$$

The main advantage of this approach is the direct link between the nebular emission and the SFR which can be mapped with high resolution across the nearby galaxy. The biggest drawback is the uncertainties related to the assumed IMF and the extinction fractions. For individual HII regions the escape fractions of ionising radiations can be as high as 40% (Pellegrini et al., 2012; Relaño et al., 2012; Crocker et al., 2013). For the galaxy as a whole however, the escape fractions are negligible (Heckman et al., 2011).

1.4.3 Specific Star Formation Rates & the Main Sequence

The specific star formation rate (sSFR), the SFR divided by the stellar mass (M_*), is the quantity that describes the effectiveness of the star formation in a galaxy. Two galaxies at a given redshift with different stellar masses will have different SFRs but, provided they are normal star-forming (SF) galaxies, the sSFR for both of them will be roughly the same. It is said that they both lie on

the so-called SF "main sequence" (MS) of the general form:

$$\log(\mathrm{SFR}) = \alpha \log M_* + \beta, \tag{1.11}$$

with α (the slope) and β (the normalization) being functions of redshift. The above relation has been shown to hold for five orders of magnitude in stellar mass (Santini et al., 2009) and from z $\sim 0-6$ (Speagle et al. 2014 and references therein). Sources with SFRs well above the MS are defined as starbursts and with SFRs below the MS as quiescent or passive. Galaxies on the MS formed stars much more effectively (higher sSFRs) in the distant universe than they do today (a decrease in sSFR by a factor of ~ 20 from z ~ 2 to z $= 0$). In addition, most works find that for the MS sources the sSFR is a declining function of the stellar mass (e.g. Karim et al. 2011). This is so-called "downsizing paradigm" for galaxy evolution (Cowie et al., 1988), the evolutionary scenario in which the more massive objects evolve quicker. The tightness of the SFR-M_* relation plays an important role in the cosmic star formation history. Since starbursts contribute only a small fraction to the global star formation rate density at z ≤ 2 (Rodighiero et al., 2011; Sargent et al., 2012), it is the MS, steadily star-forming galaxies that are responsible for the bulk of the cosmic SFR.

1.4.4 Active Galactic Nuclei Content

A very important issue for galaxy evolution models is the understanding of the time evolution of the supermassive black holes (SMBHs). It has been realised that the growth of the SMBHs and the galaxy formation process do not proceed independently. The cosmic star formation rate and the active galactic nucleus (AGN) activity, both peaking around $z \sim 2$ (Cucciati et al., 2012), appear to be related, as suggested by the correlation between the properties of the SMBHs and their hosting galaxies (Häring & Rix, 2004; Gultekin, 2009) and therefore a lot of work has been put into understanding this process in the context of the SMGs. While various tracers of an AGN exist (eg. X-ray, optical/NIR emission lines, MIR continuum emission, etc.), no single method is sufficiently successful on its own. In addition it is not straightforward to differentiate between the AGN and the star formation, both of which can manifest themselves in a similar manner. For these reasons it is necessary to use the multi-wavelength methods, where the

shortcomings of one approach can be overcome by strengths of the other.

The most common tracer of an AGN is the X-ray emission arising both from a jet and from the hot corona of the accretion disc via a scattering process. Alexander et al. (2005) in their pioneering work studied the SMGs discovered by SCUBA in the *Chandra* Deep Field North (CDF-N) which had radio associations and were spectroscopically followed-up (Chapman et al., 2005) and found the AGN fraction of $> 38^{+12}_{-10}\%$. Laird et al. (2010) worked on the Hubble Deep Field North (HDF-N) sources with *Spitzer* IR IDs from Pope et al. (2006) and found the AGN fraction of $29\% \pm 7\%$. Georgantopoulos et al. (2011) studied the LABOCA Extended *Chandra* Deep Field South Submm Survey (LESS; Weiß et al. 2009b) sources and found $28\% \pm 7\%$ of AGNs, while Johnson et al. (2013) in the CDF-S and CDF-N found the AGN fraction of 28%. The work of particular importance is that of Wang et al. (2013), where $\sim$ 100 ALMA-confirmed 870μm-selected CDF-S objects have been examined. As opposed to the previously-mentioned studies, Wang et al. (2013) had precise submm coordinates which allowed them to unambiguously identify the X-ray and FIR counterparts. They found AGN fraction of $17^{+16}_{-6}\%$.

The main problem is that the X-ray approach will miss a significant fraction of heavily-obscured AGN. For heavily-obscured systems the X-ray emission will simply be absorbed by gas and dust close to the nucleus and then re-emitted. Therefore, most obscured AGNs can be recovered by selecting sources with high MIR luminosities (caused by the emitting high-temperature gas) and low optical/NIR emission (caused by the dust absorption). Houck et al. (2005); Weedman et al. (2006a,b); Yan et al. (2007) and Polletta et al. (2008) found that most of the relatively bright 24 μm sources ($F_{24} > 0.7$ mJy) with faint optical counterparts are in fact AGN dominated. Polletta et al. (2006) confirmed that some of these sources are indeed Compton thick AGNs, as initially suggested by their low rest-frame UV fluxes. Martínez-Sansigre et al. (2005, 2007, 2008) obtained optical and *Spitzer IRS* spectra of sources with $F_{24} > 0.3$ mJy and faint optical/NIR couterparts and found the majority of them to be highly obscured AGNs. Brand et al. (2007) with his infrared spectroscopy of 10 $F_{24} > 0.8$ mJy sources with faint optical counterparts found that six of them exhibited broad Hα lines but had a strongly obscured narrow line region and UV continuum, suggesting that the obscuration is due to the dust on large scales within the

galaxy. It is therefore clear that selecting bright 24 μm sources with extreme F_{24}/F_R flux ratios is a very promising method, showing great potential in complementing X-ray surveys in selecting AGN hosting SMGs.

1.4.5 Luminosity Function

The luminosity function (LF) gives the number of sources of a given rest-frame luminosity per unit co-moving volume of space and as such is a very useful way of describing a given population. In order to calculate the LF one needs the results of the SED fitting and a redshift in order to find the distance and hence the rest-frame luminosity. Because of the poor depth of the FIR/submm images which are sensitive only to the most bright sources at high redshifts, the IR bolometric LF only extends to z $\sim$ 2.

The LF can be found in any IR/submm bands separately (24 μm, 250 μm, 450 μm, etc.) but the most meaningful is the IR bolometric LF, $L_{\rm IR}(8-1000\,\mu{\rm m})$, because it can be directly translated into the star formation rate density (SFRD). The most often used method for calculating the LF is the $1/V_{\rm max}$ method, where the LF for each luminosity, L, and redshift, z, bin are given by:

$$\Phi(L,z) = \frac{1}{\Delta L}\sum_i \frac{1}{w_i \times V_{max,i}}, \tag{1.12}$$

with ΔL being the size of the luminosity bin, w_i the completeness correction factor for the ith galaxy and $V_{max,i}$ the maximum volume at which the ith source could have been detected given the depth of the survey. The first determination of the IR bolometric LF was performed using *Spitzer* 24μm data by Le Floc'h et al. (2005) with further *Spitzer* work by Caputi et al. (2007) and Magnelli et al. (2011).

In addition, a number of works emerged which calculated the bolometric IR LFs based on the *Herschel* data. *Herschel* is better than *Spitzer* since it probes the rest-frame peak of the IR SED. In Figure 1.11 the above-mentioned *Spitzer* results are plotted together with the *Herschel* works of Magnelli et al. (2009); Casey et al. (2012a,b); Magnelli et al. (2013) and Gruppioni et al. (2013).

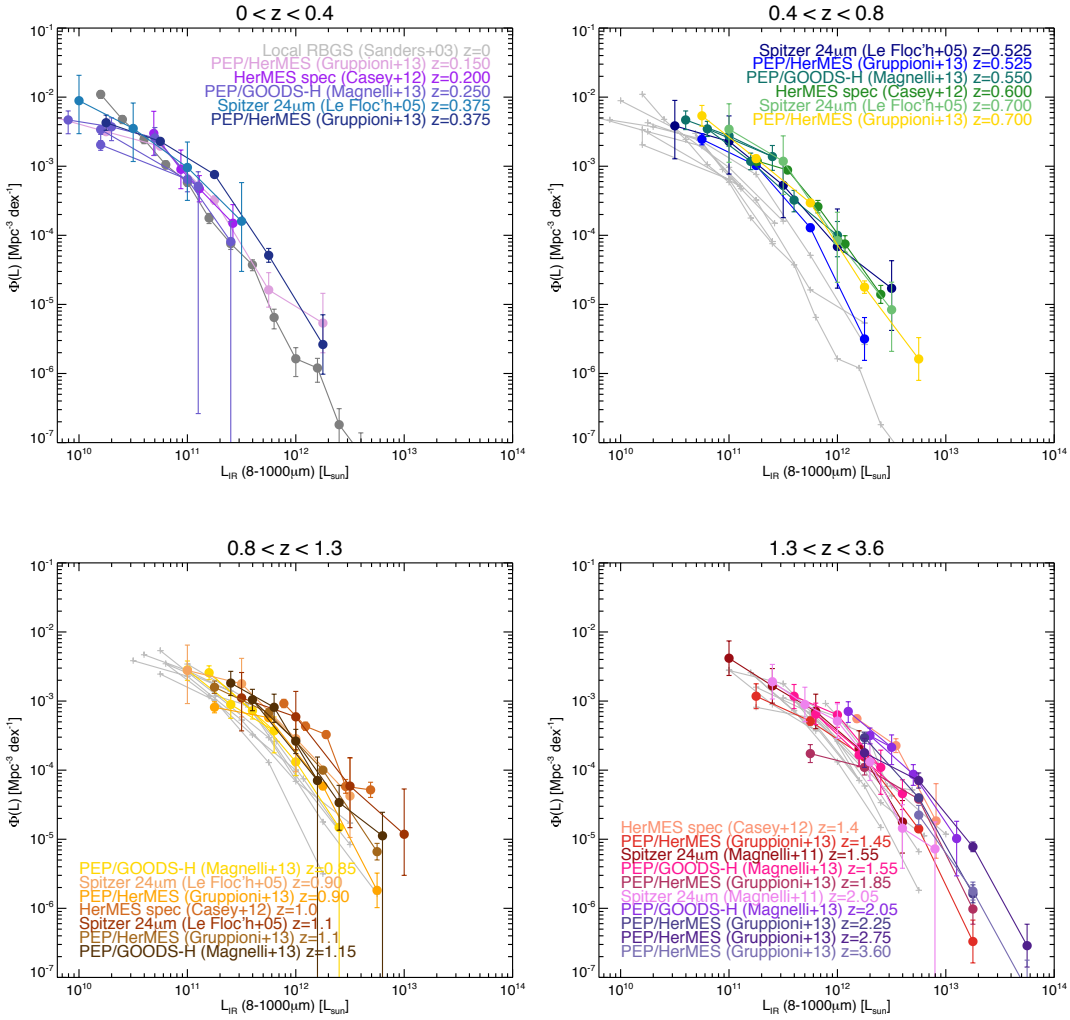

Figure 1.11: *The bolometric IR luminosity functions for a range of redshifts as depicted in the figure. The works shown include the local estimates of Sanders et al. (2003), the Spitzer 24μm-selected samples of Le Floc'h et al. (2005); Magnelli et al. (2009, 2011) and the Herschel works of Casey et al. (2012a); Magnelli et al. (2013); Gruppioni et al. (2013). The grey lines are data from lower z bins. Figure adopted from Casey, Narayanan, & Cooray (2014).*

1.4.6 Star Formation Rate Density

The star formation rate density (SFRD) describes the cosmic history of star formation - the number of stars formed in solar mass units per year per unit co-moving volume in a given epoch, and as such is one of the ultimate quantities sought in observational astronomy. To get a complete picture of the star formation in the Universe one must combine the UV-based dust-uncorrected SFRs with the IR-based dust-obscured values. The UV-based dust-uncorrected SFRs are relatively easy to estimate out to very high redshifts due to the superior depth of the UV/optical data. However, the correction from the observed UV-based SFRD to the intrinsic value is very difficult and is a subject of an ongoing debate (see Madau & Dickinson 2014 for details). On the other hand, the IR-based SFRDs calculations extend only out to $z \sim 2-3$, as can be seen in Figure 1.12, due to the poor depth of the FIR/submm data.

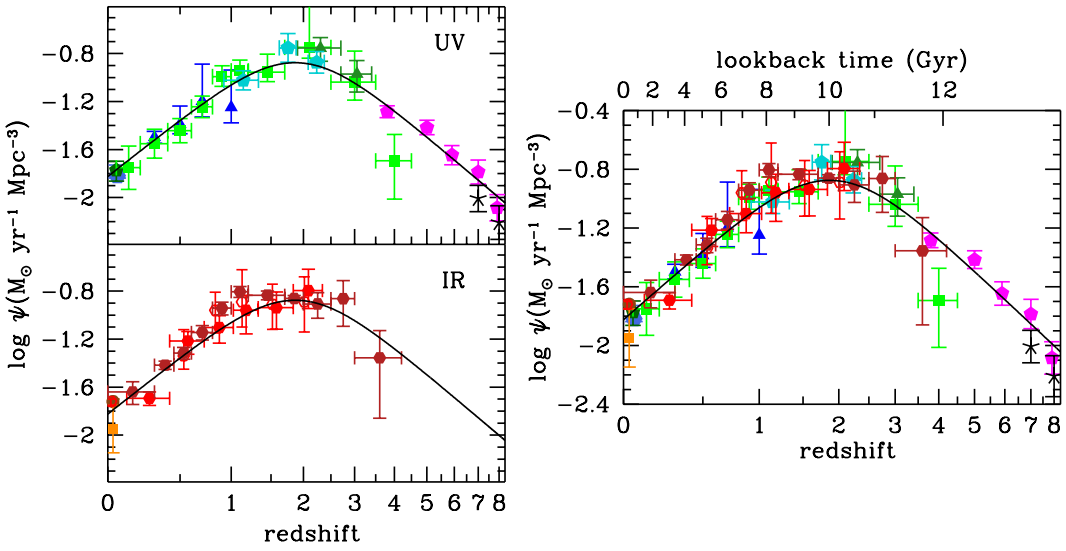

Figure 1.12: *The UV (panel a) and IR (panel b) based star formation rate densities (SFRDs, panel c combined). The clear difference in depths accessible via each selection method is visible, with UV dust-uncorrected SFRDs reaching redshifts as high as 8, while the IR dust-obscured SFRDs extending only out to* $z \sim 2-3$. *Figure adopted from Madau & Dickinson (2014).*

The IR SFRD at a given redshift is calculated by integrating the bolometric IR luminosity function multiplied by the luminosity and then converting from the IR bolometric luminosity density to the SFRD using for example Equation 1.7.

To integrate the IR LF (Figure 1.11) the luminosity dynamic range must be wide enough to have a clear picture of both faint and bright ends. Since the depth of the IR data does not yet allow to reach the faintest sources, the extrapolation has to be performed. This is usually done with the Schechter function:

$$\Phi(L)dL = \Phi_\star \left(\frac{L}{L_\star}\right)^\alpha exp\left(-\frac{L}{L_\star}\right) dL, \tag{1.13}$$

with three free parameters, the normalization point $\Phi_\star$, the characteristic luminosity $L_\star$ and the faint-end slope α. To estimate a faint-end of the Schechter function one needs to reach well beyond the knee of the LF, so that a faint-end slope could be estimated. Without deep enough data the knee area will not be reached and therefore the robust determination of the SFRD will not be possible.

1.5 Thesis aim & layout

The aim of this thesis is to present all the research that has been done by myself in order to expand on the current knowledge of submm observational astronomy. This research is mainly based on the submm data collected as a part of the SCUBA2 Cosmology Legacy Survey (S2CLS) program with the addition of a various auxiliary data (Section 2.1). The increase in both the depth and the size of the submm maps surveyed as part of the S2CLS allowed me to improve on the up-to-date knowledge of the SMG population, as presented in this Introduction.

In the next Chapter the data utilized in my research is presented and the main methods used when deriving photometric redshifts are explained. In Chapter 3, I investigate the sample of 30 bright SMGs originally detected by the AzTEC/LABOCA in the COSMOS field and later followed-up with the interferometric high-resolution SMA/PdBI observations. As explained in Subsection 1.1.4, the large search radii used for identifying the multi-waveband counterparts to the submm sources detected in a single-dish observations, require statistical methods to be used. Equipped with the interferometric data I was able to investigate the reliability of the multi-frequency identification process performed using the single-dish data. I was also able to assess the fraction of sources which could be classified as blends (composed of two or more fainter sources), as well as determine the redshift distribution and the basic physical properties of that sample.

In Chapter 4, I examine the deep S2CLS COSMOS map with the root-mean-square (RMS) noise of $1\sigma \simeq 0.25$ mJy, where 106 SMGs were detected with the significance (signal-to-noise ratio) > 5. I perform the multi-frequency identification based on the method explained in Section 2.2, calculate redshifts and basic physical properties. In particular, thanks to the depth of the data, I was able to reach the Main-Sequence (MS) regime and investigate the relation between the optically-selected star-forming (SF) galaxies and the SMGs in terms of that MS.

Chapter 5 describes how the deep COSMOS and wide UDS S2CLS maps were used to calculate the SMG contribution to the FIR-based dust-obscured star formation rate density (SFRD). As explained in Subsection 1.4.6, due to the shallow FIR/submm data, it is not possible to calculate the FIR-based SFRD at $z > 2 - 3$. The S2CLS data allowed me to extend this limit out to $z \simeq 4$. I describe how the FIR bolometric LFs were found, how the analytical form of the LFs (Schechter functions) were fitted and finally how were they integrated to estimate the lower limit on the contribution of the SMGs to the dust-obscured SFRD.

I summarize and lay out the plan for the nearest future in Chapter 6.

Chapter 2

Data, Identifications & Redshifts

In this chapter I will present information which is common to the work presented in the remaining of this thesis. The data used is listed in Section 2.1, where both the (sub)mm data, being the cornerstone of my research, and the auxiliary data is presented. The latter was necessary for identifying the multi-wavelength counterparts to the (sub)mm sources (Section 2.2), so that the optical to far-IR photometry could be collected and utilized for the redshift determination (Section 2.3).

2.1 Data

The (sub)mm data, in addition to being explained in the corresponding chapters, is briefly summarized in Table 2.1 and depicted in Figures 2.1 and 2.2. This data was used to extract the physical properties of the SMGs and to research basic characteristics of the (sub)mm population. It includes the SMA and PdBI follow-up of the brightest sources from the AzTEC and LABOCA surveys respectively and SCUBA-2 Cosmology Legacy Survey (S2CLS) COSMOS deep and UDS wide maps.

All the auxiliary data used in the following three chapters is summarized in Table 2.2. It was utilized in addition to the (sub)mm data, being the main focus of my research. It was needed for the identification of the optical counterparts to the (sub)mm sources and for the collection of the optical to far-IR photometry.

For the S2CLS deep COSMOS field the optical to mid-IR data consists of the Canada-France-Hawaii Telescope Legacy Survey (CFHTLS) COSMOS,

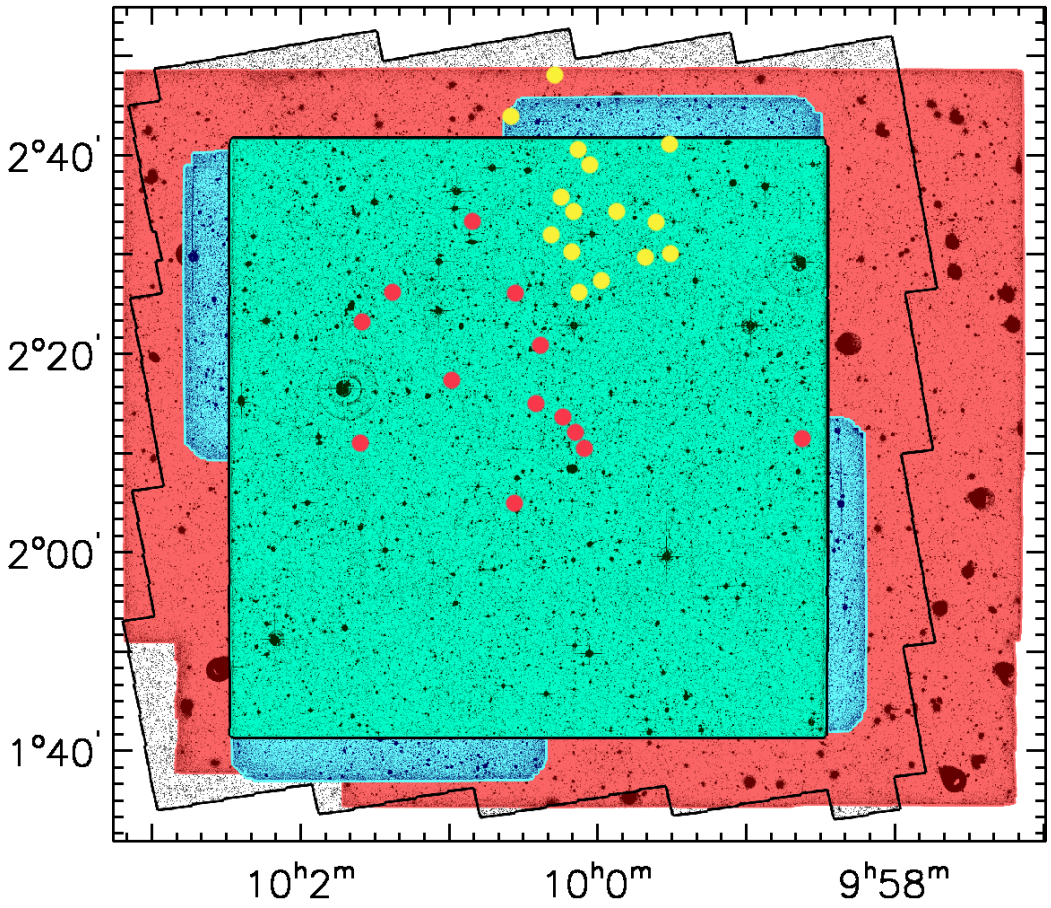

Figure 2.1: *The location of the 30 (sub-)mm sources studied in Chapter 3 within the multi-band coverage of the COSMOS field. The x and y axes are RA and Dec respectively. From the outside, the red area is the 1.5 deg^2 UltraVISTA field, the irregular black outline delineates the HST/ACS f_{814}-band imaging, the blue region is the Subaru z'-band Suprime-Cam mosiac, and the innermost green area marks the CFHTLS D2 optical data. Yellow and red dots indicate the positions of the AzTEC and LABOCA sources respectively (figure adapted from Bowler et al. (2012).*

Table 2.1: *(Sub)mm data used in the research. The columns show the name of the survey, detection wavelength, area, 1σ depth and the reference paper. In the case of the SMA/AzTEC and PdBI/LABOCA it is the AzTEC and LABOCA surveys of the COSMOS field (with quoted areas) followed-up by the SMA and PdBI interferometers respectively.*

Name	Wavelength	Area /deg^2	1σ /mJy	Reference
SMA/AzTEC	890 μm/1.1 mm	0.15	1.3	Younger et al. (2007, 2009)
PdBI/LABOCA	1.3 mm/870 μm	0.7	1.5	Smolčić et al. (2012)
S2CLS COSMOS deep	850 μm	$\simeq 0.04$	0.25	Geach et al., in prep. Koprowski et al., in prep.
	450 μm		1.5	Geach et al. (2013) Roseboom et al. (2013)
S2CLS UDS wide	850 μm	$\simeq 0.58$	1.19	Koprowski et al., in prep.

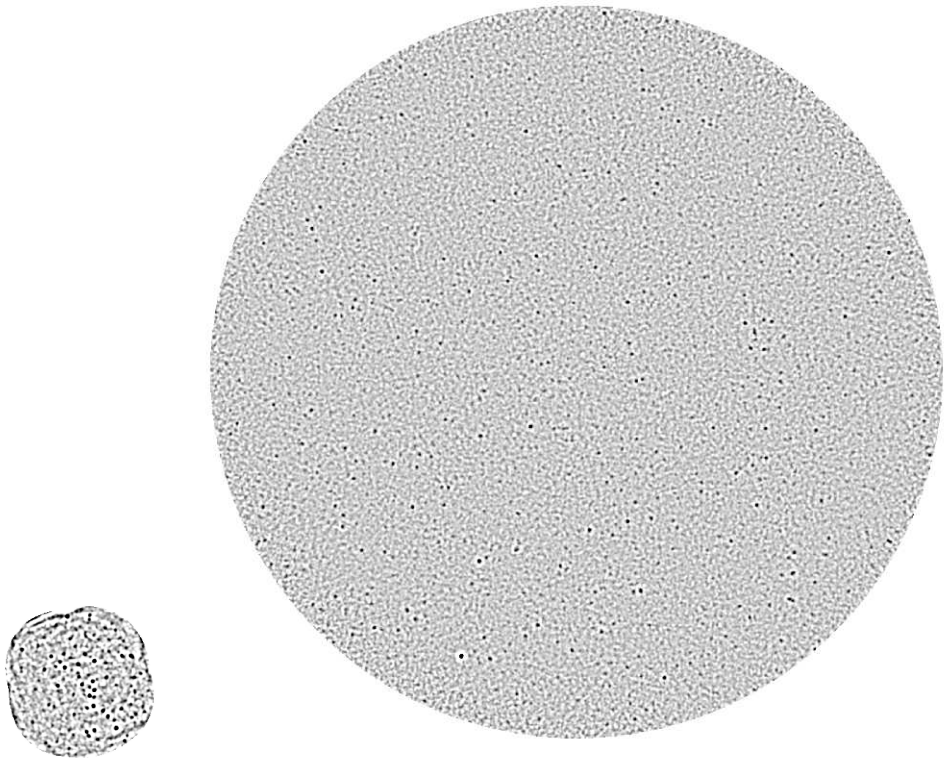

Figure 2.2: *The S2CLS deep COSMOS (left) and wide UDS (right) (sub)mm maps used in Chapter 5. This figure shows the relative sizes of both maps, where the COSMOS map is 0.042 deg^2 and the UDS is 0.58 deg^2.*

Subaru COSMOS, deep COSMOS *HST* Cosmic Assembly Near-infrared Deep Extragalactic Legacy Survey (CANDELS), UltraVISTA COSMOS and *IRAC* S-COSMOS data. From mid-IR to far-IR the *Herschel* Multi-tiered Extragalactic Survey (HerMES) COSMOS data were used. And for radio wavelengths the VLA-COSMOS Deep catalogues were utilized.

For the S2CLS wide UDS field the optical data was obtained with Subaru/SuprimeCam (Miyazaki et al., 2002), as described in Furusawa et al. (2008). The near–infrared data in the UDS field are provided by the UKIRT Infrared Deep Sky Survey (UKIDSS; Lawrence et al., 2007; Cirasuolo et al., 2010). The mid–infrared *Spitzer* data are from the *Spitzer* Public Legacy Survey of the UKIDSS Ultra Deep Survey (SpUDS; PI: J. Dunlop) described in Caputi et al. (2011).

For the extraction of far-infrared flux densities and limits I used the *Herschel* (Pilbratt et al., 2010) Multitiered Extragalactic Survey (HerMES; Oliver et al. 2012) and the Photodetector Array Camera and Spectrometer (PACS; Poglitsch et al. 2010) Evolutionary Probe (PEP; Lutz et al. 2011) data obtained with the Spectral and Photometric Imaging Receiver (SPIRE; Griffin et al. 2010) and PACS instruments, covering the entire COSMOS and UDS fields. I utilised Herschel maps at 100, 160, 250, 350 and 500 μm with beam sizes of 7.39, 11.29, 18.2, 24.9, and 36.3 arcsec, and 5σ sensitivities of 7.7, 14.7, 8.0, 6.6, and 9.5 mJy, respectively. I obtained the fluxes of each SCUBA-2 source in the following way. I extracted 120-arcsec wide stamps from each *Herschel* map around each SCUBA-2 source and used the PACS (100, 160 μm) maps to simultaneously fit Gaussians with the FWHM of the respective map, centred at all radio and 24 μm sources located within these cut-outs, and at the positions of the SCUBA-2 optical identifications (IDs, or just sub-mm positions if no IDs were selected). Then, to deconfuse the SPIRE (250, 350 and 500 μm) maps in a similar way, I used the positions of the 24 μm sources detected with PACS (at $> 3\sigma$), the positions of all radio sources, and the SCUBA-2 ID positions.

2.2 Multi-wavelength Identification

Before any of the physical properties of a given galaxy can be extracted, redshift must be found. For this purpose, multi-wavelength photometry has to be collected. As explained in the introduction, the beam sizes of the single-dish

Table 2.2: *Auxiliary data used in the research. The columns show the name of the survey and the field, filters, filters' effective wavelength, area, 5σ RMS depth in AB magnitudes unless otherwise stated and the reference paper.*

Name	Filter	λ_{eff}	Area /deg^2	5σ /AB mag	Reference
CFHTLS	u	381 nm	$\simeq 1$	26.9	Gwyn (2012)
COSMOS	g	486 nm		27.0	
	r	626 nm		26.6	
	i	769 nm		26.4	
Subaru	B	446 nm	$\simeq 2$	27.1	Taniguchi et al. (2007)
COSMOS	V	548 nm		26.7	
	g'	478 nm		27.2	
	i'	764 nm		26.1	
	r'	629 nm		26.8	
	z'	903 nm		26.0	Furusawa et al., in prep.
SXDS	B	446 nm	$\simeq 1.22$	27.9	Furusawa et al. (2008)
	V	548 nm		27.3	
	R_c	652 nm		27.2	
	i'	764 nm		27.2	
	z'	903 nm		26.1	
HST CANDELS	$F125W$	1249 nm	$\simeq 0.056$	27.4	Grogin et al. (2011)
COSMOS	$F160W$	1540 nm		27.2	
UltraVISTA	Y	1020 nm	$\simeq 1.5$	24.7	McCracken et al. (2012)
COSMOS	J	1250 nm		24.5	Bowler et al. (2012)
	H	1650 nm		24.0	
	K	2450 nm		23.8	
UKIDSS	J	1250 nm	$\simeq 0.77$	25.7	Bowler et al. (2014)
	H	1650 nm		25.1	
	K	2450 nm		25.3	
Spitzer S-COSMOS		3.6 μm	$\simeq 2$	0.9 μJy	Sanders et al. (2007)
		4.5 μm		1.7 μJy	
		5.8 μm		11.3 μJy	
		8.0 μm		14.6 μJy	
		24 μm		0.42 mJy	
Spitzer SpUDS		3.6 μm	$\simeq 0.2$	24.4	Bowler et al. (2014)
		4.5 μm		24.2	
Herschel HerMES		100 μm	$\simeq 2.0$	7.7 mJy	Oliver et al. (2012)
COSMOS		160 μm		14.7 mJy	
		250 μm		8.0 mJy	
		350 μm		6.6 mJy	
		500 μm		9.5 mJy	
Herschel HerMES		100 μm	$\simeq 0.7$	11.2 mJy	Oliver et al. (2012)
UDS		160 μm		21.4 mJy	
		250 μm		11.2 mJy	
		350 μm		9.3 mJy	
		500 μm		13.4 mJy	
VLA-COSMOS Deep		20 cm	$\simeq 0.07$	60.0 μJy	Schinnerer et al. (2010)

(sub)mm telescopes are too large for direct comparison with optical maps, so we need to find the most probable counterpart using statistical methods. In my work I use the p-statistics formalism (Subsection 1.1.4), where, for each counterpart candidate, the corrected Poisson probability that it is a chance association is calculated following Downes et al. (1986). Initially, the radio, 24 μm and 8 μm counterparts are found and only then optical equivalents are identified.

If a potential radio counterpart has a magnitude m and is situated at the distance r from the (sub)mm object, then the expected number of sources brighter than the chosen one, lying within r of the SMG is:

$$\mu = \pi r^2 N, \tag{2.1}$$

where N is the surface density of objects with magnitudes lower than m. Assuming no clustering, the sources are Poisson distributed and the probability of having at least one galaxy within radius r is:

$$\begin{aligned} P &= 1 - \text{probability of no objects} \\ &= 1 - \frac{\mu^n \exp^{-\mu}}{n!} \\ &= 1 - \exp^{-\mu}, \end{aligned}$$

where n, number of objects within r, is here equal to 0. For $\mu \ll 1$ we get:

$$P \simeq \mu. \tag{2.2}$$

It is crucial to understand what this means. The above probability (let us call it $P^\star = \pi r_\star^2 N_\star$) is the probability that at least one object will be found within r. There are however many galaxies that can individually satisfy this criterion ($P \leq P^\star$) and therefore we need to sum up all these contributions[1]. The equation 2.1 then becomes:

$$E = \int_0^{N_l} \pi r^2(N) dN, \tag{2.3}$$

[1]The analogue situation would be winning a lottery ticket. One person choosing 5 numbers out of 40 has individually a $\sim 1 \times 10^{-8}$ chance of winning. There are however $\sim 10^7$ people playing in Britain and therefore a chance of someone winning the prize is roughly equal to 0.1.

where r within which $P \leq P^{\star}$ is a function of the magnitude , ie surface density N (fainter sources are more numerous and therefore are expected to be found closer to our (sub)mm object) and N_l is the surface density of sources brighter than the detection limit of our radio image. If $P^{\star} \ll 1$ then $\pi r^2(N) = P^{\star}/N$ and so E will diverge. We therefore enforce a 2.5σ search radius within which the counterparts are being sought, scaled with the signal-to-noise ratio of our (sub)mm source detection (S/N):

$$r_s = \frac{2.5 \times 0.6 \times \mathrm{FWHM}}{\mathrm{S/N}}, \tag{2.4}$$

where FWHM is the full-width-half-maximum of the (sub)mm beam. The radius r from equation 2.3 will grow with decreasing magnitude only until it reaches r_s (at which we define the critical surface density N_c, where $P^{\star} = \pi r_s^2 N_c = \pi r_{\star}^2 N_{\star}$). The equation 2.3 therefore becomes:

$$\begin{aligned} E &= \int_0^{N_c} \pi r_s^2 dN + \int_{N_c}^{N_l} \frac{P^{\star}}{N} dN \\ &= P^{\star} \left(1 + ln\left(\frac{P_l}{P^{\star}}\right)\right), \end{aligned} \tag{2.5}$$

where $P_l = \pi r_s^2 N_l$. This introduces the correction factor to the equation 2.2 of $ln(P_l/P^{\star})$. The probability of the given radio, 24 μm or 8 μm source being a chance association is then simply:

$$P = 1 - \exp(-E). \tag{2.6}$$

To implement this method, I wrote my own routine and calculated surface densities of sources brighter than the relevant ID's magnitud. I treated counterparts with $P < 0.05$ as robust IDs and with $0.05 \leq P < 0.1$ as tentative IDs.

2.3 Redshifts

2.3.1 Optical photometric redshifts

Using the above method, the radio, 24 μm or 8 μm counterparts to the (sub)mm source was found and therefore the optical/NIR photometry collected, where available. This multi-band photometry was used to derive photometric redshifts using a χ^2 minimization method (Cirasuolo et al. 2007, 2010) with a code based on the HYPERZ package (Bolzonella et al. 2000). To create templates of galaxies, the stellar population synthesis models of Bruzual & Charlot (2003) were applied, using the Chabrier (2003) stellar initial mass function (IMF) with a lower and upper mass cut-off of 0.1 and 100 $\mathrm{M}_{\odot}$ respectively. Single and double-burst star-formation histories with a fixed solar metallicity were used. Dust reddening was taken into account using the Calzetti (2000) law within the range $0 \leq A_V \leq 6$. The HI absorption along the line of sight was applied according to Madau (1995).

2.3.2 'Long-wavelength' photometric redshifts

The 'long-wavelength' photometric redshifts were calculated using the SCUBA-2 and *Herschel* data by fitting the average SMG SED template of Michałowski et al. (2010a) with fixed dust temperature of $T_d = 35$ K. Two free parameters of the template were varied, the redshift and the normalization, and for each set of these parameters values of the SED were found at the SCUBA-2 and *Herschel* wavelengths and the value of the χ^2 calculated using:

$$\chi^2 = \sum_i \frac{(S_{\mathrm{SED}} - S_\lambda)^2}{dS_\lambda^2}, \tag{2.7}$$

where the summation is over all the wavebands used, S_{SED} is the flux density read of the SED and S_λ/dS_λ are the flux density/flux density error at the i-th waveband as measured by SCUBA-2/*Herschel*.

To find the 'long-wavelength' redshift the χ^2 was simply minimised.

Chapter 3

Properties of bright (sub-)millimetre sources

3.1 Introduction

As discovered by the Cosmic Background Explorer (COBE) satellite, the cosmic infrared background (CIRB) constitutes $\sim$ 50% of the total background light (Puget et al., 1996). Thanks to the Submillimetre Common User Bolometer Array (SCUBA; Holland et al. 1999) mounted on the James Clerk Maxwell Telescope (JCMT) it was found in the 1990s that a significant fraction of the CIRB can be resolved into discrete, individual sources called submillimetre galaxies (SMGs). Multi-wavelength follow-up studies showed that SMGs are high redshift ($z > 1$), very luminous, dust obscured galaxies with very high star formation rates (SFR) that may account for up to 50% of the cosmic star formation at these redshifts and are therefore a very important population to study.

A more thorough understanding of the nature of SMGs depends on unambiguous identifications of their multi-wavelength counterparts. This has been limited by the low resolution of submillimetre (submm) cameras ($\sim$ 15 arcsec) and faintness of SMGs in the optical. Some progress have been made with deep radio surveys, where the correlation between submm and radio continuum emission has been used (Ivison et al. 1998; Dunlop et al. 2004). Because of the far better resolution of radio images ($<$ 1 arcsec), positions of SMGs could be more accurately identified. The big downside of that, however, is the rapid dimming of the radio continuum with redshift, which makes the radio-confirmed sample

biased towards the low redshift part of the population. For this reason other methods for identifying optical and NIR counterparts were used. It was found (Ivison et al. 2007) that the *Spitzer* MIPS 24 μm waveband can be utilised as well as *Spitzer* IRAC 8 μm band (Section 1.1.4) (Ashby et al. 2006; Pope et al. 2006; Michalowski et al. 2012b). Finally, since SMGs are found to be red in the optical (Ashby et al. 2006; Michalowski et al. 2012b; Yun et al. 2012), the $i-K$ colour can also be taken into account.

With these methods, various works undertaken with SCUBA, LABOCA, AzTEC and MAMBO have generally yielded a consistent picture, whereby sources selected at $S_{850} \simeq 5\,\mathrm{mJy}$ display a redshift distribution which peaks at $z \simeq 2.5$. Despite the fact that radio and mid-infrared galaxy counterpart detection becomes increasingly difficult with increasing redshift (unlike sub-mm/mm detection), there appears to be limited room for a substantial extreme-redshift population in the typical sub-mm/mm galaxy samples studied to date. Indeed, the relatively modest disagreements between the redshift distributions of existing sub-mm galaxy samples can be attributed to cosmic variance (Michałowski et al., 2012b). Now, however, a new generation of facilities is being utilised. First, *Herschel* and the South Pole Telescope (SPT) have now delivered sufficiently large far-infrared/mm maps to uncover examples of rare, very bright, generally lensed objects, for which follow-up molecular spectroscopy has proved feasible with ALMA and the latest generation of wide bandwidth redshift receivers on single-dish (sub-)mm telescopes. For example, pre-selection of red sources from *Herschel* data has yielded a new redshift record of $z = 6.34$ for a sub-mm selected galaxy (Riechers et al., 2013), while ALMA follow-up of a bright sample of lensed sources uncovered with the SPT has yielded a redshift distribution which apparently peaks at $z > 3$ (Vieira et al., 2013; Weiß et al., 2013). In parallel with these sub-mm/mm spectroscopic studies of bright lensed sources, ALMA has also recently been used to undertake a systematic imaging study of unlensed sources in the Chandra Deep Field South (Karim et al., 2013; Hodge et al., 2013), as originally uncovered in the LABOCA LESS survey (Weiß et al., 2009b).

These new studies have produced results which some have regarded as casting doubt on our existing knowledge of the (sub-)mm source population. First, it has been claimed that the (apparently robustly established) redshift distribution of (sub-)mm sources has been biased low (Vieira et al., 2013), questioning the

reliability of the aforementioned galaxy identification techniques based on the supporting radio-near/mid-infrared imaging. Second, it has been suggested that a substantial fraction of bright (sub-)mm sources in single-dish surveys arise from blends, raising additional concerns about the effectiveness of identification methods applied to large-beam sub-mm maps (Wang et al., 2011; Karim et al., 2013; Hodge et al., 2013).

The first of these claims might seem surprising, given the high completeness of galaxy identifications in previous blank-field surveys, and the robustness of photometric redshifts (consistently yielding $z_{median} \simeq 2.5$). Nevertheless, by the end of 2012, over ten sub-mm galaxies had already been spectroscopically confirmed at $z > 4$ (Coppin et al., 2009; Capak et al., 2008, 2011; Schinnerer et al., 2008; Daddi et al., 2009a; Knudsen et al., 2009; Riechers et al., 2010; Cox et al., 2011; Smolčić et al., 2011; Combes et al., 2012; Walter et al., 2012), and it has been suggested by several authors that the most luminous sub-mm/mm galaxies appeared to lie at preferentially higher redshifts than their more moderate luminosity counterparts (e.g. Ivison et al. 2002; Wall et al. 2008; Dunlop 2011; Michałowski et al. 2012b). The second claim, regarding prevalent source blending, seems equally surprising given that previous sub-mm/mm interferometry with the SMA and PdBI interferometers had suggested that serious multiplicity was not a big issue (e.g. Iono et al. 2006; Younger et al. 2007, 2009; Hatsukade et al. 2010).

Motivated by this controversy and confusion, and by the ever-improving multi-frequency dataset in the Cosmological Evolution Survey (COSMOS) field (including UltraVISTA: McCracken et al. 2012; Bowler et al. 2012), I have undertaken a fresh investigation of the properties of bright (but unlensed) sub-mm/mm galaxies as selected from the largest flux-limited sub-mm sample with interferometric follow-up observations. My sample consists of the 30 brightest sub-mm/mm sources in the COSMOS field which were originally uncovered with AzTEC and LABOCA, and which have subsequently been imaged with the Submillimeter Array (SMA) (Younger et al., 2007, 2009) and the Plateau de Bure Interferometer (PdBI) (Smolčić et al., 2012). My aim was to combine the $\simeq 0.2$ arcsec positional accuracy delivered by the sub-mm/mm interferometry, with the latest Subaru, UltraVISTA and *Spitzer* optical-infrared photometry to unambiguously establish the galaxy identifications, redshifts (z), stellar masses ($M_\star$) and specific star-formation rates ($sSFR$) for a well-defined sample of bright

sub-mm sources. At the same time, I have taken the opportunity to revisit the issue of source multiplicity, and the robustness of galaxy identifications established using the statistical associations with radio/infrared sources which would have been deduced based on the original single-dish sub-mm/mm positions.

The remainder of this Chapter is structured as follows. In Section 2, I describe the published (sub-)mm samples in the COSMOS field with interferometric follow-up, and summarize the latest multi-frequency data that I have used to uncover and study the galaxies which produce the detected sub-mm/mm emission. Next, in Section 3, I describe the process of galaxy identification, and the extraction of robust optical-infared multi-wavelength photometry. Then, in Section 4, I present and discuss the derived properties of the galaxies, with special emphasis on the derived redshift distribution of bright (sub-)mm sources, and the stellar masses of the associated galaxies. In Section 5, I consider further my findings in the context of the latest *Herschel*/SPT/ALMA studies detailed above, and include a reassessment of how reliably galaxy counterparts can actually be established purely on the basis of the original single-dish sub-mm/mm maps (and hence to what extent higher-resolution sub-mm/mm imaging impacts on our understanding of the sub-mm galaxy population). My conclusions are summarized in Section 6.

Throughout I use the AB magnitude system (Oke, 1974), and assume a flat cosmology with $\Omega_m = 0.3, \Omega_\Lambda = 0.7$ and $H_0 = 70$ km s^{-1}Mpc^{-1}.

3.2 Data

The AzTEC/COSMOS survey covers 0.15 deg^2 of the COSMOS field at 1.1 mm with an rms noise of 1.3 mJy beam^{-1} (Scott et al., 2008). The published AzTEC/COSMOS catalogue consists of 44 sources with $S/N \geq 3.5\sigma$. The brightest fifteen of these sources were then followed up with the SMA (Younger et al., 2007, 2009), effectively yielding a flux-limited sample of millimetre selected galaxies with refined positions. All 15 of these sources were detected with the SMA, providing sub-millimetre positions accurate to $\simeq 0.2$ arcsec (see Table 3.3). Two of the sources were split by the SMA into two distinct components; AzTEC11 was subdivided into north and south components and AzTEC14 into west and east. In the case of AzTEC11 however, as can be seen from Figure 1 of Younger

Table 3.1: *A summary of the optical and near-infrared imaging data utilised in this study. Column 1 gives the filter bandpass names, column 2 their effective wavelengths, column 3 the FWHM of the bandpasses, column 4 gives the 5σ photometric depths (AB mag) within a 2-arcsec diameter aperture and column 5 gives the seeing in arcsec. The u, g, r, i imaging was delivered by the CFHT Legacy Survey, the z' imaging was obtained with the refurbished Suprime-Cam on Subaru (Bowler et al., 2012) while the Y, J, H, K_s imaging was provided by UltraVISTA DR1 (McCracken et al., 2012).*

filter	λ_{eff}/nm	$FWHM$/nm	5σ/AB mag	seeing/″
u	381.1	65.2	26.9	0.80
g	486.2	143.6	27.0	0.65
r	625.8	121.7	26.6	0.65
i	769.0	137.0	26.4	0.65
z'	903.7	85.6	26.3	1.15
Y	1020	100	24.7	0.82
J	1250	180	24.5	0.79
H	1650	300	24.0	0.76
K_s	2150	300	23.8	0.75

et al. (2009), the resolution of the SMA image is not high enough to clearly separate the components. For this reason I decided to continue to treat AzTEC11 as a single (albeit somewhat extended) galaxy for the purpose of this study.

The LABOCA/COSMOS survey covers the inner $\simeq 0.7\,\mathrm{deg}^2$ of the COSMOS field, delivering a sub-millimetre map at $\lambda = 870\,\mu$m with an rms noise level of $1.5\,\mathrm{mJy\,beam}^{-1}$ (Navarrete et al. in preparation). The 28 brightest $870\,\mu$m sources were chosen for IRAM PdBI follow-up observations with the requirement that the signal-to-noise $\mathrm{S/N_{LABOCA}} \gtrsim 3.8$ (Smolčić et al., 2012). Most of these were detected with the IRAM interferometer. To create a well-defined and (near) flux-limited sample for the present study I selected the 16 objects with $\mathrm{S/N_{PdBI}} \gtrsim 4.0$. These are listed in Table 3.4. However, as described in the notes on individual sources in Appendix A, the PdBI position of COSLA-38 is so far from the original LABOCA position, and so close to the edge of the beam that it is hard to be confident it is the same source. For this reason I have excluded COSLA-38, and all further analysis is thus performed on a final sample of 30 (sub-)mm sources.

I used the refined positions provided by the SMA and PdBI interferometry to identify galaxy counterparts in the available multi-frequency imaging. The

Table 3.2: *A summary of the wider-area Subaru optical imaging (Taniguchi et al., 2007) utilised in the study of AzTEC7 and AzTEC12. Column 1 gives the filter bandpass names, column 2 their effective wavelengths, column 3 the FWHM of the bandpasses, column 4 gives the 5σ photometric depths (AB mag) within a 2-arcsec diameter aperture and column 5 gives the seeing in arcsec.*

filter	λ_{eff}/nm	$FWHM$/nm	5σ/AB mag	seeing/″
B	446.0	89.7	27.14	0.95
V	548.4	94.6	26.75	1.33
g'	478.0	126.5	27.26	1.58
i'	764.1	149.7	26.08	0.95
r'	629.5	138.2	26.76	1.05
z'	903.7	85.6	26.00	1.15

location of the AzTEC/SMA and LABOCA/PdBI sources within the key available multi-wavelength imaging in the COSMOS field is illustrated in Figure 2.1 of Chapter 2. This imaging consists of the public IRAC imaging obtained via the S-COSMOS survey (Sanders et al., 2007), the new near-infrared imaging provided by UltraVISTA DR1 (McCracken et al., 2012), and optical imaging from the CFHT Legacy Survey (Gwyn, 2011), and Subaru (Taniguchi et al., 2007). The details of this imaging are summarized in Table 3.1 and Table 3.2, with the latter table being relevant for AzTEC7 and AzTEC12 which lie just outside the deep CFHT MegaCam pointing (see Figure 2.1 in Chapter 2), and thus required use of the (somewhat shallower) Subaru imaging available over the whole COSMOS field.

3.3 Galaxy counterparts and multi-wavelength photometry

Initially, I searched for galaxy counterparts in the UltraVISTA DR1 K_s-band imaging, using a (deliberately generous) search radius of 3 arcsec around the interferometric (sub-)mm positions. Near-infrared counterparts were found for all of the (sub-)mm sources except for AzTEC14.W, COSLA-6N, COSLA-17S and COSLA-128. However, as can be seen in Figure 3.1, for AzTEC2 (A2.S), 13, 14.E, COSLA-8, 19 and 23S the (sub-)mm to K_s positional offset is too large

Table 3.3: *The fifteen brightest COSMOS AzTEC mm sources chosen for SMA interferometric follow-up observations which were utilised in the present study. Column 1 gives the source name, column 2 the SMA position, column 3 the SMA* 890 μm *signal-to-noise ratio, column 4 the AzTEC 1.1 mm signal-to-noise ratio (Younger et al., 2007, 2009), colum 5 the SMA flux density, column 6 the de-boosted AzTEC* 1.1 *mm flux density (Scott et al., 2008). AzTEC14 was resolved by the SMA into the east and west components. AzTEC11, even though it was also just resolved by the SMA into two components, is treated here as a single, extended SMG with an* 890 μm *flux density which is the sum of the flux densities of both components (Table 1 of Younger et al. (2007).*

SMA ID	SMA coords (J2000)		S/N	S/N	$F_{890\,\mu m}$	$F_{1.1\,mm}$
	RA	Dec	SMA	AzTEC	/mJy	/mJy
AzTEC1	09 : 59 : 42.86	+ 02 : 29 : 38.2	14.2	8.3	15.6 ± 1.1	$9.3^{+1.3}_{-1.3}$
AzTEC2	10 : 00 : 08.05	+ 02 : 26 : 12.2	12.4	7.4	12.4 ± 1.0	$8.3^{+1.3}_{-1.3}$
AzTEC3	10 : 00 : 20.70	+ 02 : 35 : 20.5	5.8	5.9	8.7 ± 1.5	$5.9^{+1.3}_{-1.3}$
AzTEC4	09 : 59 : 31.72	+ 02 : 30 : 44.0	7.5	5.3	14.4 ± 1.9	$5.2^{+1.3}_{-1.4}$
AzTEC5	10 : 00 : 19.75	+ 02 : 32 : 04.4	7.1	6.2	9.3 ± 1.3	$6.5^{+1.2}_{-1.4}$
AzTEC6	10 : 00 : 06.50	+ 02 : 38 : 37.7	6.6	6.3	8.6 ± 1.3	$6.3^{+1.3}_{-1.2}$
AzTEC7	10 : 00 : 18.06	+ 02 : 48 : 30.5	8.0	6.4	12.0 ± 1.5	$7.1^{+1.4}_{-1.4}$
AzTEC8	09 : 59 : 59.34	+ 02 : 34 : 41.0	10.9	5.7	19.7 ± 1.8	$5.5^{+1.3}_{-1.3}$
AzTEC9	09 : 59 : 57.25	+ 02 : 27 : 30.6	4.1	5.6	9.0 ± 2.2	$5.8^{+1.3}_{-1.5}$
AzTEC10	09 : 59 : 30.76	+ 02 : 40 : 33.9	5.3	5.1	5.3 ± 1.0	$4.7^{+1.3}_{-1.3}$
AzTEC11	10 : 00 : 08.91	+ 02 : 40 : 10.2	8.2	5.1	14.4 ± 1.9	$4.7^{+1.3}_{-1.3}$
AzTEC12	10 : 00 : 35.29	+ 02 : 43 : 53.4	7.5	4.8	13.5 ± 1.8	$4.5^{+1.3}_{-1.5}$
AzTEC13	09 : 59 : 37.05	+ 02 : 33 : 20.0	4.5	4.8	8.2 ± 1.8	$4.4^{+1.3}_{-1.4}$
AzTEC14	...	...	...	4.7	...	$4.3^{-1.4}_{-1.4}$
AzTEC14.E	10 : 00 : 10.03	+ 02 : 30 : 14.7	5.0	...	5.0 ± 1.0	...
AzTEC14.W	10 : 00 : 09.63	+ 02 : 30 : 18.0	3.9	...	3.9 ± 1.0	...
AzTEC15	10 : 00 : 12.89	+ 02 : 34 : 35.7	4.4	4.6	4.4 ± 1.0	$4.2^{+1.3}_{-1.4}$

Table 3.4: *The sixteen brightest COSMOS LABOCA sub-mm sources which were followed up with the IRAM PdBI and are utilised here. Column 1 gives the source name, column 2 the PdBI position, columns 3 and 4 give the PdBI and LABOCA signal-to-noise ratios, while columns 5 and 6 give the PdBI and LABOCA flux densities. (Smolčić et al., 2012). Note that COSLA-38 was excluded from the analysis presented here due to the very large offset between the PdBI and LABOCA positions - see Notes on Individual Objects in Appendix A.*

PdBI ID	PdBI coords (J2000)		S/N	S/N	$F_{1.3mm}$	$F_{870\mu m}$
	RA	Dec	PdBI	LABOCA	/mJy	/mJy
COSLA-5	10 : 00 : 59.521	+ 02 : 17 : 02.57	4.1	5.0	2.04 ± 0.49	12.5 ± 2.6
COSLA-6N	10 : 01 : 23.640	+ 02 : 26 : 08.42	5.4	4.7	2.66 ± 0.49	16.0 ± 3.3
COSLA-6S	10 : 01 : 23.570	+ 02 : 26 : 03.62	4.8	4.7	3.08 ± 0.65	16.0 ± 3.3
COSLA-8	10 : 00 : 25.550	+ 02 : 15 : 08.44	4.2	4.6	2.65 ± 0.62	6.9 ± 1.6
COSLA-16N	10 : 00 : 51.585	+ 02 : 33 : 33.56	4.3	4.2	1.39 ± 0.32	14.0 ± 3.6
COSLA-17N	10 : 01 : 36.811	+ 02 : 11 : 09.66	4.6	4.2	3.55 ± 0.77	12.5 ± 3.2
COSLA-17S	10 : 01 : 36.772	+ 02 : 11 : 04.87	5.3	4.2	3.02 ± 0.57	12.5 ± 3.2
COSLA-18	10 : 00 : 43.190	+ 02 : 05 : 19.17	4.5	4.2	2.15 ± 0.48	10.0 ± 2.6
COSLA-19	10 : 00 : 08.226	+ 02 : 11 : 50.68	4.1	4.1	3.17 ± 0.76	6.7 ± 1.8
COSLA-23N	10 : 00 : 10.161	+ 02 : 13 : 34.95	7.3	3.9	3.42 ± 0.47	6.4 ± 1.6
COSLA-23S	10 : 00 : 10.070	+ 02 : 13 : 26.87	6.2	3.9	3.70 ± 0.60	6.4 ± 1.6
COSLA-35	10 : 00 : 23.651	+ 02 : 21 : 55.22	4.2	3.8	2.15 ± 0.51	8.2 ± 2.2
COSLA-38	10 : 00 : 12.590	+ 02 : 14 : 44.31	4.4	3.7	8.19 ± 1.85	5.8 ± 1.6
COSLA-47	10 : 00 : 33.350	+ 02 : 26 : 01.66	5.3	3.6	3.11 ± 0.59	9.0 ± 2.8
COSLA-54	09 : 58 : 37.989	+ 02 : 14 : 08.52	5.0	3.6	3.26 ± 0.65	11.6 ± 4.1
COSLA-128	10 : 01 : 37.990	+ 02 : 23 : 26.50	4.8	3.1	4.50 ± 0.94	11.0 ± 3.5

for the association to be trusted. Also, for the reasons detailed in Section A, the optical/infrared counterparts labelled A2.N , A6 and C5 were also not deemed reliable. This leaves a total of 18/30 (sub-)mm sources with robust near-infrared galaxy counterparts (note that in Section 3.5.2 I discuss the extent to which the same galaxy counterparts would have been identified without the availability of (sub-)mm interferometric observations).

After ensuring that all the optical–infrared imaging was accurately astrometrically–aligned to the K_s-band imaging (see Bowler et al. 2012), multi-band aperture photometry was performed at all available wavelengths through 2-arcsec diameter apertures, with multiple 2-arcsec diameter apertures placed on blank-sky regions within $\simeq 30$ arcsec of the source in order to reliably estimate the local photometric uncertainty in each band. With the obvious exception of the IRAC imaging, the imaging data are fairly well matched in terms of seeing quality, but all aperture magnitudes were subsequently corrected to total utilising the measured point spread function in each band. Photometry in the IRAC bands was taken from the S-COSMOS imaging, again corrected to total assuming the sources were not significantly resolved at IRAC wavelengths.

3.4 Source properties

3.4.1 Photometric redshifts

The multi-band photometry described above was used to derive photometric redshifts using a method outlined in Section 2.3. For the (sub-)mm sources for which no optical near-infrared counterpart was found in the available imaging, long-wavelength photometric redshift estimates were derived from their 24 μm to 20 cm SEDs (including the radio flux densities given by Smolčić et al. 2012) using the method outlined in Section 2.3. Given the potential complications of dust temperature varying with redshift (e.g. Aretxaga et al. 2007; Amblard et al. 2010), me and my supervisors experimented with various template libraries, but found that the strongest correlation between redshifts derived from the long-wavelength data and the known optical–near-infrared redshifts (either spectroscopic or photometrically estimated) was achieved by fitting the long-wavelength data with this average template (see Figure 3.2). Thus, treating the shorter-wavelength redshift information as a training set, I adopted values for z_{LW}

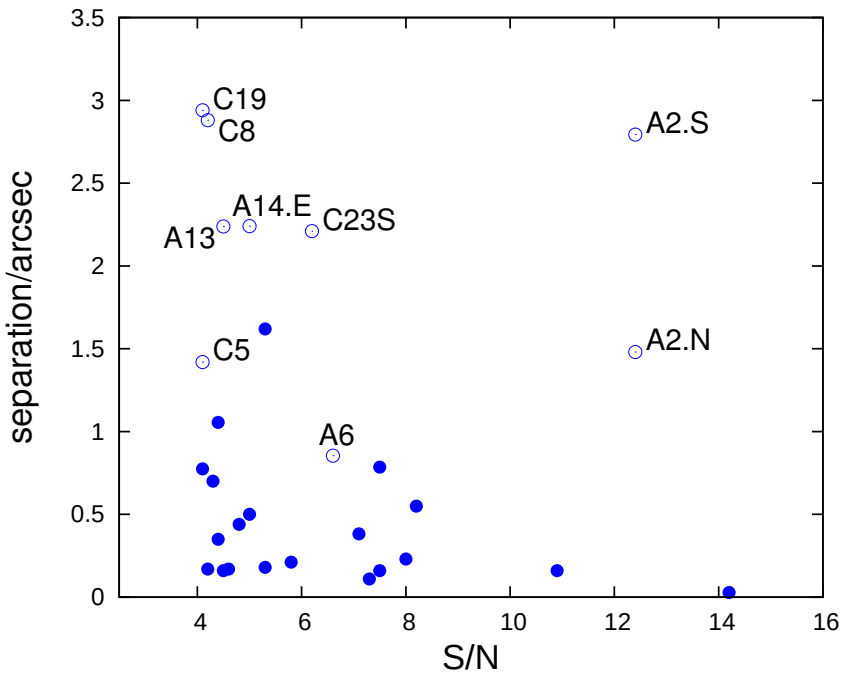

Figure 3.1: *The interferometric S/N of each (sub-)mm detection is plotted here as a function of angular separation between the (sub-)mm interferometric position and the nearest potential near-infrared/optical counterpart in the available imaging. The empty circles represent objects for which we regard the multi-frequency match as incorrect given the positional accuracy delivered by the interferometry (i.e. all objects with a separation* > 2 *arcsec). AzTEC2 was initially matched to a bright foreground galaxy (A2.S) in the wings of which a fainter, possibly lensed object was discovered (A2.N) after careful image analysis. However, because the radio counterpart of AzTEC2 is exactly at the position of the SMA ID, both these possible near-infrared counterparts can be excluded. COSLA-5 was matched to an optical object (C5), as was AzTEC6 (A6), for which Smolčić et al. (2012) derived photometric redshifts of* $z_{est} \simeq 0.85$ *and* $z_{est} \simeq 0.82$ *respectively. However, these relatively low-redshift possible identifications can be excluded due to the lack of any radio detections in the available VLA 1.4 GHz imaging, which securely places the (sub-)mm sources at higher redshifts (at least* $z > 1.5$*; see Figure 3.3, and Section A. The blue filled dot with a separation of 1.62 arcsec is my optical counterpart for AzTEC10, which I selected on the basis of* $8\,\mu m$ *flux density and* $i - K$ *colour. The filled blue dot with a separation of 1.05 arcsec indicates our chosen identification for AzTEC15.*

based on fitting the far-infrared−radio data with the Michałowski et al. (2010a) template, and these are the values listed in column 4 of Table 3.5.

The resulting redshift measurements and estimates are summarised in Table 3.5. As a basic test of the reliability of redshift estimates, I compare (in Figure 3.2) my photometric redshifts with the spectroscopic measurements for the five sources in our sample for which reliable optical spectroscopy of the current galaxy counterparts has been obtained (Smolčić et al., 2012); the mean offset is $\Delta z/(1 + z_{spec}) = 0.009 \pm 0.026$, consistent with zero. In the lower panel of this figure we compare our optical/near-infrared photometric redshift estimates with my long-wavelength photometric redshifts for those sources for which both estimates are available. This shows that the z_{LW} redshift estimates are certainly consistent with the optical/near-infrared photometric redshifts, albeit with more scatter and with a trend for some high-redshift sources to have redshift underestimated by z_{LW}. This suggests that at least some of the most distant (sub-)mm galaxies in my sample may have higher dust temperatures compared to the average $z \simeq 2 - 3$ (sub-)mm galaxies SED template utilised here to derive z_{LW}.

In Figure 3.3, I plot our objects on the redshift−millimetre/radio flux-density ratio plane, both using my final redshifts (Table 3.5) and using the redshifts given for these same objects by Smolčić et al. (2012) (column 4 of Table 3.5). I plot the redshift information in this way both to clarify the extent to which the redshift estimates differ from those adopted by Smolčić et al. (2012) on a source-by-source basis, and to demonstrate that all my adopted redshifts (z_{spec}, or failing that z_{phot}, or failing that z_{LW}) are consistent with the anticipated redshift dependence of the millimetre/radio flux-density ratio displayed by a reasonable range of template long-wavelength SEDs (as detailed in the plot legend). This plot serves to emphasize that the redshifts given for at least 6 (and more likely 8) of these (sub-)mm sources by Smolčić et al. (2012) are clearly incorrect, as the resulting flux-density ratios are inconsistent with (i.e. much larger than) even extreme choices of cool SEDs at the relevant redshifts.

3.4.2 Redshift distribution

The differential redshift distribution derived for my complete 30-source sample is presented in Fig. 3.4, where it is compared with several recently-published redshift distributions for (sub-)mm source samples. The median redshift derived for our

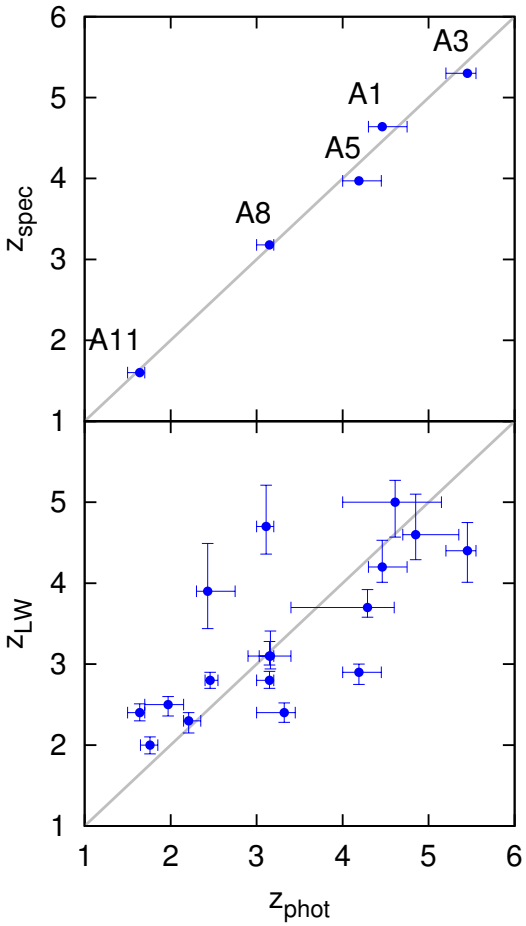

Figure 3.2: *Upper panel: optical/near-infrared photometric redshifts plotted versus the spectroscopic redshifts for the five sources with reliable spectroscopy (Smolčić et al., 2012), demonstrating the accuracy of* z_{phot}*. Lower panel: the optical/near-infrared photometric redshifts* (z_{phot}) *are compared with the long-wavelength mm/radio estimates* (z_{LW}) *for those objects for which both measurements are possible (see Table 3.5) in order to check for accuracy and potential bias; the significantly greater uncertainty in* z_{LW} *is apparent, but the mean value of* z_{phot}/z_{LW} *is* 1.2 ± 0.36*, consistent with unity, and thus indicating no major systematic bias.*

Table 3.5: *Spectrocopic redshifts (z_{spec}), optical/near-infrared photometric redshifts (z_{phot}), 'long-wavelength' (sub-)mm/radio redshift estimates (z_{LW}), Smolčić et al. (2012) redshifts (z_S) and stellar masses calculations (M_*) for the (sub-)mm galaxies in my final 30-source COSMOS sample. Note that stellar masses can only be estimated for the 18 sources for which an optical/near-infrared counterpart was secured in the available imaging data. Errors on the photometric redshifts were derived from the redshift values corresponding to χ^2 values higher by $\Delta\chi^2 = 1$ from the minimum-χ^2 solution and these photometric redshift errors are propagated through to the derived random errors on the stellar masses (which they dominate). In the case of the Smolčić et al. (2012) redshifts, the values without errors are the optical spectroscopic redshifts for their chosen galaxy identifications (albeit we reject several of these as implausible for the (sub-)mm sources; see Fig. 4) and the two lower limits are mm-to-radio estimates (which are clearly consistent with our the estimates of z_{LW}).*

Source	z_{spec}	z_{phot}	z_{LW}	z_S	$\log_{10}(M_*/\mathrm{M}_\odot)$
AzTEC1	4.64	$4.46^{+0.29}_{-0.16}$	$4.20^{+0.33}_{-0.19}$	$4.26^{+0.17}_{-0.20}$	$11.30^{+0.04}_{-0.03}$
AzTEC2	-	-	$3.60^{+0.13}_{-0.18}$	1.125	-
AzTEC3	5.30	$5.45^{+0.10}_{-0.25}$	$4.40^{+0.35}_{-0.39}$	5.299	$10.93^{+0.01}_{-0.03}$
AzTEC4	-	$4.61^{+0.54}_{-0.61}$	$5.00^{+0.27}_{-0.43}$	$4.10^{+0.43}_{-1.11}$	$11.53^{+0.08}_{-0.10}$
AzTEC5	3.97	$4.19^{+0.26}_{-0.19}$	$2.90^{+0.10}_{-0.15}$	3.971	$11.49^{+0.04}_{-0.03}$
AzTEC6	-	-	$3.86^{+4.91}_{-0.92}$	0.802	-
AzTEC7	-	$1.76^{+0.09}_{-0.11}$	$2.00^{+0.10}_{-0.11}$	$2.30^{+0.10}_{-0.10}$	$11.56^{+0.03}_{-0.04}$
AzTEC8	3.18	$3.15^{+0.05}_{-0.15}$	$2.80^{+0.11}_{-0.10}$	3.179	$11.23^{+0.01}_{-0.03}$
AzTEC9	-	$4.85^{+0.50}_{-0.15}$	$4.60^{+0.50}_{-0.31}$	1.357	$11.02^{+0.07}_{-0.02}$
AzTEC10	-	$5.00^{+2.00}_{-0.50}$	$4.90^{+0.60}_{-0.41}$	$2.79^{+1.86}_{-1.29}$	$11.76^{+0.25}_{-0.08}$
AzTEC11	1.60	$1.64^{+0.06}_{-0.14}$	$2.40^{+0.11}_{-0.10}$	1.599	$10.95^{+0.02}_{-0.05}$
AzTEC12	-	$2.46^{+0.09}_{-0.06}$	$2.80^{+0.10}_{-0.10}$	$2.54^{+0.13}_{-0.33}$	$11.35^{+0.02}_{-0.02}$
AzTEC13	-	-	$4.70^{+1.25}_{-1.04}$	> 3.59	-
AzTEC14	-	-	$3.38^{+1.00}_{-0.54}$	> 3.03	-
AzTEC15	-	$2.43^{+0.32}_{-0.13}$	$3.90^{+0.59}_{-0.46}$	$3.01^{+0.12}_{-0.36}$	$11.19^{+0.08}_{-0.03}$
COSLA-5	-	-	$2.50^{+0.26}_{-0.17}$	$0.85^{+0.07}_{-0.06}$	-
COSLA-6N	-	-	$3.72^{+1.42}_{-0.63}$	$4.01^{+1.51}_{-0.83}$	-
COSLA-6S	-	-	$4.05^{+1.70}_{-0.71}$	$0.48^{+0.19}_{-0.22}$	-
COSLA-8	-	-	$1.90^{+0.11}_{-0.22}$	$1.83^{+0.41}_{-1.31}$	-
COSLA-16N	-	$2.21^{+0.14}_{-0.06}$	$2.30^{+0.10}_{-0.15}$	$2.16^{+0.12}_{-0.25}$	$11.38^{+0.04}_{-0.02}$
COSLA-17N	-	$3.11^{+0.09}_{-0.11}$	$4.70^{+0.51}_{-0.34}$	$3.37^{+0.14}_{-0.22}$	$11.09^{+0.02}_{-0.02}$
COSLA-17S	-	-	$3.94^{+1.64}_{-0.70}$	$0.70^{+0.21}_{-0.22}$	-
COSLA-18	-	$1.97^{+0.18}_{-0.27}$	$2.50^{+0.10}_{-0.14}$	$2.90^{+0.31}_{-0.43}$	$11.37^{+0.05}_{-0.08}$
COSLA-19	-	-	$3.50^{+0.34}_{-0.34}$	$3.98^{+1.62}_{-0.90}$	-
COSLA-23N	-	$4.29^{+0.31}_{-0.89}$	$3.70^{+0.22}_{-0.12}$	$4.00^{+0.67}_{-0.90}$	$11.53^{+0.05}_{-0.16}$
COSLA-23S	-	-	$4.80^{+2.25}_{-0.86}$	$2.58^{+1.52}_{-2.48}$	-
COSLA-35	-	$3.16^{+0.24}_{-0.26}$	$3.10^{+0.31}_{-0.16}$	$1.91^{+1.75}_{-0.64}$	$11.46^{+0.05}_{-0.06}$
COSLA-47	-	$3.32^{+0.13}_{-0.32}$	$2.40^{+0.12}_{-0.12}$	$2.36^{+0.24}_{-0.24}$	$11.54^{+0.03}_{-0.07}$
COSLA-54	-	$3.15^{+0.05}_{-0.15}$	$3.10^{+0.18}_{-0.11}$	$2.64^{+0.38}_{-0.26}$	$11.62^{+0.01}_{-0.03}$
COSLA-128	-	-	$4.90^{+2.27}_{-0.90}$	$0.10^{+0.19}_{-0.00}$	-

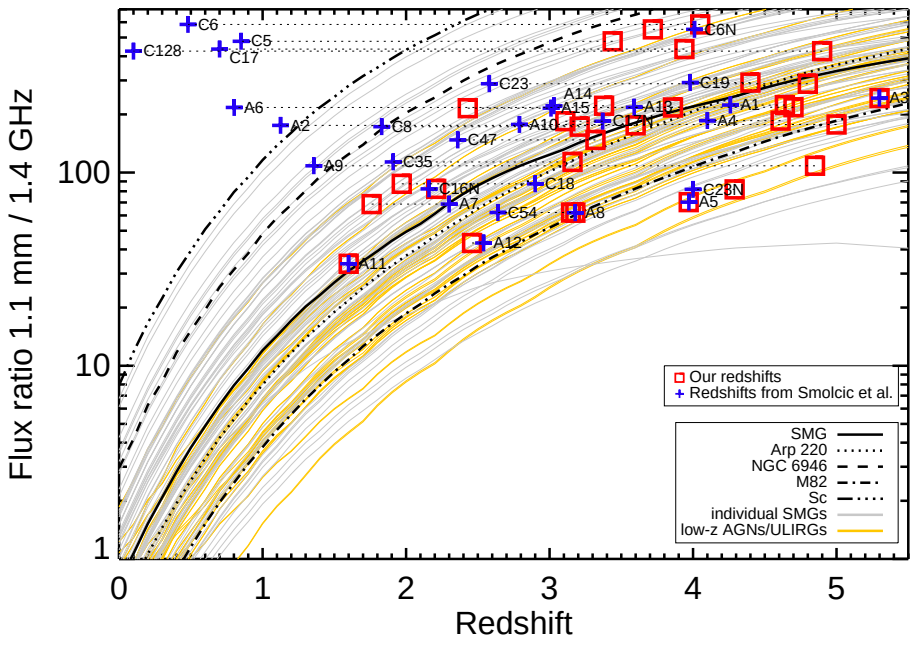

Figure 3.3: *The millimetre/radio flux-density ratio of the 30 COSMOS (sub-)mm sources plotted against their redshifts as derived in the present study (red squares) and in the previous study by Smolčić et al. (2012) (blue crosses). These data points showing the positions of the individual sources on this diagram are overlaid on a range of curves indicating the expected redshift dependence of the observed value of the 1.1mm/1.4GHz flux-density ratio as derived from a wide range of observed galaxy SEDs (figure adapted from Michałowski et al. (2012b). This plot serves to illustrate three key points. First, it shows that the redshifts derived here (whether spectroscopic redshifts, optical–near-infrared photometric estimates, or long-wavelength SED fits) all result in reasonable values for the mm/radio flux-density ratios. Second, it is clear that the redshifts adopted by Smolčić et al. (2012) for at least six of the sources are implausible, in the sense that they are inconsistent with the form of any plausible long-wavelength SED. Third, by connecting the alternative redshift estimates of each source with dotted lines, it is made clear which sources have had their redshifts most dramatically revised in the current work (see also Section A).*

COSMOS sample is $z_{med} = 3.44 \pm 0.16$, whereas for the AzTEC/SHADES sample it is $z_{med} = 1.89 \pm 0.06$ (Michałowski et al., 2012b), and for the sample of Chapman et al. (2005), $z_{med} = 2.14 \pm 0.06$. Clearly, the redshift distribution of my (sub-)mm sample lies at somewhat higher redshift than the majority of recently-published redshift distributions for (sub-)mm selected samples. In part this could be due to the fact that there are no obvious biases in the identification techniques used here, whereas several previously-published redshift distributions contain only sources with robust radio identifications. However, as I explore further below, it may also be due to the fact that the sample considered here is confined to significantly more luminous (sub-)mm sources than, for example, the source samples considered by Michałowski et al. (2012b), or Yun et al. (2012), or Simpson et al. (2014). I re-emphasize that, despite the fact that most of the (sub-)mm sources are in common, my redshift distribution lies at significantly higher redshift than that published by Smolčić et al. (2012); as discussed above (and detailed in Figure 3.3) in part this is undoubtedly due to my rejection of several of the lower-redshift candidate identifications proposed by Smolčić et al. (2012), but it is also in part a result of my deliberate exclusion of some of the less luminous LABOCA/PdBI sources in an effort to achieve a homogenous bright source sample.

Interestingly, as shown in Fig. 3.5, the redshift distribution derived here is basically identical to that produced by Vieira et al. (2013) from their ALMA follow-up CO spectroscopy of the lensed mm-selected galaxy sample from the SPT (the K-S test yields $p = 0.991$). This is potentially important because, until now, it has been claimed that the SPT redshift distribution is inconsistent with any (sub-)mm source redshift distribution derived without the benefit of ALMA CO spectroscopy (see Vieira et al. 2013).

It is reassuring that these two redshift distributions are so clearly consistent, as it is hard to imagine that my rather robust and well-validated photometric redshift estimation techniques should yield a significantly biased redshift distribution. However, it needs to be explained why the sample studied here yields a redshift distribution consistent with the SPT results, while most other studies of (sub-)mm galaxies clearly do not. As justified further below, I believe there is good evidence that this is primarily a result of 'downsizing' in the star-forming population, and that both our COSMOS sample and the SPT sample are biased to significantly higher-luminosity sources than most other studies (e.g. Michałowski et al. 2012b;

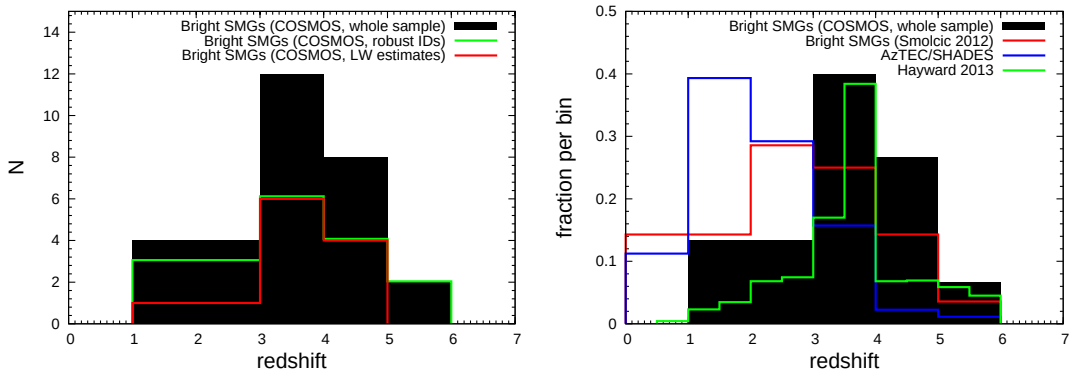

Figure 3.4: **Left panel***: The redshift distribution of my full 30-source sample of luminous (sub-)mm sources in the COSMOS field (Table 3.5). The mean redshift is* $\bar{z} = 3.53 \pm 0.19$*. Where available, optical spectroscopic redshifts (*z_{spec}*) have been used (5 sources), with optical/near-infrared photometric estimates (*z_{phot}*) then used where judged robust (13 sources), and long-wavelength redshift estimates (*z_{LW}*) adopted for the remaining objects (12 sources).* **Right panel** *Redshift distribution for the whole COSMOS sample with overlaid distributions derived for the COSMOS sources by Smolčić et al. (2012) (*$\bar{z} = 2.8 \pm 0.3$*), and for the robust galaxy identifications in the AzTEC/SHADES survey presented by Michałowski et al. (2012b) (*$\bar{z} = 2.0 \pm 0.1$*). In addition I plot the Hayward et al. (2013) simulated redshift distribution for mm-selected sources with* $F_{1.1\,\mathrm{mm}} > 4\,mJy$*, which is consistent with the observed redshift distribution presented here for comparably luminous sources.*

Simpson et al. 2014; Swinbank et al. 2014). Of course, part of the reason the SPT sources are so *apparently* bright is that they are lensed, but it transpires that in general the lensing factors are not sufficiently extreme to remove the overall bias of the bright/large SPT survey towards the most intrinsically luminous mm sources (for example, the de-lensed 860 μm flux densities of four SPT sources with completed lens modelling reported by Hezaveh et al. (2013) are 5, 6, 16, and 23 mJy).

The above comparison and discussion suggests that there is a correlation between (sub-)mm luminosity and mean redshift, in the sense that more luminous sources lie, on average, at systematically higher redshifts. Such a correlation has been suggested before (e.g. Dunlop et al. 1994; Ivison et al. 1998; Dunlop 2011; Michałowski et al. 2012b; Smolčić et al. 2012) and, as discussed above, provides arguably the most natural explanation for the consistency of the redshift

distribution presented here with that derived from the bright SPT surveys.

In an attempt to better establish the statistical evidence for this, I plot in Fig. 3.6 the 1.1 mm flux density for the sources studied here and in the SHADES AzTEC survey Michałowski et al. (2012b) versus their redshifts. A correlation is apparent, and calculation of the Spearman rank coefficient for the flux-redshift correlation is yields 0.4557, rejecting the null hypothesis of no correlation with a significance value $p < 10^{-6}$. However, this result is potentially biased by the fact that it includes only the identified sources in the AzTEC/SHADES sample. When the AzTEC/SHADES sources with no secure identifications/redshifts are included (with redshifts scattered randomly between the lower limit implied by the mm/radio flux ratio and $z = 6$), the Spearman rank coefficient drops to 0.116, yielding $p = 0.025$. I thus conclude that the data do indeed support the existence of a correlation between (sub-)mm luminosity and typical redshift, but that more dynamic range and improved redshift completeness for the fainter samples is required to establish the significance and form of this relation beyond doubt.

3.4.3 Stellar masses and specific star formation rates

For the 18 galaxies for which I secured a robust optical-infrared identification, my collaborator Michele Cirasuolo was able to use the results of the two-component SED fitting which was used to obtain photometric redshifts to obtain an estimate of the stellar mass of each (sub-)mm selected galaxy. As described in Michałowski et al. (2012b), he assumed a Chabrier (2003) stellar IMF, and the stellar masses are based on the models of Bruzual & Charlot (2003) adopting a two-component star-formation history. Where a robust spectroscopic redshift was available he adopted it, but otherwise derived the mass based on the photometric redshift. The results are tabulated in the final column of Table 3.5. The median stellar mass is $M_\star \simeq 2.2 \times 10^{11}\,\mathrm{M}_\odot$, in excellent agreement with the average stellar mass of $z \simeq 2$ sub-mm galaxies by Michałowski et al. (2012b).

I also used the redshifts and (sub-)mm flux densities of the identified sources to estimate their star-formation rates (SFR). The SFRs were calculated from the (sub-)mm flux densities assuming the average (sub-)mm SED template of Michałowski et al. (2010a). Due to the negative K-correction, a flux density of 1 mJy at $\lambda \simeq 1$ mm corresponds approximately to a total (bolometric) infrared luminosity of $\simeq 10^{12}\,\mathrm{L}_\odot$ at $z > 1$, which converts to a $SFR \simeq 100\,\mathrm{M}_\odot\mathrm{yr}^{-1}$ after

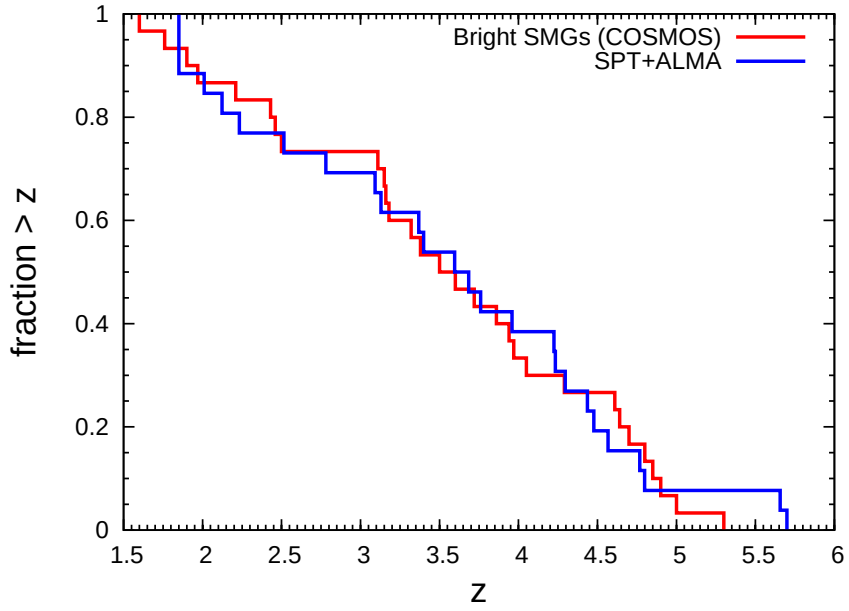

Figure 3.5: *A comparison of my estimated cumulative redshift distribution for the bright 30-source COSMOS sample considered here, and that published by Vieira et al. (2013) from ALMA follow-up CO spectroscopy of the lensed mm sources uncovered by the SPT. It is visually obvious that the redshift distributions are indistinguishable, and indeed application of the K-S test yields a significance value* $p = 0.991$.

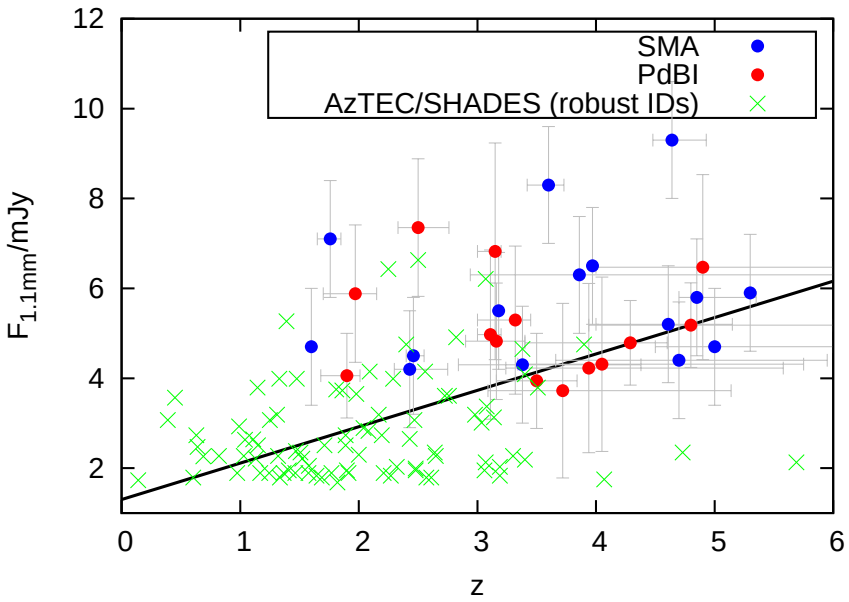

Figure 3.6: *1.1 mm flux density versus redshift. Red and blue dots represent our LABOCA and AzTEC samples respectively. Black crosses are AzTEC/SHADES sources with robust galaxy counterparts (Michałowski et al., 2012b). The fluxes are those measured by the single dish facilities, with LABOCA 870 μm flux densities converted to 1.1 mm estimated measurements assuming the mean sub-mm galaxy SED template of Michałowski et al. (2010a). The blue line is the best-fitting straight line;* $F_{1.1\,\mathrm{mm}} = (0.73 \pm 0.12)z + (1.73 \pm 0.33)$. *The Spearman correlation coefficient is 0.4557; the resulting significance level (p) is less than* 10^{-6}, *indicating a highly significant correlation between redshift and mm flux density (and hence luminosity).*

converting to a Chabrier (2003) IMF (Kennicutt 1998).

Armed with stellar masses and estimates of SFR, I have then proceeded to derive the specific star-formation rate of each source ($sSFR$). The results are plotted in Figure 3.7, where I show both the values derived from the original single-dish measurements, and those derived assuming the interferometric flux densities. While individual values vary (see figure caption for details), it can be seen that in both cases the median value is $sSFR \simeq 2.5\,\mathrm{Gyr}^{-1}$. This is essentially identical to the average $sSFR$ displayed by 'normal' star-forming galaxies on the 'main sequence' of star formation at $z > 2$ (e.g. González et al. 2010, but see also Stark et al. 2013) and is again consistent with the findings of Michałowski et al. (2012b); while some subset of (sub-)mm selected galaxies might display values $sSFR$ which place them above the main sequence, in general they display star-formation rates which are perfectly consistent with the main-sequence expectation based on their high stellar masses (see also Roseboom et al. 2013).

3.5 Single dish versus interferometric measurements

3.5.1 Multiplicity and number counts

Recently, ALMA observations of 122 870 μm sources in the Extended Chandra Deep Field South (ECDFS) from the Laboca LESS survey (Weiß et al., 2009b) have been presented, first by Karim et al. (2013), and then in more detail by Hodge et al. (2013). This sample includes twelve bright objects with original single-dish flux-density measurements of $S_{870} > 9\,\mathrm{mJy}$. From this 'ALESS' study, Karim et al. (2013) reported that source multiplicity is common, and that most bright (sub-)mm sources uncovered in single-dish surveys to date are in fact artificial, resulting from blends of fainter (albeit sometimes physically associated) sources within the original single-dish beam. Indeed, Karim et al. (2013) went so far as to claim that $S_{870} > 9\,\mathrm{mJy}$ may represent a physical limit to the luminosity of a star-forming galaxy.

However, it is clear that this conclusion is at odds with the sample under study here, in which nine objects retain flux-densities $S_{870} > 9\,\mathrm{mJy}$ within a single component in the high-resolution interferometric follow-up. It also runs

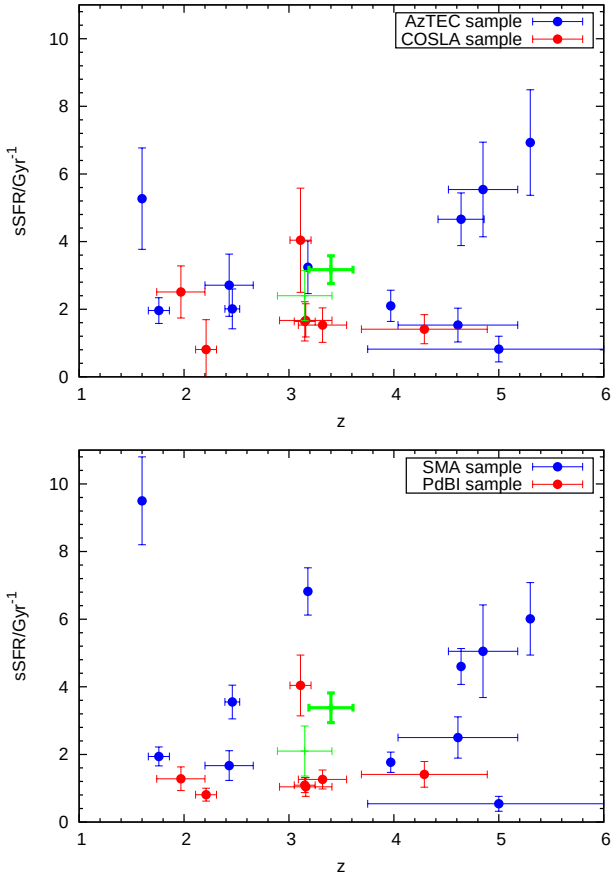

Figure 3.7: *Specific star-formation rate (sSFR) versus redshift. The upper panel shows sSFR values based on AzTEC (blue dots) and LABOCA (red dots) flux densities, while in the lower panel I plot sSFR values based on SMA (blue dots) and PdBI (red dots) interferometric flux densities. The green points with error bars show the median (thinner error bars) and mean (thicker error bars) values of sSFR and z in each panel; in the upper panel the median* $sSFR = 2.40 \pm 0.74\ Gyr^{-1}$ *(mean* $sSFR = 3.17 \pm 0.41\ Gyr^{-1}$*) while in the lower panel median* $sSFR = 2.1 \pm 0.74\ Gyr^{-1}$ *(mean* $sSFR = 3.38 \pm 0.44\ Gyr^{-1}$*). I conclude that the typical value of* $sSFR \simeq 2.5\ Gyr^{-1}$*, consistent with the 'main sequence' of star-forming galaxies at* $z > 2$*, and that this conclusion is basically unaffected by whether I adopt the single-dish or interferometric measurements of (sub-)mm flux density. Errors on sSFR are dominated by the combined effects of the uncertainties in stellar mass (see Table 3.5) and the uncertainties in the long-wavelength flux-density measurements. Errors in redshifts are as given in Table 3.5, with no horizontal error bar visible for those sources with spectroscopic redshift measurements.*

contrary to the results of various other SMA follow-up studies of SCUBA sources, which have generally suggested that (sub-)mm source multiplicity is rare (e.g. Downes et al. 1999; Iono et al. 2006; Younger et al. 2007, 2009; Cowie et al. 2009; Hatsukade et al. 2010).

A more detailed account of the ALESS results has now been published by Hodge et al. (2013), facilitating an assessment of the prevalence of multiplicity. In fact, contrary to the claims advanced in Karim et al. (2013) (and repeated in the abstract of Hodge et al. 2013), the ALMA results show that significant multiplicity is not common at all, consistent with previous studies (including the sample under study here). Specifically, for the 20 brightest LESS sources for which Hodge et al. (2013) report ALMA results, only 5 reveal multiple ALMA subcomponents, and in only 2 of these 5 does the secondary component contribute $> 20\%$ of the flux density, thereby potentially significantly distorting the flux density and/or position of the original single-beam LABOCA source. Moreover, table 3 from Hodge et al. (2013) confirms that for the brightest 20 LESS sources, the radio identification technique in fact already yielded the correct galaxy counterpart in 17/20 cases (Biggs et al., 2011).

Thus the ALMA results in fact confirm that multiplicity is *not* common, with only $\simeq 10\%$ of bright sources showing a significant (e.g. $> 20\%$) flux contribution from a secondary component. This result is confirmed by recent reports of SMA follow-up of SCUBA2 sources, which conclude that only $\simeq 12\%$ of the $850\,\mu$m sources in SCUBA2 samples arise from blends of multiple fainter sources (Chen et al., 2013a).

In the present study I have also investigated whether there is any evidence that, on average, significantly less (sub-)mm flux-density is returned by the interferometric observations as compared to the original single-dish measurements. Here this is complicated by the fact that the AzTEC sources were followed up with (SMA) interferometry at shorter wavelengths, while the COSLA sources were followed up with (PdBI) interferometry at longer wavelengths. However, at least this brings some symmetry to the problem, potentially ameliorating somewhat any biases introduced by an incorrect choice of long-wavelength SED when performing the necessary k-corrections. In addition, I have performed this test with two different long-wavelength SED templates. Using the average SMG template described in Section 4.1 (applied at the relevant redshifts), I find

that the mean interferometric/single-dish flux-density ratio for the 30 sources is $F_{int}/F_{single} = 0.96 \pm 0.09$ (median $F_{int}/F_{single} = 0.89$). Using an Arp220 template, I find that mean $F_{int}/F_{single} = 0.98 \pm 0.08$ (median $F_{int}/F_{single} = 0.90$). Thus, while we acknowledge that the current sample is not ideal for this test, I find no significant evidence that either multiplicity or very extended emission is (on average) present at a level than can distort the true flux density of the sources in the large-beam single-dish measurements (at least with the beam sizes utilised here) by more than $\simeq 10\%$.

In summary, it now appears extremely unlikely that the number counts of (sub-)mm sources derived from single-dish surveys (e.g. Coppin et al. 2006; Austermann et al. 2010) have been significantly distorted by source blending, and the new interferometry results reinforce the success of previous galaxy counterpart identification programs which have concluded that $\simeq 80\%$ of (sub-)mm sources can have their galaxy counterparts correctly identified via sufficiently deep ancillary radio and/or Spitzer data. For completeness, I now explore this issue further, focussing on what conclusions would be drawn from the 30-source sample considered here, both with and without the extra information provided by interferometric follow-up.

3.5.2 The reliability of (sub-)mm galaxy identifications

Given the afore-mentioned success of the pre-ALMA LESS identification program (Biggs et al., 2011), it is of interest to consider the extent to which the galaxy counterparts in the present COSMOS (sub-)mm sample would have been successfully identified without the assistance of the SMA and PdBI interferometric follow-up.

In the fifteen years since the discovery of (sub-)mm sources, several methods have been proposed to identify their galaxy counterparts in the face of the relatively poor positional accuracy provided by single-dish (sub-)mm imaging. As already discussed, deep radio (generally 1.4 GHz VLA) imaging and deep mid-infrared (generally 24 μm *Spitzer* MIPS) imaging have proved particularly powerful in identifying galaxy counterparts, due to the fact these wavelengths also trace star-formation activity (e.g. Ivison et al. 2010), provide improved positional accuracy (especially at radio wavelengths) and yield source densities on the sky which are generally low enough to yield statistically-significant associations (e.g.

Ivison et al. 2002, 2007; Dunlop et al. 2010; Wardlow et al. 2011; Yun et al. 2012; Michałowski et al. 2012b). It has also been found that (sub-)mm sources generally display very red optical-infrared ($i-K$) colours (e.g. Smail et al. 2004; Ashby et al. 2006; Michałowski et al. 2012b; Yun et al. 2012), apparently caused by a combination of dust obscuration and the presence of underlying massive evolved stellar populations (Michałowski et al., 2012a). Finally, it is now also well-established that (sub-)mm galaxies are among the brightest galaxies at rest-frame near-infrared wavelengths, again due to their large stellar masses. At high redshifts this manifests itself as (sub-)mm galaxies appearing to be among the apparently brightest objects in *Spitzer* 8 μm IRAC imaging (Pope et al., 2006, 2008; Dye et al., 2008; Hainline et al., 2009; Wardlow et al., 2011; Michałowski et al., 2012a; Targett et al., 2013).

In order to test these methods I selected VLA 1.4 GHz, *Spitzer* MIPS 24 μm, IRAC 8 μm, and red ($i-K>2$) counterparts to the (sub-)mm galaxies in the COSMOS sample in a similar way to that presented in Michałowski et al. (2012b). Following the method outlined in Dunlop et al. (1989) and Ivison et al. (2007), I assessed the reliability of each potential galaxy identification by calculating the corrected Poissonian probability, p, that each association could have been occurred by chance given our search parameters. Specifically, I applied this technique to the original pre-interferometric (sub-)mm source detections, using a search radius of $r_s = 2.5 \times 0.6 \times \mathrm{FWHM}/(\mathrm{S/N})$, where FWHM is the full-width-half-maximum of the single-dish beam, and S/N is the signal:noise ratio of the original (deboosted) AzTEC or LABOCA detection (for details see Section 2.2). Armed with interferometrically-refined coordinates from the subsequent SMA and PdBI observations, I can here test the success/reliability of such multi-frequency association methods directly.

Table 3.6: *The results of my attempt to establish galaxy identifications for the (sub-)mm sources based on statistical associations between the original single-dish (sub-)mm positions and potential counterparts in the multi-wavelength imaging. RA and DEC refer to the position of the K-band counterpart (except in the case of AzTEC2 where the position refers to the radio counterpart), and 'Offset' is the distance in arcsec from this position and the original single-dish (sub-)mm source position. Objects highlighted in bold indicate the 16 sources for which the identification chosen here is confirmed as correct by the improved positional accuracy provided by the SMA and PdBI interferometric observations. COSLA-23 (as identified in the LABOCA map) was matched to an object close to the position of COSLA-23N (as identified by PdBI). No significant association was found with COSLA-23S.*

ID	RA (deg)	DEC (deg)	Dist (")	K (AB)	$i-K$ (AB)	p_{i-K}	$S_{8\mu m}$ (μJy)	$p_{8\mu m}$	$S_{24\mu m}$ (mJy)	$p_{24\mu m}$	S_{VLA} (mJy)	p_{VLA}
AzTEC1	149.92859	2.49393	3.5	23.44	1.60	> 0.1	14.0 ± 2.4	0.036	-	-	-	-
AzTEC2	150.03343	2.43671	0.1	> 24.57	-	-	-	-	0.181 ± 0.027	0.002	0.076 ± 0.014	0.001
AzTEC3	150.08629	2.58898	2.1	23.94	1.16	> 0.1	10.5 ± 2.3	0.059	-	-	-	-
AzTEC4	149.88196	2.51215	4.3	23.76	3.16	0.031	17.5 ± 2.0	0.083	-	-	-	-
AzTEC5	150.08240	2.53456	1.7	23.38	2.79	0.041	23.4 ± 2.2	0.028	0.189 ± 0.013	0.017	0.126 ± 0.015	0.002
AzTEC7	150.07529	2.80841	2.7	21.13	3.18	0.003	57.3 ± 2.6	0.025	0.441 ± 0.012	0.006	0.132 ± 0.022	0.003
AzTEC8	149.99721	2.57804	4.8	23.30	2.98	0.072	34.6 ± 2.5	0.065	-	-	-	-
AzTEC9	149.98870	2.45840	1.7	24.15	1.52	> 0.1	-	-	-	-	0.068 ± 0.013	0.002
AzTEC10	149.87819	2.67563	1.9	23.54	4.24	0.031	17.3 ± 2.3	0.031	0.086 ± 0.016	0.021	-	-
AzTEC11	150.03726	2.66956	3.2	21.48	1.90	0.036	42.0 ± 2.5	0.043	0.488 ± 0.011	0.008	0.302 ± 0.045	0.002
AzTEC12	150.14708	2.73144	1.4	21.51	2.74	0.004	56.9 ± 2.4	0.010	0.261 ± 0.011	0.007	0.098 ± 0.016	0.002
AzTEC15	150.05586	2.57334	5.1	19.90	2.16	0.014	26.2 ± 2.2	> 0.1	-	-	-	-
COSLA-5	150.24872	2.28574	3.3	19.92	2.63	0.003	26.1 ± 2.2	0.060	-	-	-	-
COSLA-8	150.10641	2.25154	4.0	22.04	3.98	0.023	26.4 ± 2.2	0.080	0.560 ± 0.017	0.012	0.112 ± 0.010	0.006
COSLA-16	150.21494	2.55951	3.1	20.83	2.57	0.009	36.4 ± 2.5	0.049	0.339 ± 0.025	0.016	0.122 ± 0.013	0.004
COSLA-18	150.17992	2.08863	2.9	22.18	5.14	0.018	35.3 ± 2.0	0.044	0.320 ± 0.069	0.022	0.078 ± 0.014	0.005
COSLA-19	150.03380	2.19506	6.2	20.92	2.27	0.059	-	-	-	-	-	-
COSLA-23	150.04231	2.22635	1.8	23.21	3.72	0.025	14.4 ± 2.4	0.048	0.135 ± 0.035	0.066	0.059 ± 0.011	0.003
COSLA-35	150.09857	2.36537	3.9	22.49	4.35	0.037	31.8 ± 2.5	0.075	0.168 ± 0.017	0.049	0.043 ± 0.011	0.010
COSLA-47	150.13901	2.43378	6.6	22.46	3.33	0.070	22.3 ± 2.4	> 0.1	-	-	-	-
COSLA-128	150.40825	2.39440	8.0	17.63	1.19	> 0.1	17.2 ± 2.3	0.020	0.864 ± 0.032	0.015	0.172 ± 0.048	0.010

The results of this test of the identification process are summarised in Table 3.6. Additional details can be found in the caption to this table (see also Section A), but the key result is that 16 of the 30 sources would have been successfully identified on the basis of the single-dish (sub-)mm positions and the available multi-frequency follow-up imaging. These 16 objects (marked in bold in Table 3.6) are 15 of the 18 sources for which stellar masses are given in Table 3.5, plus AzTEC2, which is a purely radio identification confirmed by the interferometric positions. This means that $16/19 = 84\%$ of the galaxy identifications achievable with the aid of the improved interferometric positional accuracy would be correctly identified on the basis of the original single-dish data. The three additional galaxy identifications secured with the aid of the SMA and PbBI data comprise new galaxy counterparts for COSLA-54 and COSLA-17N, and a revised identification for AzTEC15 where a surprisingly large positional shift is reported between the original AzTEC position and the SMA peak.

Interestingly, three further identifications suggested by the single-dish positions are formally excluded by the interferometric data, but without the new positions yielding a new alternative identification. In two of these cases (COSLA-5 and COSLA-8) the proposed single-dish identification was statistically compelling but now appears unacceptable given the reduced error on the mm position delivered by PdBI. One possible explanation of such apparently conflicting conclusions is that both these objects could be lensed, and that the optical-infrared counterpart yielding the statistically significant association is the lensing object. In my analysis I have, in effect, guarded against this possibility by adopting the long-wavelength redshift estimate for these objects. Finally, the apparently significant identification of COSLA-128 listed in the last row of Table B1 is formally excluded by the PdBI follow-up, but this is primarily because the PdBI position is $\simeq 11$ arcsec from the LABOCA position (for reasons that are hard to explain).

In summary, while the interferometric observations clearly add important extra information on the AzTEC and LABOCA sources, for this luminous sample I find that $\simeq 80 - 85\%$ of the galaxy identifications which are *achievable given the depth of the supporting multi-frequency data* would have been successfully secured without the aid of the interferometric follow-up. In other words the main cause of failed identification is not blending or inadequate positional accuracy

in the single-dish (sub-)mm positions, but supporting multi-wavelength data of inadequate depth to reveal the galaxy counterparts of the more high-redshift sources in the current sample. Of course, as the supporting data become deeper then the improved positional accuracy provided by interferometry (or, for example, SCUBA-2 450 μm imaging) will become increasingly valuable as the source densities in the supporting data rise.

For completeness, I show in the online version, Figures 3.8 and 3.9, how the locations of the sources on the flux-density–redshift plane vary depending on whether one adopts the identifications based on single-dish or interferometric positions, and also whether one adopts the single-dish (Figure 3.8) or interferometric (Figure 3.9) flux densities. The average (sub-)mm flux density inferred from the interferometry is only $\simeq 10\%$ lower than the single-dish average, and in all four panels the average redshift of the identified sources lies just below $z = 3.5$ while the average redshift of the sources which currently lack optical-infrared is (as anticipated) slightly higher (but still at $z < 4$). It is thus unsurprising that our main science results are little changed by whether I adopt the single-dish or interferometric positions and flux densities in my analysis.

3.6 Conclusions

I have presented a new analysis of the brightest sample of unlensed (sub-)mm sources with existing (pre-ALMA) interferometric (SMA or PdBI) follow-up observations. Because these sources lie within the COSMOS field, I have been able to exploit the latest Subaru, UltraVISTA and *Spitzer* optical-infrared photometry to better establish their redshifts (z), stellar masses ($M_\star$) and specific star-formation rates ($sSFR$). I have also explored the extent to which the supporting data in the field could have been used to reliably identify the galaxy counterparts *without* the improved positional accuracy provided by sub-mm/mm interferometry. I find that the bright (sub-)mm sources in the COSMOS field display a redshift distribution indistinguishable from that of the lensed SPT sources (Vieira et al., 2013), peaking at $z_{median} \simeq 3.5$. I also find that the typical stellar mass of the most luminous (sub-)mm sources is independent of redshift for $z \simeq 2 - 5$, with median $M_\star \simeq 2 \times 10^{11}\,\mathrm{M}_\odot$ assuming a Chabrier (2003) IMF. Consequently, their typical specific star-formation rates

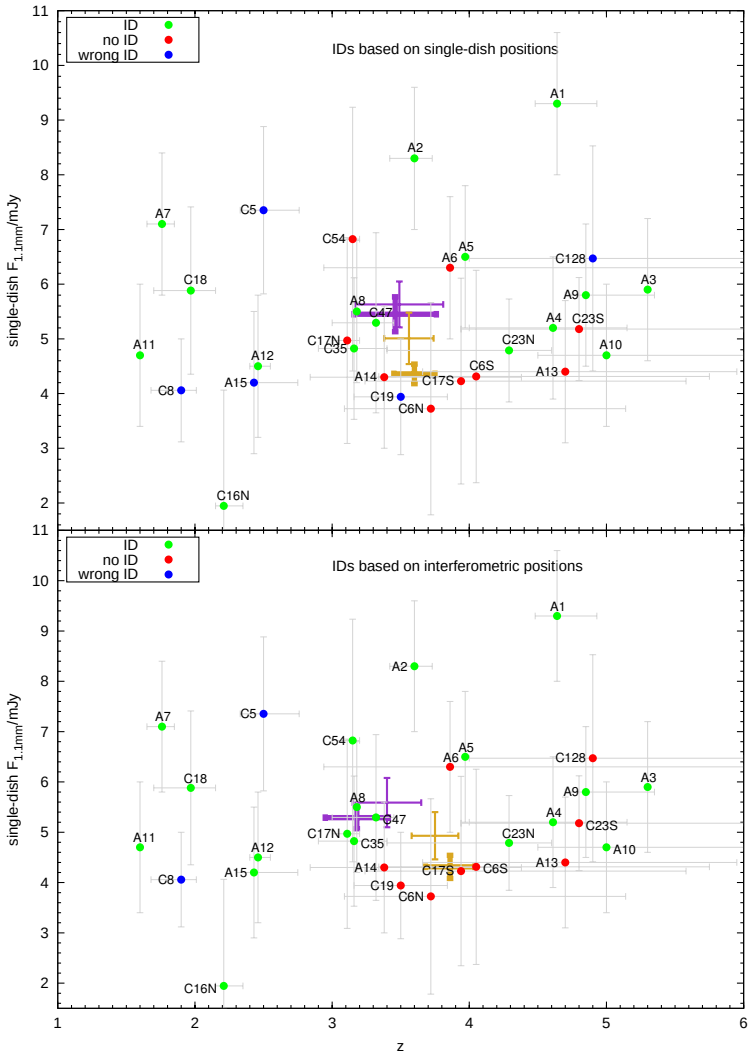

Figure 3.8: *Single-dish 1.1 mm flux densities plotted against redshift. Flux densities are taken directly from the 1.1 mm AzTEC observations or scaled from the LABOCA 870 µm measurements using* $F_{870\,\mu m}/F_{1.1\,\mathrm{mm}} = 1.7$ *(Michalowski et al. 2010). Green dots show objects which were correctly identified using the single-dish positions (upper panel) or interferometric positions (lower panel). Red dots indicate the unidentified sources, while blue dots indicate sources which formally have statistically acceptable identifications which we are confident are not in fact the correct galaxy counterparts (usually due to a severe mismatch between,* z_{phot} *and* z_{LW} *as produced by, for example, galaxy-galaxy lensing). The violet points with error bars show median (thicker errorbars) and mean (thinner errorbars) values for all the identified sources. The brown points with error bars indicate the corresponding average values for the unidentified sources.*

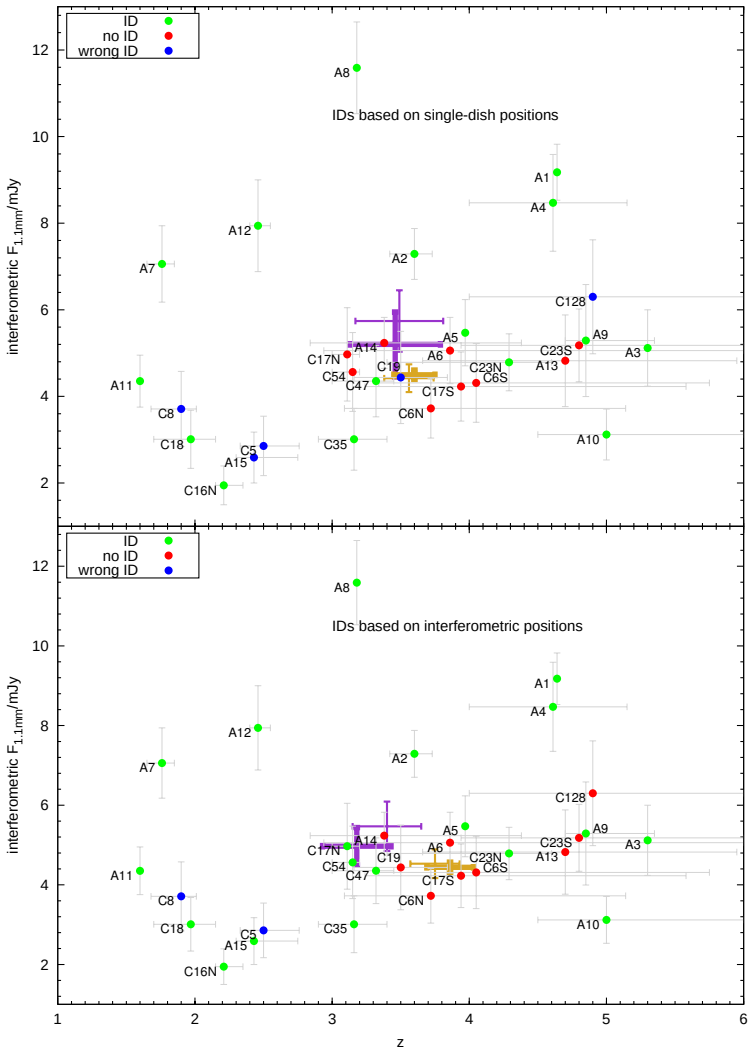

Figure 3.9: *Interferometric 1.1 mm flux densities plotted against redshift. Flux densities are scaled from the SMA 890 µm measurements using* $F_{890\,\mu m}/F_{1.1\,\mathrm{mm}} = 1.7$*, and scaled from the PdBI 1.3 mm measurements using* $F_{1.3mm}/F_{1.1\,\mathrm{mm}} = 0.7$*. Green dots show objects which were correctly identified using the single-dish positions (upper panel) or interferometric positions (lower panel). Red dots indicate the unidentified sources, while blue dots indicate sources which formally have statistically acceptable identifications which we are confident are not in fact the correct galaxy counterparts (usually due to a severe mismatch between,* z_{phot} *and* z_{LW} *as produced by, for example, galaxy-galaxy lensing). The violet points with error bars show median (thicker errorbars) and mean (thinner errorbars) values for all the identified sources. The brown points with error bars indicate the corresponding average values for the unidentified sources.*

also remain approximately constant out to the highest redshifts probed, at $sSFR \simeq 2.5\,\mathrm{Gyr}^{-1}$. I note that, consistent with recent ALMA interferometric follow-up of the LESS sub-mm sources (Hodge et al. 2013), and SMA follow-up of SCUBA2 sources (Chen et al. 2013), source blending is *not* a serious issue in the study of luminous (sub-)mm sources uncovered by ground-based, single-dish ($FWHM < 18\,\mathrm{arcsec}$) surveys; only $\simeq 10 - 15\%$ of bright ($S_{850} \simeq 5 - 10\,\mathrm{mJy}$) (sub-)mm sources arise from significant blends, and so the conclusions of my study are largely unaffected by whether I adopt the original single-dish mm/sub-mm flux densities/positions, or the interferometric flux densities/positions. My results suggest that apparent disagreements over the redshift distribution of (sub-)mm sources are simply a result of "down-sizing" in dust-enshrouded star-formation, consistent with existing knowledge of the star-formation histories of massive galaxies. They also indicate that bright (sub-)mm-selected galaxies at high redshift are, on average, subject to the same star-formation rate-limiting processes as less luminous objects, and lie on the "main sequence" of star-forming galaxies.

Chapter 4

The star forming 'main sequence' of the submm-selected galaxies

4.1 Introduction

It is now well known that approximately half of the starlight in the Universe is re–processed by cosmic dust and re–emitted at far–infrared wavelengths (Dole et al. 2006). However, due to a combination of the inescapable physics of diffraction, the molecular content of our atmosphere, and the technical difficulties of sensitive high-background imaging, it has proved difficult to connect the UV/optical and far–infrared/sub–mm views of the Universe into a consistent and complete picture of galaxy formation/evolution. Thus, while the advent of SCUBA on the 15–m James Clerk Maxwell Telescope (JCMT) in the late 1990s (Holland et al., 1999) enabled the first discovery of distant dusty galaxies with star–formation rates SFR $\simeq 1000\,\mathrm{M_{\odot}yr^{-1}}$ (Smail et al., 1997; Barger et al., 1998; Hughes et al., 1998; Eales et al., 1999), such objects initially seemed too extreme and unusual to be easily related to the more numerous, 'normal' star–forming galaxies being uncovered at UV/optical wavelengths at comparable redshifts ($z \simeq 2-4$) by Keck (e.g. Steidel et al. 1996) and the Hubble Space Telescope (HST) (e.g. Madau et al. 1996). In recent years the study of rest–frame UV–selected galaxies has been extended out beyond $z \simeq 10$, while a number of sub–mm selected galaxies have now been confirmed at $z > 4$ (Capak et al. 2008; Coppin et al. 2009; Daddi et al. 2009b,a; Knudsen et al. 2010; Riechers et al. 2010; Cox et al. 2011; Combes et al. 2012; Weiß et al. 2013) with the current redshift record holder at z =

6.34 (Riechers et al., 2013). However, while such progress is exciting, at present there is still relatively little meaningful intersection between these UV/optical and far–infrared/sub–mm studies of the high–redshift Universe.

At more moderate redshifts, however, recent years have seen increasingly successful efforts to bridge the gap between the unobscured and dust-enshrouded views of the evolving galaxy population. Of particular importance in this endeavour has been the power of deep 24 μm imaging with the MIPS instrument on board *Spitzer*, which has proved capable of providing a useful estimate of the dust–obscured star–formation activity in a significant fraction of optically–selected galaxies out to $z \simeq 1.5 - 2$ (e.g. Caputi et al. 2006; Elbaz et al. 2010). Indeed, MIPS imaging of the GOODS survey fields played a key role in establishing what has proved to be a fruitful framework for the study of galaxy evolution, namely the existence of a so–called "main sequence" (MS) for star–forming galaxies, in which star–formation rate is found to be roughly proportional to stellar mass ($SFR \propto M_{\star}$; Noeske et al., 2007; Daddi et al., 2007; Renzini & Peng, 2015), with a normalisation that rises with increasing redshift (e.g. Daddi et al. 2007; Karim et al. 2011; Rodighiero et al. 2011; Michałowski et al. 2012a).

Interest in the MS of star–forming galaxies has continued to grow (see Speagle et al. 2014 for a useful and comprehensive overview), not least because of the difficulty encountered by most current models of galaxy formation in reproducing its apparently rapid evolution between $z \simeq 0$ and $z \simeq 2$. However, it has, until now, proved very difficult to extend the robust study of the MS beyond $z \simeq 2$ and to the highest masses (e.g. Steinhardt et al. 2014; Salmon et al. 2015; Leja et al. 2015). This is because an increasing fraction of star formation is enshrouded in dust in high–mass galaxies, and Spitzer MIPS and Herschel become increasingly ineffective in the study of dust–enshrouded SF with increasing redshift (due to a mix of wavelength and resolution limitations), as the far–infrared emission from dust is redshifted into the sub–mm/mm regime.

A complete picture of star–formation in more massive galaxies at high–redshift can therefore only be achieved with ground–based sub–mm/mm observations, which provide image quality at sub–mm wavelengths that is vastly superior to what can currently be achieved from space. The challenge, then, is to connect the population of dusty, rapidly star–forming high–redshift galaxies revealed by ground–based sub–mm/mm surveys to the population of more moderate star–

forming galaxies now being revealed by optical/near–infrared observations out to the highest redshifts. On a source–by–source basis this can now be achieved by targeted follow–up of known optical/infrared–selected galaxies with ALMA (e.g. Ono et al. 2014). However, this will inevitably produce a biased perspective which can only be re–balanced by also continuing to undertake ever deeper and wider sub–mm/mm surveys capable of detecting highly–obscured objects (again, potentially, for ALMA follow–up; Karim et al. 2013; Hodge et al. 2013), and thus completing our census of star–forming galaxies in the young Universe.

This is one of the primary science drivers for the SCUBA–2 Cosmology Legacy Survey (S2CLS). The S2CLS is advancing the field in two directions. First, building on previous efforts with SCUBA (e.g. Scott et al. 2002, 2006; Coppin et al. 2006), MAMBO (e.g. Bertoldi et al. 2000; Greve et al. 2004), LABOCA (e.g. Weiß et al. 2009b) and AzTEC (e.g. Austermann et al. 2010; Scott et al. 2012), the S2CLS is using the improved mapping capabilities of SCUBA–2 (Holland et al., 2013) to extend surveys for bright ($S_{850} > 5$ mJy) sub–mm sources to areas of several square degrees, yielding large statistical samples of such sources (> 1000). Second, the S2CLS is exploiting the very dryest (Grade–1) conditions at the JCMT on Mauna Kea, Hawaii to obtain very deep 450 μm imaging of small areas of sky centred on the HST CANDELS fields (Grogin et al., 2011), which provide the very best multi–wavelength supporting data to facilitate galaxy counterpart identification and study. The first such deep 450 μm image has been completed in the centre of the COSMOS–CANDELS/UltraVISTA field, with the results reported by Geach et al. (2013) and Roseboom et al. (2013). Here I utilise the ultra–deep 850 μm image of the same region, which was automatically obtained in parallel with the 450 μm imaging. While the dryest weather is more essential for the shorter–wavelength imaging at the JCMT, such excellent conditions (and long integrations) inevitably also benefit the parallel 850 μm imaging. Consequently, the 850 μm data studied here constitute the deepest ever 850 μm survey ever undertaken over an area $\simeq 150$ arcmin^2.

The depth of the new S2CLS 850 μm imaging is typically $\sigma_{850} \simeq 0.25$ mJy. This is important because it means that galaxies detected near the limit of this survey have SFR $\simeq 100\,\mathrm{M_{\odot}\ yr^{-1}}$, which is much more comparable to the highest SFR values derived from UV/optical/near–infrared studies than the typical SFR sensitivity achieved with previous single-dish sub–mm/mm imaging (i.e. SFR

$\simeq 1000\,\mathrm{M}_{\odot}\ \mathrm{yr}^{-1}$ as a result of $\sigma_{850} \simeq 2$ mJy). Ultimately, of course, ALMA will provide even deeper sub–mm surveys with the resolution required to overcome the confusion limit of the single–dish surveys. However, because of its modest field of view ($\sim$ 20 arcsec at 850 μm) it is observationally expensive to survey large areas of blank sky with ALMA, and contiguous mosaic surveys are hard to justify at depths where the source surface density is significantly less than one per pointing. Thus, at the intermediate depths probed here, the S2CLS continues to occupy a unique and powerful niche in the search for dust-enshrouded star–forming galaxies.

The fact that previous sub–mm/mm surveys were only generally capable of detecting very extreme objects has undoubtedly contributed to some of the confusion/controversy over the nature of galaxies selected at sub–mm/mm wavelengths; while Michałowski et al. (2012b) and Roseboom et al. (2013) have presented evidence that sub–mm selected galaxies lie on the high mass end of the MS at z = 2−3, others have continued to argue that, like many local ULIRGs, they are extreme pathological objects driven by recent major mergers (e.g. Hainline et al. 2011). Some of this debate reflects disagreements over the stellar masses of the objects rather than their star–formation rates (e.g. Michałowski et al. 2014). Nevertheless, the fact that even high–mass galaxies on the MS lay right at the detection limits of previous sub–mm surveys inevitably resulted in many sub–mm selected objects apparently lying above the MS, fueling arguments about whether they were indeed significant outliers, or whether we have simply been uncovering the positive tail in SFR around the MS (see Roseboom et al. 2013).

The much deeper 850 μm survey studied here is capable of settling this issue, provided of course I can overcome the now customary challenge of identifying the galaxy counterparts of most of the sub–mm sources, and determining their redshifts, SFRs and stellar masses ($\mathrm{M}_{\star}$) (e.g. Ivison et al. 2007; Dunlop et al. 2010; Biggs et al. 2011; Wardlow et al. 2011; Michałowski et al. 2012a; Koprowski et al. 2014). However, in this effort, I am also aided by the depth of the SCUBA–2 data, and by the additional positional information provided by the (unusual) availability of 450 μm detections (with FWHM $\simeq$ 8 arcsec) for 50% of the sample. I also benefit hugely from the unparalleled multi–frequency supporting data available in the CANDELS fields, provided by HST, Subaru, CFHT, Vista, *Spitzer*, *Herschel* and the VLA.

This chapter is structured as follows. In Section 4.2 I present the multi-wavelength data utilized in this work. Section 4.3 describes how the identification process for all the SCUBA-2 sources was performed. In section 4.4 the complete redshift distribution for the whole sample is presented, followed by the description of the physical properties in Section 4.5. I summarize in Section 4.6. Throughout I use the AB magnitude system (Oke, 1974), and assume a flat cosmology with $\Omega_m = 0.3, \Omega_\Lambda = 0.7$ and $H_0 = 70$ km s^{-1}Mpc^{-1}.

4.2 Data

4.2.1 SCUBA-2 imaging & source extraction

I used the deep 850 μm and 450 μm S2CLS imaging of the central $\simeq 150$ arcmin^2 of the COSMOS/UltraVISTA field, coincident with the Spitzer SEDS (Ashby et al., 2013) and HST CANDELS (Grogin et al., 2011) imaging. The observations were taken with SCUBA-2 mounted on the JCMT between October 2011 and March 2013, reaching depths of $\sigma_{850} \simeq 0.25$ mJy and $\sigma_{450} \simeq 1.5$ mJy. In order to enable effective 450 μm observations, only the very best/dryest conditions were used (i.e. $\tau_{225\mathrm{GHz}} < 0.05$), and to maximise depth the imaging was undertaken with a "daisy" mapping pattern (Bintley et al., 2014).

The details of the reduction process are described in Roseboom et al. (2013), and so only a brief description is given here. The data were reduced by my collaborators Jim Geach and Isaac Roseboom with the SMURF package[1] V1.4.0 (Chapin et al., 2013) with flux calibration factors (FCFs) of 606 Jy pW^{-1} Beam^{-1} for 450 μm and 556 Jy pW^{-1} Beam^{-1} for 850 μm (Dempsey et al., 2013).

The noise-only maps were constructed by inverting an odd half of the ~ 30 min scans and stacking them all together. In the science maps the large-scale background was removed by applying a high-pass filter above 1.3 Hz to the data (equivalent to 120 arcsec given the SCUBA-2 scan rate). Then a "whitening filter" was applied to suppress the noise in the map whereby the Fourier Transform of the map is divided by the noise-only map power spectrum, normalised by the white-noise level and transformed back into real space. The effective point-source response function (PRF) was constructed from a Gaussian with a full-width-half-maximum (FWHM) of 14.6 arcsec following the same procedure. Finally, the

[1] http://www.starlink.ac.uk/docs/sun258.htx/sun258.html

real sources with a signal-to-noise ratio (SNR) of better than five were extracted by convolving the whitened map with the above PRF (see §4.2 of Chapin et al. 2013).

A total of 106 850 μm sources were found within the map with a SNR > 5. The photometry at 450 μm was performed in the same manner, but assuming the PRF at 450 μm to be a Gaussian of FWHM = 8 arcsec. The 450 μm counterparts to the 850 μm sources were adopted if a 450 μm-selected source was found within 6 arcsec of the 850 μm centroid. Otherwise, for the purpose of SED fitting, the 450 μm flux density was measured at the 850 μm position (flags 1 and 0 in Table 4.1 respectively).

The 850 μm image and the sources extracted from it are shown in Figure 4.1, while the positions and sub-mm photometry for the sources are listed Table 4.1.

The completeness of the 850 μm catalogue was assessed by my collaborator Isaac Roseboom by injecting sources of known flux density into the noise-only maps. Overall 104 objects were used, split into 10 logarithmically-spaced flux-density bins between 1 and 60 mJy. In total 2000 simulated maps were created and the source extraction was performed in the same way as with the real maps. The completeness was then assessed by dividing the number of extracted sources by the number of sources inserted into the noise-only maps (Figure 4.2).

4.2.2 Supporting multi-frequency data

This first deep S2CLS pointing within the COSMOS/UltraVISTA field was chosen to maximise the power of the available ancillary multi-wavelength data, in particular the HST Cosmic Assembly Near-infrared Deep Extragalactic Legacy Survey (CANDELS)[2] imaging (Grogin et al., 2011). In addition, the optical Canada-France-Hawaii Telescope Legacy Survey (CFHTLS; Gwyn 2012), the Subaru/Suprime-Cam z'-band (Taniguchi et al. 2007, Furusawa et al., in preparation) and UltraVISTA near-infrared data (McCracken et al., 2012) were used. The catalogues were made by my collaborator Rebecca Bowler by smoothing all the ground-based and HST data to the seeing of the UltraVISTA Y-band image with the Gaussian of FWHM = 0.82 arcsec (for details, see Bowler et al. 2012, 2014). The catalogue was selected in the smoothed CANDELS H-band image and photometry was measured in 3 arcsec apertures using the dual-mode

[2]http://candels.ucolick.org

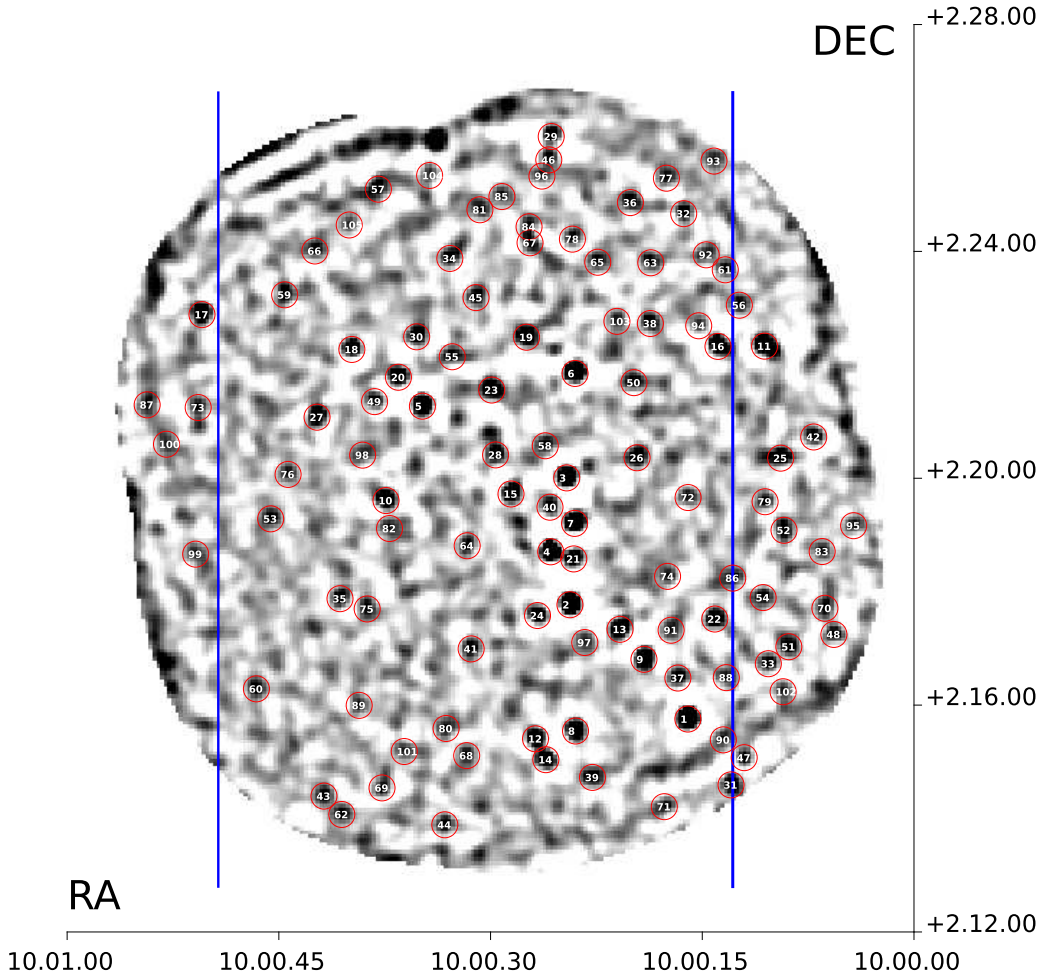

Figure 4.1: *The SCUBA-2 850 μm map of a sub-region of the COSMOS field. All the sources used in this research with* SNR $> 5\sigma$ *are highlighted with red circles with the white ID number in the middle. As explained in Section 4.2.2 two optical/near-IR catalogues were utilised in this work. The catalogue with the HST CANDELS and deconfused IRAC data which contains sources extracted from the map covering the CANDELS area (enclosed by the two blue vertical lines) and the catalogue without the HST data (outside the blue lines) which was used only for 20 sources.*

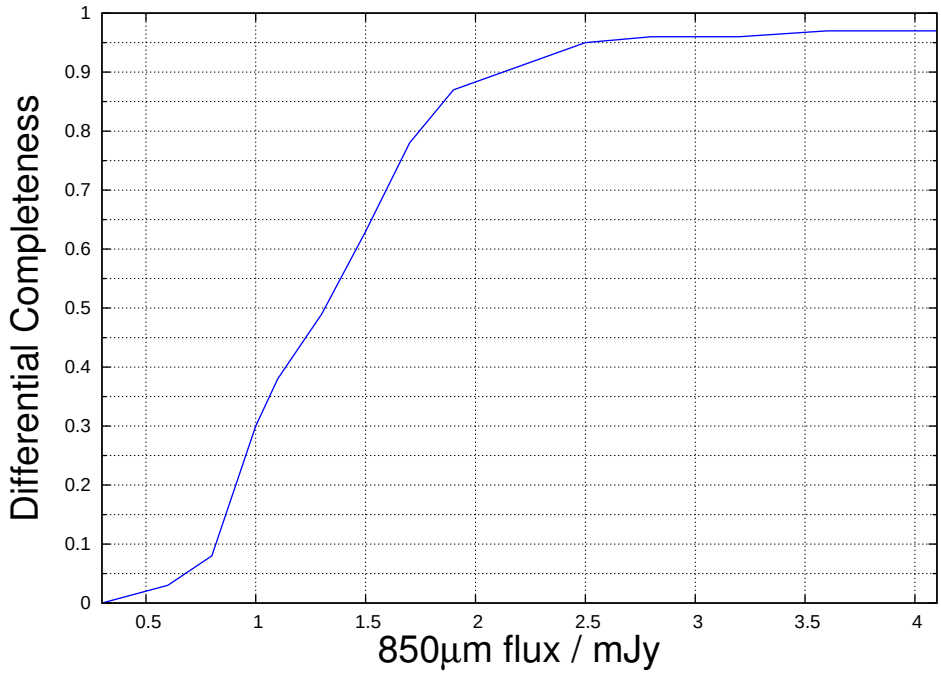

Figure 4.2: *Completeness of the 850 μm sample as a function of the flux based on 2000 simulated maps with source extraction made on 10^4 artificially created objects.*

Table 4.1: *The whole sample utilised in this work. The second last column shows the SCUBA-2 colour. If the significance of the 450 μm detection is less than 2σ, the SCUBA-2 colour becomes a limit with $S_{450} < S_{450}+2\sigma$. The flag tells whether the 450 μm flux was taken from 450 μm catalogue (1) or simply measured at 850 μm position (0, if no 450 μm source with $S_{450} > 4\sigma$ was found within 6 arcsec from 850 μm position).*

ID	RA_{850} /deg	DEC_{850} /deg	S_{850} /mJy	ΔS_{850} /mJy	SNR_{850}	S_{450} /mJy	ΔS_{450} /mJy	SNR_{450}	S_{850}/S_{450}	flag
1	150.06518	2.26412	15.64	0.38	41.69	26.99	2.38	11.34	0.58	1
2	150.09985	2.29772	10.20	0.28	36.82	17.74	1.77	10.00	0.58	1
3	150.10079	2.33499	7.33	0.23	32.02	10.32	1.41	7.34	0.71	1
4	150.10549	2.31327	7.79	0.24	31.96	23.42	1.53	15.35	0.33	1
5	150.14320	2.35607	7.88	0.26	29.98	19.71	1.54	12.78	0.40	1
6	150.09833	2.36568	8.20	0.28	29.20	22.81	1.80	12.71	0.36	1
7	150.09847	2.32162	7.04	0.25	28.44	16.66	1.53	10.88	0.42	1
8	150.09820	2.26061	6.44	0.33	19.32	14.89	2.13	6.98	0.43	1
9	150.07809	2.28168	5.88	0.32	18.56	15.45	2.03	7.62	0.38	1
10	150.15390	2.32833	4.75	0.26	18.17	11.15	1.55	7.17	0.43	1
11	150.04264	2.37371	7.34	0.41	17.85	23.66	2.87	8.23	0.31	1
12	150.10996	2.25832	5.54	0.34	16.55	8.91	2.13	4.18	0.62	1
13	150.08512	2.29050	4.87	0.30	16.25	12.79	1.97	6.50	0.38	1
14	150.10692	2.25218	5.83	0.36	16.03	23.81	2.38	9.99	0.24	1
15	150.11717	2.33026	3.41	0.21	15.95	6.53	1.31	4.99	0.52	1
16	150.05633	2.37363	5.42	0.35	15.53	24.31	2.39	10.17	0.22	1
17	150.20799	2.38297	7.34	0.47	15.50	15.66	2.68	5.83	0.47	1
18	150.16393	2.37274	6.13	0.40	15.43	31.22	1.96	15.90	0.20	1
19	150.11258	2.37633	4.35	0.29	15.14	9.91	1.84	5.37	0.44	1
20	150.15024	2.36457	4.55	0.31	14.46	13.31	1.76	7.56	0.34	1
21	150.09873	2.31118	3.68	0.26	13.89	9.08	1.62	5.61	0.41	1
22	150.05727	2.29352	4.60	0.33	13.88	12.83	2.19	5.87	0.36	1
23	150.12283	2.36081	3.16	0.24	13.36	10.41	1.50	6.94	0.30	1
24	150.10937	2.29455	3.43	0.27	12.58	11.88	1.74	6.84	0.29	1
25	150.03791	2.34079	4.56	0.36	12.49	9.20	2.48	3.71	0.50	0
26	150.08011	2.34091	3.27	0.27	11.97	10.70	1.77	6.06	0.31	1
27	150.17416	2.35283	4.07	0.34	11.83	8.82	2.01	4.38	0.46	1
28	150.12169	2.34175	2.48	0.21	11.59	10.56	1.30	8.13	0.23	1
29	150.10535	2.43531	6.47	0.57	11.31	18.98	3.59	5.28	0.34	1
30	150.14489	2.37645	3.37	0.32	10.54	8.44	1.78	4.75	0.40	1
31	150.05250	2.24477	7.85	0.76	10.40	14.21	5.63	2.52	0.55	0
32	150.06641	2.41264	4.72	0.46	10.29	6.49	3.18	2.04	0.73	0
33	150.04153	2.28039	4.01	0.42	9.53	6.73	2.60	2.59	0.60	0
34	150.13514	2.39948	3.03	0.32	9.39	11.12	1.94	5.73	0.27	1
35	150.16742	2.29950	3.29	0.35	9.36	11.12	1.91	5.84	0.30	1
36	150.08208	2.41590	3.95	0.43	9.11	10.88	2.91	3.74	0.36	0
37	150.06812	2.27618	3.06	0.34	9.08	11.70	2.08	5.62	0.26	1
38	150.07620	2.38036	3.14	0.35	8.87	12.41	2.27	5.46	0.25	1
39	150.09322	2.24697	3.69	0.43	8.63	11.67	2.83	4.12	0.32	1
40	150.10570	2.32638	1.94	0.23	8.52	7.87	1.38	5.72	0.25	1
41	150.12888	2.28474	2.47	0.29	8.48	0.96	1.91	0.50	> 0.51	0
42	150.02819	2.34702	3.80	0.45	8.36	0.76	2.97	0.26	> 0.57	0
43	150.17214	2.24149	4.97	0.59	8.35	3.39	3.87	0.88	> 0.45	0
44	150.13663	2.23305	4.66	0.57	8.23	2.28	3.48	0.66	> 0.50	0
45	150.12744	2.38798	2.52	0.31	8.21	4.50	1.87	2.41	0.56	0
46	150.10606	2.42844	3.94	0.48	8.14	14.48	3.09	4.69	0.27	1
47	150.04863	2.25278	4.95	0.62	8.04	3.14	4.64	0.68	> 0.40	0
48	150.02227	2.28899	5.05	0.63	8.00	16.71	3.63	4.60	0.30	1
49	150.15725	2.35741	2.58	0.33	7.83	10.44	1.84	5.67	0.25	1
50	150.08103	2.36298	2.39	0.31	7.79	0.75	1.95	0.38	> 0.51	0
51	150.03551	2.28537	3.56	0.46	7.76	1.63	2.76	0.59	> 0.50	0
52	150.03693	2.31959	2.85	0.37	7.72	1.68	2.47	0.68	> 0.43	0
53	150.18780	2.32296	2.54	0.33	7.64	15.59	1.84	8.46	0.16	1
54	150.04307	2.29982	2.87	0.36	7.63	10.50	2.36	4.45	0.27	1
55	150.13442	2.37059	2.06	0.27	7.55	10.13	1.68	6.04	0.20	1
56	150.05005	2.38574	3.09	0.41	7.50	7.69	2.95	2.61	0.40	0
57	150.15614	2.41984	3.38	0.45	7.30	2.77	2.72	1.02	> 0.41	0
58	150.10709	2.34444	1.62	0.22	7.24	4.98	1.36	3.66	0.32	0

Table 4.1: (continued).

ID	RA_{850} /deg	DEC_{850} /deg	S_{850} /mJy	ΔS_{850} /mJy	SNR_{850}	S_{450} /mJy	ΔS_{450} /mJy	SNR_{450}	S_{850}/S_{450}	flag
59	150.18368	2.38879	2.83	0.39	7.22	10.40	2.14	4.86	0.27	1
60	150.19199	2.27300	3.25	0.46	7.12	0.68	2.95	0.23	> 0.49	0
61	150.05419	2.39615	3.06	0.43	7.10	8.03	3.08	2.61	0.38	0
62	150.16689	2.23608	4.61	0.65	7.08	8.03	4.13	1.95	> 0.28	0
63	150.07608	2.39821	2.70	0.39	6.85	0.89	2.62	0.34	> 0.44	0
64	150.13004	2.31505	1.59	0.23	6.82	8.63	1.45	5.95	0.18	1
65	150.09167	2.39837	2.71	0.40	6.78	11.02	2.49	4.42	0.25	1
66	150.17480	2.40168	2.70	0.40	6.76	9.29	2.18	4.27	0.29	1
67	150.11157	2.40409	2.38	0.35	6.73	3.22	2.27	1.42	> 0.31	0
68	150.13019	2.25338	2.37	0.36	6.68	7.01	2.29	3.06	0.34	0
69	150.15507	2.24389	3.10	0.47	6.63	-2.98	3.02	-0.99	> 0.51	0
70	150.02490	2.29668	3.43	0.52	6.63	3.49	3.16	1.11	> 0.35	0
71	150.07211	2.23837	4.44	0.67	6.62	-6.58	4.78	-1.38	> 0.46	0
72	150.06512	2.32922	1.93	0.29	6.60	8.04	2.09	3.84	0.24	0
73	150.20910	2.35567	2.82	0.43	6.60	18.21	2.40	7.57	0.15	1
74	150.07115	2.30605	2.07	0.32	6.55	2.53	2.21	1.15	> 0.30	0
75	150.15943	2.29648	2.34	0.35	6.40	10.40	1.96	5.32	0.22	1
76	150.18268	2.33601	2.01	0.32	6.31	-0.32	1.83	-0.17	> 0.55	0
77	150.07148	2.42307	3.22	0.51	6.28	3.97	3.60	1.10	> 0.29	0
78	150.09911	2.40516	2.51	0.39	6.23	5.50	2.49	2.21	0.46	0
79	150.04249	2.32799	2.20	0.35	6.19	3.49	2.36	1.48	> 0.27	0
80	150.13624	2.26135	2.06	0.34	6.05	-0.66	2.16	-0.30	> 0.48	0
81	150.12630	2.41379	2.21	0.37	5.98	1.27	2.35	0.54	> 0.37	0
82	150.15286	2.32011	1.59	0.27	5.93	3.65	1.60	2.29	0.43	0
83	150.02572	2.31335	2.75	0.46	5.93	6.50	2.92	2.22	0.42	0
84	150.11186	2.40879	2.18	0.37	5.92	-1.58	2.36	-0.67	> 0.46	0
85	150.11984	2.41767	2.32	0.39	5.87	7.06	2.52	2.80	0.33	0
86	150.05200	2.30554	1.91	0.33	5.87	2.38	2.23	1.07	> 0.28	0
87	150.22409	2.35646	3.71	0.64	5.83	-1.10	3.16	-0.35	> 0.59	0
88	150.05389	2.27630	2.11	0.37	5.68	0.83	2.27	0.37	> 0.39	0
89	150.16178	2.26814	2.15	0.38	5.67	13.81	2.32	5.96	0.16	1
90	150.05476	2.25801	2.59	0.46	5.63	-5.87	3.14	-1.87	> 0.41	0
91	150.07011	2.29022	1.82	0.32	5.60	3.47	2.07	1.67	> 0.24	0
92	150.05980	2.40055	2.37	0.43	5.57	4.56	3.01	1.52	> 0.22	0
93	150.05751	2.42810	4.36	0.78	5.57	14.01	5.47	2.56	0.31	0
94	150.06199	2.37970	1.95	0.35	5.53	-2.09	2.40	-0.87	> 0.41	0
95	150.01647	2.32095	3.42	0.62	5.51	3.28	3.58	0.92	> 0.33	0
96	150.10807	2.42369	2.39	0.45	5.36	1.88	2.82	0.67	> 0.32	0
97	150.09548	2.28661	1.53	0.29	5.31	0.28	1.88	0.15	> 0.38	0
98	150.16077	2.34168	1.54	0.29	5.29	9.34	1.73	5.40	0.17	1
99	150.20984	2.31258	2.53	0.48	5.29	15.46	2.73	5.67	0.16	1
100	150.21841	2.34489	2.79	0.53	5.25	1.80	2.72	0.66	> 0.38	0
101	150.14854	2.25458	2.01	0.38	5.22	-2.33	2.44	-0.95	> 0.41	0
102	150.03720	2.27215	2.66	0.51	5.21	14.78	3.25	4.55	0.18	1
103	150.08604	2.38099	1.94	0.36	5.18	13.00	2.28	5.70	0.15	1
104	150.14108	2.42386	2.29	0.45	5.10	15.70	2.83	5.55	0.15	1
105	150.16471	2.40932	2.04	0.40	5.04	4.68	2.27	2.06	0.44	0
106	150.20893	2.35022	2.12	0.42	5.02	3.52	2.40	1.47	> 0.25	0

function in SExtractor (Bertin & Arnouts, 1996) on all other PSF homogenised images.

The *Spitzer* IRAC flux densities at 3.6 μm and 4.5 μm were measured from the S-COSMOS survey (Sanders et al., 2007) by my collaborator Fernando Buitrago, after image deconfusion based on the UltraVISTA K_s-band image; using GALFIT (Peng et al., 2002) the K_s-band images were modelled, and the corresponding structural parameters were then applied to both the 3.6 μm and 4.5 μm data and the flux-densities allowed to vary until the optimum fit to the IRAC image of each object was achieved (after convolution with the appropriate PSFs). The infinite-resolution scaled model IRAC images created in this way were than smoothed again to match the seeing of the UltraVISTA Y-band image, after which the IRAC flux densities were measured within 3 arcsec apertures. For the small number of objects selected from the SCUBA-2 map which lay outside the area with CANDELS HST imaging (see Figure 4.1) the K_s-band UltraVISTA image was used as the primary image for near-infrared candidate counterpart selection.

The 24 μm catalogue was constructed by my collaborator Isaac Roseboom, using the MIPS 24 μm imaging from the S-COSMOS survey (Le Floc'h et al., 2009). The source extraction was performed on the publicly-available imaging using the STARFINDER IDL package (Diolaiti et al., 2000). The resulting catalogue covers ~ 2.1 deg^2 and reaches the depth of $\sigma \simeq 13$ μJy (for details, see Roseboom et al. 2012a).

For the extraction of far-infrared flux densities and limits I used the *Herschel* HerMES (Oliver et al., 2012) and the PACS (Poglitsch et al., 2010) Evolutionary Probe (PEP; Lutz et al. 2011) data obtained with the SPIRE (Griffin et al., 2010) and PACS instruments, covering the entire COSMOS and UDS fields (see Section 2.1 for details). Finally, the Very Large Array (VLA) COSMOS Deep catalogue was used where the additional VLA A-array observations at 1.4 GHz were obtained and combined with the existing data from the VLA-COSMOS Large project (for details, see Schinnerer et al. 2010). This catalogue covers $\simeq 250$ arcmin^2 and reaches a sensitivity of $\sigma = 12$ μJy beam^{-1}.

4.3 SCUBA-2 Source Identification

In order to find the optical counterparts for sub-mm sources, for which positions are measured with relatively large beams, a simple closest-match approach is not sufficiently accurate. I therefore use the method outlined in Subsection 2.2 where I adopt the 2.5σ search radius around the SCUBA-2 position based on the signal-to-noise ratio (SNR): $r_s = 2.5 \times 0.6\times$ FWHM/SNR, where FWHM 15 arcsec. In order to account for systematic astrometry shifts (caused by pointing inaccuracies and/or source blending; e.g. Dunlop et al. 2010) I enforce a minimum search radius of 4.5 arcsec. Within this radius I calculate the corrected Poisson probability, p, that a given counterpart could have been selected by chance.

For reasons explained in Subsection 1.1.4, the VLA 1.4 GHz and Spitzer MIPS 24 μm and IRAC 8 μm (with addition of 3.6 μm) bands were chosen for searching for galaxy counterparts. In the case of the MIPS 24 μm band, the minimum search radius was increased to 5 arcsec to account for the significant MIPS beam size ($\simeq$ 6 arcsec). The optical/near-infrared catalogues were then matched with these coordinates using a search radius of r = 1.5 arcsec and the closest match taken to be the optical counterpart. In addition, I utilised the Herschel, SCUBA-2 and VLA photometry to help isolate likely incorrect identifications (Section 4.4.2).

The results of the identification process are summarized in Table 4.2, where the most reliable IDs ($p < 0.05$) are marked in bold, the tentative IDs ($0.05 < p < 0.1$) are marked in italics and incorrectly identified sources (as discussed in Section 4.4.2) are marked with asterisks.

As seen in Table 4.3 (before the corrections of Section 4.4.2) at 1.4 GHz the ID success rate is only 14% (15 out of 106 sources, all with $p < 0.05$) but at 24 μm the success rate is 69% (73 out of 106, 62 of which have $p < 0.05$). Combining both methods, the successful identification rate is 70% (74 out of 106, 63 of which have $p < 0.05$). The striking difference in these statistics is due to the fact that the S-COSMOS 24 μm imaging utilised here is relatively deeper than the radio data currently available in the COSMOS field.

I found that 57 of the 106 SCUBA-2 sources (54%) had 8 μm counterparts, 37 of which have $p < 0.05$. However, unsurprisingly, several of these identifications simply confirmed the identifications already secured via the radio and/or 24 μm cross matching, and the search for 8 μm counterparts only added 5 new identifications (2 of which have $p < 0.05$) to the results described above.

Table 4.2: *The results of the p-statistics as explained in Sec. 4.3. The columns show our ID, optical/NIR coordinates and flux, distance between the given ID and the 850 μm coordinate and the p-value for 3.6 μm, 8.0 μm, 24 μm and 1.4 GHz bands respectively. If a given ID is shown more than once, the source with lowest p-value was treated as a correct association. The robust IDs ($p \leq 0.05$) are shown in bold, the tentative ($0.05 < p \leq 0.1$) in italic and the sources for which the optical/NIR IDs were rejected (as in Sec. 4.4.2) are marked with asterisks.*

ID SC850-	RA_{opt} deg	DEC_{opt} deg	RA_{VLA} deg	DEC_{VLA} deg	$S_{8.0}$ μJy	$dist_{8.0}$ "	$p_{8.0}$	S_{24} mJy	$dist_{24}$ "	p_{24}	S_{VLA} μJy	$dist_{VLA}$ "	p_{VLA}
1*	150.06460	2.26405	...	...	18.88	2.47	*0.062*	0.13	2.18	**0.036**	...	...	...
2*	150.10014	2.29713	150.09994	2.29721	35.00	2.23	**0.032**	0.16	1.42	**0.016**	0.187	1.85	**0.001**
4	150.10546	2.31285	150.10535	2.31284	24.71	1.57	**0.026**	0.23	0.65	**0.003**	0.058	1.62	**0.002**
5	150.14304	2.35585	150.14323	2.35602	14.21	0.66	**0.011**	0.14	0.40	**0.002**	0.517	0.20	**0.000**
6	150.09854	2.36536	150.09865	2.36538	31.79	1.35	**0.016**	0.24	1.20	**0.007**	0.043	1.60	**0.002**
7	150.09866	2.32081	...	...	15.93	3.16	*0.092*	0.12	2.30	**0.041**	...	...	...
8	150.09790	2.26001	...	...	9.47	1.91	*0.070*	...	...	...	...	...	...
9	150.07911	2.28180	...	...	...	...	...	0.33	1.35	**0.003**	...	...	...
9	...	...	...	...	27.09	2.21	**0.040**	0.31	1.97	**0.012**	...	...	...
9	...	...	...	...	14.09	3.85	0.116	0.30	4.05	**0.035**	...	...	...
10	150.15374	2.32800	...	...	19.41	1.36	**0.026**	...	...	...	...	...	...
11	150.04326	2.37348	150.04318	2.37357	20.86	2.15	**0.047**	0.27	1.30	**0.004**	0.100	2.03	**0.002**
13*	150.08440	2.29049	...	...	59.24	2.71	**0.027**	0.42	2.43	**0.010**	...	...	...
14	150.10641	2.25161	150.10635	2.25161	26.43	2.94	*0.059*	0.58	2.53	**0.007**	0.112	2.89	**0.003**
15	150.11754	2.32996	...	...	14.97	1.69	**0.044**	0.16	1.33	**0.009**	...	...	...
16	150.05657	2.37375	150.05649	2.37383	107.95	0.88	**0.003**	0.46	0.78	**0.001**	0.088	0.90	**0.001**
17	150.20797	2.38308	...	...	21.93	0.71	**0.008**	0.07	0.15	**0.001**	...	...	...
18	150.16357	2.37242	150.16351	2.37251	34.47	1.64	**0.020**	0.56	1.41	**0.003**	0.138	1.72	**0.001**
19	150.11255	2.37654	...	...	10.47	0.76	**0.018**	0.10	0.93	**0.013**	...	...	...
20	150.15026	2.36414	...	...	30.45	1.54	**0.021**	0.21	1.00	**0.007**	...	...	...
21	150.09867	2.31118	...	...	11.97	0.37	**0.005**	0.18	0.90	**0.007**	...	...	...
22	150.05706	2.29286	...	...	14.36	2.45	*0.073*	0.16	2.09	**0.028**	...	...	...
23	150.12294	2.36096	...	...	12.93	0.61	**0.011**	0.23	0.65	**0.002**	...	...	...
24	150.10909	2.29433	...	...	21.57	1.37	**0.024**	0.22	0.64	**0.002**	...	...	...
25	150.03729	2.34057	150.03740	2.34071	9.31	2.50	*0.096*	0.07	1.69	**0.040**	0.062	1.86	**0.003**
26	150.07937	2.34056	150.07925	2.34052	13.55	3.04	*0.096*	0.16	2.82	**0.042**	0.061	3.38	**0.005**
26	...	...	...	...	...	...	...	0.18	2.68	**0.022**	...	...	...
28	150.12181	2.34131	...	...	10.69	1.76	*0.059*	0.10	2.09	**0.042**	...	...	...
29*	150.10525	2.43499	...	...	13.36	1.21	**0.030**	0.08	0.89	**0.014**	...	...	...
31	150.05248	2.24555	...	...	37.59	2.89	**0.043**	0.38	1.50	**0.003**	...	...	...
33	150.04098	2.28063	...	...	11.41	1.89	*0.062*	0.08	2.74	*0.068*	...	...	...
34*	150.13513	2.39942	150.13495	2.39930	14.60	0.38	**0.004**	0.17	0.32	**0.001**	0.056	0.96	**0.001**
35	150.16771	2.29876	...	...	16.71	2.85	*0.080*	0.32	2.62	**0.018**	...	...	...
36*	150.08187	2.41556	...	...	...	...	...	0.64	0.72	**0.001**	...	...	...
37	150.06811	2.27569	...	...	29.14	1.92	**0.030**	0.45	1.53	**0.004**	...	...	...
38	150.07527	2.37940	...	...	...	...	...	0.13	1.28	**0.017**	...	...	...
40*	150.10531	2.32590	...	...	...	...	...	0.06	3.12	**0.050**	...	...	...
42*	150.02754	2.34577	...	...	...	...	...	0.16	4.32	*0.069*	...	...	...
43	150.17186	2.24070	...	...	18.90	2.87	*0.074*	0.21	2.77	**0.032**	...	...	...
44*	150.13702	2.23222	150.13658	2.23252	46.55	2.98	**0.038**	0.22	2.39	**0.024**	0.045	1.94	**0.003**
45	150.12715	2.38786	...	...	12.64	1.21	**0.031**	0.06	0.98	**0.020**	...	...	...
46	150.10590	2.42879	...	...	...	...	...	0.13	1.99	**0.033**	...	...	...
47	150.04825	2.25144	...	...	...	...	...	0.13	4.21	**0.047**	...	...	...
48	150.02141	2.28867	...	...	20.33	3.16	*0.079*	...	...	...	...	...	...
49	150.15747	2.35803	...	...	...	...	...	0.19	3.38	**0.047**	...	...	...

Table 4.2: (continued).

ID SC850-	RA_{opt} deg	DEC_{opt} deg	RA_{VLA} deg	DEC_{VLA} deg	$S_{8.0}$ μJy	$dist_{8.0}$ "	$p_{8.0}$	S_{24} mJy	$dist_{24}$ "	p_{24}	S_{VLA} μJy	$dist_{VLA}$ "	p_{VLA}
51	150.03652	2.28617	...	...	...	...	...	0.10	3.63	**0.049**	...	...	...
53	150.18763	2.32250	...	...	46.19	1.80	**0.018**	0.24	1.73	**0.013**	...	...	...
54	150.04241	2.29985	...	...	19.09	2.46	*0.061*	0.09	2.47	*0.056*	...	...	...
55	150.13354	2.37042	...	...	15.81	3.32	*0.097*	0.10	2.10	**0.027**	...	...	...
56	150.05002	2.38607	...	...	...	...	...	0.05	1.15	**0.026**	...	...	...
59	150.18497	2.38894	...	...	...	...	...	0.11	4.48	*0.088*	...	...	...
61	150.05397	2.39590	...	...	11.07	1.39	**0.042**	0.16	0.73	**0.006**	...	...	...
62	150.16691	2.23582	...	...	20.71	0.89	**0.013**	0.37	0.69	**0.002**	...	...	...
63*	150.07672	2.39860	...	...	12.09	2.56	*0.086*	...	...	...	...	...	...
64	150.13074	2.31408	...	...	...	...	...	0.18	4.05	*0.059*	...	...	...
65*	150.09156	2.39904	...	...	58.66	2.46	**0.024**	0.16	2.19	**0.018**	...	...	...
66	150.17561	2.40159	...	...	27.26	2.72	*0.052*	0.16	2.34	**0.034**	...	...	...
67	150.11132	2.40320	...	...	9.76	3.36	0.121	0.11	3.22	*0.067*	...	...	...
68	150.13001	2.25269	...	...	10.88	2.59	*0.092*	0.18	2.63	**0.034**	...	...	...
71*	150.07194	2.23867	...	...	...	...	...	0.08	2.14	*0.050*	...	...	...
72*	150.06456	2.32903	...	...	111.50	2.24	**0.012**	0.29	1.99	**0.013**	...	...	...
73	150.20962	2.35525	150.20955	2.35531	1446.07	2.32	**0.001**	1.46	2.07	**0.001**	0.273	2.09	**0.001**
74	150.07066	2.30514	...	...	10.24	3.65	0.130	0.05	3.68	*0.096*	...	...	...
75	150.15933	2.29680	...	...	8.45	1.30	**0.047**	0.07	1.47	**0.034**	...	...	...
77*	150.07027	2.42297	...	...	...	...	...	0.10	3.72	**0.050**	...	...	...
78	150.09944	2.40487	...	...	10.07	1.28	**0.042**	0.10	1.08	**0.010**	...	...	...
79	150.04118	2.32813	...	...	...	...	...	0.13	3.85	**0.043**	...	...	...
79	...	...	...	...	43.14	3.81	*0.059*	...	...	...	...	...	...
81*	150.12582	2.41354	...	...	...	...	...	...	...	...	...	...	...
83	150.02492	2.31287	...	...	12.00	3.40	0.127	0.16	4.09	**0.041**	...	...	...
84*	150.11154	2.40957	...	...	19.59	3.09	*0.086*	0.04	3.05	*0.086*	...	...	...
86	150.05166	2.30585	...	...	73.38	1.75	**0.012**	0.34	1.67	**0.008**	...	...	...
87	150.22434	2.35644	...	...	11.10	0.74	**0.017**	0.09	0.98	**0.016**	...	...	...
88*	150.05456	2.27535	...	...	82.07	4.21	**0.044**	0.27	3.35	**0.019**	...	...	...
88	...	...	...	...	31.33	2.41	**0.043**	...	...	...	...	...	...
89	150.16255	2.26808	...	...	...	...	...	0.07	1.39	**0.032**	...	...	...
91	150.07060	2.28920	...	...	12.83	4.01	0.149	0.18	4.25	**0.040**	...	...	...
92	150.05916	2.39982	...	...	21.66	3.63	0.100	0.09	4.54	*0.064*	...	...	...
93*	150.05785	2.42723	...	...	44.59	3.25	**0.049**	0.07	3.23	*0.088*	...	...	...
95	150.01640	2.32096	...	...	14.17	0.27	**0.003**	...	...	...	...	...	...
98	150.16186	2.34092	...	...	46.07	4.71	*0.081*	0.31	4.68	**0.043**	...	...	...
99	150.21020	2.31167	150.21013	2.31168	93.38	3.50	**0.031**	0.91	3.11	**0.005**	0.227	3.41	**0.003**
102	150.03745	2.27186	150.03670	2.27098	20.84	1.32	**0.026**	...	...	...	0.075	1.03	**0.001**
102	...	...	150.03738	2.27194	61.12	4.82	*0.068*	0.71	3.56	**0.009**	0.080	4.57	**0.008**
103	150.08514	2.38195	...	...	...	...	...	0.39	2.45	**0.008**	...	...	...
105*	150.16426	2.40881	...	...	12.05	2.25	*0.088*	0.27	2.36	**0.012**	...	...	...

In total, therefore, I identified radio/mid-infrared counterparts for 80 of the 106 SCUBA-2 850 μm sources (67 of which have $p < 0.05$; see Table 4.2), and hence achieved an identification success rate of 75%. The identification success rate achieved in each individual waveband is given in Table 4.3. To complete the connection between the SCUBA-2 sources and their host galaxies, within the area covered by the CANDELS *HST* WFC3/IR imaging (Figure 4.1) I matched the statistically-significant mid-infrared and radio counterparts to the galaxies in the CANDELS H_{160}-band imaging using a maximum matching radius of 1.5 arcsec. This yielded accurate positions for the optical identifications of 60 of the SCUBA-2 sources. For those few SCUBA-2 sources which lie outside the CANDELS *HST* imaging, I matched the statistically-significant mid-infrared and radio counterparts to the galaxies in the K_S-band UltraVISTA imaging (using the same maximum matching radius). This yielded accurate positions for the optical identifications of the remaining 20 sources. I note that galaxies SC850-37, 46 and 61, even though successfully identified in the optical/near-infrared, turned out to be too close to a foreground star for reliable photometry and therefore no optical redshifts or stellar masses were derived and utilised in the subsequent analysis.

4.4 Redshifts

4.4.1 Photometric redshifts

For all the identified sources, the multi-band photometry was collected and the optical-infrared photometric redshifts were calculated using the method outlined in Section 2.3. The optical-infrared photometric redshifts for the 77 optically-identified sources for which photometry could be reliably extracted (i.e. the 80 identified sources excluding SC850-37, 46 and 61) are given in Table 4.4. Also given in this table are the optical spectroscopic redshifts where available. I note that, in general, z_{spec} and z_p are in excellent agreement, except for the two SCUBA-2 sources which are associated with active galactic nuclei (AGN; sources 65 and 72), presumably because no AGN template was included in the photometric redshift fitting procedure.

In addition, for every SCUBA-2 source I used the 450 and 850 μm photometry as well as the Herschel 100, 160, 250, 350, 500 μm and VLA 1.4 GHz flux densities (or limits) to obtain 'long-wavelength' photometric redshifts (z_{LW}) as explained in

Section 2.3. The resulting 'long-wavelength' redshift estimates for all 106 sources are also given in Table 4.4.

4.4.2 Redshift/identification refinement

Given the statistical nature of the identification process described above, there is always a possibility that some identifications are incorrect (as revealed by interferometric follow-up – e.g. Hodge et al. 2013), and indeed, even when the probability of chance coincidence is extremely small, it can transpire that the optical counterpart is not, in fact, the correct galaxy identification, but is actually an intervening galaxy, gravitationally lensing a more distant sub-mm source (e.g. Dunlop et al. 2004). In either case, a mis-identification will lead to an under-estimate of the true redshift of the sub-mm source, and indeed dramatic discrepancies between z_p and z_{LW} can potentially be used to isolate mis-identified sources.

In Figure 4.3 I have therefore plotted z_{LW} versus z_p in an attempt to test the consistency of these two independent redshift estimators. From this plot it can be seen that, for the majority of sources, the two redshift estimates are indeed consistent, with the normalized offset in z_{LW} ($r = (z_{LW} z_p)/(1 + z_p)$) displaying a Gaussian distribution with $\sigma = 0.14$. However, there is an extended *positive* tail to this distribution, indicative of the fact that a significant subset of the identifications have a value of z_p which is much smaller than the (identification independent) 'long-wavelength' photometric redshift of the SCUBA-2 source, z_{LW}. Given the aforementioned potential for mis-identification (and concomitant redshift under-estimation) I have chosen to reject the optical identifications (and hence also z_p) for the sources that lie more than 3σ above the 1:1 redshift relation (see Figure 4.3 and caption for details). This may lead to the rejection of a few correct identifications, but this is less important than the key aim of removing any significant redshift biases due to mis-identifications, and also the value of retaining only the most reliable set of identified sources for further study.

The effect of this cut is the rejection of 18 of the 80 optical identifications derived in Section 4.3. These rejected optical IDs are flagged with asterisks in Table 4.2 and zeros in Table 4.4. As tabulated in Table 4.3, with this redshift refinement, the effective optical ID success rate for the most reliable ($p < 0.05$) IDs drops from 63% to 51%, while the overall ($p < 0.1$) ID success rate drops

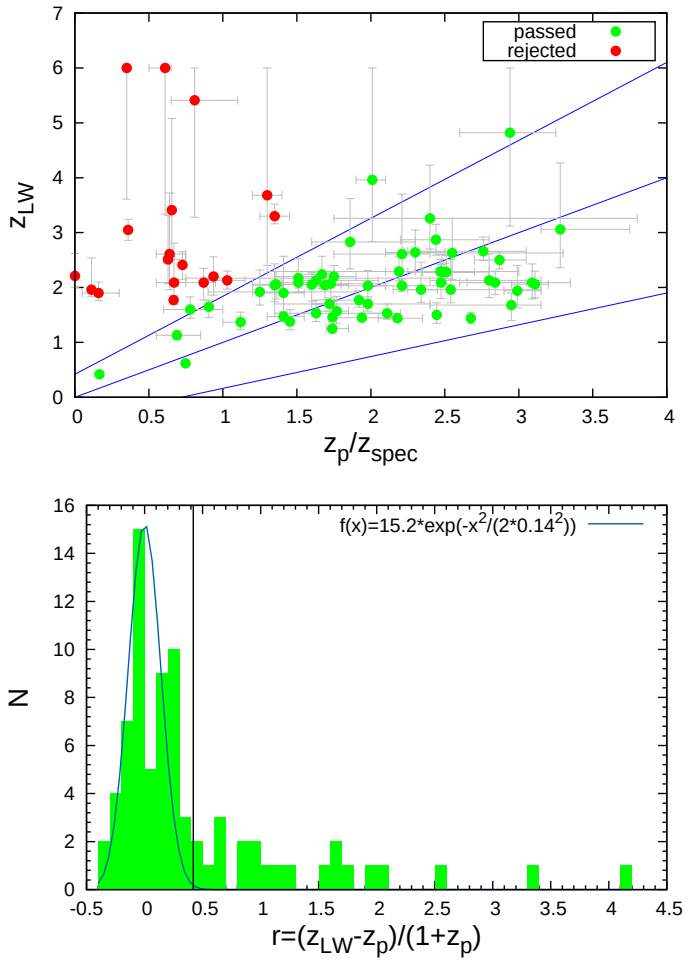

Figure 4.3: *The upper panel shows the 'long–wavelength' photometric redshifts (z_{LW}) derived for the SCUBA–2 sources plotted against the optical–infrared photometric redshifts (z_p) of the optical identifications. The central blue solid line shows the 1:1 relation. As illustrated in the lower panel, the sources lying below the 1:1 relation display a distribution of normalized redshift offsets (i.e.* $r = (\mathrm{z_{LW}} - \mathrm{z_p})/(1 + \mathrm{z_p})$*) which is approximately Gaussian with* $\sigma = 0.14$*. The positive side of this distribution is also reasonably well fitted by this same Gaussian, but there is a long positive tail, indicative of the fact that a significant subset of the identifications have a value of* z_p *which is much smaller than the (identification independent) 'long–wavelength' photometric redshift of the SCUBA–2 source (*z_{LW}*). Given the potential for mis–identification (e.g. through galaxy–galaxy gravitional lensing) we view such discrepancies as evidence that* z_p*, or more likely the galaxy identification itself, is in error. The upper and lower blue solid lines in the upper panel show the* $\pm 3\sigma$ *limits of the Gaussian distribution, and so we choose to reject the optical identifications (and hence also* z_p*) for the sources that lie above the* 3σ *limit (red dots). This same* 3σ *limit is shown by the black vertical line in the lower panel.*

Table 4.3: *The radio/IR/optical identification statistics for the 850 μm S2CLS COSMOS sample used in this chapter. The number of reliably (with the Poissonian probability of chance association, p, of less than 0.05), tentatively (with $0.05 < p \leq 0.1$) and all ($p \leq 0.1$) identified sources are shown (with the percentage, out of 106, in the brackets). The columns give the ID success rate at a given band followed by the overall radio/IR ID success rate (all four radio/IR bands used here), the optical ID success rate (before the corrections of Section 4.4.2) and the optical ID success rate after the corrections. The number of optical IDs drops from 80 to 61 which predicts the approximate level of the reliability rate of my identified sample (before the corrections of Section 4.4.2) of $\sim 75\%$.*

	1.4GHz	24μm	8.0μm	3.6μm	radio/IR overall	optical before corr.	optical after corr.
reliable ($p \leq 0.05$)	15 (14%)	62 (58%)	37 (35%)	22 (21%)	67 (63%)	67 (63%)	53 (50%)
tentative ($0.05 < p \leq 0.1$)	0 (0%)	11 (10%)	20 (19%)	18 (17%)	13 (12%)	13 (12%)	8 (8%)
all ($p \leq 0.1$)	15 (14%)	73 (69%)	57 (54%)	40 (38%)	80 (75%)	80 (75%)	61 (58%)

from 75% to 58%. However, while this reduces the number of reliably identified SCUBA-2 sources to $\simeq 50\%$ of the sample, this has the advantage or removing the most dubious identifications. Moreover, I stress that I retain redshift information for every one of the 106 SCUBA-2 sources, in the form of z_{LW} if neither z_{spec} nor a reliable value for z_p are available.

4.4.3 Redshift distribution

The differential redshift distribution for my SCUBA-2 galaxy sample is presented in Figure 4.4. In the upper panel the black area depicts the redshift distribution for the sources with reliable optical IDs (and hence z_{spec} or z_p), while the histogram indicated in blue includes the additional unidentified SCUBA-2 sources with meaningful measurements of z_{LW}. Finally, the green histogram containing the green arrows indicates the impact of also including those sources for which only lower limits on their estimated redshifts could be derived from the long-wavelength photometry. The mean and median redshifts for the whole sample are $z = 2.38 \pm 0.09$ (strictly speaking, a lower limit) and $z_{med} = 2.21 \pm 0.06$ respectively whereas, for the confirmed optical IDs with optical spectroscopic/photometric redshifts the corresponding numbers are $z = 1.97 \pm 0.09$ and $z_{med} = 1.96 \pm 0.07$. This shows that, as expected, the radio/infrared identification process biases the mean redshift towards lower redshifts, but in this case only by about $\simeq 10\%$ in

Table 4.4: *The physical properties for the whole COSMOS sample. The columns show respectively the ID name, spectroscopic redshift, optical photometric redshift, Herschel/SCUBA-2 'long-wavelength' redshift, the value of* $r = (z_{LW} - z_p)/(1 + z_p)$ *(Sec. 4.4.2), the flag, final redshift, star formation rate (SFR) and the stellar mass* ($M_\star$)*. If the source's optcal/NIR ID was rejected (as in Sec. 4.4.2) it is flagged here with 0, if it was accepted it is flagged with 1 and if no ID was found the flag is 2. For objects flagged with 1 the final redshift (z) is the optical photometric redshift* (z_p) *and therefore the stellar mass exists. For flags 0 and 2 the redshift becomes* z_{LW}.

ID SC850-	z_{spec}	z_p	z_{LW}	r	flag	z	SFR $/M_\odot yr^{-1}$	$\log(M_\star)$ $/M_\odot$
1	...	$1.35^{+0.10}_{-0.10}$	$3.30^{+0.22}_{-0.14}$	0.83	0	$3.30^{+0.22}_{-0.14}$	282.8 ± 32.8	...
2	0.3600	$0.39^{+0.11}_{-0.09}$	$3.05^{+0.19}_{-0.19}$	1.98	0	$3.05^{+0.19}_{-0.19}$	171.2 ± 11.2	...
3	...	...	$3.53^{+0.30}_{-0.30}$	...	2	$3.53^{+0.30}_{-0.30}$	447.6 ± 14.5	...
4	...	$1.51^{+0.19}_{-0.11}$	$2.09^{+0.08}_{-0.10}$	0.23	1	$1.51^{+0.19}_{-0.11}$	325.4 ± 9.6	$10.21^{+0.77}_{-0.45}$
5	...	$2.21^{+0.24}_{-0.21}$	$2.03^{+0.11}_{-0.10}$	-0.06	1	$2.21^{+0.24}_{-0.21}$	444.3 ± 13.1	$10.36^{+0.77}_{-0.68}$
6	...	$2.50^{+0.20}_{-0.15}$	$2.28^{+0.16}_{-0.11}$	-0.06	1	$2.50^{+0.20}_{-0.15}$	490.2 ± 15.1	$11.35^{+0.65}_{-0.49}$
7	...	$2.87^{+0.18}_{-0.17}$	$2.50^{+0.15}_{-0.16}$	-0.10	1	$2.87^{+0.18}_{-0.17}$	447.6 ± 14.5	$11.01^{+0.51}_{-0.48}$
8	...	$2.44^{+0.36}_{-0.24}$	$2.87^{+0.28}_{-0.28}$	0.12	1	$2.44^{+0.36}_{-0.24}$	356.2 ± 17.5	$9.54^{+1.00}_{-0.67}$
9	...	$1.75^{+0.15}_{-0.40}$	$2.20^{+0.20}_{-0.15}$	0.16	1	$1.75^{+0.15}_{-0.40}$	261.5 ± 13.3	$10.45^{+0.57}_{-1.52}$
10	...	$2.51^{+0.29}_{-0.26}$	$2.28^{+0.31}_{-0.22}$	-0.07	1	$2.51^{+0.29}_{-0.26}$	279.8 ± 14.2	$10.94^{+0.90}_{-0.81}$
11	...	$1.63^{+0.42}_{-0.13}$	$2.13^{+0.10}_{-0.11}$	0.19	1	$1.63^{+0.42}_{-0.13}$	261.1 ± 13.9	$10.82^{+1.73}_{-0.53}$
12	...	...	$3.47^{+0.65}_{-0.50}$	...	2	$3.47^{+0.65}_{-0.50}$	409.6 ± 17.8	...
13	...	$1.03^{+0.12}_{-0.13}$	$2.13^{+0.17}_{-0.16}$	0.54	0	$2.13^{+0.17}_{-0.16}$	261.5 ± 13.3	...
14	...	$2.18^{+0.17}_{-0.13}$	$1.44^{+0.05}_{-0.05}$	-0.23	1	$2.18^{+0.17}_{-0.13}$	409.6 ± 17.8	$11.04^{+0.59}_{-0.45}$
15	...	$2.30^{+0.20}_{-0.20}$	$2.64^{+0.41}_{-0.36}$	0.10	1	$2.30^{+0.20}_{-0.20}$	186.9 ± 11.1	$10.93^{+0.66}_{-0.66}$
16	0.6670	$0.99^{+0.11}_{-0.09}$	$1.77^{+0.08}_{-0.07}$	0.66	0	$1.77^{+0.08}_{-0.07}$	69.5 ± 5.0	$10.64^{+0.59}_{-0.48}$
17	...	$2.76^{+0.29}_{-0.51}$	$2.66^{+0.26}_{-0.17}$	-0.03	1	$2.76^{+0.29}_{-0.51}$	442.9 ± 25.7	$10.79^{+0.83}_{-1.46}$
18	...	$1.94^{+0.21}_{-0.19}$	$1.45^{+0.05}_{-0.03}$	-0.17	1	$1.94^{+0.21}_{-0.19}$	429.9 ± 16.2	$10.68^{+0.76}_{-0.69}$
19	...	$2.48^{+0.52}_{-1.18}$	$2.29^{+0.31}_{-0.22}$	-0.05	1	$2.48^{+0.52}_{-1.18}$	257.0 ± 15.5	$10.95^{+1.64}_{-3.71}$
20	...	$2.19^{+0.11}_{-0.09}$	$2.29^{+0.27}_{-0.17}$	0.03	1	$2.19^{+0.11}_{-0.09}$	255.5 ± 15.4	$11.17^{+0.39}_{-0.32}$
21	...	$1.98^{+0.42}_{-0.63}$	$1.70^{+0.13}_{-0.13}$	-0.09	1	$1.98^{+0.42}_{-0.63}$	203.6 ± 12.4	$10.89^{+1.53}_{-2.30}$
22	...	$1.51^{+0.94}_{-0.76}$	$2.17^{+0.35}_{-0.25}$	0.26	1	$1.51^{+0.94}_{-0.76}$	194.3 ± 13.5	$11.19^{+4.19}_{-3.39}$
23	...	$1.92^{+0.08}_{-0.17}$	$1.77^{+0.17}_{-0.13}$	-0.05	1	$1.92^{+0.08}_{-0.17}$	172.5 ± 11.1	$10.60^{+0.29}_{-0.62}$
24	...	$1.72^{+0.03}_{-0.12}$	$1.70^{+0.11}_{-0.13}$	-0.01	1	$1.72^{+0.03}_{-0.12}$	171.2 ± 11.2	$10.92^{+0.12}_{-0.48}$
25	...	$2.84^{+0.21}_{-0.24}$	$2.09^{+0.21}_{-0.22}$	-0.20	1	$2.84^{+0.21}_{-0.24}$	299.8 ± 21.2	$10.93^{+0.60}_{-0.68}$
26	2.6760	$2.61^{+0.09}_{-0.26}$	$1.44^{+0.10}_{-0.10}$	-0.34	1	2.68	217.9 ± 15.1	$10.48^{+0.26}_{-0.75}$
27	...	...	$2.49^{+0.44}_{-0.34}$	...	2	$2.49^{+0.44}_{-0.34}$	17.3 ± 2.0	...
28	...	$2.11^{+0.09}_{-0.16}$	$1.53^{+0.17}_{-0.11}$	-0.19	1	$2.11^{+0.09}_{-0.16}$	157.8 ± 10.7	$10.85^{+0.31}_{-0.56}$
29	0.7270	$0.71^{+0.14}_{-0.11}$	$2.41^{+0.24}_{-0.26}$	0.97	0	$2.41^{+0.24}_{-0.26}$	132.5 ± 19.5	...
30	...	...	$2.54^{+0.48}_{-0.41}$	...	2	$2.54^{+0.48}_{-0.41}$	128.9 ± 11.2	...
31	...	$2.47^{+0.08}_{-0.12}$	$2.29^{+0.22}_{-0.15}$	-0.05	1	$2.47^{+0.08}_{-0.12}$	450.5 ± 36.5	$11.23^{+0.26}_{-0.39}$
32	...	...	$2.92^{+0.64}_{-0.45}$	...	2	$2.92^{+0.64}_{-0.45}$	57.8 ± 7.9	...
33	...	$2.40^{+1.40}_{-0.65}$	$3.26^{+0.97}_{-0.56}$	0.25	1	$2.40^{+1.40}_{-0.65}$	206.6 ± 21.4	$11.66^{+4.80}_{-2.23}$
34	0.0010	$0.04^{+0.06}_{-0.04}$	$2.21^{+0.41}_{-0.21}$	2.21	0	$2.21^{+0.41}_{-0.21}$	164.2 ± 19.1	...
35	...	$1.36^{+0.24}_{-0.16}$	$2.06^{+0.23}_{-0.27}$	0.30	1	$1.36^{+0.24}_{-0.16}$	102.3 ± 10.5	$10.90^{+1.11}_{-0.74}$
36	...	$0.16^{+0.14}_{-0.11}$	$1.90^{+0.20}_{-0.14}$	1.50	0	$1.90^{+0.20}_{-0.14}$	132.5 ± 19.5	...
37	...	...	$1.56^{+0.20}_{-0.12}$	...	2	$1.56^{+0.20}_{-0.12}$	261.5 ± 13.3	...
38	...	$1.98^{+0.12}_{-0.28}$	$2.03^{+0.28}_{-0.39}$	0.02	1	$1.98^{+0.12}_{-0.28}$	174.5 ± 16.8	$10.71^{+0.43}_{-1.01}$
39	...	...	$2.58^{+0.63}_{-0.42}$	...	2	$2.58^{+0.63}_{-0.42}$	356.2 ± 17.5	...
40	...	$0.87^{+0.08}_{-0.17}$	$2.09^{+0.26}_{-0.32}$	0.65	0	$2.09^{+0.26}_{-0.32}$	447.6 ± 14.5	...
41	...	...	> 3.92	...	2	> 3.92	171.2 ± 11.2	...
42	0.9370	$0.96^{+0.09}_{-0.11}$	$2.20^{+0.36}_{-0.34}$	0.65	0	$2.20^{+0.36}_{-0.34}$	299.8 ± 21.2	...
43	...	$1.86^{+0.44}_{-0.26}$	$2.83^{+0.79}_{-0.49}$	0.34	1	$1.86^{+0.44}_{-0.26}$	176.2 ± 22.1	$10.90^{+1.68}_{-0.99}$
44	0.1220	$0.13^{+0.12}_{-0.13}$	$1.96^{+0.58}_{-0.12}$	1.64	0	$1.96^{+0.58}_{-0.12}$	16.8 ± 2.9	...
45	...	$3.28^{+0.47}_{-0.13}$	$3.06^{+1.21}_{-0.70}$	-0.05	1	$3.28^{+0.47}_{-0.13}$	164.2 ± 19.1	$10.58^{+1.16}_{-0.32}$
46	...	...	$1.88^{+0.21}_{-0.14}$	...	2	$1.88^{+0.21}_{-0.14}$	132.5 ± 19.5	...
47	...	$2.55^{+0.75}_{-0.45}$	$2.63^{+0.63}_{-0.48}$	0.02	1	$2.55^{+0.75}_{-0.45}$	282.8 ± 32.8	$11.12^{+2.35}_{-1.41}$

Table 4.4: (continued).

ID SC850-	z_{spec}	$z_{\rm p}$	$z_{\rm LW}$	r	flag	z	SFR $/{\rm M}_\odot{\rm yr}^{-1}$	$\log({\rm M}_\star)$ $/{\rm M}_\odot$
48	...	$3.11^{+0.09}_{-0.16}$	$2.06^{+0.24}_{-0.25}$	-0.26	1	$3.11^{+0.09}_{-0.16}$	369.5 ± 37.6	$11.32^{+0.25}_{-0.44}$
49	...	$1.60^{+0.25}_{-0.20}$	$2.05^{+0.22}_{-0.30}$	0.17	1	$1.60^{+0.25}_{-0.20}$	108.5 ± 11.8	$9.48^{+0.91}_{-0.73}$
50	...	...	$1.95^{+0.87}_{-0.27}$	...	2	$1.95^{+0.87}_{-0.27}$	490.2 ± 15.1	...
51	...	$2.01^{+0.09}_{-0.11}$	$3.96^{+2.04}_{-1.12}$	0.65	1	$2.01^{+0.09}_{-0.11}$	152.4 ± 20.8	$10.82^{+0.32}_{-0.40}$
52	...	...	$3.18^{+2.82}_{-1.28}$	...	2	$3.18^{+2.82}_{-1.28}$	48.4 ± 8.2	...
53	...	$1.41^{+0.14}_{-0.11}$	$1.47^{+0.09}_{-0.08}$	0.02	1	$1.41^{+0.14}_{-0.11}$	120.6 ± 9.8	$11.51^{+0.67}_{-0.53}$
54	...	$3.09^{+0.26}_{-0.44}$	$2.09^{+0.34}_{-0.30}$	-0.24	1	$3.09^{+0.26}_{-0.44}$	204.5 ± 22.4	$11.02^{+0.70}_{-1.19}$
55	...	$1.74^{+0.11}_{-0.04}$	$1.25^{+0.13}_{-0.08}$	-0.18	1	$1.74^{+0.11}_{-0.04}$	128.9 ± 11.2	$11.27^{+0.45}_{-0.16}$
56	...	$2.80^{+0.35}_{-0.40}$	$2.13^{+0.48}_{-0.31}$	-0.18	1	$2.80^{+0.35}_{-0.40}$	194.9 ± 23.6	$10.76^{+0.99}_{-1.13}$
57	...	...	$3.36^{+2.47}_{-0.72}$	...	2	$3.36^{+2.47}_{-0.72}$	143.9 ± 17.0	...
58	...	...	$2.45^{+0.60}_{-0.49}$	...	2	$2.45^{+0.60}_{-0.49}$	157.8 ± 10.7	...
59	...	$1.69^{+0.11}_{-0.04}$	$2.04^{+0.22}_{-0.26}$	0.13	1	$1.69^{+0.11}_{-0.04}$	120.9 ± 13.8	$10.30^{+0.42}_{-0.15}$
60	...	...	> 3.60	...	2	> 3.60	25.6 ± 3.9	...
61	...	...	$1.47^{+0.16}_{-0.14}$	...	2	$1.47^{+0.16}_{-0.14}$	57.8 ± 7.9	...
62	...	$1.67^{+0.08}_{-0.17}$	$2.24^{+0.33}_{-0.26}$	0.21	1	$1.67^{+0.08}_{-0.17}$	129.6 ± 17.3	$10.96^{+0.33}_{-0.70}$
63	...	$0.81^{+0.29}_{-0.16}$	$5.41^{+0.59}_{-2.13}$	2.54	0	$5.41^{+0.59}_{-2.13}$	57.8 ± 7.9	...
64	...	$1.63^{+0.47}_{-0.28}$	$1.53^{+0.24}_{-0.15}$	-0.04	1	$1.63^{+0.47}_{-0.28}$	85.5 ± 9.4	$10.69^{+1.91}_{-1.14}$
65	2.4750	$0.13^{+0.07}_{-0.03}$	$2.09^{+0.33}_{-0.29}$	-0.11	1	2.48	132.5 ± 19.5	...
66	...	$1.77^{+0.08}_{-0.12}$	$1.57^{+0.27}_{-0.22}$	-0.07	1	$1.77^{+0.08}_{-0.12}$	143.9 ± 17.0	$10.84^{+0.31}_{-0.47}$
67	...	$2.34^{+0.11}_{-0.19}$	$1.96^{+0.50}_{-0.23}$	-0.11	1	$2.34^{+0.11}_{-0.19}$	134.3 ± 18.0	$10.09^{+0.33}_{-0.57}$
68	...	$0.78^{+0.22}_{-0.18}$	$1.60^{+0.23}_{-0.16}$	0.46	1	$0.78^{+0.22}_{-0.18}$	16.8 ± 2.9	$9.71^{+1.20}_{-0.98}$
69	...	...	> 4.59	...	2	> 4.59	129.6 ± 17.3	...
70	...	...	$4.97^{+1.03}_{-1.79}$	...	2	$4.97^{+1.03}_{-1.79}$	369.5 ± 37.6	...
71	...	$0.63^{+0.12}_{-0.03}$	$2.51^{+0.80}_{-0.44}$	1.15	0	$2.51^{+0.80}_{-0.44}$	450.5 ± 36.5	...
72	2.4460	$0.30^{+0.10}_{-0.05}$	$1.50^{+0.22}_{-0.15}$	-0.27	1	2.45	217.9 ± 15.1	...
73	0.1660	$0.18^{+0.07}_{-0.08}$	$0.42^{+0.02}_{-0.03}$	0.22	1	0.17	6.2 ± 0.0	$10.40^{+0.62}_{-0.71}$
74	...	$2.99^{+0.16}_{-0.09}$	$1.94^{+0.46}_{-0.31}$	-0.26	1	$2.99^{+0.16}_{-0.09}$	133.2 ± 19.2	$10.89^{+0.44}_{-0.25}$
75	...	$1.73^{+0.37}_{-0.13}$	$2.07^{+0.23}_{-0.31}$	0.12	1	$1.73^{+0.37}_{-0.13}$	109.6 ± 13.2	$10.62^{+1.44}_{-0.51}$
76	...	...	> 3.58	...	2	> 3.58	120.6 ± 9.8	...
77	...	$0.64^{+0.11}_{-0.09}$	$2.61^{+1.11}_{-0.65}$	1.20	0	$2.61^{+1.11}_{-0.65}$	57.8 ± 7.9	...
78	...	$2.21^{+0.19}_{-0.46}$	$2.61^{+1.09}_{-0.64}$	0.12	1	$2.21^{+0.19}_{-0.46}$	132.5 ± 19.5	$10.29^{+0.61}_{-1.47}$
79	...	$1.25^{+0.65}_{-0.35}$	$1.92^{+0.40}_{-0.24}$	0.30	1	$1.25^{+0.65}_{-0.35}$	48.4 ± 8.2	$9.63^{+2.78}_{-1.50}$
80	...	...	> 3.42	...	2	> 3.42	16.8 ± 2.9	...
81	...	$0.61^{+0.04}_{-0.11}$	> 3.34	3.35	0	> 3.34	134.3 ± 18.0	...
82	...	...	$2.63^{+1.38}_{-0.75}$	...	2	$2.63^{+1.38}_{-0.75}$	279.8 ± 14.2	...
83	...	$1.35^{+0.05}_{-0.15}$	$2.04^{+0.39}_{-0.30}$	0.29	1	$1.35^{+0.05}_{-0.15}$	70.5 ± 12.2	$10.31^{+0.22}_{-0.66}$
84	0.3500	$0.35^{+0.15}_{-0.10}$	> 3.61	4.19	0	> 3.61	134.3 ± 18.0	...
85	...	...	$1.51^{+0.26}_{-0.24}$	...	2	$1.51^{+0.26}_{-0.24}$	134.3 ± 18.0	...
86	1.4530	$1.36^{+0.19}_{-0.11}$	$1.38^{+0.22}_{-0.15}$	-0.03	1	1.45	75.8 ± 10.2	$11.11^{+0.89}_{-0.52}$
87	...	$2.94^{+0.31}_{-0.34}$	$4.82^{+1.18}_{-1.70}$	0.48	1	$2.94^{+0.31}_{-0.34}$	200.9 ± 35.4	$10.77^{+0.85}_{-0.93}$
88	...	$1.30^{+0.10}_{-0.10}$	$3.68^{+2.32}_{-1.28}$	1.03	0	$3.68^{+2.32}_{-1.28}$	206.6 ± 21.4	...
89	0.9050	$0.90^{+0.15}_{-0.10}$	$1.65^{+0.12}_{-0.20}$	0.39	1	0.91	25.6 ± 3.9	$9.78^{+0.77}_{-0.51}$
90	...	...	$1.96^{+1.14}_{-0.31}$	...	2	$1.96^{+1.14}_{-0.31}$	282.8 ± 32.8	...
91	...	$1.41^{+0.14}_{-0.21}$	$1.90^{+0.67}_{-0.36}$	0.20	1	$1.41^{+0.14}_{-0.21}$	64.6 ± 11.1	$10.53^{+0.61}_{-0.92}$
92	...	$1.12^{+0.03}_{-0.12}$	$1.37^{+0.18}_{-0.14}$	0.12	1	$1.12^{+0.03}_{-0.12}$	57.8 ± 7.9	$10.51^{+0.15}_{-0.59}$
93	0.6550	$0.64^{+0.06}_{-0.09}$	$3.41^{+1.67}_{-0.85}$	1.66	0	$3.41^{+1.67}_{-0.85}$	57.8 ± 7.9	...
94	...	...	> 4.31	...	2	> 4.31	69.5 ± 5.0	...
95	...	$2.54^{+0.61}_{-0.29}$	$1.96^{+0.55}_{-0.24}$	-0.16	1	$2.54^{+0.61}_{-0.29}$	192.0 ± 31.9	$10.67^{+1.84}_{-0.87}$
96	...	...	> 3.12	...	2	> 3.12	134.3 ± 18.0	...
97	...	...	> 3.34	...	2	> 3.34	171.2 ± 11.2	...
98	...	$0.69^{+0.16}_{-0.14}$	$1.13^{+0.09}_{-0.08}$	0.26	1	$0.69^{+0.16}_{-0.14}$	17.3 ± 2.0	$11.03^{+1.04}_{-0.91}$
99	0.7480	$0.69^{+0.06}_{-0.09}$	$0.62^{+0.03}_{-0.04}$	-0.07	1	0.75	91.0 ± 2.1	$10.54^{+0.37}_{-0.56}$
100	...	...	> 3.53	...	2	> 3.53	200.9 ± 35.4	...
101	...	...	> 3.96	...	2	> 3.96	16.8 ± 2.9	...
102	1.7410	$1.64^{+0.06}_{-0.14}$	$1.46^{+0.21}_{-0.16}$	-0.10	1	1.74	133.5 ± 17.5	$10.40^{+0.24}_{-0.55}$
103	...	$2.95^{+0.20}_{-0.55}$	$1.68^{+0.22}_{-0.28}$	-0.32	1	$2.95^{+0.20}_{-0.55}$	151.8 ± 21.6	$10.54^{+0.53}_{-1.14}$
104	...	...	$1.68^{+0.18}_{-0.29}$	...	2	$1.68^{+0.18}_{-0.29}$	134.3 ± 18.0	...
105	...	$0.67^{+0.08}_{-0.12}$	$2.09^{+0.72}_{-0.40}$	0.85	0	$2.09^{+0.72}_{-0.40}$	143.9 ± 17.0	...
106	...	...	$2.75^{+1.66}_{-0.83}$	...	2	$2.75^{+1.66}_{-0.83}$	6.2 ± 0.0	...

redshift.

In the lower panel of Figure 4.4 I compare the redshift distribution of the deep 850 μm selected sample studied here with example redshift distributions from previous studies. Although my sample is somewhat deeper/fainter than the sub-mm samples studied by previously by Chapman et al. (2005) and Michałowski et al. (2012b), the redshift distributions displayed by the optically-identified subset of sources from each study are remarkably consistent; I find z = 1.97$\pm$0.09, while Chapman et al. (2005) reported z = 2.00 $\pm$ 0.09, and Michałowski et al. (2012b) reported z = 2.00 $\pm$ 0.10.

While inclusion of my adopted values of z_{LW} for my unidentified sources moves the mean redshift up to at least z $\simeq$ 2.4, it is clear that the redshift distribution found here cannot be consistent with that found in the previous Chapter for the subset of very bright sub-mm/mm sources in the COSMOS field (see also Smolčić et al. 2012), for which z = 3.53 $\pm$ 0.19. This is not due to any obvious inconsistency in redshift estimation techniques, as can be seen from Table 4.5 (discussed further below), and indeed the analysis methods used here are near identical to those employed in the previous Chapter. Rather, as discussed in that Chapter, there must either be a strong bias for the most luminous sub-mm/mm sources (i.e. $\bar{S}_{850\mu\mathrm{m}} > 8$ mJy) to lie at significantly higher redshifts than the more typical sources studied here, or the COSMOS bright source sample selected by Younger et al. (2007, 2009) and Smolčić et al. (2012) must be unusually dominated by a high-redshift over-density in the COSMOS field.

4.4.4 Previous literature associations

Five of the sub-mm sources in my SCUBA-2 COSMOS sample have been previously studied in some detail, and so I compare my ID positions and redshifts with the pre-existing information in Table 4.5. Four of these bright sources were previously the subject of interferometric mm/sub-mm observations, yielding robust optical identifications and photometric redshifts in good agreement with my results. The source separation for SC850-29 (2.03 arcsec) is perfectly plausible since this is the separation between the original AzTEC single-dish coordinate and my chosen ID. The small separations between the positions of my adopted IDs for SC850-6 and 31 and their mm/sub-mm interferometric centroids confirm the reliability of my ID selection. For SC850-1 the rather large source separation

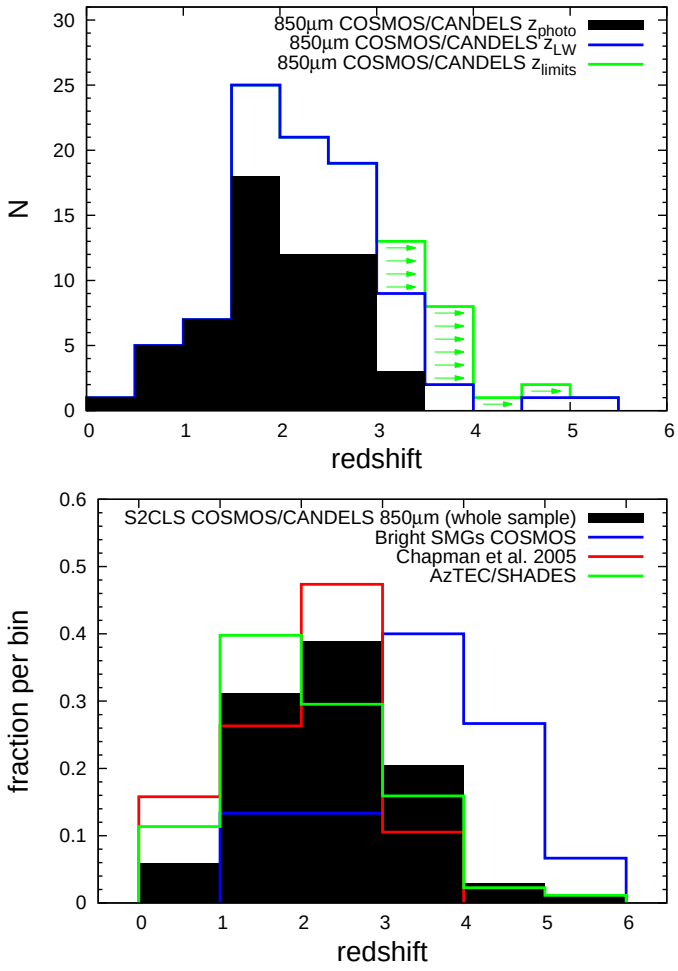

Figure 4.4: ***Upper panel:*** *The redshift distribution of my full 106-source S2CLS 850 μm sample in the COSMOS field (Table 4.4). The black area shows the distribution for the 58 sources with confirmed spectroscopic or optical photometric redshifts with the mean value of* $\bar{z} = 1.97 \pm 0.09$. *The blue line depicts the 'black' sample with the addition of the 'long-wavelength' sources for which the redshifts were found from Herschel/SCUBA-2 data and the green arrows are the objects with redshift limits also derived from the 'long-wavelength' data for which no detection was found in Herschel bands. The mean redshift for the whole sample is* $\bar{z} = 2.38 \pm 0.09$. ***Lower panel:*** *Redshift distribution for the whole S2CLS COSMOS sample with overlaid distributions derived by Chapman et al. (2005) with* $\bar{z} = 2.00 \pm 0.09$, *and for the robust galaxy identifications in the AzTEC/SHADES survey presented by Michałowski et al. (2012b) with* $\bar{z} = 2.00 \pm 0.10$. *In addition I plot the redshift distribution of the sample of luminous (sub-)mm sources in the COSMOS field from the previous Chapter with* $\bar{z} = 3.53 \pm 0.19$.

Table 4.5: Five sources in my COSMOS sample that have been studied before. Four of them (the ones with z_{other}) were followed-up with the interferometric observations. The columns show respectively my ID, ID from previous work (full previous ID for the AzTEC source is AzTEC_J100025.23+022608.0), interferometric RA and Dec (single-dish coordinates for the AzTEC source where no interferometric follow-up was done), the separation between the interferometric ID (except AzTEC) and the optical ID found in this work, final redshifts (Table 4.4), the redshifts from previous works, and references.

ID SC850-	ID_{other}	RA /deg	Dec /deg	separation /arcsec	z	z_{other}	reference
1	MM1	150.0650	2.2636	2.62	$3.30^{+0.22}_{-0.14}$	$3.10^{+0.50}_{-0.60}$	Aravena et al. 2010
6	COSLA-35	150.0985	2.3653	0.13	$2.50^{+0.20}_{-0.15}$	$3.16^{+0.24}_{-0.26}$	Smolčić et al. 2012
14	COSLA-8	150.1064	2.2523	2.76	$2.18^{+0.17}_{-0.13}$	$1.90^{+0.11}_{-0.22}$	Smolčić et al. 2012
29	AzTEC	150.1051	2.4356	2.03	$2.41^{+0.24}_{-0.26}$	...	Scott et al. 2008
31	COSLA-38	150.0525	2.2456	0.27	$2.47^{+0.08}_{-0.12}$	$2.44^{+0.12}_{-0.11}$	Smolčić et al. 2012

of 2.62 arcsec supports our rejection of the optical ID for this source. Finally, the rather large separation for SC850-14 clearly casts doubt on my adopted ID, but in this case z_p is very similar to z_{LW} (which, of course, is why I did not reject the ID) and so the final redshift distribution is unaffected by whether or not the ID is correct.

4.5 Colours and physical properties

4.5.1 850/450 colour versus redshift

Figure 4.5 shows the SCUBA-2 colours (S_{850}/S_{450}) of my sources as a function of their redshifts. Green points represent robust optical IDs for which redshifts have been found using the optical/near-IR photometry. Red points depict the optical IDs that were rejected using the method of Section 4.4.2 (and plotted at their z_{LW}) and the blue points are the objects without the optical IDs all of which have redshifts found using the 'long-wavelength' data. The three black curves represent the evolution of the sub-mm colour with redshift for the SED of the M51 (T_d = 25 K, Silva et al. 1998), average SED template of SMGs from Michałowski et al. (2010b) (T_d = 35 K) and the SED of the Arp 220 (T_d = 45 K). The black points with the thick error bars are the median values for the 'green' data (black solid error bars) and for the 'red+blue' data (black dashed error bars). It can be seen that the sub-mm colour correlates with the redshift,

with the Spearman rank coefficient of 0.465, rejecting the null hypothesis of no correlation with a significance value of $p < 10^6$.

It is clear that sources for which redshifts were found using the 'long-wavelength' data (red+blue points, dashed error bars) follow roughly the 35 K black curve. This is caused by the fact that when finding these redshifts the average SED from Michałowski et al. (2010a) with the effective $T_d = 35$ K was used. The apparent dispersion of red+blue sources about the 35 K line is caused simply by the addition of the *Herschel* data. What is interesting however, is the fact that the green points, for which redshifts were found from the optical/near-IR data, also follow the similar track. This justifies the usage of the 35 K average SED template for the 'long-wavelength' sample. The median redshifts for the 'green' data are slightly lower that for the 'red+blue' data. This is most likely the result of the bias present in the process of identifying the optical counterparts to the sub-mm data. As explained in Section 4.4.2 the optical IDs that were rejected (and most galaxies with no IDs at all) lie at relatively higher redshifts (Figure 4.3).

The minimum dust temperature of a galaxy is set by the Cosmic Microwave Background (CMB) at the mean redshift of SMGs $\simeq 2$: $T_d = 3 \times 2.72\,\mathrm{K} \simeq 8\,\mathrm{K}$. Clearly there are no sources in my sample with such low temperatures (empty top-left area of Figure 4.5). Interestingly there are also no sources with temperatures significantly higher than 45 K (empty bottom-right area of Figure 4.5). It has been found in the previous works that the mean dust temperatures of SMGs are at the approximate level of 35 K (Kovács et al. 2006; Coppin et al. 2008; Michałowski et al. 2010b,a) which is in perfect agreement with my findings. Magnelli et al. (2012) found a slightly higher average dust temperature of ~ 40 K which likely comes from the bias introduced by the *Herschel* PACS-SPIRE detection requirement.

Finally, the mean value of redshifts for all sources with $S_{850}/S_{450} > 0.5$ is $\bar{z} = 2.99 \pm 0.18$ with the minimum value of 1.95. This is a convenient result as it gives a very neat way of selecting high-redshift SMGs based only on SCUBA-2 850 and 450 μm data, provided the 450 μm data is deep enough.

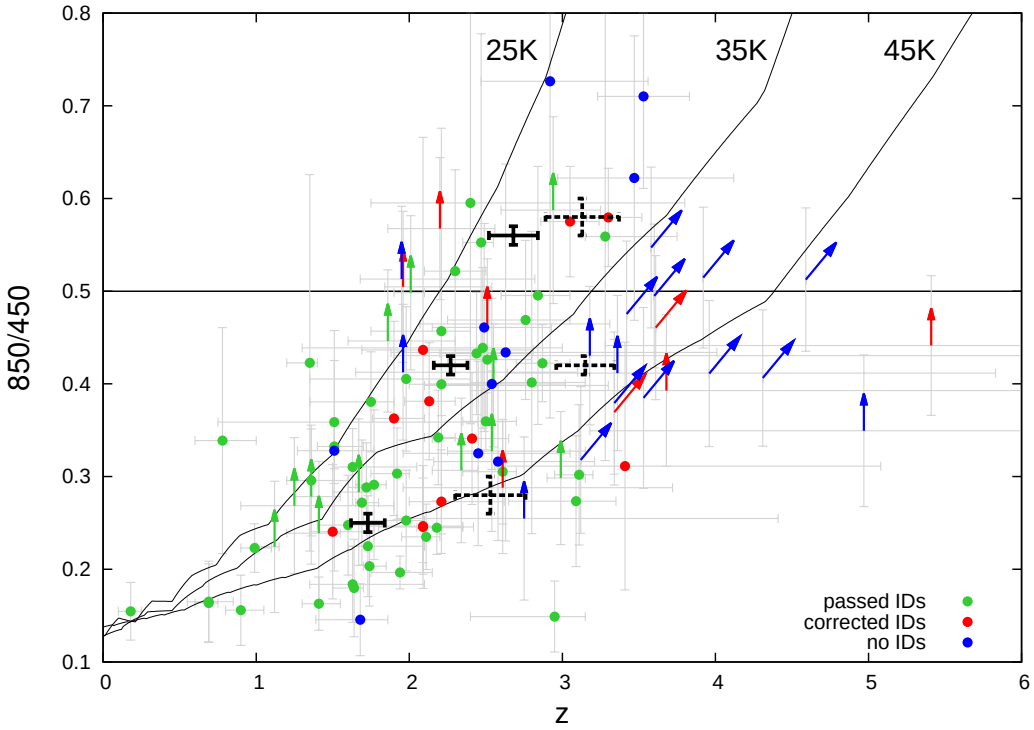

Figure 4.5: *The SCUBA-2 colour (S_{850}/S_{450}, Table 4.1) plotted against my final redshifts (Table 4.4). The green points are the sources with confirmed optical IDs (as in Section 4.4.2) and spectroscopic plus optical/near-IR photometric redshifts. The red points are the objects initially assigned an optical ID but rejected by the corrections of the Section 4.4.2 and the blue points are the sources without any IDs all of which have redshifts found using Herschel/SCUBA-2 'long-wavelength' data. The arrows represent the limits. The black solid curves show the evolution of the sub-mm colour with redshift for the SED of the M51 ($T_d = 25\,K$, Silva et al. 1998), average SED template of SMGs from Michałowski et al. (2010a) ($T_d = 35\,K$) and the SED of the Arp 220 ($T_d = 45\,K$). The black points with thick solid and dashed error bars are the median values for the 'green' data and the 'red+blue' data respectively. The 'red+blue' data has redshifts found from the same SED from which the 35 K curve was extracted and therefore roughly follows that curve. The 'green' data however has optical photometric redshifts and shows that the choice of the dust temperature for my average SED template was appropriate. The correlation between the SCUBA-2 colour and redshift can be clearly seen with the Spearman rank coefficient of 0.465, rejecting the null hypothesis of no correlation with a significance value of $p < 10^{-6}$. The selection of sources with SCUBA-2 colour > 0.5 would yield a sample with $\bar{z} = 2.99 \pm 0.18$ and $z_{min} = 1.95$.*

4.5.2 Stellar masses and star-formation rates

For the 58 SCUBA–2 sources for which I have secure optical identifications+redshifts (after the sample refinement discussed in Section 4.4.2) I was able to use the results of the SED fitting (used to determine z_p) to obtain an estimate of the stellar mass, $M_\star$, for each galaxy. The derived stellar masses were based on the models of Bruzual & Charlot (2003) assuming double–burst star–formation histories (see Michałowski et al. 2012b), and I assumed a Chabrier (2003) IMF.

I was also able to estimate the star–formation rate, SFR, for each of these sources by using the average long–wavelength SED of the sub–mm galaxies from Michałowski et al. (2010a), applied to the 850 μm flux–density of each source at the relevant photometric redshift, to estimate the far–infrared luminosity of each source.

The resulting SFRs are plotted against $M_\star$ in Fig. 4.6. In the main plot, for clarity I have confined attention to the sources with $z_p > 1.5$ because, as shown in the inset plot, due to the impact of the negative K–correction at 850 μm, at $z > 1.5$ the flux–density limit of the current sample essentially equates to SFR $\simeq 100$ M$_\odot$ yr^{-1} at all higher redshifts. In this plot I also show the position of the 'Main-Sequence' (MS) of star–forming galaxies, as deduced at $z \simeq 2.5$ by Elbaz et al. (2011), and at $z > 1.5$ by Rodighiero et al. (2011). The sensitivity of my deep SCUBA–2 sample to values of SFR as low as 100 M$_\odot$ yr^{-1} means that, for objects with stellar masses $M_\star > 7 \times 10^{10}$ M$_\odot$, I was able for the first time to properly compare the positions of sub–mm selected galaxies on the SFR:$M_\star$ plane with the MS in an unbiased manner.

4.5.3 Specific star-formation rates

In Figure 4.7, I collapse the information shown in Figure 4.6 into distributions of specfic SFR. The black histogram shows the distribution of sSFR for the whole robustly-identified sample of SCUBA-2 sources at $z > 1.5$, but this can be subdivided by mass into the sub-sample with $M_\star > 7 \times 10^{10}$ M$_\odot$ (blue histogram) and the complementary sub-sample of sources with $M_\star < 7 \times 10^{10}$ M$_\odot$ (red histogram). Referring back to Figure 4.6, it can be seen that, at lower stellar masses the measurement of sSFR is inevitably biased high by the effective SFR limit > 100 M$_\odot$ yr^{-1} , and so it is difficult to tell if these SCUBA-2 sources

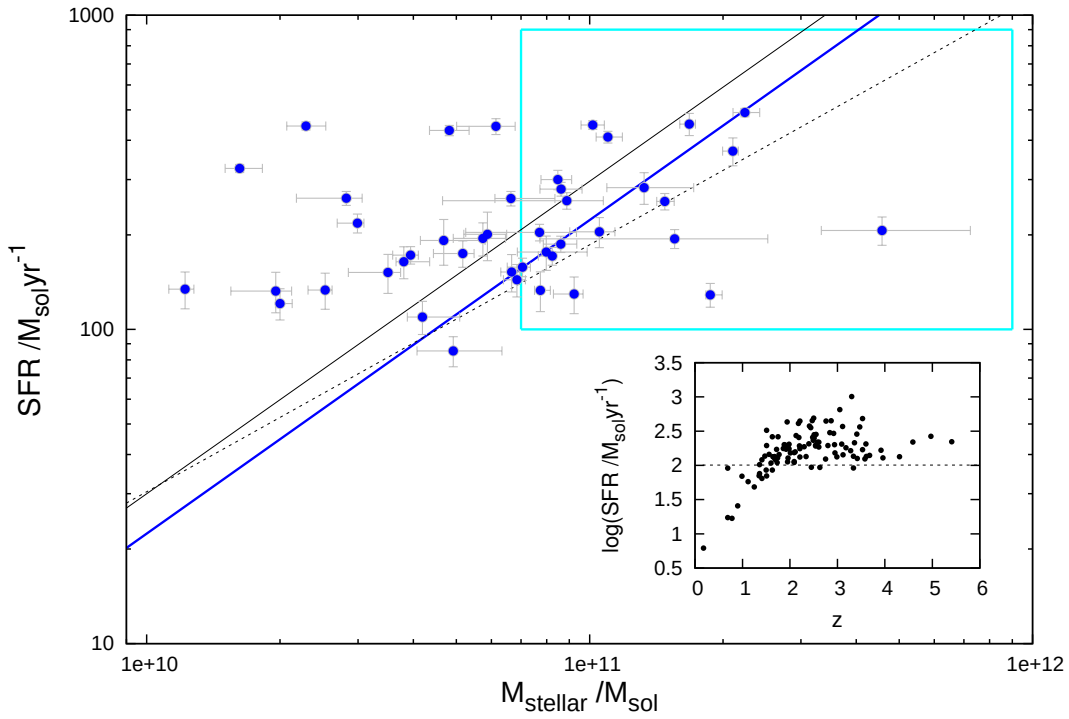

Figure 4.6: *The star–formation rate (SFR) as a function of stellar mass ($M_\star$) for the robustly identified SCUBA–2 sources with $z > 1.5$. As can be seen from the inset plot, due to the impact of the negative K–correction at 850 μm, for $z > 1.5$ the flux–density limit of the current sample essentially equates to SFR $\simeq 100\,M_\odot$ yr^{-1} . The black solid line in the main plot shows the position of the so–called 'Main–Sequence' (MS) of star–forming galaxies at $z \simeq 2.5$ as deduced by Elbaz et al. (2011), while the black dashed line depicts the MS at $z > 1.5$ as given by Rodighiero et al. (2011). The sensitivity of my deep SCUBA–2 sample to values of SFR as low as 100 $M_\odot$ yr^{-1} means that, for objects with stellar masses $M_\star > 7 \times 10^{10}\,M_\odot\,yr^{-1}$ (i.e., inside the cyan rectangle), I am able for the first time to properly compare the positions of sub–mm selected galaxies on the SFR:$M_\star$ plane with the MS in an unbiased manner. As shown in Fig. 4.7, I find that, confining my attention to $M_\star > 7\times10^{10}\,M_\odot\,yr^{-1}$, the SCUBA–2 sources display a Gaussian distribution in specific SFR peaking at $sSFR = 2.25 \pm 0.19\,Gyr^{-1}$ (corresponding to the main sequence shown here by the blue solid line), demonstrating that the SCUBA–2 sources lie on the high–mass end of the normal star–forming MS at $z \simeq 2$.*

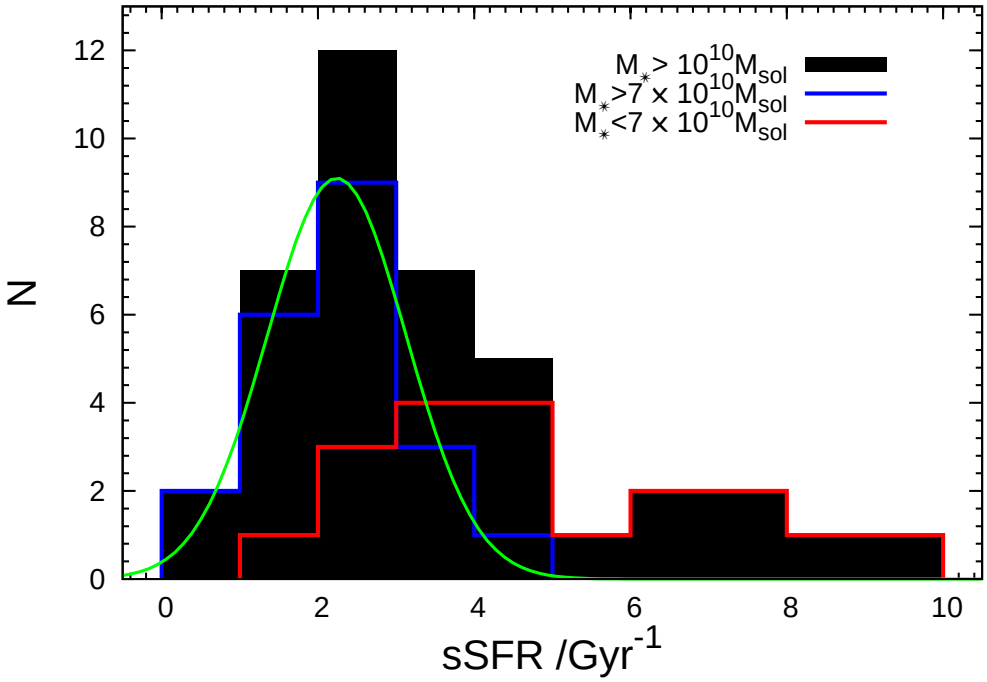

Figure 4.7: *The distribution of specific star–formation rate, sSFR, as derived from the values of SFR and $M_\star$ plotted in Fig. 4.6. The black histogram shows the distribution for the whole robustly–identified sample of SCUBA–2 sources at* $z > 1.5$ *plotted in Fig. 4.6, but this can be subdivided by mass into the sub–sample with* $M_\star > 7 \times 10^{10}\, M_\odot$ *(blue histogram) and the complementary sub–sample of sources with* $M_\star < 7 \times 10^{10}\, M_\odot$ *(red histogram). It can be seen that, for the high–mass sample, in which SFR is not biased by the effective flux–density limit of the deep SCUBA–2 survey, the distribution resembles closely a Gaussian peaked at* $sSFR = 2.25\, Gyr^{-1}$ *with* $\sigma = 0.89\, Gyr^{-1}$*, as shown by the green curve. This demonstrates that, where their distribution on the SFR:*$M_\star$ *plane can now finally be probed in an unbiased manner, the SCUBA–2 galaxies lie on the MS of star–forming galaxies at* $z \simeq 2$*.*

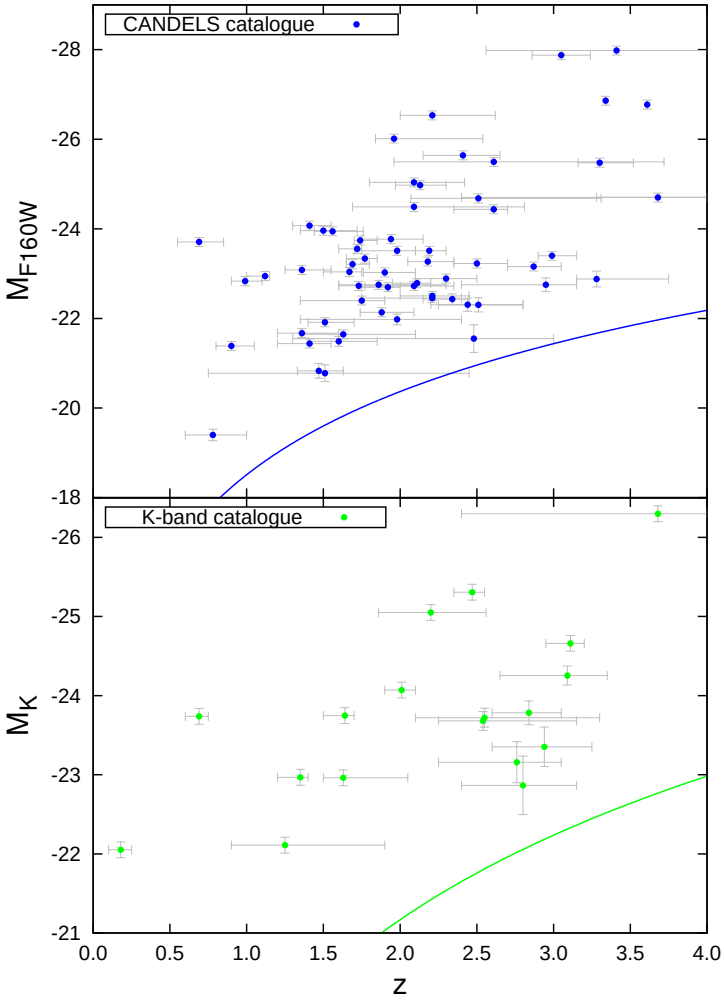

Figure 4.8: *The CANDELS H-band (top panel) and the UltraVISTA K_s-band (bottom panel) absolute magnitudes plotted as a function of redshifts. The blue and green solid curves represent the detection limits of my CANDELS H-band and the UltraVISTA K_s-band selected catalogues respectively. It can be seen that all the sources are well above the detection limits and therefore the sample is not biased towards high* $M_\star$ *(low sSFRs).*

genuinely lie above the MS, or if I am simply sampling the high-sSFR tail of the distribution around the MS. However, at $M_\star > 7 \times 10^{10}$ $M_\odot$ it is clear that the SFR limit would not produce a significantly biased sampling of the distribution of galaxies on the MS. In essence, because of the depth of the SCUBA-2 imaging, for sub-mm selected galaxies with $M_\star > 7 \times 10^{10}$ $M_\odot$ I should now be able to perform the first unbiased estimate of their sSFR at $z \simeq 1.5 - 3$.

In fact, for the high-mass sub-sample, in which SFR is not biased by the effective flux-density limit of the deep SCUBA-2 survey, the distribution of sSFR resembles closely a Gaussian peaked at sSFR = 2.25 Gyr^{-1} with $\sigma = 0.89$ Gyr^{-1} . This Gaussian fit is shown by the green curve in Figure 4.7, and is completely consistent with the normalization and scatter ($\simeq 0.25$ dex) in the MS reported by Rodighiero et al. (2011).

Finally, to check whether I could be biased towards high-mass (and hence low sSFR) objects at high redshift, as a consequence of the flux-density limits of my optical/near-infrared catalogues, I plot the near-infrared (CANDELS H-band and UltraVISTA K_S-band) absolute magnitudes of my source IDs against redshift in Figure 4.8. The measured values are generally not close to the detection limits of my catalogues and therefore I conclude that the sample is not biased against high sSFRs at high redshifts on account of an inability to detect low-mass galaxies.

I conclude, therefore, within the stellar mass range where I am able to sample the distribution of sSFR in an unbiased way, the sub-mm sources uncovered from this deep SCUBA-2 850 μm image, display exactly the mean sSFR and scatter expected from galaxies lying on the high-mass end of the star-forming main-sequence at $z \simeq 2$.

There has been a lot of debate in the literature about the dependence of the sSFR on the redshift (Stark et al., 2009; González et al., 2010; McLure et al., 2011; Karim et al., 2011; Elbaz et al., 2011). While there seems to be a consensus on the shape of that correlation at $z < 2$, where sSFR decreases monotonically with time, the behaviour at $z > 2$ is somewhat less obvious. To investigate how the SMGs fit into this scenario, I plot in Figure 4.9 the mean values of the sSFR as a function of redshift for my unbiased sample together with the sSFR values from the previous chapter alongside the up-to-date results for normal star-forming galaxies (Damen et al., 2009; Noeske et al., 2007; Daddi et al., 2007; Reddy et al., 2012b; Stark et al., 2009; González et al., 2010; Gonzalez et al., 2012; Bouwens

et al., 2012; Stark et al., 2013). It is obvious from that plot that SMGs exhibit normal star-forming behaviour (as oppose to the 'starburst' scenario) and that their enormous SFRs are simply caused by their huge stellar masses. In addition it can be seen that indeed, at least up to z $\sim$ 3, sSFR exhibits a minor increase with redshift. At $z > 3$ the issue is more complicated because at these redshifts, the different treatment of the contribution to the SED from the emission lines causes a lot of scatter in the inferred values of the sSFR.

4.5.4 The 'main sequence' and its evolution

Given that the SCUBA–2 sources seem to, in effect, define the high–mass end of the star–forming main sequence (MS) of galaxies over the redshift range probed by my sample (i.e. $1.5 < z < 3$) it is of interest to explore how the inferred normalization and slope of the MS as derived here compares to that derived from other independent studies based on very different selection techniques over a wide range of redshifts.

Thus, in Fig. 4.9 I divide my (high–mass) sample into three redshift bins to place the inferred evolution of sSFR within the wider context of studies spanning virtually all of cosmic time (i.e. $0 < z < 8$).

The first obvious striking feature of Fig. 4.9 is that my new determination of average sSFR over the redshift range $1.5 < z < 3$ follows very closely the trend defined by the original studies of the MS undertaken by Noeske et al. (2007) and Daddi et al. (2007). Since such studies were based on very different samples, sampling lower stellar masses, this result also implies that I find no evidence for a high–mass turnover in the MS at these redshifts (i.e. a decline in sSFR, or change in the slope of the MS above some characteristic mass). Evidence for a decline in the slope of the MS above a stellar mass $\log(M_{\star}/M_{\odot}) \simeq 10.5$ has been presented by several authors (e.g. Whitaker et al. 2012, 2014; Tasca et al. 2014) but these results are based on optical/near–infrared studies, and suffer from two problems. First, as recently discussed by Johnston et al. (2015), the results of optically–based studies depend crucially on how one selects star–forming galaxies, and colour selection can yield an apparent turn–over in the MS at high masses simply due to increased contamination from passive galaxies/bulges. Second, at the high SFRs of interest here, it is well known that SED fitting to optical–infrared data struggles to capture the total star–formation rate because the vast majority of the

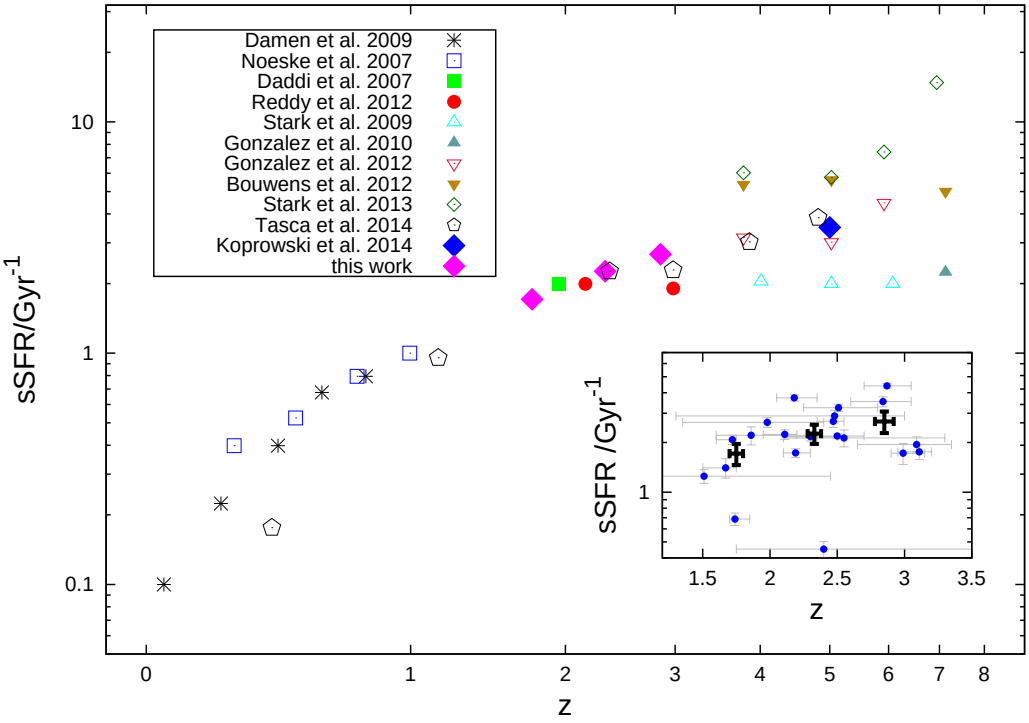

Figure 4.9: *Mean sSFR as a function of the redshift. The results of this work (inset plot with the mean values represented by black points with thick error bars) calculated using the unbiased sample (from inside the cyan rectangle in Fig. 4.6) are shown by the magenta diamonds. It can be seen that the evolution of characteristic sSFR (equivalent to the normalization of the MS) inferred from the SCUBA–2 galaxies is in excellent accord with the results from many other studies.*

star–formation activity in high–mass galaxies is deeply obscured. It is therefore interesting that other recent studies of the MS based on far–infrared/sub–mm data also find no evidence for a high mass turnover in the MS at high–redshift; for example Schreiber et al. (2015), from their Herschel stacking study of the MS, report that any evidence for a flattening of the MS above $\log(M_\star/M_\odot) \simeq 10.5$ becomes less prominent with increasing redshift and vanishes by $z \simeq 2$.

As is clear from Fig. 4.6, the present study does not provide sufficient dynamic range to enable a new measurement of the precise value and redshift evolution of the slope of the MS (see Speagle et al. 2014 for results from a compilation of 25 studies). Nevertheless, the advantages of sub–mm selection for an unbiased study of the high–mass end of the MS are clear (i.e. no contamination from

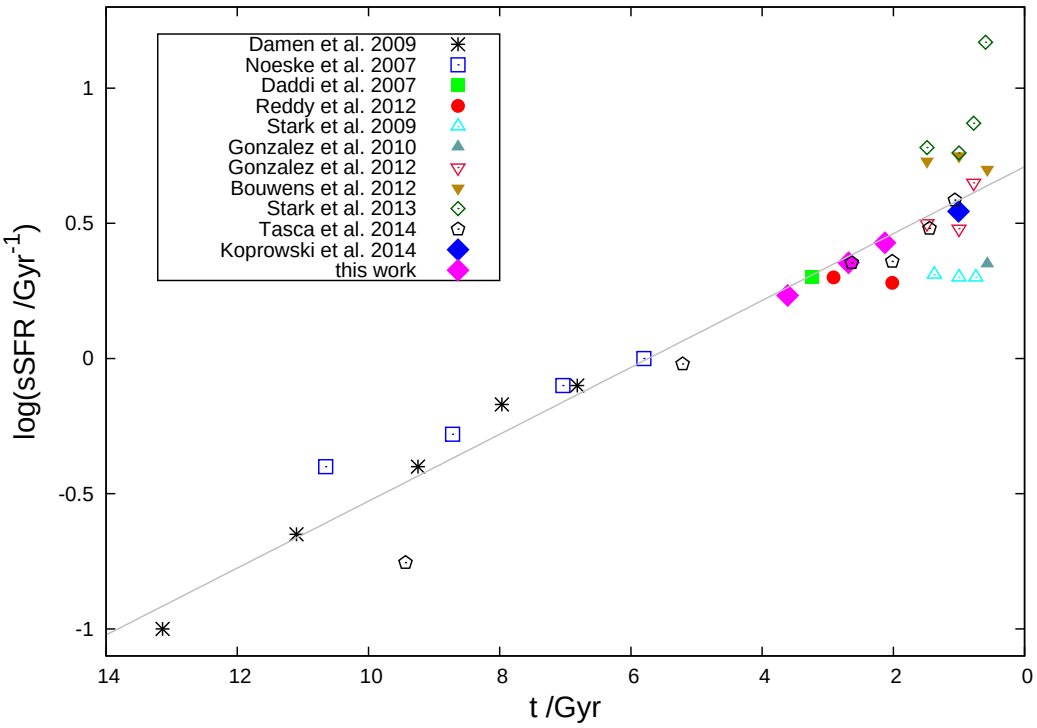

Figure 4.10: *Mean sSFR as a function of cosmic time. Data/symbols are as in Fig. 4.9. The straight–line fit to the data has the form* $log_{10}(sSFR/Gyr^{-1}) = -0.12(t/Gyr)+0.71$.

passive galaxies, and a complete census of dust-enshrouded star formation), and my results show that the slope of the MS must remain close to unity up to stellar masses $M_{\star} \simeq 2 \times 10^{11}$ $M_{\odot}$ at $z \simeq 2 - 3$. I note that it is sometimes claimed that studies of the MS based on far–IR or sub–mm selected samples yield vastly different determinations of the SFR-$M_{\star}$ relation from the MS (e.g. Rodighiero et al. 2014), but it needs to be understood that this is because previous studies based on such samples did not reach sufficient sensitivity in SFR (for individual objects) to properly sample the MS at high redshift. As emphasized in Section 4.5.3, and in Fig. 4.6, even the deepest ever 850 μm survey analysed here only enables me to properly explore the MS at the very highest masses, due to the effective SFR sensitivity limit; clearly the sources detected in the present study at lower masses are outliers from the MS, and can only provide indirect information of the scatter in the MS at masses of a few $\times 10^{10}$ $M_{\odot}$, rather than its normalization.

Finally, looking to higher redshifts, Fig. 4.9 shows that the present study does not provide useful information on characteristic sSFR beyond $z \simeq 3$, but also demonstrates that the trend indicated here over $1.5 < z < 3$ extends naturally out to my previous determination of sSFR in very high–redshift sub–mm/mm galaxies at $z \simeq 5$ (Koprowski et al., 2014). There is currently considerable debate over the normalization of the MS at $z \simeq 4$, due in large part to uncertainty over the impact of nebular emission lines on the estimation of stellar masses (see e.g. Stark et al. 2013; Smit et al. 2014). However, the sub–mm studies of high–mass star–forming galaxies are clearly consistent with the results of several existing studies (e.g. Steinhardt et al. 2014), and (despite their supposedly extreme star–formation rates) sub–mm–selected galaxies provide additional support for the presence of a 'knee' in the evolution of sSFR around $z \simeq 2$ (as originally suggested by the results of González et al. 2010; Gonzalez et al. 2012). The ability of theoretical models of galaxy formation to reproduce this transition remains the subject of continued debate, with smooth cold accretion onto dark matter halos leading to expectations that sSFR should rise $\propto (1+z)^{2.5}$ (Dekel et al., 2009, 2013; Faucher-Giguère et al., 2011; Rodriguez-Puebla et al., 2015), and a range of hydrodynamical and semi–analytic models of galaxy formation yielding predictions of characteristic sSFR at $z \simeq 2$ that fall short of the results shown in Fig. 4.9 by a factor of 2 - 6 (see discussion in Johnston et al. 2015, and references therein). However, in Fig.

4.10 I show that when the redshift axis is re–cast in terms of cosmic time, there is really no obvious feature in the evolution of characteristic sSFR. Rather, the challenge for theoretical models is to reproduce the apparently simple fact that $\log_{10}$(sSFR) is a linear function of the age of the Universe, at least out to the highest redshifts probed to date.

4.6 Summary

I have investigated the multi–wavelength properties of the galaxies selected from the deepest 850 μm survey undertaken to date with SCUBA–2 on the JCMT. This deep 850 μm imaging was taken in parallel with deep 450 μm imaging in the very best observing conditions as part of the SCUBA–2 Cosmology Legacy Survey. A total of 106 sources ($> 5\sigma$) were uncovered at 850 μm from an area of $\simeq 150$ arcmin^2 in the centre of the COSMOS/UltraVISTA/CANDELS field, imaged to a typical depth of $\sigma_{850} \simeq 0.25$ mJy. Aided by radio, mid–IR, and 450 μm positional information, I established statistically–robust galaxy counterparts for 80 of these sources ($\simeq 75\%$).

By combining the optical–infrared photometric redshifts, z_p, of these galaxies with independent 'long–wavelength' estimates of redshift, z_{LW} (based on Herschel/SCUBA–2/VLA photometry), I have been able to refine the list of robust galaxy identifications. This approach has also enabled me to complete the redshift content of the whole sample, yielding $\bar{z} = 2.38 \pm 0.09$, a mean redshift comparable with that derived from all but the brightest previous sub–mm samples.

Because my new deep 850 μm selected galaxy sample reaches flux densities equivalent to star–formation rates SFR $\simeq 100$ M$_\odot$ yr^{-1}, I have been able to confirm that sub–mm galaxies form the high–mass end of the 'main sequence' (MS) of star–forming galaxies at $z > 1.5$ (with a mean specific SFR of sSFR $= 2.25 \pm 0.19$ Gyr^{-1} at $z \simeq 2.5$). My results are consistent with no significant flattening of the MS towards high stellar masses at these redshifts (i.e. SFR continues $\propto$ M$_\star$), suggesting that reports of such flattening are based on contamination by passive galaxies/bulges, and/or underestimates of dust–enshrouded star–formation activity in massive star–forming galaxies. However, my findings contribute to the growing evidence that average sSFR rises only

slowly at high redshift, from sSFR $\simeq$ 2 Gyr^{-1} at z $\simeq$ 2 to sSFR $\simeq$ 4 Gyr^{-1} at z $\simeq$ 5. These results are consistent with a rather simple evolution of global characteristic sSFR, in which $\log_{10}$(sSFR) is a linear function of the age of the Universe, at least out to the highest redshifts probed to date.

Chapter 5

(Sub-)millimetre Galaxy Luminosity Function

5.1 Introduction

One of the main goals of observational astronomy is to understand the origin and growth of the galaxies we observe today. In order to do so one must learn about the time evolution of galaxies selected at different wavelengths. The useful quantity that allows this is the luminosity function (LF), since it gives information about the statistical nature of galaxy evolution. Calculated at different redshifts, the LF describes the number of sources with given luminosities per comoving volume at that redshift and as such is the most direct way of exploring the evolution of a given galaxy population.

It is now well known that approximately half of the starlight in the Universe is absorbed by dust and re-emitted in the IR-sub(mm) (Dole et al., 2006). Therefore if one wants to complete picture of the star formation across the cosmic time, the dusty galaxies selected at IR-(sub)mm must be investigated. However, due to the large beam sizes the calculation of the bolometric IR LF has been limited in redshift. The *Infrared Astronomical Satellite* (*IRAS*; Neugebauer et al. 1984) and the *Infrared Space Observatory* (*ISO*; Kessler et al. 1996) allowed the determination of the IR LF only out to $z \leq 0.3$ (Saunders et al., 1990) and $z < 1$ (Pozzi et al., 2004), respectively. *Spitzer* 24 μm data extended the redshift range out to $z \sim 2$ (e.g. Le Floc'h et al. 2005; Caputi et al. 2007; Rodighiero et al. 2010). *Spitzer* 70 μm data allowed the determination of the FIR LF out to $z \sim 1.2$

(Magnelli et al., 2009; Patel et al., 2013), though Magnelli et al. (2011) reached z $\simeq$ 2.3 with stacking. Since the rest-frame IR SED peaks at $\sim$ 100 μm, in order to probe the high redshift galaxies one needs to observe at (sub)mm wavelengths. The single-dish beam sizes of $\sim 15-20$ arcsec and the shallow depth of (sub)mm maps (SFR $\simeq 1000\,\mathrm{M_\odot\,yr^{-1}}$) limits the FIR LFs for the sources selected at these wavelengths to the identification of the galaxies at the very bright end of the LF (Chapman et al., 2005; Wardlow et al., 2011; Roseboom et al., 2012b).

Armed with the S2CLS deep COSMOS data investigated in the previous Chapter (SFR $> 100\,\mathrm{M_\odot\,yr^{-1}}$) I have decided to estimate the contribution of the (sub)mm-selected galaxies to the global star formation rate density (SFRD) out to redshift $\sim$ 4. The S2CLS deep COSMOS and wide UDS data (Table 2.1) includes (sub)mm galaxies with a range of 850 μm fluxes $\sim 1.5-15$ mJy and redshifts $\sim 1-4.5$. This gives a sufficiently wide redshift and 850 μm flux dynamic range for these kind of calculations to be attempted.

The rest of this Chapter is structured as follows. In the next Section, I will describe the data used. In Section 5.3, the redshift distributions for each sample will be shown. The methodology used for the determination of the LFs will be presented in Section 5.4, and the calculation of the contribution of the (sub)mm-selected sources to the global SFRD in Section 5.5. Finally, I will discuss the results in Section 5.6 and summarize my findings in Section 5.7.

Throughout I use the AB magnitude system (Oke, 1974), and assume a flat cosmology with $\Omega_m = 0.3, \Omega_\Lambda = 0.7$ and $H_0 = 70$ km s^{-1}Mpc^{-1}.

5.2 Data

5.2.1 (Sub)mm data

The deepest (sub)mm data used here is the S2CLS deep COSMOS data from the previous Chapter. It is the 850 μm imaging of the central $\simeq$ 150 arcmin^2 of the COSMOS/UltraVISTA field. The root-mean-square (RMS) noise of this map is $\simeq$ 0.25 mJy and it contains 106 sources with signal-to-noise ratio (SNR) of > 5 and mean 850 μm flux density of $\bar{S} = 3.1$ mJy (details in Section 4.2.1). To extend the luminosity range of the sample, I added the $\simeq$ 0.58 deg^2 S2CLS wide UDS data with $\sigma_{850} \simeq 1.2$ mJy, where 283 sources where detected at 850 μm with SNR > 3.5 and $\bar{S} = 5$ mJy (details of the map–making process are in

Table 5.1: *The (sub)mm data used for the determination of the IR LFs. The columns show respectively the name of the field, the detection wavelength, the area in deg^2, the 1σ RMS depth, the number of sources detected and the minimum SNR of the detectections.*

Field	detection wavelength	area /deg^2	RMS depth /mJy	number of sources	SNR
S2CLS deep COSMOS	850 μm	0.042	0.25	106	> 5
S2CLS wide UDS	850 μm	0.58	1.2	283	> 3.5

Geach et al. 2013). Table 5.1 summarizes the data used here and Figure 2.2 in Chapter 2 shows their relative sizes.

5.2.2 Completeness of the (sub)mm data

The completeness for the S2CLS deep COSMOS data is plotted in Figure 4.2 with all the calculations explained in Subsection 4.2.1. For the S2CLS wide UDS field, the completeness was estimated by comparing the number counts determined for both S2CLS fields (i.e. COSMOS deep and UDS wide). The number counts were calculated by summing the number of sources in a given flux range and dividing by the area of the field and by the flux–density bin size (Figure 5.1). It can be seen that, for overlapping flux densities, only the faintest S2CLS wide UDS bin ($4 - 5$ mJy) shows a disagreement between both number counts. For the S2CLS deep COSMOS field, the completeness at $S_{850} > 4$ mJy, as seen in Figure 4.2, is $\simeq 100\%$. This means that the completeness at $S_{850} = 4 - 5$ mJy for the S2CLS wide UDS sample is:

$$C_{4.5} = \frac{dN/dS_{\rm UDS}}{dN/dS_{\rm COSMOS}} = \frac{246\,{\rm deg}^{-2}}{359\,{\rm deg}^{-2}} \simeq 69\%, \tag{5.1}$$

where both dN/dS values are from the $4 - 5$ mJy flux density bin. The completeness values for the remaining bright flux density bins in the S2CLS wide UDS sample are $\simeq 100\%$.

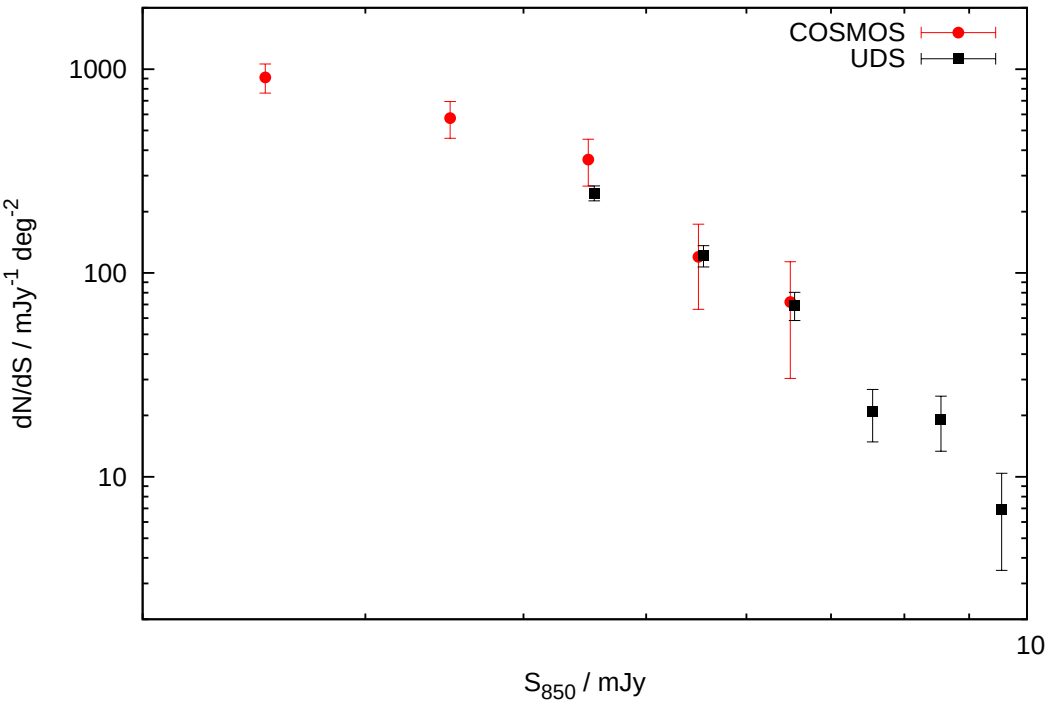

Figure 5.1: *Differential number counts for both S2CLS samples. In red are the values for the deep COSMOS sources and in black for the wide UDS galaxies. At* $S_{850} = 4.5$ *mJy the deep COSMOS sample is* $\simeq 100\%$ *complete (Figure 4.2), so to estimate the completeness for the UDS sources at that flux level I simply divided the UDS number counts by the COSMOS number counts (Equation 5.1). At higher UDS fluxes, as can be seen from this figure, the completeness is* $\simeq 100\%$.

5.2.3 Ancillary data

Multi-frequency data were used for the multi-wavelength identification as well as the SED fitting in order to determine the optical and 'long-wavelength' photometric redshifts (Section 5.3). For the S2CLS deep COSMOS field, the ancillary data are summarized in Section 4.2.2. The deep S2CLS pointing was selected to maximize the multi-wavelength data coverage which consists of the HST Cosmic Assembly Near-infrared Deep Extragalactic Legacy Survey (CANDELS) imaging (Grogin et al., 2011), the optical Canada-France-Hawaii Telescope Legacy Survey (CFHTLS; Gwyn 2012), the Subaru/Suprime-Cam z'-band (Taniguchi et al. 2007, Furusawa et al., in preparation) and UltraVISTA near-infrared data (McCracken et al., 2012). In addition, the *Spitzer* IRAC 3.6 μm and 4.5 μm, the *Spitzer* MIPS 24 μm and the Very Large Array (VLA) COSMOS Deep catalogues were used (Table 2.2). For the S2CLS wide UDS field, the optical data was obtained with Subaru/SuprimeCam (Miyazaki et al., 2002), as described in Furusawa et al. (2008). The near–infrared data in the UDS field are provided by the UKIRT Infrared Deep Sky Survey (UKIDSS; Lawrence et al., 2007; Cirasuolo et al., 2010). The mid–infrared *Spitzer* data are from the *Spitzer* Public Legacy Survey of the UKIDSS Ultra Deep Survey (SpUDS; PI: J. Dunlop) described in Caputi et al. (2011). This ancillary data were used by my collaborator Rebecca Bowler to construct the optical catalogues used for the determination of the optical photometric redshifts.

For both the S2CLS deep COSMOS and wide UDS fields the *Herschel* (Pilbratt et al., 2010) HerMES (Oliver et al., 2012) and the PACS Evolutionary Probe (PEP; Lutz et al. 2011) data obtained with the SPIRE (Griffin et al., 2010)) and PACS (Poglitsch et al., 2010) instruments, covering the entire COSMOS and UDS fields were used for the determination of the 'long-wavelength' redshifts (see Section 2.1 for details).

5.3 Redshifts

5.3.1 Multi-wavelength identification

For the S2CLS deep COSMOS sample, the identification procedure is explained in Section 4.3. 80 sources were identified in the optical, 18 of which were later

Table 5.2: *The success rate of the optical identification process for the samples used here. For both samples all the sources have been identified in IR Herschel bands.*

	S2CLS deep COSMOS	S2CLS wide UDS
N of sources	106	283
N of optical IDs	62	168
N of IR IDs	106	283

rejected based on the redshift refinement of Subsection 4.4.2. In short, the optical IDs for galaxies with optical photometric redshifts significantly different from the 'long-wavelength' photometric redshifts were rejected. The rationale for this is that, whenever the 'long-wavelength' redshift is significantly higher than the optical photometric redshift, the galaxy identified in the optical is not the submm source but simply a foreground object (a lens), or that it is in fact an AGN for which no AGN template was available during the determination of the optical photometric redshift, and therefore the estimate of that redshift was wrong. In addition, all the galaxies in the deep COSMOS sample were identified in the IR *Herschel* bands. The complete statistics for this sample is presented in Table 4.3.

For the S2CLS wide UDS sample both optical and 'long–wavelength' photometric redshifts were calculated. For the optical redshifts determination, the procedure was identical as for the deep COSMOS field. For the 'long–wavelength' redshifts, the IDs in the *Herschel* bands were required and found for all 283 sources. As explained in Section 4.2.2, the deconfusion of the UDS *Herschel* maps were performed following the same procedure as for the deep COSMOS sample. 100, 160, 250, 350 and 500 μm *Herschel* maps were used with beam sizes of 7.39, 11.29, 18.2, 24.9, and 36.3 arcsec, and 5σ sensitivities of 7.7, 14.7, 8.0, 6.6, and 9.5 mJy, respectively. To find the IR flux for each SCUBA-2 source, the 120-arcsec wide stamps from each *Herschel* map around each SCUBA-2 source were exctracted and the PACS (100, 160 μm) maps used to fit Gaussians with the FWHM of the respective map, centred at all radio and 24 μm sources located within these cut-outs, and at the positions of the SCUBA-2 optical identifications (IDs, or just sub-mm positions if no IDs were selected). Then, to deconfuse the SPIRE (250, 350 and 500 μm) maps in a similar way, the positions of the 24 μm sources detected with PACS (at $> 3\sigma$), the positions of all radio sources, and the

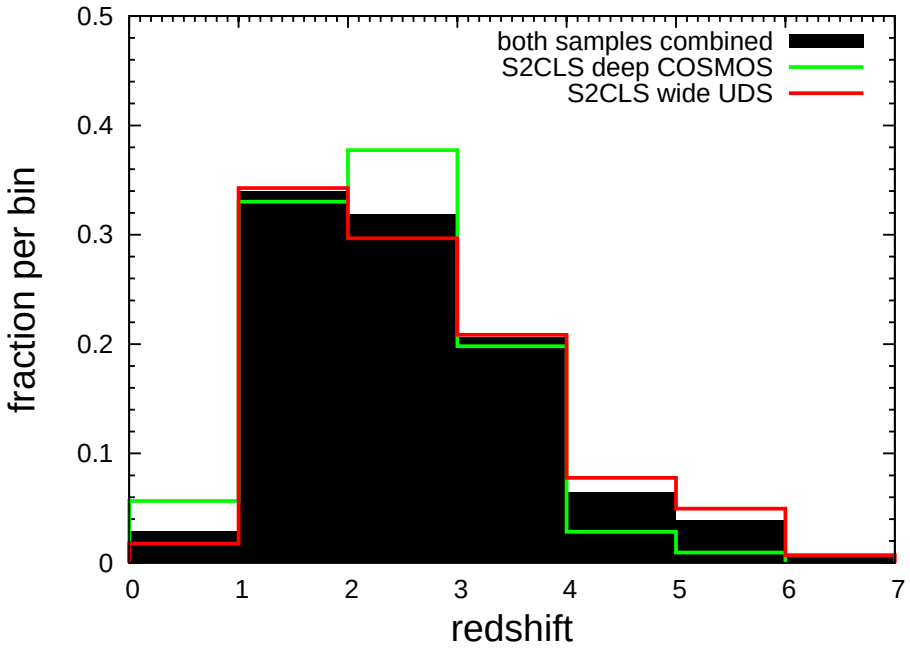

Figure 5.2: *Redshift distributions for the (sub)mm samples used here as indicated on the plot. The mean redshifts for the S2CLS deep COSMOS and wide UDS fields are* $\bar{z} = 2.38 \pm 0.09$ *and* $\bar{z} = 2.68 \pm 0.07$ *respectively and for both samples combined the mean redshift is* $\bar{z} = 2.50 \pm 0.05$*. In the case of the S2CLS deep COSMOS sample 62 optical and 44 'long-wavelength' photometric redshifts were used. For the S2CLS wide UDS sample 168 optical and 115 'long-wavelength' photometric redshifts were calculated (Table 5.2).*

SCUBA-2 ID positions were used.

5.3.2 Redshift distributions

For objects with confirmed optical IDs in the S2CLS deep COSMOS and wide UDS samples, the optical photometric redshifts were calculated using the method outlined in Section 2.3 (Table 4.4). In addition, with the help of the *Herschel* data, the 'long-wavelength' redshifts were calculated (Section 2.3) for both S2CLS deep COSMOS and wide UDS samples by fitting the average SMG template of Michałowski et al. (2010a) as explained in the second subsection of 2.3.

The redshift distributions for both samples used here are shown in Figure 5.2. The mean redshifts for the S2CLS deep COSMOS and wide UDS samples are $\bar{z} = 2.38 \pm 0.09$, $\bar{z} = 2.68 \pm 0.07$ respectively and for both samples combined it is

$\bar{z} = 2.50 \pm 0.05$. For the two S2CLS samples the redshift completeness is 100%, since either optical or 'long-wavelength' photometric redshifts were determined for all the sources.

5.4 The luminosity function

Calculations of the IR luminosity functions have been divided into three main steps. First, for every source, the maximum redshift, z_{max}, at which that source could have been detected in each field, given the survey's detection limit, was calculated (Subsection 5.4.1). Second, the maximum comoving volume that a given source could occupy in a given redshift bin, V_{max}, was determined (Subsection 5.4.2). Finally, the IR LFs were calculated (Subsection 5.4.3).

5.4.1 Calculation of z_{max}

I decided to calculate initially the luminosity functions at the rest-frame wavelength of 250 μm and then convert to the total IR ($8 - 1000\,\mu$m). To get the rest-frame 250 μm luminosity, L_{250}, I first calculated the rest–frame luminosity at the wavelength of $\lambda_s = \lambda_d/(1+z)$, where λ_d is the detection wavelength of the given survey and z is the redshift of the source, using the formula:

$$L_{\lambda_s} = S_{\lambda_d} \times 4\pi\, D_L^2/(1+z), \tag{5.2}$$

with S_{λ_d} being the flux at the detection wavelength and D_L the luminosity distance. The luminosity distance was calculated via:

$$D_L = R_0\, S_k(r) \times (1+z) = R_0\, r \times (1+z), \tag{5.3}$$

where R_0 is the value of the scale factor at the present and $S_k = r$ for flat Universe. Furthermore:

$$R_0\, dr = \frac{c}{H_0} \left[\Omega_v + \Omega_m (1+z)^3\right]^{-1/2} dz, \tag{5.4}$$

where c is the speed of light, H_0 is the Hubble constant and Ω_v and Ω_m are the vacuum density parameter and the mass density parameter respectively. The radiation density parameter, Ω_r, was ignored (valid at times after $\sim 10^5$ years,

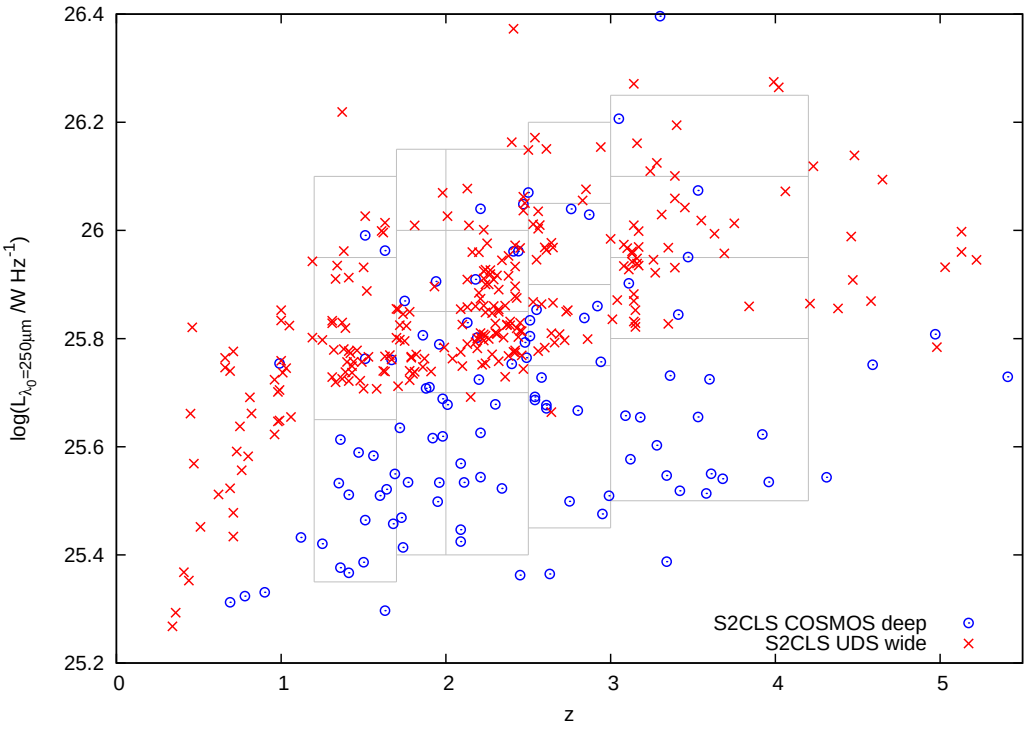

Figure 5.3: *The 250 μm rest–frame luminosity versus redshift plane coverage for the samples used here. The blue dots and red squares represent the S2CLS deep COSMOS and the S2CLS wide UDS samples respectively. The areas enclosed by the grey rectangles depict the redshift and luminosity bins used for the calculations of the IR LFs.*

z $\lesssim$ 50).

To translate L_{λ_s} into L_{250} I use the average SMG template with the dust temperature of $T_d = 35$ K from Michałowski et al. (2010a). The results of these calculations are shown in Figure 5.3.

The rest-frame SED determined for each source from the calculations of the L_{250} allowed me to find the maximum redshift at which this source would have been detected in a given map used here. This was done by calculating the flux density at the detection wavelength of the given survey (λ_d, column 2 of Table 5.1) using Equation 5.2 for a range of redshifts $z = 0 - 6$ and determining the redshift at which S_{λ_d} was smaller than the 1σ RMS noise times the SNR (columns 4 and 6 in Table 5.1 respectively). This way z_{max} for each source and field was calculated (2 values of z_{max}, one for each field, for every source) and used in the calculations of V_{max}.

5.4.2 Calculation of V_{max}

The sample was binned in redshift, as depicted in Figure 5.3. In a given bin the final maximum redshift at which each source could have been detected in that redshift bin, z_{max}^{bin}, was found for every source by comparing z_{max} from the previous subsection with the redshift limits of a given redshift bin. If z_{max} was found to be lower than the upper limit of the given redshift bin, then $z_{max}^{bin} = z_{max}$. If not, z_{max}^{bin} was set to the value of the upper limit of that redshift bin.

To find the maximum comoving volume of space that is available to each source, V_{max}, I use the following formula:

$$V_{max} = V_{max}^{\rm COS} + V_{max}^{\rm UDS}, \tag{5.5}$$

where $V_{max}^{\rm FIELD}$ is the maximum volume available for each source in a S2CLS deep COSMOS and wide UDS fields respectively.

To calculate $V_{max}^{\rm FIELD}$ for each galaxy in a given field I use the following formula:

$$V_{max}^{\rm FIELD} = A_{\rm FIELD} \times \int_{z_{low}}^{z_{max}^{bin}} \frac{c}{H_0} \frac{(1+z')^2 D_A^2}{\sqrt{\Omega_k (1+z')^3 + \Omega_v}} dz', \tag{5.6}$$

where $A_{\rm FIELD}$ is the solid angle subtended by given field on the sky in steradians and D_A is the angular-diameter distance defined as:

$$D_A = \frac{c}{H_0} \int_0^{z'} \frac{dz''}{\sqrt{\Omega_m (1+z'')^3 + \Omega_v}} / (1+z'). \tag{5.7}$$

Therefore, as an output of Equation 5.5, I get the maximum comoving volume of space available to each source which I can then use for the calculations of the LFs.

5.4.3 Calculation of the IR LFs

Each redshift interval was binned in luminosity, as in Table 5.3. To get the total IR luminosity, $L_{\rm IR}$, I have multiplied L_{250} for each source by a common factor determined from the shape of the average SMG template from Michałowski et al. (2010a):

$$L_{\rm IR} = 4.34 \times 10^{-14} \times L_{250}, \tag{5.8}$$

Table 5.3: *The luminosity/redshift bins, as depicted in Figure 5.3. The luminosity here is the rest-frame 250 μm luminosity in log(W Hz^{-1}), but the corresponding widths of the luminosity bins are the same for both the 250 μm and for the total IR luminosities. The size of the luminosity bins is 0.15 dex except for the first bin, where it is equal to 0.3. This was done to include a statistically significant number of sources in each luminosity/redshift bin.*

z	1.2-1.7	1.7-2.0	2.0-2.5	2.5-3.0	3.0-4.2
ΔL	25.35-25.65	25.40-25.70	25.40-25.70	25.45-25.75	25.50-25.80
	25.65-25.80	25.70-25.85	25.70-25.85	25.75-25.90	25.80-25.95
	25.80-25.95	25.85-26.00	25.85-26.00	25.90-26.05	25.95-26.10
	25.95-26.10	26.00-26.15	26.00-26.15	26.05-26.20	26.10-26.25

where $L_{\rm IR}$ is in $L_{\odot}$ and L_{250} is in W Hz^{-1}. Then, to calculate the LF at each redshift/luminosity bin, I have used the following formula:

$$\Phi(L,z) = \frac{1}{\Delta L}\sum_{i}\frac{1}{w_i \times V_{max}}, \tag{5.9}$$

with ΔL as in Table 5.3, w_i being the completeness and V_{max} the maximum comoving volume available for each source determined using Equation 5.5. The errors on $\Phi(L,z)$ were calculated using the Poissonian approach, where:

$$d\Phi(L,z) = \Phi(L,z) \times \frac{\sqrt{N}}{N}, \tag{5.10}$$

with N being the number of sources in each luminosity/redshift bin. The results of these calculations are depicted in Figure 5.4. In addition, the best-fit Schechter functions are plotted, where:

$$\Phi_{Sch}(L,z) = \Phi_{\star}\left(\frac{L}{L_{\star}}\right)^{\alpha} exp\left(\frac{-L}{L_{\star}}\right), \tag{5.11}$$

with $\Phi_{\star}$ being the normalization parameter, α the faint-end slope and $L_{\star}$ the characteristic luminosity which roughly marks the border between the linear fit, determined by the $(L/L_{\star})^{\alpha}$, and the exponential fit. The value of α was fixed here to the value presented in Gruppioni et al. (2013) equal to $\alpha = -0.2$. The reason for this, as explained in Section 5.6, is the lack of reliable information at faint luminosities.

The goodness of the Schechter fit was determined with the χ^2 minimisation

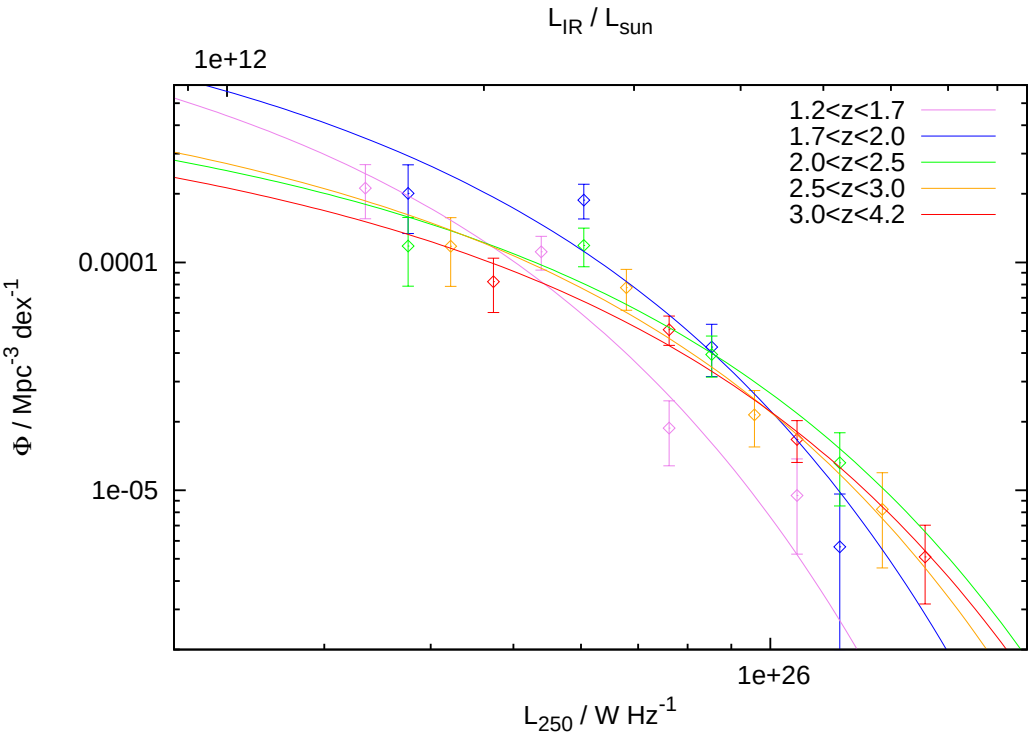

Figure 5.4: *The LFs for five redshifts bins calculated using Equation 5.9. The best-fit Schechter functions (Equation 5.11) are plotted as well, where the faint-end slope was fixed following Gruppioni et al. (2013) at the value of* $\alpha = -0.2$*. As discussed in Section 5.6 the faint-end slope was fixed because there was not enough information at the faint luminosities for it to be determined by the fit.*

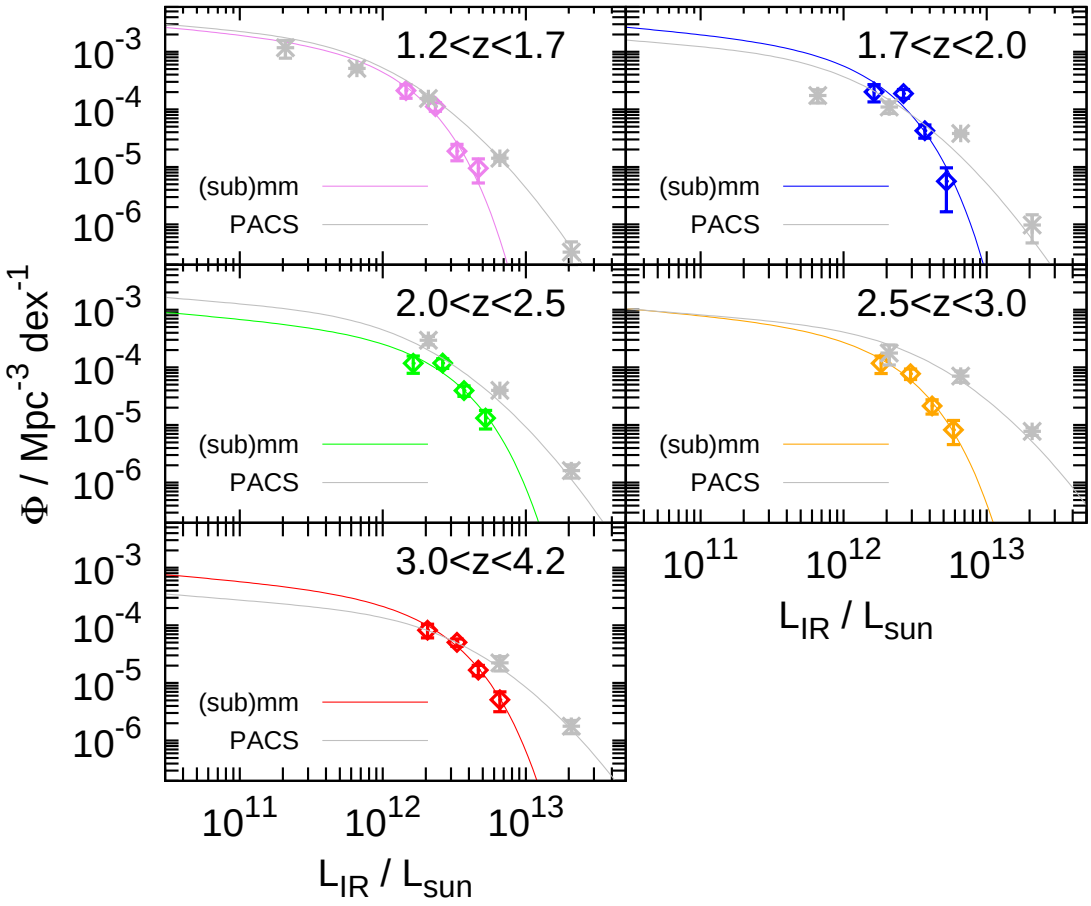

Figure 5.5: *The comparison of the IR LFs calculated in this work to the IR LFs from Gruppioni et al. (2013). The redshift bins are identical in both cases. The faint-end slope, as can be seen, was fixed at the Gruppioni et al. (2013) value of* $\alpha = -0.2$. *As discussed in Section 5.6, the differences in the bright-end shape of the LFs in each redshift bin may be caused by a combination of effects: the Eddington bias which causes the overestimate of the number of luminous sources in Gruppioni et al. (2013), the statistical variations in determined redshifts which can cause the overestimated redshift source to appear unnaturally bright in the upper redshift bin due to the positive K-correction at the Herschel PACS selection wavebands and source blending in the Herschel SPIRE bands in Gruppioni et al. (2013), which can make few faint sources appear as one very bright object, and therefore overestimate the calculations of the total IR luminosity.*

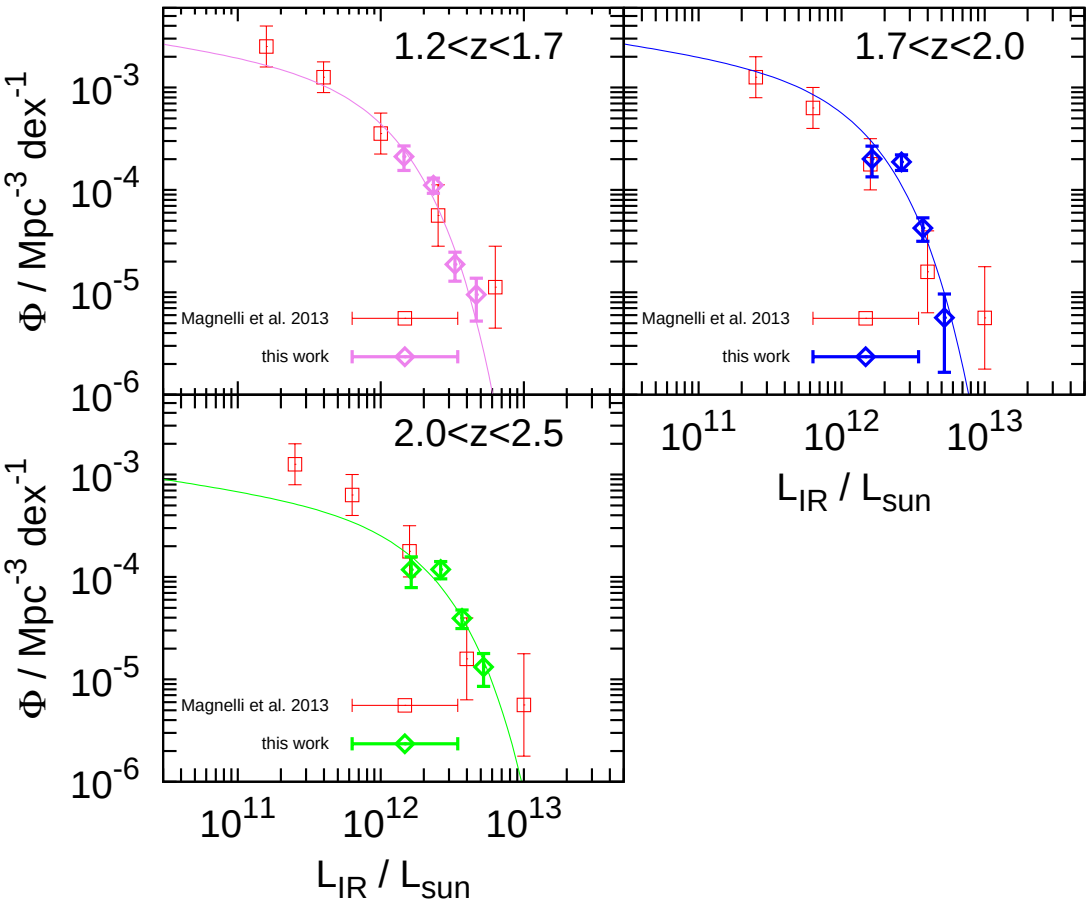

Figure 5.6: *The comparison of the IR LFs calculated in this work to the IR LFs from Magnelli et al. (2011). The redshift bins in Magnelli et al. (2011) are* $1.3 < z < 1.8$ *and* $1.8 < z < 2.3$*, so the first bin is compared with* $1.2 < z < 1.7$ *and the second with both* $1.7 < z < 2.0$ *and* $2.0 < z < 2.5$*. Data points in every redshift bin agree well within the error bars. Magnelli et al. (2011) detects more sources at the faint-end of the highest redshift bin shown here than what my Schechter fit does but this is simply a consequence of a fixed value of* α*. With more data at the faint-end, as discussed in Section 5.6, it will be possible to determine* α *and compare the fit to the Magnelli et al. (2011) faint-end data properly.*

Table 5.4: *The bet-fit Schechter function parameters at each redshift bin. The value of α has been fixed based on the low-redshift findings of Gruppioni et al. (2013). The luminosity is the rest-frame 250 μm luminosity. The errors are based on the 1σ contours from Figure 5.8.*

redshift range	α	$\log(\Phi_\star/\mathrm{Mpc^{-3}\,dex^{-1}})$	$\log(L_\star/\mathrm{L_\odot})$
$1.2 < z < 1.7$	-0.2[a]	$-2.85^{+0.18}_{-0.14}$	$25.31^{+0.06}_{-0.07}$
$1.7 < z < 2.0$	-0.2[a]	$-2.88^{+0.15}_{-0.14}$	$25.42^{+0.05}_{-0.07}$
$2.0 < z < 2.5$	-0.2[a]	$-3.39^{+0.20}_{-0.20}$	$25.60^{+0.07}_{-0.06}$
$2.5 < z < 3.0$	-0.2[a]	$-3.31^{+0.18}_{-0.22}$	$25.54^{+0.07}_{-0.08}$
$3.0 < z < 4.2$	-0.2[a]	$-3.46^{+0.16}_{-0.17}$	$25.59^{+0.04}_{-0.05}$

[a] Fixed value

method, where, for each redshift bin, and set of Schechter function parameters, the value of χ^2 is calculated using the following:

$$\chi^2 = \sum_i \frac{(\Phi_{Sch}(L,z) - \Phi(L,z))^2}{d\Phi(L,z)^2}, \tag{5.12}$$

where the summation is done over all the luminosity bins in a given redshift bin and $\Phi_{Sch}(L,z)$, $\Phi(L,z)$ and $d\Phi(L,z)$ were calculated using Equations 5.11, 5.9 and 5.10 respectively. The best-fit free parameters of $\Phi_{Sch}(L,z)$ ($\Phi_\star$, α and $L_\star$) are then determined by simply minimising χ^2 (Table 5.4).

In Figure 5.5 the IR LFs from this work are compared with IR LFs from Gruppioni et al. (2013). The redshift bins are identical in both works. Also, as seen in the Figure, the faint-end slope is in both cases identical ($\alpha = -0.2$). The differences in the bright-end slopes are discussed in Section 5.6. In addition I compare my findings with those of Magnelli et al. (2011) in Figure 5.6. Here, the data agrees very well (within the error bars). The number of faint sources ($L_{\mathrm{IR}} \sim 5 \times 10^{11}\,L_\odot$), as predicted by my Schechter fit, is smaller than the number of sources as determined by Magnelli et al. (2011). The reason for this is the faint-end slope fixed at the values of $\alpha = -0.2$ (see Section 5.6 for details).

5.5 Star formation rate density

Having determined the IR LFs for a range of redshifts, it is now possible to calculate the total IR luminosity density ($\rho_{\rm IR}$). This was done following the equation:

$$\rho_{\rm IR} = \int_{L_{min}}^{\infty} L_{\rm IR}\, \Phi(L_{\rm IR}, z)\, dlogL, \tag{5.13}$$

where L_{min} was set to be equal to $0.03L_{\star}$. To convert to the star–formation–rate density (SFRD), I used the relation of Kennicutt (1998):

$$SFRD = 4.5 \times 10^{-44}\, \rho_{\rm IR}, \tag{5.14}$$

where $\rho_{\rm IR}$ is in erg/s/Mpc^3 and the SFRD is in $M_{\odot}$/year/Mpc^3. The results of this calculation are depicted in Figure 5.7 as blue points. The results of the manual integration of the luminosity functions at the j-th redshift bin following the formula:

$$SFRD_{man,j} = 4.5 \times 10^{-44} \times \sum_{i=1}^{4} L_i\, \Phi_i(L_i, z_j)\, \Delta logL_i, \tag{5.15}$$

where L_i is the centre value of the i-th luminosity bin, $\Phi_i(L_i, z)$ is the luminosity function value at the i-th luminosity bin and $\Delta logL_i$ is the width of the i-th luminosity bin in log space, were also calculated and are plotted as green points. In addition I plot the results of Gruppioni et al. (2013) (red points), where the conversion from $\rho_{\rm IR}$ to the SFRD was again done using Equation 5.14, and the best–fit function for the total SFRD from Madau & Dickinson (2014).

To calculate the errors on the manually-found values of the SFRD, I simply assumed the Poissonian errors:

$$dSFRD_{man,j} = SFRD_{man,j} \times \frac{\sqrt{N}}{N}, \tag{5.16}$$

where N is the number of luminosity bins in each redshift bin = 4. Therefore the error on $SFRD_{man,j}$ is simply equal to $0.5\, SFRD_{man,j}$.

The errors on the integrated values of the SFRD were calculated using the following method. The errors on the free parameters of the Schechter function ($\Phi_{\star}$, $L_{\star}$, no errors on α since it was fixed) are plotted in Figure 5.8 where 1σ

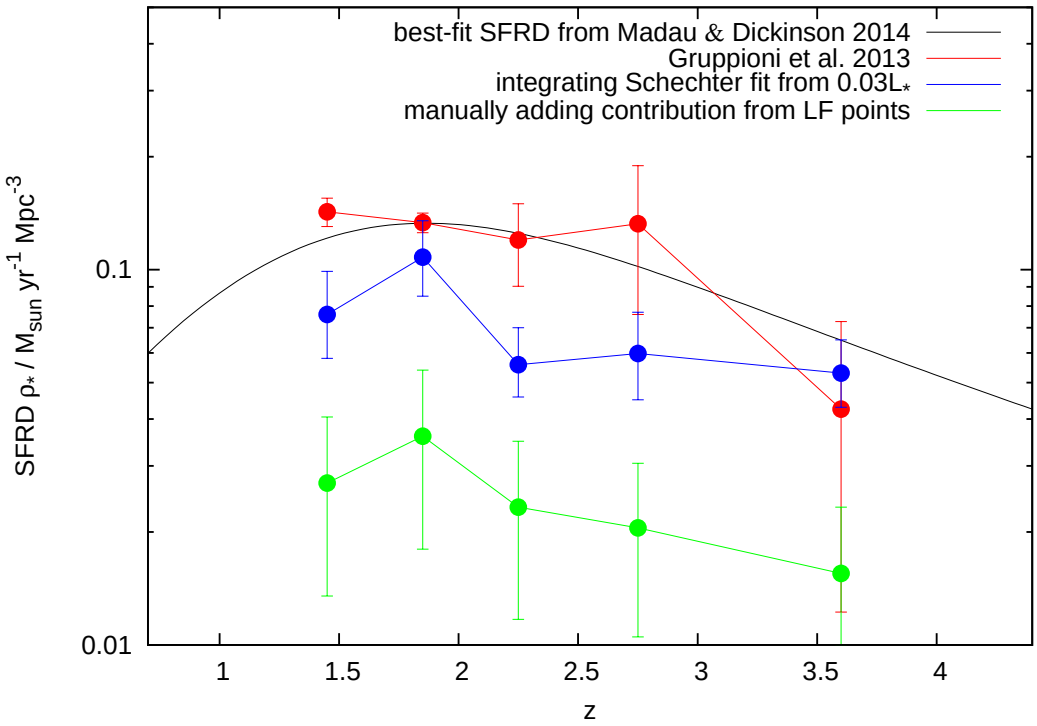

Figure 5.7: *The IR-based star formation rate density (SFRD) calculated using Equation 5.14 (blue points) compared with the manual integration of the SFRD following Equation 5.15 (green points) and the results of Gruppioni et al. (2013) (red points), where the conversion from ρ_{IR} to the SFRD was done using Equation 5.14. The black line depicts the best-fitting function to the total SFRD as found by Madau & Dickinson (2014).*

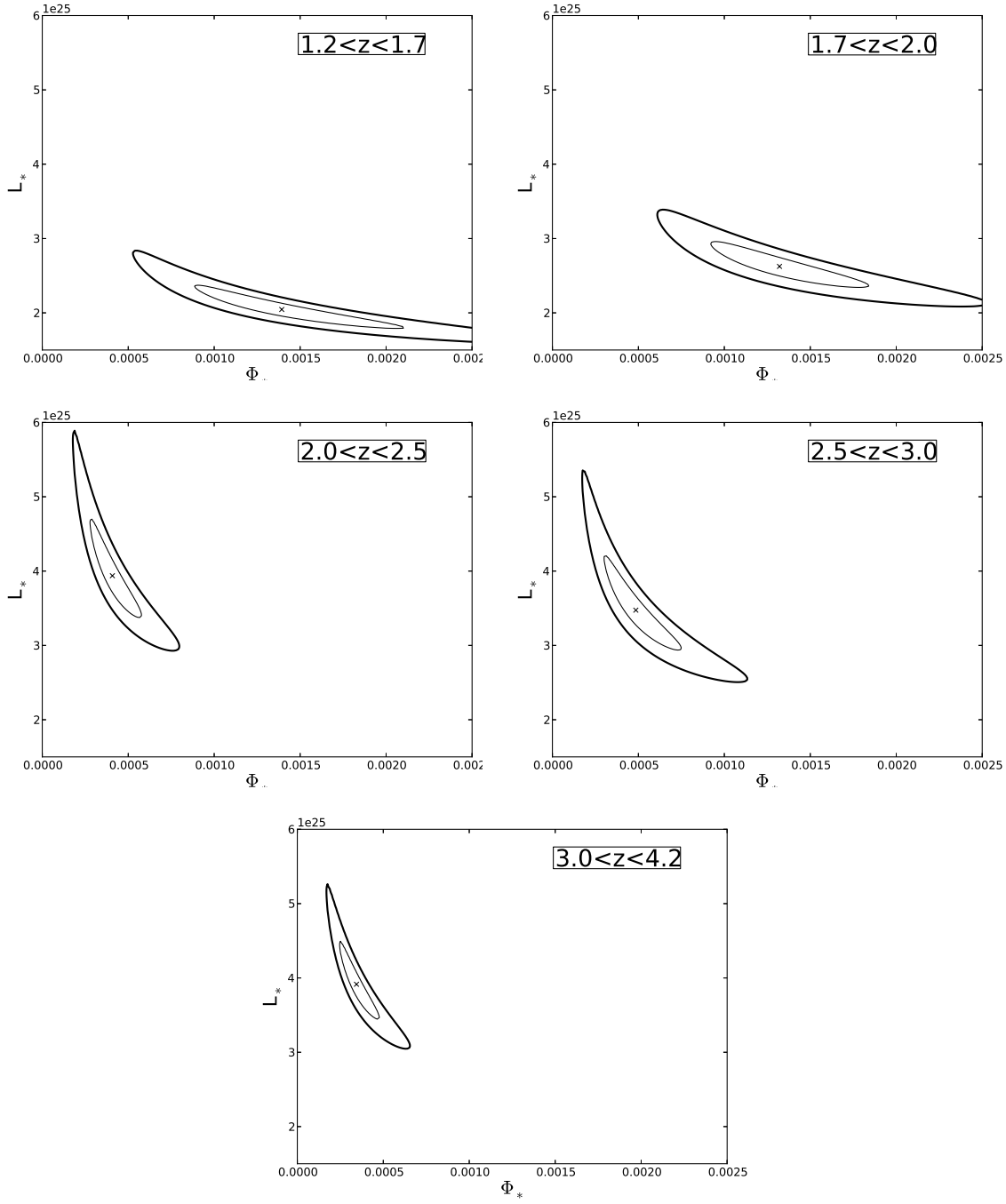

Figure 5.8: *The confidence intervals for $L_\star$ and $\Phi_\star$ for each redshift bin (as depicted in the figure) derived from the χ^2 minimisation method. The most probable value for each parameter is shown as a cross and the 1σ and 2σ confidence intervals ($\Delta\chi^2 = 1$ & 4 respectively) are shown as solid black contours.*

(inner contour) and 2σ (outer contour) errors are assumed to be equal to the values of the free parameters for which χ^2 increases by 1 and 4 respectively. Values of $\Phi_\star$ and $L_\star$ corresponding to the 1σ confidence interval were used to fit a set of new Schechter functions. For each one of those the SFRD was calculated following Equations 5.13 and 5.14. The maximum and minimum values of the SFRD calculated that way were then set as the upper and lower limit on the SFRD in each redshift bin (blue error bars in Figure 5.7).

5.6 Discussion

It is important to identify possible sources of systematic errors, biases which influence the derived values of Φ in Figure 5.4. A minor effect that has to be considered here is the inability to detect sources in a given luminosity bin with warmer dust temperature. The IR emission from these sources will peak at shorter wavelengths and therefore they will not be detectable at 850 μm. This may slightly underestimate the values of Φ. Also, as seen in Figure 5.3, 'long-wavelength' redshifts were used for the S2CLS wide UDS sample and for 44 sources in the S2CLS deep COSMOS sample which are known to be much less accurate than the optical photometric redshifts (Figure **??**). This, as discussed in Section 5.3.2, introduces a considerable scatter in the inferred values of 'long-wavelength' redshifts.

When comparing my results to Gruppioni et al. (2013) a disagreement between the bright end values can be clearly seen. This is most likely caused by a combination of the following effects. As explained in Section 1.2.3, the distribution of sources' flux densities undergoes statistical variations. Since there are many more low flux sources than high flux ones a galaxy of a given, observed flux density is much more likely an object with the observed brightness boosted up, rather than statistically lowered. This effect is called the 'Eddington bias' and will cause the number of the bright galaxies to be overestimated, affecting both mine and Gruppioni et al. (2013) samples. Converting from the statistically raised flux density at the detection wavelength to the rest-frame luminosity overestimates that luminosity. In my work, the negative K-correction (Figure 1.2) at the detection wavelength (850 μm) ensures that the boosting factor will remain roughly constant. In Gruppioni et al. (2013) however, since the selection

of the sources was made in *Herschel* PACS wavebands (70, 100 and 160 μm), the positive K-correction will significantly increase the boosting factor.

Another effect is based on the fact that some of the inferred redshifts may be somewhat imprecise. If the redshift for a given source is sufficiently underestimated to transport that source to a lower redshift bin, the inferred value of the IR luminosity will also be underestimated. Since many sources contribute to the low luminosity bins, it will not affect the faint-end of the LF in that redshift bin significantly. If, on the other hand, the redshift is too high and the source ends up in the higher redshift bin, its inferred IR luminosity will be highly overestimated, due to the positive K-correction at the *Herschel* PACS wavebands.

Finally, since *Herschel* SPIRE bands have large beam sizes (18.2, 24.9, and 36.3 arcsec in 250, 350 and 500 μm respectively), the effects of blending have to be taken into account. When estimating the IR luminosity, Gruppioni et al. (2013) used all the *Herschel* bands and since at SPIRE bands, fluxes are likely to be overestimated due to blending, the inferred values of the IR luminosities will also be overestimated. Since the values of the bright end of the LFs are usually determined based on a small number of sources, the combination of the above effects will likely cause the bright-ends of the IR LFs in Gruppioni et al. (2013) to be significantly overestimated and have to be interpreted with caution.

At the faint end both me and Gruppioni et al. (2013) fix the value of α. This is caused by the lack of sufficient data at the faint end of the LFs. The confusion noise for the SCUBA-2 850 μm band naturally sets the limit on the minimum flux density of the detected sources of ~ 1 mJy. To extend this limit, (sub)mm observatories with smaller beam sizes (LMT or ALMA) must be used. Since I did not have deeper data to use in this work, α had to be fixed based on the low redshift findings of Gruppioni et al. (2013). The comparison with Magnelli et al. (2011), as depicted in Figure 5.6, shows a good agreement in all redshift bins.

As can be seen in Figure 5.4 (see also Figure 5.8) and Table 5.4, the IR LF undergoes a slight evolution from z $\sim 1.2-2$, followed by virtually no evolution at higher redshifts. This suggests that there are more high luminosity ($L_{250} > 10^{26}$ W Hz^{-1}) and less low luminosity ($L_{250} < 5 \times 10^{25}$ W Hz^{-1}) galaxies at redshifts > 2 than at redshifts < 2. It also means that the values of the integrals of the IR LFs – SFRDs change with redshifts. The evolution of the SFRD with redshift is shown in Figure 5.7. The manually added contributions to the SFRD from

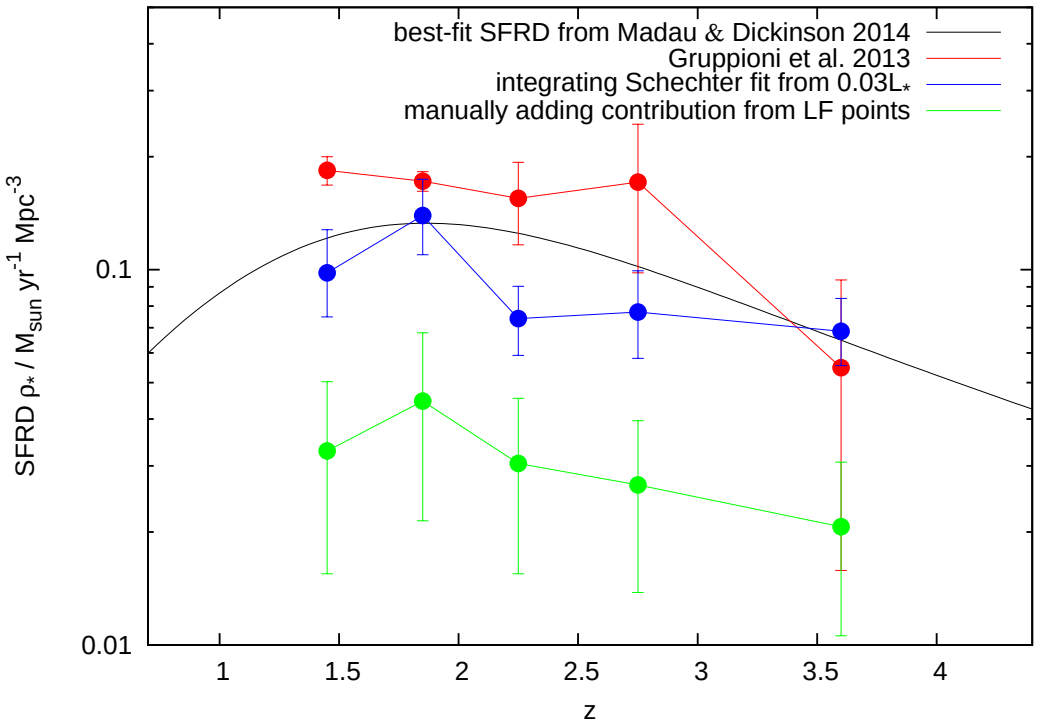

Figure 5.9: *The corrected star formation rate density (SFRD) calculated using Equation 5.17 (blue points) compared with the manual integration of the SFRD following Equation 5.15 (green points) and the results of Gruppioni et al. (2013) (red points), where the conversion from ρ_{IR} to the SFRD was done using Equation 5.14. The black line depicts the best-fitting function to the total SFRD as found by Madau & Dickinson (2014).*

individual data points in the IR LFs found in this work are shown in green. This is the lower limit on the contribution of the (sub)mm-selected galaxies to the total SFRD as found in this work. The blue points represent the calculations of the SFRDs based on the integrations of the best-fit Schechter functions (Table 5.4), the red points represent the results of Gruppioni et al. (2013), where $\rho_{\rm IR}$ was converted to the SFRD using Equation 5.14, and the black solid line depicts the best-fitting line to the total SFRD from Madau & Dickinson (2014).

In Figure 5.9 the total values of SFRD are shown (UV + IR), where the correction from the IR to the total SFRD for each data set were made following Reddy & Steidel (2009):

$$\mathrm{SFRD}_{total} \simeq 1.3 \times \mathrm{SFRD}_{\rm IR}. \tag{5.17}$$

It can be seen that the redshift evolution of my data (blue points) roughly follows the best-fit black line. The SFRDs of Gruppioni et al. (2013) clearly seem to be overestimated. As discussed above, this is most likely a consequence of the overestimated values at the bright-end of the IR LFs, caused by a combination of effects related to the *Herschel* PACS and SPIRE wavebands.

5.7 Summary

In this chapter I have estimated the (sub)mm-selected galaxies' contribution to the total SFRD. I have used the S2CLS deep COSMOS and wide UDS samples to calculate the rest-frame 250 μm luminosity functions for redshifts $1.2-4.2$. To convert from the 250 μm to the total IR luminosity the average SMG template of Michałowski et al. (2010a) was used. The total IR luminosity density, $\rho_{\rm IR}$, was determined with the $1/V_{max}$ method and the IR-based SFRD calculated using the relation of Kennicutt (1998).

I found that the IR-based SFRD peaks at z $\simeq$ 2 and steadily declines at higher redshifts. Assuming the ratio of the IR and UV-based SFRDs, $\mathrm{SFRD}_{\rm IR}/\mathrm{SFRD}_{\rm UV}$, of about 3.5 at redshifts $\sim 1.5-4$ (Reddy & Steidel, 2009), I estimated that (sub)mm-selected galaxies can fully account for the total SFRD as traced by the best-fitting function from Madau & Dickinson (2014).

However, because of the lack of the sufficient data at the faint-end of the IR LFs, the faint-end slope, α, had to be fixed at the value found for low redshifts by

Gruppioni et al. (2013). Deeper (sub)mm data (collected with LMT or ALMA) is absolutely necessary for the faint-end slope to be determined at high redshifts and the contribution of the submm-selected galaxies to the total SFRD calculated without any assumptions based on the low-redshift findings.

Chapter 6

Summary & Future plans

Throughout my PhD I have managed to deepen our understanding of the population of the (sub)mm-selected galaxies mainly thanks to the S2CLS efforts. The data collected during this unique survey allowed me to investigate closely the physical properties of these dusty objects. The large beam sizes of the single-dish (sub)mm observations can be decreased with the aid of the current state-of-the-art interferometers, like SMA, PdBI or ALMA. However, due to the modest fields of view ($\sim$ 20 arcsec at 850 μm for ALMA) the large sky surveys are extremely observationally expensive and the advancement of the current knowledge of the (sub)mm populations still largely relies on the single-dish data. To deal with the large beam sizes of the single-dish maps, I have used the p-statistics methodology to identify the multi-wavelengths counterparts to the SMGs. I have also managed to quantify the reliability of that method, based on the interferometric follow-ups, to be at the level of 75%. To account for this I have used the 'long-wavelength' redshifts determined using the SCUBA-2 and *Herschel* data to identify the optical IDs which were wrongly associated with the (sub)mm sources. This simple method allowed me to maximise both the reliability and the completeness of the photometric redshift estimations.

With the multi-band photometry, collected using the p-statistics, redshifts and other physical properties of the (sub)mm-selected sources were found. This population was determined to lie at the mean redshift of $\simeq 2.3$ with the 1σ scatter of ~ 1 at the average fluxes of $S_{850} \sim 3$ mJy and $\bar{z} \simeq 3.5$ with the similar scatter at the bright end ($S_{850} \sim 10$ mJy). I found this to be most likely caused by the combination of two effects: the cosmic variance and the correlation between

the (sub)mm flux and the redshift, where brighter galaxies tend to lie at higher redshifts.

Stellar masses and star formation rates were also found to be at the level of $M_\star \gtrsim 10^{10}\,M_\odot$ and SFR $\gtrsim 100\,M_\odot\ yr^{-1}$ respectively. Thanks to the depth of the S2CLS deep COSMOS map, I was able to investigate the relation between the SFR and the stellar mass for these galaxies in terms of the 'so-called' main sequence. I found that the (sub)mm-selected sources lie mainly on the star forming main sequence which makes them the high-mass extension of the normal star forming galaxies.

Finally, I was able to determine the SMGs contribution to the global star formation density. I found that the density of the star formation rate peaks at $z \sim 2$ with only the slight decline at higher redshifts. The total SFRD found here, after the addition of the UV contribution, follows closely the best-fitting function as found by Madau & Dickinson (2014). However, since the depth of the (sub)mm data is still relatively shallow (SFR $\sim 100\,M_\odot\ yr^{-1}$ as oppose to $\sim 10\,M_\odot\ yr^{-1}$ for the UV-selected sources) the above results rely on the assumption that the faint-end slope of the Schechter fit to the data remains constant at high redshifts. The only way to determine the evolution of the faint-end slope empirically is to collect the deeper (sub)mm data. For this reason, in the nearest future I plan to add two other deep S2CLS fields to the data of Chapter 5, namely the second S2CLS deep COSMOS daisy and the EGS field. This will add more reliable data at the faint-end of the IR LF and decrease the error bars. To extend the understanding of the faint-end of the IR LF, I will also add the ultra-deep data that is being collected as a part of the on-going ALMA Cycle 2 Hubble Ultra Deep Field (HUDF) survey (PI: Jim Dunlop), where ~ 100 sources are expected to be detected at the SFR level of $\simeq 25\,M_\odot\ yr^{-1}$. This will extend the IR LF to IR luminosities ~ 5 times lower than the lowest ones found in this work. In addition, since the HUDF has reliable redshifts estimated for every source, it will be possible to calculate the IR LF at the luminosities below the ALMA detection limit through stacking. All this will significantly increase the redshift/luminosity dynamic range and make the calculation of the contribution of the (sub)mm-selected galaxies to the total SFRD possible with the accuracy not achievable before.

In addition, I plan to use the very high-resolution interferometric CO data of a lensed LBG (the Cosmic Eye, Smail et al. 2007; Coppin et al. 2007) being

collected as a part of another Cycle 2 ALMA project (PI: Kristen Coppin), matched in resolution to HST/IFU observations, where the molecular gas and the star formation will be compared on the same scales in the lensing source plane. This will be done by determining the mass of the molecular gas ,M_{H_2}, from the luminosity of the CO lines and comparing to the SFR, calculated from the luminosity of the L_α line, on the pixel to pixel basis. In addition, the dynamics of the system will be mapped out by measuring the 'Doppler shifts' in the emission lines across the whole structure.

I also plan to use the unprecedentedly deep 850 μm continuum observations of 10 targeted 'typical/regular' LBGs, collected as a part of yet another ongoing Cycle 2 ALMA project (PI: Kristen Coppin) to look at their cold dust and ISM properties in detail across a range of LBG morphologies which has not been done in a systematic way yet because ALMA is needed to get down to sufficient depths (stacking reveals some clues: e.g. Coppin et al. 2015). Another projects I intend to be involved in in the near future are the IRAM 30-m project on a sample of CO in local mergers to look at the supposed 'bimodality' of the Kennicutt-Schmidt star formation relation and a S2CLS-based project involving looking at the AGN-Star Formation connection through *HST*-CANDELS morphologies of those SMG counterparts with IRAC colours suggestive of significant AGN power (e.g. Coppin et al. 2010) to compare with the morphologies of the more ubiquitous SF-dominated SMGs.

Appendix A

Notes on individual objects from Chapter 3

AzTEC1. A robust single identification only 0.03 arcsec from the SMA position, which would also be selected by the 8 μm method based on the original AzTEC position. Both z_{phot} and z_{LW} are in excellent agreement with the spectroscopic redshift of $z = 4.64$.

AzTEC2. A secure radio and 24 μm identification without a visible optical or K-band counterpart (and hence no stellar mass estimate in Table 3.5). An alternative object 1.4 arcsec away from the SMA position was selected by Smolčić et al. (2012) and found to have a spectroscopic redshift $z = 1.125$. However, since the radio position is only 0.39 arcsec from the SMA position and the mm/radio flux ratio yields a long-wavelength redshift estimate of $z_{LW} = 3.60$, this low-redshift object cannot be the correct identification (its mm/radio flux-density ratio is $\simeq 150$, inconsistent with such a low redshift. The correct radio identification would still have been secured without the improved positional accuracy provided by the SMA interferometry.

AzTEC3. Similar to AzTEC1, a robust single identification 0.21 arcsec from the SMA position, which would also be selected by the 8 μm method based on the original AzTEC position. Both z_{phot} and z_{LW} are in good agreement with the spectroscopic redshift of $z = 5.30$.

AzTEC4. A robust single identification 0.78 arcsec from the SMA position. z_{phot} and z_{LW} are in good agreement that the source has a redshift in the range $z = 4.5 - 5$. This source would have been successfully identified on the basis of

the original AzTEC position by both the $i-K$ and $8\,\mu$m methods.

AzTEC5. A robust single identification 0.38 arcsec from the SMA position. z_{phot} is in excellent agreement with the spectroscopic redshift $z = 3.97$, while z_{LW} is somewhat under-estimated. This source would have been securely identified using all four types of statistical association on the basis of the original AzTEC position.

AzTEC6. Not identified with any method either using the AzTEC position or the refined SMA position. There is an optical object $\simeq 1$ arcsec from the SMA position for which we find $z_{phot} = 1.12$ (this is also the ID adopted by Smolčić et al. (2012), with $z_{spec} = 0.82$), but as with AzTEC2 this optical counterpart can be excluded as the correct identification not just because of its relatively large positional offset, but also because its mm/radio flux-density ratio of $\simeq$ 150 is inconsistent with $z < 1.5$ ($z_{LW} \simeq 3.9$). The lack of any optical-infrared counterpart means that no stellar mass estimate for this object can be included in Table 3.5.

AzTEC7. A robust single identification 0.23 arcsec from the SMA position. z_{phot} and z_{LW} are in good agreement that the source has a redshift $z \simeq 2$. Like AzTEC5, this source would have been securely identified using all four types of statistical association on the basis of the original AzTEC position.

AzTEC8. A robust single identification 0.16 arcsec from the SMA position. Both z_{phot} and z_{LW} are in good agreement with the spectroscopic redshift of $z = 3.18$. This source would have been successfully identified on the basis of the original AzTEC position by both the $i-K$ and $8\,\mu$m methods.

AzTEC9. A robust single identification 0.77 arcsec from the SMA position. Like AzTEC4, z_{phot} and z_{LW} are in good agreement that the source has a redshift in the range $z = 4.5-5$. The radio identification would have been correctly selected on the basis of the original AzTEC position. Smolčić et al. (2012) selected a different object $\simeq 2.8$ arcsec from the SMA position with a photometric redshift of $z_{phot} \simeq 1.07$ and a spectroscopic redshift $z = 1.357$. However, not only is such a large positional offset very unlikely, but AzTEC9 has a large mm/radio flux ratio of $\simeq 100$, completely inconsistent with such a low redshift. I therefore conclude that the counterpart selected by Smolčić et al. (2012) cannot be correct, and that the true identification is the higher redshift galaxy listed in Table 3.5.

AzTEC10. There are three potential counterparts within 2 arcsec of the SMA

position. Using the SMA coordinates alone I would choose the closest and the brightest one, but because of the 8 μm flux and the very red $i - K$ colour of the more distant object ($\simeq 1.5$ arcsec from the SMA position), I chose it as the most likely identification. The photometric redshift determination yielded a very flat χ^2 curve with a formal minimum at $z > 7$. Even though such an extreme redshift is very unlikely, stacking the optical data shows that it is undetected in the optical wavebands suggesting $z > 5$. Also our mm/radio estimate gives a redshift of $z_{LW} = 3.12$ (arguably biased low due to using a cold SED template appropriate for lower-redshift objects). Considering this, and the probability distribution for the optical-infrared z_{phot}, for this object I adopt a redshift $z \simeq 5$. This object would have been correctly identified using all but the radio identification technique on the basis of the original AzTEC position.

AzTEC11. This source is split into two components by the SMA imaging, but it may be an extended object and therefore I continue to treat it as a single source. z_{phot} is in excellent agreement with the spectroscopic redshift $z = 1.60$, while this time z_{LW} is somewhat over-estimated. This source would have been securely identified using all four types of statistical association on the basis of the original AzTEC position.

AzTEC12. A robust single identification 0.16 arcsec from the SMA position. z_{phot} and z_{LW} are in good agreement that the source has a redshift $z \simeq 2.5$. Again, this source would have been securely identified using all four types of statistical association on the basis of the original AzTEC position.

AzTEC13. This object was not associated with any optical or IRAC counterpart using either the SMA or AzTEC position. A weak radio detection yields $z_{LW} \simeq 4.7$, but no stellar mass can be given in Table 3.5.

AzTEC14. Like AzTEC13 this object was not associated with any optical or IRAC counterpart using either the SMA or AzTEC position. The weak radio flux density measurement yields $z_{LW} \simeq 3.4$, but no stellar mass can be given in Table 3.5.

AzTEC15. A robust single identification 1.05 arcsec away from the SMA position. This source could not have been identified on the basis of the AzTEC position because the SMA centroid is shifted by more than 10 arcsec. z_{phot} and z_{LW} suggest $z \simeq 3$.

COSLA-5. This object has two possible optical counterparts less than 1.5 arcsec

from the PdBI position. The first one is 1.3 arcsec away with $z_{phot} = 0.85$, and is the identification adopted by Smolčić et al. (2012). However, because my mm/radio redshift estimate yields $z_{LW} \simeq 3.44$, we conclude that this cannot be the correct counterpart. The second possible optical counterpart is 1.1 arcsec away, but is only visible in the z'- and K_s-bands, and so no reliable optical/infrared photometric redshift could be derived. I thus cautiously adopt $z_{LW} = 2.5$, and do not give a stellar mass estimate in Table 3.5.

COSLA-6N. This object was not associated with any optical or IRAC counterpart on the basis of either the LABOCA or PdBI position. The weak radio flux measurement suggests $z_{LW} \simeq 3.7$, but no stellar mass estimate can be given in Table 3.5.

COSLA-6S. This object has an optical counterpart 0.5 arcsec from the PdBI position, for which Smolčić et al. (2012) derived $z_{phot} = 0.48$. However, once again because my mm/radio redshift estimate yields $z_{LW} \simeq 4$, and completely excludes $z < 1$, I conclude that this cannot be the correct identification (although clearly it could be a lensing galaxy). I thus adopt $z_{LW} \simeq 4$ as the best estimate of the redshift of the sub-mm source, but cannot provide a stellar mass estimate in Table 3.5.

COSLA-8. This object has no secure optical nor IRAC counterpart. It was associated by Smolčić et al. (2012) with an optical object 1 arcsec from the PdBI peak which was found to have $z_{phot} = 1.83^{+0.4}_{-1.31}$ based on two $\sim 3\sigma$ data points. Given the unreliability of this measurement, I choose here to adopt my mm/radio redshift estimate, but in fact this is perfectly consistent with the redshift given by Smolčić et al. (2012).

COSLA-16N. A robust single identification 0.70 arcsec from the PdBI position. z_{phot} and z_{LW} are in good agreement that the source has a redshift $z \simeq 2.25$. This source would have been securely identified using all four types of statistical association on the basis of the original LABOCA position.

COSLA-17N. A robust single identification 0.17 arcsec from the PdBI position, but this would not have been secured on the basis of the LABOCA position.

COSLA-17S. This object was not associated with any optical or IRAC counterpart. A weak radio flux measurement leads to $z_{LW} \simeq 4$, but I cannot provide a stellar mass estimate in Table 3.5.

COSLA-18. A robust single identification 0.16 arcsec from the PdBI position.

z_{phot} and z_{LW} are in good agreement that the source has a redshift $z \simeq 2$. This source would have been securely identified using all four types of statistical association on the basis of the original LABOCA position.

COSLA-19. This object was not associated with any optical or IRAC counterpart. A weak radio flux measurement leads to $z_{LW} \simeq 3.5$, but I cannot provide a stellar mass estimate in Table 3.5.

COSLA-23N. A robust single identification 0.11 arcsec from the PdBI position. z_{phot} and z_{LW} are in good agreement that the source has a redshift $z \simeq 4$. This object would have been correctly identified using all but the 24 μm identification technique on the basis of the original LABOCA position.

COSLA-23S. This object was not associated with any optical or IRAC counterpart. Smolčić et al. (2012) found an optical counterpart $\simeq 0.9$ arcsec from the PdBI peak with a redshift of $z_{phot} = 2.58^{+1.52}_{-2.48}$ based on one $\sim 3\sigma$ data point. I derive a mm/radio redshift estimate of $z_{LW} = 4.80$, and take it to be a more reliable redshift estimate, but cannot provide a stellar mass estimate in Table 3.5.

COSLA-35. A robust single identification 0.17 arcsec from the PdBI position. z_{phot} and z_{LW} are in excellent agreement that the source has a redshift $z \simeq 3$. This object would have been correctly identified using all but the 24 μm identification technique on the basis of the original LABOCA position.

COSLA-38. The PdBI coordinates for this object are $\simeq 15$ arcsec distant from the original LABOCA centroid, placing this object at the edge of the PdBI beam. In addition, the quoted PdBI flux density is higher than the original LABOCA flux density, raising the possibility that, for whatever reason, it is not the same source. For this reason we decided to exclude it from the main analysis, and so it does not appear in Table 3.5.

COSLA-47. A robust single identification 0.18 arcsec from the PdBI position. z_{phot} and z_{LW} are in reasonable agreement that the source has a redshift $z \simeq 3$. This object would have been tentatively identified on the basis of $i - K$ colour given the original LABOCA position.

COSLA-54. A robust single identification 0.50 arcsec from the PdBI position. z_{phot} and z_{LW} are in excellent agreement that the source has a redshift $z \simeq 3$. This object could not have been identified on the basis of the LABOCA position.

COSLA-128. This object was not associated with any optical or IRAC

counterpart given the PdBI position. I adopt $z_{LW} = 4.90$, but cannot provide a stellar mass estimate in Table 3.5.

Bibliography

Alexander D.M., Bauer F.E., Chapman S.C., Smail I., Blain A.W., Brandt W.N., Ivison R.J., 2005, ApJ, 632, 736

Amblard A., et al., 2010, A&A, 518, L9

Aravena M., Younger J.D., Fazio G.G., Gurwell M., Espada D., Bertoldi F., Capak P., Wilner D., 2010, ApJ, 719, L15

Aretxaga I., et al., 2007, MNRAS, 379, 1571

Aretxaga I., et al., 2011, MNRAS, 415, 3831

Ashby M.L.N., et al., 2006, ApJ, 644, 778

Ashby M.L.N., et al., 2013, ApJ, 769, 80

Austermann J.E., et al., 2010, MNRAS, 401, 160

Banerji M., Chapman S.C., Smail I., Alaghband-Zadeh S., Swinbank A.M., Dunlop J.S., Ivison R.J., Blain A.W., 2011, MNRAS, 418, 1071

Barger A.J., Cowie L.L., Sanders D.B., Fulton E., Taniguchi Y., Sato Y., Kawara K., Okuda H., 1998, Nat, 394, 248

Barnard V.E., Vielva P., Pierce-Price D.P.I., Blain A.W., Barreiro R.B., Richer J.S., Qualtrough C., 2004, MNRAS, 352, 961

Baugh C.M., Lacey C.G., Frenk C.S., Granato G.L., Silva L., Bressan A., Benson A.J., Cole S., 2005, MNRAS, 356, 1191

Beelen A., et al., 2008, A&A, 485, 645

Bertin E., Arnouts S., 1996, A&A Suppl., 117, 393

Bertoldi F., et al., 2000, A&A, 360, 92

Bertoldi F., et al., 2007, ApJS, 172, 132

Béthermin M., et al., 2012, A&A, 542, A58

Biggs A.D., et al., 2011, MNRAS, 413, 2314

Bintley D., et al., 2014, In: Society of Photo-Optical Instrumentation Engineers (SPIE) Conference Series, vol. 9153 of Society of Photo-Optical Instrumentation Engineers (SPIE) Conference Series, 3

Blain A.W., 1996, MNRAS, 283, 1340

Blain A.W., Jameson A., Smail I., Longair M.S., Kneib J.P., Ivison R.J., 1999, MNRAS, 309, 715

Blain A.W., Smail I., Ivison R.J., Kneib J.P., Frayer D.T., 2002, Phys. Rep., 369, 111

Borys C., Chapman S., Halpern M., Scott D., 2003, MNRAS, 344, 385

Bouwens R.J., et al., 2012, ApJ, 754, 83

Bowler R.A.A., et al., 2012, MNRAS, 426, 2772

Bowler R.A.A., et al., 2014, MNRAS, 440, 2810

Brand K., et al., 2007, ApJ, 663, 204

Bruzual G., Charlot S., 2003, MNRAS, 344, 1000

Burgarella D., Buat V., Iglesias-Páramo J., 2005, MNRAS, 360, 1413

Calzetti D., 2001, PASP, 113, 1449

Calzetti D., 2013, Star Formation Rate Indicators, 419

Calzetti D., Kinney A.L., Storchi-Bergmann T., 1994, ApJ, 429, 582

Capak P., et al., 2008, ApJ, 681, L53

Capak P., et al., 2011, ApJ, 730, 68

Caputi K.I., et al., 2006, ApJ, 637, 727

Caputi K.I., et al., 2007, ApJ, 660, 97

Caputi K.I., Cirasuolo M., Dunlop J.S., McLure R.J., Farrah D., Almaini O., 2011, MNRAS, 413, 162

Casey C.M., et al., 2012a, ApJ, 761, 140

Casey C.M., et al., 2012b, ApJ, 761, 139

Casey C.M., et al., 2013, MNRAS, 436, 1919

Casey C.M., Narayanan D., Cooray A., 2014, Phys. Rep., 541, 45

Chabrier G., 2003, ApJ, 586, L133

Chapin E.L., et al., 2009, MNRAS, 398, 1793

Chapin E.L., et al., 2011, MNRAS, 411, 505

Chapin E.L., Berry D.S., Gibb A.G., Jenness T., Scott D., Tilanus R.P.J., Economou F., Holland W.S., 2013, MNRAS, 430, 2545

Chapman S.C., Lewis G.F., Scott D., Borys C., Richards E., 2002, ApJ, 570, 557

Chapman S.C., Smail I., Blain A.W., Ivison R.J., 2004, ApJ, 614, 671

Chapman S.C., Blain A.W., Smail I., Ivison R.J., 2005, ApJ, 622, 772

Charlot S., Fall S.M., 2000, ApJ, 539, 718

Chary R., Elbaz D., 2001, ApJ, 556, 562

Chen C.C., Cowie L.L., Barger A.J., Casey C.M., Lee N., Sanders D.B., Wang W.H., Williams J.P., 2013a, ApJ, 762, 81

Chen C.C., Cowie L.L., Barger A.J., Casey C.M., Lee N., Sanders D.B., Wang W.H., Williams J.P., 2013b, ApJ, 776, 131

Cirasuolo M., et al., 2007, MNRAS, 380, 585

Cirasuolo M., McLure R.J., Dunlop J.S., Almaini O., Foucaud S., Simpson C., 2010, MNRAS, 401, 1166

Clements D.L., et al., 2010, A&A, 518, L8

Combes F., et al., 2012, A&A, 538, L4

Condon J.J., 1992, ARA&A, 30, 575

Coppin K., et al., 2006, MNRAS, 372, 1621

Coppin K., et al., 2008, MNRAS, 384, 1597

Coppin K., et al., 2010, ApJ, 713, 503

Coppin K.E.K., et al., 2007, ApJ, 665, 936

Coppin K.E.K., et al., 2009, MNRAS, 395, 1905

Coppin K.E.K., et al., 2015, MNRAS, 446, 1293

Cowie L.L., Lilly S.J., Gardner J., McLean I.S., 1988, ApJ, 332, L29

Cowie L.L., Barger A.J., Kneib J.P., 2002, AJ, 123, 2197

Cowie L.L., Barger A.J., Wang W.H., Williams J.P., 2009, ApJ, 697, L122

Cox P., et al., 2011, ApJ, 740, 63

Crocker A.F., et al., 2013, ApJ, 762, 79

Cucciati O., et al., 2012, A&A, 539, A31

da Cunha E., Charlot S., Elbaz D., 2008, MNRAS, 388, 1595

Daddi E., et al., 2007, ApJ, 670, 156

Daddi E., Dannerbauer H., Krips M., Walter F., Dickinson M., Elbaz D., Morrison G.E., 2009a, ApJ, 695, L176

Daddi E., et al., 2009b, ApJ, 694, 1517

Dale D.A., Helou G., 2002, ApJ, 576, 159

Dale D.A., Helou G., Contursi A., Silbermann N.A., Kolhatkar S., 2001, ApJ, 549, 215

Damen M., Förster Schreiber N.M., Franx M., Labbé I., Toft S., van Dokkum P.G., Wuyts S., 2009, ApJ, 705, 617

Dekel A., et al., 2009, Nat, 457, 451

Dekel A., Zolotov A., Tweed D., Cacciato M., Ceverino D., Primack J.R., 2013, MNRAS, 435, 999

Dempsey J.T., et al., 2013, MNRAS, 430, 2534

Devlin M.J., et al., 2009, Nat, 458, 737

Diolaiti E., Bendinelli O., Bonaccini D., Close L., Currie D., Parmeggiani G., 2000, A&A Suppl., 147, 335

Dole H., et al., 2006, A&A, 451, 417

Dowell C.D., et al., 2003, In: Phillips T.G., Zmuidzinas J. (eds.) Millimeter and Submillimeter Detectors for Astronomy, vol. 4855 of Society of Photo-Optical Instrumentation Engineers (SPIE) Conference Series, 73–87

Downes A.J.B., Peacock J.A., Savage A., Carrie D.R., 1986, MNRAS, 218, 31

Downes D., et al., 1999, A&A, 347, 809

Dunlop J.S., 2011, In: Wang W., Lu J., Luo Z., Yang Z., Hua H., Chen Z. (eds.) Galaxy Evolution: Infrared to Millimeter Wavelength Perspective, vol. 446 of Astronomical Society of the Pacific Conference Series, 209

Dunlop J.S., Peacock J.A., Savage A., Lilly S.J., Heasley J.N., Simon A.J.B., 1989, MNRAS, 238, 1171

Dunlop J.S., Hughes D.H., Rawlings S., Eales S.A., Ward M.J., 1994, Nat, 370, 347

Dunlop J.S., et al., 2004, MNRAS, 350, 769

Dunlop J.S., et al., 2010, MNRAS, 408, 2022

Dye S., et al., 2008, MNRAS, 386, 1107

Eales S., Lilly S., Gear W., Dunne L., Bond J.R., Hammer F., Le Fèvre O., Crampton D., 1999, ApJ, 515, 518

Eales S., Lilly S., Webb T., Dunne L., Gear W., Clements D., Yun M., 2000, AJ, 120, 2244

Eales S., et al., 2010, PASP, 122, 499

Eddington A.S., 1913, MNRAS, 73, 359

Elbaz D., et al., 2010, A&A, 518, L29

Elbaz D., et al., 2011, A&A, 533, A119

Farrah D., Afonso J., Efstathiou A., Rowan-Robinson M., Fox M., Clements D., 2003, MNRAS, 343, 585

Faucher-Giguère C.A., Kereš D., Ma C.P., 2011, MNRAS, 417, 2982

Furusawa H., et al., 2008, ApJS, 176, 1

Galametz M., et al., 2012, MNRAS, 425, 763

Geach J.E., et al., 2013, MNRAS, 432, 53

Georgantopoulos I., Rovilos E., Comastri A., 2011, A&A, 526, A46

Glenn J., et al., 2010, MNRAS, 409, 109

González V., Labbé I., Bouwens R.J., Illingworth G., Franx M., Kriek M., Brammer G.B., 2010, ApJ, 713, 115

Gonzalez V., Bouwens R., llingworth G., Labbe I., Oesch P., Franx M., Magee D., 2012, ArXiv e-prints

Greve T.R., Ivison R.J., Bertoldi F., Stevens J.A., Dunlop J.S., Lutz D., Carilli C.L., 2004, MNRAS, 354, 779

Greve T.R., Pope A., Scott D., Ivison R.J., Borys C., Conselice C.J., Bertoldi F., 2008, MNRAS, 389, 1489

Greve T.R., et al., 2012, ApJ, 756, 101

Griffin M.J., et al., 2010, A&A, 518, L3

Grogin N.A., et al., 2011, ApJS, 197, 35

Gruppioni C., et al., 2013, MNRAS, 432, 23

Gultekin K., 2009, ArXiv e-prints

Gwyn S.D.J., 2011, ArXiv e-prints

Gwyn S.D.J., 2012, AJ, 143, 38

Hainline L.J., Blain A.W., Smail I., Frayer D.T., Chapman S.C., Ivison R.J., Alexander D.M., 2009, ApJ, 699, 1610

Hainline L.J., Blain A.W., Smail I., Alexander D.M., Armus L., Chapman S.C., Ivison R.J., 2011, ApJ, 740, 96

Häring N., Rix H.W., 2004, ApJ, 604, L89

Hatsukade B., et al., 2010, ApJ, 711, 974

Hatsukade B., Ohta K., Seko A., Yabe K., Akiyama M., 2013, ApJ, 769, L27

Hayward C.C., Narayanan D., Kereš D., Jonsson P., Hopkins P.F., Cox T.J., Hernquist L., 2013, MNRAS, 428, 2529

Heckman T.M., et al., 2011, ApJ, 730, 5

Helou G., 1986, ApJ, 311, L33

Helou G., Soifer B.T., Rowan-Robinson M., 1985, ApJ, 298, L7

Hezaveh Y.D., et al., 2013, ApJ, 767, 132

Hodge J.A., et al., 2013, ApJ, 768, 91

Holland W.S., et al., 1999, MNRAS, 303, 659

Holland W.S., et al., 2013, MNRAS, 430, 2513

Houck J.R., et al., 2005, ApJ, 622, L105

Hughes D.H., et al., 1998, Nat, 394, 241

Iono D., et al., 2006, ApJ, 640, L1

Ivison R.J., Smail I., Le Borgne J.F., Blain A.W., Kneib J.P., Bezecourt J., Kerr T.H., Davies J.K., 1998, MNRAS, 298, 583

Ivison R.J., et al., 2002, MNRAS, 337, 1

Ivison R.J., et al., 2007, MNRAS, 380, 199

Ivison R.J., et al., 2010, MNRAS, 402, 245

Ivison R.J., et al., 2013, ApJ, 772, 137

Johnson S.P., et al., 2013, MNRAS, 431, 662

Johnston R., Vaccari M., Jarvis M., Smith M., Giovannoli E., Häußler B., Prescott M., 2015, ArXiv e-prints

Karim A., et al., 2011, ApJ, 730, 61

Karim A., et al., 2013, MNRAS, 432, 2

Kelly B.C., Shetty R., Stutz A.M., Kauffmann J., Goodman A.A., Launhardt R., 2012, ApJ, 752, 55

Kennicutt R.C., Evans N.J., 2012, ARA&A, 50, 531

Kennicutt R.C. Jr., 1998, ARA&A, 36, 189

Kessler M.F., et al., 1996, A&A, 315, L27

Knudsen K.K., van der Werf P.P., Kneib J.P., 2008, MNRAS, 384, 1611

Knudsen K.K., Neri R., Kneib J.P., van der Werf P.P., 2009, A&A, 496, 45

Knudsen K.K., Kneib J.P., Richard J., Petitpas G., Egami E., 2010, ApJ, 709, 210

Koprowski M.P., Dunlop J.S., Michałowski M.J., Cirasuolo M., Bowler R.A.A., 2014, MNRAS, 444, 117

Kovács A., Chapman S.C., Dowell C.D., Blain A.W., Ivison R.J., Smail I., Phillips T.G., 2006, ApJ, 650, 592

Kreysa E., et al., 1999, Infrared Physics and Technology, 40, 191

Kroupa P., 2001, MNRAS, 322, 231

Laird E.S., Nandra K., Pope A., Scott D., 2010, MNRAS, 401, 2763

Laurent G.T., et al., 2005, ApJ, 623, 742

Lawrence A., et al., 2007, MNRAS, 379, 1599

Le Floc'h E., et al., 2005, ApJ, 632, 169

Le Floc'h E., et al., 2009, ApJ, 703, 222

Leja J., van Dokkum P.G., Franx M., Whitaker K.E., 2015, ApJ, 798, 115

Lindner R.R., et al., 2011, ApJ, 737, 83

Lutz D., et al., 2011, A&A, 532, A90

Madau P., Dickinson M., 2014, ARA&A, 52, 415

Madau P., Ferguson H.C., Dickinson M.E., Giavalisco M., Steidel C.C., Fruchter A., 1996, MNRAS, 283, 1388

Magnelli B., Elbaz D., Chary R.R., Dickinson M., Le Borgne D., Frayer D.T., Willmer C.N.A., 2009, A&A, 496, 57

Magnelli B., Elbaz D., Chary R.R., Dickinson M., Le Borgne D., Frayer D.T., Willmer C.N.A., 2011, A&A, 528, A35

Magnelli B., et al., 2012, A&A, 539, A155

Magnelli B., et al., 2013, A&A, 553, A132

Maraston C., 2005, MNRAS, 362, 799

Martínez-Sansigre A., Rawlings S., Lacy M., Fadda D., Marleau F.R., Simpson C., Willott C.J., Jarvis M.J., 2005, Nat, 436, 666

Martínez-Sansigre A., et al., 2007, MNRAS, 379, L6

Martínez-Sansigre A., Lacy M., Sajina A., Rawlings S., 2008, ApJ, 674, 676

McCracken H.J., et al., 2012, A&A, 544, A156

McLure R.J., et al., 2011, MNRAS, 418, 2074

Michałowski M., Hjorth J., Watson D., 2010a, A&A, 514, A67

Michałowski M.J., Watson D., Hjorth J., 2010b, ApJ, 712, 942

Michałowski M.J., Dunlop J.S., Cirasuolo M., Hjorth J., Hayward C.C., Watson D., 2012a, A&A, 541, A85

Michałowski M.J., et al., 2012b, MNRAS, 426, 1845

Michałowski M.J., Hayward C.C., Dunlop J.S., Bruce V.A., Cirasuolo M., Cullen F., Hernquist L., 2014, ArXiv e-prints

Miyazaki S., et al., 2002, PASJ, 54, 833

Mocanu L.M., et al., 2013, ApJ, 779, 61

Murphy E.J., 2009, ApJ, 706, 482

Negrello M., Perrotta F., González-Nuevo J., Silva L., de Zotti G., Granato G.L., Baccigalupi C., Danese L., 2007, MNRAS, 377, 1557

Negrello M., et al., 2010, Science, 330, 800

Neugebauer G., et al., 1984, ApJ, 278, L1

Noeske K.G., et al., 2007, ApJ, 660, L43

Oke J.B., 1974, ApJS, 27, 21

Oke J.B., et al., 1995, PASP, 107, 375

Oliver S., et al., 2010a, MNRAS, 405, 2279

Oliver S.J., et al., 2010b, A&A, 518, L21

Oliver S.J., et al., 2012, MNRAS, 424, 1614

Ono Y., Ouchi M., Kurono Y., Momose R., 2014, ApJ, 795, 5

Osterbrock D.E., Ferland G.J., 2006, Astrophysics of gaseous nebulae and active galactic nuclei

Patel H., Clements D.L., Vaccari M., Mortlock D.J., Rowan-Robinson M., Pérez-Fournon I., Afonso-Luis A., 2013, MNRAS, 428, 291

Pellegrini E.W., Oey M.S., Winkler P.F., Points S.D., Smith R.C., Jaskot A.E., Zastrow J., 2012, ApJ, 755, 40

Peng C.Y., Ho L.C., Impey C.D., Rix H.W., 2002, AJ, 124, 266

Pilbratt G.L., et al., 2010, A&A, 518, L1

Poglitsch A., et al., 2010, A&A, 518, L2

Polletta M., Weedman D., Hönig S., Lonsdale C.J., Smith H.E., Houck J., 2008, ApJ, 675, 960

Polletta M.d.C., et al., 2006, ApJ, 642, 673

Pope A., et al., 2006, MNRAS, 370, 1185

Pope A., et al., 2008, ApJ, 675, 1171

Pozzi F., et al., 2004, ApJ, 609, 122

Puget J.L., Abergel A., Bernard J.P., Boulanger F., Burton W.B., Desert F.X., Hartmann D., 1996, A&A, 308, L5

Reddy N., et al., 2012a, ApJ, 744, 154

Reddy N.A., Steidel C.C., 2009, ApJ, 692, 778

Reddy N.A., Pettini M., Steidel C.C., Shapley A.E., Erb D.K., Law D.R., 2012b, ApJ, 754, 25

Relaño M., Kennicutt R.C. Jr., Eldridge J.J., Lee J.C., Verley S., 2012, MNRAS, 423, 2933

Renzini A., Peng Y.j., 2015, ApJ, 801, L29

Riechers D.A., et al., 2010, ApJ, 720, L131

Riechers D.A., et al., 2013, Nat, 496, 329

Rieke G.H., Alonso-Herrero A., Weiner B.J., Pérez-González P.G., Blaylock M., Donley J.L., Marcillac D., 2009, ApJ, 692, 556

Rodighiero G., et al., 2010, A&A, 515, A8

Rodighiero G., et al., 2011, ApJ, 739, L40

Rodighiero G., et al., 2014, MNRAS, 443, 19

Rodriguez-Puebla A., Primack J.R., Behroozi P., Faber S.M., 2015, ArXiv e-prints

Roseboom I.G., et al., 2012a, MNRAS, 426, 1782

Roseboom I.G., et al., 2012b, MNRAS, 419, 2758

Roseboom I.G., et al., 2013, MNRAS, 436, 430

Salmon B., et al., 2015, ApJ, 799, 183

Salpeter E.E., 1955, ApJ, 121, 161

Sanders D.B., Mazzarella J.M., Kim D.C., Surace J.A., Soifer B.T., 2003, AJ, 126, 1607

Sanders D.B., et al., 2007, ApJS, 172, 86

Santini P., et al., 2009, A&A, 504, 751

Sargent M.T., Béthermin M., Daddi E., Elbaz D., 2012, ApJ, 747, L31

Saunders W., Rowan-Robinson M., Lawrence A., Efstathiou G., Kaiser N., Ellis R.S., Frenk C.S., 1990, MNRAS, 242, 318

Schechter P., 1976, ApJ, 203, 297

Schinnerer E., et al., 2008, ApJ, 689, L5

Schinnerer E., et al., 2010, ApJS, 188, 384

Schreiber C., et al., 2015, A&A, 575, A74

Scott K.S., et al., 2008, MNRAS, 385, 2225

Scott K.S., et al., 2012, MNRAS, 423, 575

Scott S.E., et al., 2002, MNRAS, 331, 817

Scott S.E., Dunlop J.S., Serjeant S., 2006, MNRAS, 370, 1057

Shapley A.E., Steidel C.C., Pettini M., Adelberger K.L., 2003, ApJ, 588, 65

Siebenmorgen R., Krügel E., 2007, A&A, 461, 445

Silva L., Granato G.L., Bressan A., Danese L., 1998, ApJ, 509, 103

Simpson J.M., et al., 2014, ApJ, 788, 125

Siringo G., et al., 2009, A&A, 497, 945

Siringo G., et al., 2010, The Messenger, 139, 20

Smail I., Ivison R.J., Blain A.W., 1997, ApJ, 490, L5

Smail I., Ivison R., Blain A., Kneib J.P., 1998, In: American Astronomical Society Meeting Abstracts #192, vol. 30 of Bulletin of the American Astronomical Society, 1152

Smail I., Ivison R.J., Blain A.W., Kneib J.P., 2002, MNRAS, 331, 495

Smail I., Chapman S.C., Blain A.W., Ivison R.J., 2004, ApJ, 616, 71

Smail I., et al., 2007, ApJ, 654, L33

Smit R., et al., 2014, ApJ, 784, 58

Smith A.J., et al., 2012, MNRAS, 419, 377

Smolčić V., et al., 2011, ApJ, 731, L27

Smolčić V., et al., 2012, A&A, 548, A4

Speagle J.S., Steinhardt C.L., Capak P.L., Silverman J.D., 2014, ApJS, 214, 15

Spilker J.S., et al., 2014, ApJ, 785, 149

Staguhn J.G., et al., 2012, In: Society of Photo-Optical Instrumentation Engineers (SPIE) Conference Series, vol. 8452 of Society of Photo-Optical Instrumentation Engineers (SPIE) Conference Series

Stark D.P., Ellis R.S., Bunker A., Bundy K., Targett T., Benson A., Lacy M., 2009, ApJ, 697, 1493

Stark D.P., Schenker M.A., Ellis R., Robertson B., McLure R., Dunlop J., 2013, ApJ, 763, 129

Steidel C.C., Giavalisco M., Pettini M., Dickinson M., Adelberger K.L., 1996, ApJ, 462, L17

Steinhardt C.L., et al., 2014, ApJ, 791, L25

Sutherland W., Saunders W., 1992, MNRAS, 259, 413

Swetz D.S., et al., 2011, ApJS, 194, 41

Swinbank A.M., Smail I., Chapman S.C., Blain A.W., Ivison R.J., Keel W.C., 2004, ApJ, 617, 64

Swinbank A.M., et al., 2014, MNRAS, 438, 1267

Taniguchi Y., et al., 2007, ApJS, 172, 9

Targett T.A., et al., 2013, MNRAS, 432, 2012

Tasca L.A.M., et al., 2014, ArXiv e-prints

van Dokkum P.G., Conroy C., 2010, Nat, 468, 940

Vieira J.D., et al., 2010, ApJ, 719, 763

Vieira J.D., et al., 2013, Nat, 495, 344

Wall J.V., Pope A., Scott D., 2008, MNRAS, 383, 435

Walter F., et al., 2012, Nat, 486, 233

Wang N., et al., 1996, Appl. Opt., 35, 6629

Wang S.X., et al., 2013, ApJ, 778, 179

Wang W.H., Cowie L.L., Barger A.J., Williams J.P., 2011, ApJ, 726, L18

Wardlow J.L., et al., 2011, MNRAS, 415, 1479

Wardlow J.L., et al., 2013, ApJ, 762, 59

Webb T.M., et al., 2003, ApJ, 582, 6

Weedman D.W., Le Floc'h E., Higdon S.J.U., Higdon J.L., Houck J.R., 2006a, ApJ, 638, 613

Weedman D.W., et al., 2006b, ApJ, 651, 101

Weiß A., Ivison R.J., Downes D., Walter F., Cirasuolo M., Menten K.M., 2009a, ApJ, 705, L45

Weiß A., et al., 2009b, ApJ, 707, 1201

Weiß A., et al., 2013, ApJ, 767, 88

Whitaker K.E., van Dokkum P.G., Brammer G., Franx M., 2012, ApJ, 754, L29

Whitaker K.E., et al., 2014, ApJ, 795, 104

Wilson G.W., et al., 2008, MNRAS, 386, 807

Yan L., et al., 2007, ApJ, 658, 778

Younger J.D., et al., 2007, ApJ, 671, 1531

Younger J.D., et al., 2009, ApJ, 704, 803

Yun M.S., et al., 2012, MNRAS, 420, 957

Zavala J.A., Aretxaga I., Hughes D.H., 2014, MNRAS, 443, 2384

Publications

Koprowski M. P., Dunlop J. S., Michałowski M. J., Cirasuolo M., Bowler R. A. A. A reassessment of the redshift distribution and physical properties of luminous (sub-)millimetre galaxies. In *Monthly Notices of the Royal Astronomical Society*, 2014.

Koprowski M. P., Dunlop J. S., Michałowski M. J., Roseboom I., Geach J. E., et al. The SCUBA-2 Cosmology Legacy Survey: galaxies in the deep 850m survey, and the star-forming main sequence. Submitted to *Monthly Notices of the Royal Astronomical Society*, 2015.

Geach J. E., et al. (including Koprowski M. P.). A Submillimeter Galaxy Illuminating its Circumgalactic Medium: Lyα Scattering in a Cold, Clumpy Outflow. In *Astrophysical Journal*, 2014.

Michałowski M. J., et al. (including Koprowski M. P.). Spatially-resolved dust properties of the GRB 980425 host galaxy. In *Astronomy and Astrophysics*, 2014.

Michałowski M. J., et al. (including Koprowski M. P.). VizieR Online Data Catalog: Imaging GRB 980425 in millimetic and submm (Michalowski+, 2014). VizieR Online Data Catalog, 2013.